Fakultät für Medizin

Lehrstuhl für Biologische Bildgebung

Design and Synthesis of Calcium Sensors for Photoacoustic Imaging

Sheryl Roberts

Vollständiger Abdruck der von der Fakultät für Medizin der Technischen Universität München zur Erlangung des akademischen Grades eines

Doctor of Philosophy (Ph.D.)
genehmigten Dissertation.

Vorsitzende: Prof. Dr. Agnes Görlach

Prüfer der Dissertation:

1. Prof. Dr. Vasilis Ntziachristos
2. Prof. Dr. Thorsten Bach

Die Dissertation wurde am 23.08.2017 bei der Fakultät für Medizin der Technischen Universität München eingericht und durch die Fakultät für Medizin am 12.09.2017 angenommen.

Department of Medicine

Chair of Biological Imaging

Design and Synthesis of Calcium Sensors for Photoacoustic Imaging

Sheryl Roberts

Complete reprint of a thesis approved by the Department of Medicine of Technische Universität München for attaining the title of

Doctor of Philosophy (Ph.D.).

Chair: Prof. Dr. Agnes Görlach

Examiners of dissertation:

1. Prof. Dr. Vasilis Ntziachristos
2. Prof. Dr. Thorsten Bach

The dissertation was submitted to the PhD program in the Department of Medicine of the Technische Technische Universität München on the 23.08.2017 and accepted by the Technische Universität München on the 12.09.2017.

Dedicated to my mother, a true warrior

I still look for your face in the crowd. If only you could see me now.

This doctoral dissertation was prepared at the Technical University Muenchen (Medical Faculty, TUM) and Helmholtz Zentrum Muenchen (Institute of Biological and Medical Imaging) under the guidance and supervision of Prof. Gil Westmeyer. Involved are my dissertation committee, with Prof. Thorsten Bach (TUM Organic Chemistry Department) and Prof. Vasilis Ntziachristos (TUM Biological and Medical Imaging.)

Abstract

Contrast agents have provided us invaluable insights into the organisation and function of biological systems. The class of fluorescent calcium sensors has for instance uncovered remarkable details of neuronal activity. With the ultimate goal towards non-invasive neuroimaging of brain function using photoacoustic tomography, this dissertation evaluates synthetic strategies to develop calcium-responsive sensors for photoacoustic imaging. Photophysical characterisations of near-infrared metallochromic compounds responsive to divalent metals as well as a calcium-specific compounds based on a semi-cyanine scaffold are provided. These examples provide interesting starting points for the synthesis of chromic, near-infrared sensors for molecular imaging *via* photoacoustics.

Zusammenfassung

In der medizinischen Bildgebung werden Kontrastmittel zur Gewinnung wertvoller Erkenntnisse über den Aufbau und die Funktion biologischer Organismen eingesetzt. Insbesondere die Klasse der fluoreszierenden Kalziumsensoren hat bemerkenswerte Einsichten in die neuronalen Aktivitäten von Gehirnzellen ermöglicht. Diese Dissertation evaluiert synthetische Methoden zur Entwicklung kalziumreaktiver Kontrastmittel für die photoakustische Bildgebung mit dem Ziel der nichtinvasiven neuronalen Bildgebung von Gehirnaktivität mittels photoakustischer Tomografie. Die photophysischen Eigenschaften einer nahinfrarot-metallochromischen Verbindung, die auf einem Semicyanin-Gerüst basiert und selektive Affiniät zu Kalzium aufweist, werden vorgestellt.Die vorgestellten Beispiele bieten interessante Ansatzpunkte für die Synthese chromischer nahinfrarot-Kontrastmittel für die molekulare Bildgebung mittels photoakustischer Methoden.

Table of Contents

Goals and overall objectives

It was the primary goal of my dissertation work to develop a chemical platform for generating molecular sensors for photoacoustic imaging. In particular, it was my goal to design, synthesize and characterize a new sensor for the key second messenger calcium that can be read out by photoacoustic imaging in live tissue. This multi-disciplinary project will exploit the versatility of chemical reactions coupled with *in- vitro* and *in vivo* characterisation of molecules and ultimately in combination with optoacoustic imaging as a tool for studying brain activations. contrast agents (CAs) are to be synthetically modified in order to tune their affinity towards intracellular concentrations of calcium and by going deeper into biological tissue than microscopy. This work is to contribute towards the long-standing goal of non-invasive neuroimaging of brain function *via* photoacoustic imaging technologies. Fig. 1 shows the general workflow of my projects.

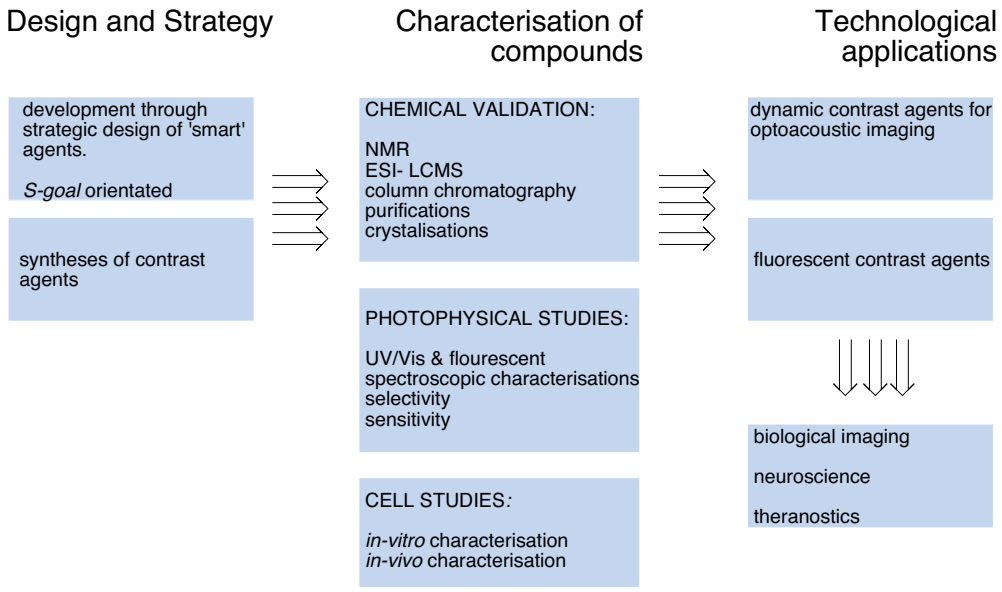

Figure 1: **Broad objectives of project.** The summary of project executions, chemical workflow, validation and evaluating technological applications of new probe.

Structure of the dissertation

There are three chapters. The first chapter is mainly concern with introducing the photoacoustic technology. The goal is to introduce and highlight the latest advances in exogenous and endogenous contrast agents for molecular Photoacoustic imaging (PAI) and its considerations for *in vivo* molecular PAI. Its current challenges are discussed and we tackle some of the problems and demands for much needed molecular neuroimaging probes. The details of this chapter will mainly focus on the structural, chemical and photophysical characteristics of the current photoacoustic agents. The second chapter highlights the key design and syntheses towards the new generation of cyanines for dynamic sensing. It starts with introducing the cyanine dye family and how ligands can be functionalised onto the core, in particular, calcium sensing moieties. Chapter 2 explores our attempts to synthesise functional indoles, the precursors needed to form the cyanine core, in three different strategies (A, B and C). The rational design and results for each strategy are discussed. The third and last chapter, describes in further detail Strategy C. The promising results in Strategy C, shown in Chapter 2 were investigated in further details as the platform to diversity our chemical platform. Chapter 3 presents and discusses several aspects of the lead compound Ca^{2+}-Selective Photoacoustic Agent (CaSPA)-550. Chapter 3 explores in detail *in vitro* and *in vivo* characterisations of CaSPA-550 AM.

Chapter 1

Sensors for photoacoustic tomography: a literature review

Objectives

PAI is a powerful non-invasive imaging tool. It offers a unique combination of high performance imaging characteristics such as deep tissue penetration of several centimeters with a high light-scattering independent spatial resolution (≈100 μm), ultrasensitive detection of probes/target (sub-picomole) and real-time imaging capabilities.[1,2] Its potential for molecular imaging have been shown in several proof-of-concept visualisations of biological processes.[3–6] In this chapter, as part of the dissertation, I introduce the chemical, physical and biochemical characteristics of existing PA contrast agents, highlighting its key applications. Present challenges for molecular PAI are addressed and the key topic of this dissertation examined: the synthetic approaches and design of novel small-molecule probes for dynamic photoacoustic imaging.

1.1 Why photoacoustics?

Current imaging technologies are powerful tools giving us information in everyday preclinical research, diagnostics and therapeutic monitoring. The aim of molecular imaging is to see and quantify biological events at molecular and cellular levels in a *non-invasive* approach. In this way, it can give us an opportunity to detect, stage, predict and monitor diseases. The selection of a particular imaging modality depends on the biological processes that are to be visualised and what type of information needed to be obtained. The present *non-invasive* techniques such as MRI suffers from **intrinsic insensitivity** and limited by **low spatiotemporal resolution**, namely Positron emmission tomography (PET), Fluorescence molecular tomography–X-ray computed tomography (FMT-XCT) and Single-photon emission computed tomography (SPECT). Multi-spectral optoacoustic tomography (MSOT) addresses these limitations.

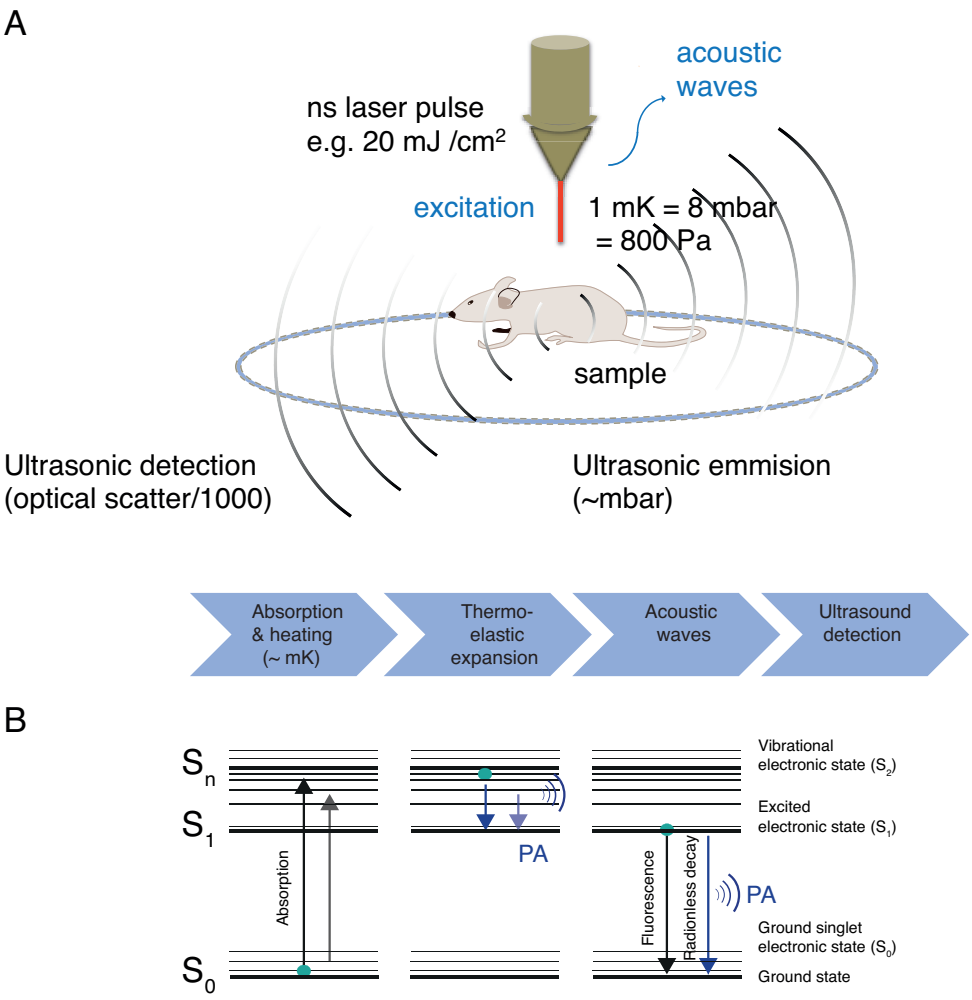

Figure 1.1: **Principles of photoacoustic tomography**. (A) An agent of interest absorbs light. Fast absorption transients by agents causes small pressure waves which are due to thermo-elastic expansion. Acoustic waves are detected by the transducers. A variety of back projection algorithms are used to reconstruct photoacoustic images. (B) General Jablonski diagram showing a typical energy transition paths of a photoacoustic agent after optical excitation. An agent in a ground state (S_o) can be found in an excited state (S_1) after absorption of light. It undergoes rotational and vibrational modes (according to Kasha's rule) creating local tissue heating before emitting its photons in a radiative or non-radiative fashion.

PAI technology uses a combination of high optical contrast of light for excitation of absorbers with the high spatial resolution of ultrasound detection.[7–9]The fact that sound waves do not scatter as much as photons is a distinctive feature of PAI that overcomes the traditional depth limitation of optical imaging. PAI at near-infrared (NIR) window can achieve a penetration depth of several centimeters with a resolution on the order of a few hundred micrometers.[10] PAI is one of the

fastest growing imaging techniques, already adopted for pre-clinical *in vivo* imaging in small animals. Several relevant studies for PAI includes primary thyroid tumor detection,[11] therapeutic monitoring[12,13] and for the identification and assessment of metastatic lymph nodes.[14,15]

1.2 Endogenous contrast agents for photoacoustic imaging

1.2.1 Intrinsic chromophores

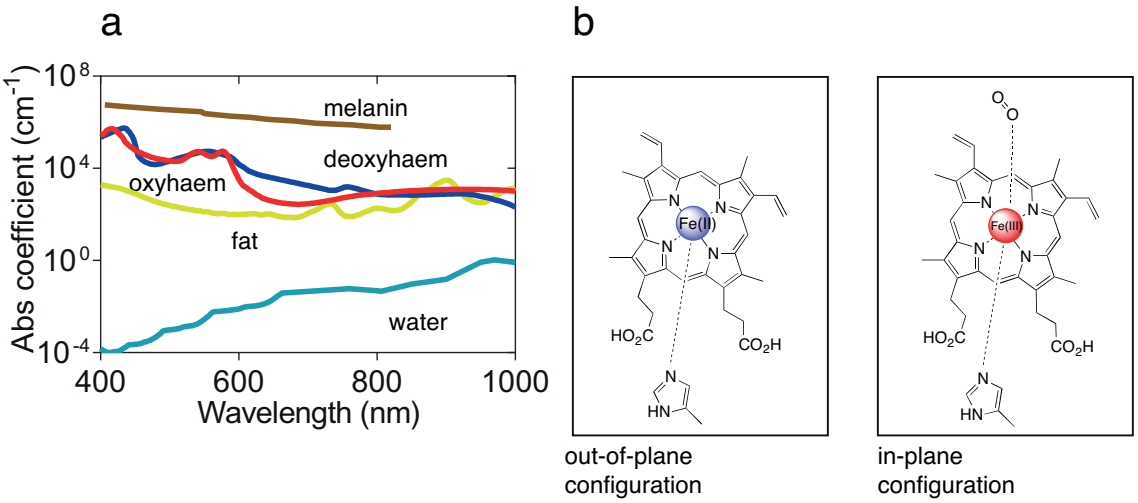

Figure 1.2: **Photoacoustic imaging of endogenous chromophores**. (a) Absorption spectra of the main endogenous tissue chromophores: melanin (brown line, 1M); oxyheamoglobin (red line, 1 M); deoxyhaemoglobin (blue line, 1 M); fat (green line, 1M) and water (cyan line, 1M) at their typical concentrations in the human body. (b) Heme is a strongly absorbing iron-containing phorphyrin ring. It exists in two various configurations in the absence (left) and presence (right) of oxygen which are spectrally distinct in its absorption spectrum.

Table 1.1: An overview of intrinsic chromophores investigated for photoacoustic imaging

intrinsic chromophores	**notable abs peak(s) (nm)**	**REF**
Haemoglobin	500- 600	3,13,16
melanin	764	17–19
lipids	1210	15
water	975	20

Endogenous absorbers, primarily haemoglobin, lipids, melanin and water are exploited for structural and functional information in biological systems. Haemoglobin, which delivers oxygen throughout the body, changes in structural and electronic configuration in the presence and absence of oxygen, shown in Fig. 1.2. Its absorption is spectroscopically distinct at 660 and 940 nm with and without oxygen, making it possible to measure haemoglobin concentration and oxygen saturation levels. Useful applications includes the validation of PAI for quantitative measure of ovarian tumour response to antiangiogenic therapy shown by Bohndiek *et al.*[16] and imaging of tumour vasculature shown by Laufer *et al.*[13]. Real-time *non-invasive* acquisition of haemodynamics in the whole mouse brain without contrast enhancement was successfully implemented by Gottschalk *et al.*[3]. PA implementations without the use of exogenous CAs is of clinical advantage and relevant to physiology and pathology. However, these methods have limited detection depth. An exogenous CAs is often needed to enhance contrast-to-noise signals, allowing visualisations of vasculature mapping, functional imaging of haemodynamic parameter such as variations in blood oxygenation, total haemoglobin and cerebral volume changes and functional photoacoustic imaging (fPAI).[21]

Disruption of metabolic enzymatic pathways leads to its associated diseases. PAI was able to map, for the first time, lipid biodistribution *in vivo* on the basis of absorption peaks at 930 and 1210 nm (overtone of C-H bonds).[15] Melanin, a naturally occurring pigment found in skin, hair and eyes absorbs intensely and accounts for most of the optical contrast found in the visible region in mammalian systems. At 764 nm, it has a higher extinction coefficient than oxy/deoxy haemoglobin and can be spectrally unmixed from haemoglobin as shown from studies using melanin- pigmented primary melanomas[17,18] and metastatic melanoma cells.[19]

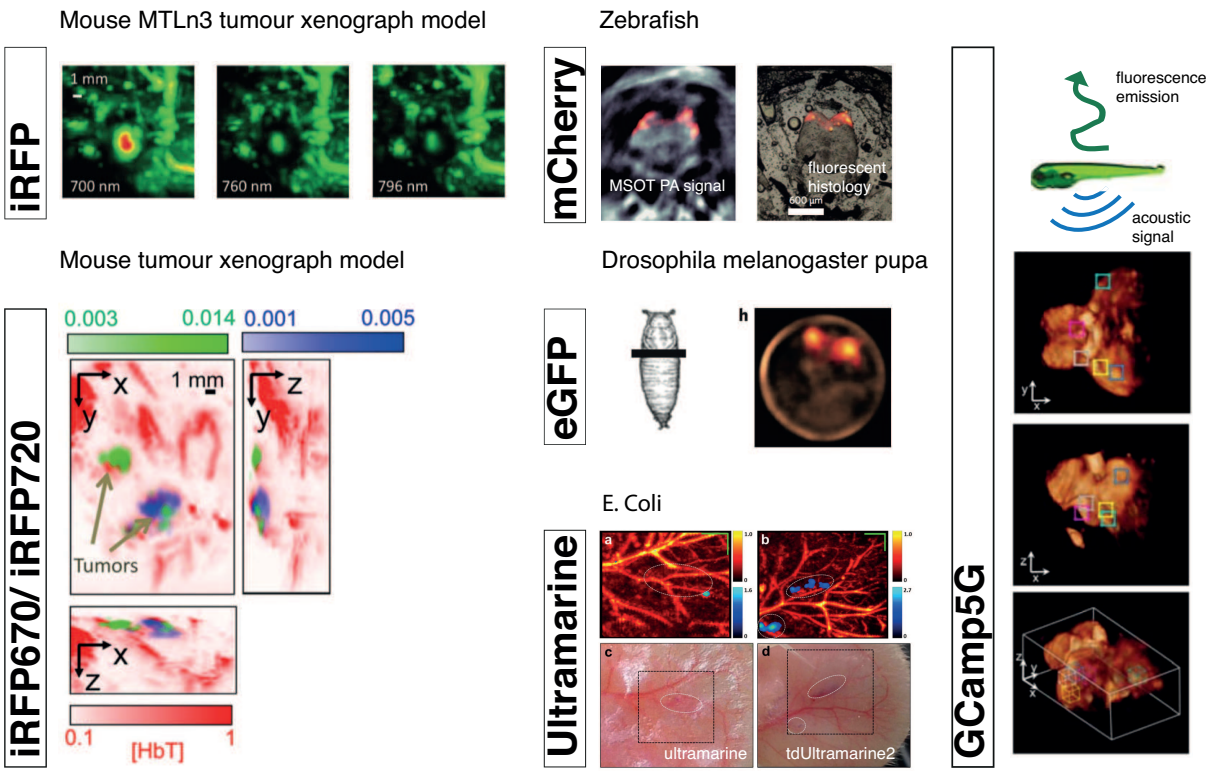

Figure 1.3: **Biological studies and imaging of various genetically encoded sensors using photoacoustic tomography.** Imaging of iRFP,[22,23] iRFP670[24] and iRFP720[24] in mouse xenograph models; mCherry in adult zebrafish;[25] eGFP in drosophila melanogaster pupa[25] and ultramarine[26] and tdUltramarine2 in E. coli pellet injected into ear of a rat.[26] Further details on the photophysical properties of these chromoproteins, refer to Table 1.2

1.2.2 Genetically encoded chromophores

Table 1.2: **Purified genetically encoded (GE) chromophores investigated for photoacoustic imaging.** Using GE chromophores in simultaneous deep-tissue imaging is a non-invasive technique for studying biological processes *in vivo*. Its potential is towards studying complex physiological and pathogenic processes for prolonged time periods and molecular and cellular level in the future.

GE chromophores	**Abs$_{max}$ (nm)**	ε (M^{-1} cm^{-1})	**REF**
iRFP		-	22
iRFP670	645	114, 000	24
iRFP720	703	96, 000	24
mNeptune	600	59, 000	24
E2-Crimsom	603	58, 500	24
eqFP670	603	70 ,000	24
iRFP713	692	98, 000	24
mCherry	587	-	25
eGFP	488	-	25
ultramarine	585	64, 400	26
tdUltramarine 2	587	81,500	26
cjBlue	610	52, 700	26
cjBlue2	603	56, 600	26

Molecular imaging with reporter genes is well-established utilising fluorescence as read-out and allowing direct visualisation of cellular, sub-cellular activation and protein- protein interactions *in vivo*.[27,28] Under the control of a promoter of interest, a reporter gene expresses proteins that either provide fluorescent and PA contrast or produces a product that yield PA signals. The first report on the photoacoustic visualisation of these reporter proteins, mCherry and eGFP fluorescent proteins (FPs), was shown by Razansky *et al.*[25] in an adult zebrafish. With the use of mCherry, the limitation of optical microscopy was achieved beyond penetration depths while providing high sensitivity and spatial resolution. The green fluorescent protein (GFP) family is however, too short of a wavelength for *in vivo* applications beyond transparent organisms, inferring strong background

signals by endogenous CAs. There have been some attempts to obtain photoacoustic contrast from genetically expressed proteins. In particular the red shifted variants of phytochrome-based NIR FPs. The first variant of this was iRFP[23] and the other study has been successfuly performed to track neural calcium dynamics in a zebrafish brain labelled with a genetically encoded GCaMP5G, demonstrated by Sela *et al.* [29].

1.3 Exogenous contrast agents in photoacoustic imaging

1.3.1 Parameters to consider for ”smart” PA agent design

The design study for NIR probes is based on two essential structural features: a target-binding moiety and a chromophore. At least one target-binding moiety is connected to at least one strong absorbing chromophore. To function as a dynamic sensor, the target-binding moiety must either alter its electronic or chemical structure as a probe. Variation in the electronic structure (electron transfer and/or internal charge transfer) can lead to a change in absorption and/or emission properties. The ideal ”smart” CAs for PAI is described in detail below.

1.3.2 Photophysical properties

There are several important factors to consider when one is to design synthetic molecules for PAI. We aim to synthesise probes that are in the long wavelength range (550-950 nm), to maximise the penetration depth by avoiding the strong absorption from intrinsic chromophores. High extinction coefficient (ε), ideally $\geq$200,000 M^{-1} cm^{-1}) with characteristic absorption spectrum is desirable to ensure high sensitivity detection which can be detected even at low concentrations and avoid unambiguous identification. It is desirable to have low quantum yield (ϕ) at ≤ 0.1 to maximise the non-radiative conversion of light energy to heat.[10] To date, many of the NIR dyes for photoacoustic imaging are for enhancing image contrast[30,31] and they are activatable.[32–34] It is of importance to create photostable compounds, showing dynamic and reversible absorption changes in response to a specific analytes. Analytes, specifically calcium, play major roles in many biological functions.[35] Compounds that possess elongated π-systems generally exhibit NIR absorption. The longer the π-system, the longer its wavelength is. In search for well-suited near infrared dyes for

photoacoustic imaging, one can greatly benefit from combining future work with computational chemistry to predict absorption and fluorescence of intended targets. Despite impressive advances in this field, a robust and user-friendly virtual spectrometer is not yet available. Currently, whether a molecule emits radiation after excitation are govern by radiative and non-radiative processes and these are often unpredictable. Examples of promising computational methods that simulates these processes are Newton-X (newtonx.org) and virtual spectrometer.[36] Their efforts expand towards molecular dynamic simulations beyond the Born-Oppenheimer approximation. The evergrowing field of computational spectroscopy can, in the near future, help to provide absolute contributions of different classes of dye states to spectral bands.

1.3.3 Biocompatability

Not only do targeted PA agents have to be physiologically relevant, they must overcome cellular barriers. The biological target should be expressed at an early stage of disease state and found at low levels in off-target tissues. The prerequisites extend to its biocompatibilities being characteristically photostable. It should ideally be non-toxic.

1.3.4 Synthetic molecules for molecular photoacoustic imaging

Based on their chemical behaviour, small-molecule probes for PAI can be categorised into three broad classes, namely passive, activatable and dynamic probes. Table 1.3 summarises PAI studies of several commercially available and synthesised PA agents that have been investigated for photoacoustic imaging. The corresponding structures are shown in Fig. 1.4. It is not surprising that these dyes come from cyanines, pyropyrroles, alexa fluors and bodipys. Their structural core consist of π-conjugated system, distinct to NIR chromophores in which electrons are delocalised. As a result, they are typically with high extinction coefficient and less energy would be needed for light excitation. Their well-defined energy gap between the lowest unoccupied molecular orbital (LUMO) and highest occupied molecular orbital (HOMO) gives out distinct absorption peak shown in Fig. 1.1.

The earliest record of introducing CAs for high image PA contrast between the blood vessels against background tissues was a study carried out by Wang *et al.*[37]. Indocyanine green (ICG) was chosen since it is widely establish in clinical settings as an angiography agent. To prolong the circulation of ICG in blood, polyethylene glycol (PEG) was conjugated to ICG. It helps to stabilise the ICG, broadening its absorption peaks, enabling 805 nm wavelength imaging. Spectroscopic properties of native ICG was compared to ICG-PEG. It was used in combination with the high sensitivity of fluorescence molecular tomography (FMT) and high spatial resolution of photoacoustic tomography (PAT) for the first time.[38] Up to now, commercially available fluorochromes are essential synthetic biological fluorescent sensors. Its performance and biodistribution, namely Alexa fluor 750, was the first small molecule to be resolved (25 fmol sensitivity and 150 μm spatial resolution) in biological tissues of small animal by means of MSOT, carried out by Razansky *et al.*[39]. pyrrolopyrrole cyanine (PPCy) was pointed out as a promising PA class of compounds by Bai and Achilefu[40], due to its non-fluorescent and high-absorbing properties. Two derivatives of PPCy were synthesised, reported and spectroscopically characterised (ε_{DMSO} 58 000 cm^{-1} M^{-1}, no fluorescence and ε_{DMSO} 111 000 cm^{-1} M^{-1}, 81% QY). Although the aim was to provide agents for PAI, none of these labels were tested in PA systems. In the same year, *non-invasive* vasculature imaging of mice were shown for the first time with PAI.[34] Evans blue, an agent that binds tightly to albumin serum in the blood vessels was used for *in vivo* imaging and monitor. The agent is ideal for blood brain barrier (BBB) studies since albumin does not diffuse to the cerebrospinal fluid. Commercially available 2,2'-(1,8-dihydroxy-3,6- disulfonaphthylene-2,7-bisazo)bisbenzenearsonic acid (Arsenazo-III) was evaluated as a PA agent for calcium detection at 680 nm with its absorbance and PA good signal intensity at 25 μM.[41] Arsenazo-III is difficult for intracellular delivery, here a liposomal encapsulation mechanism was used for introduction into the cytosol but was never shown *in vitro*. More recently published work by Dana *et al.*[42] claim an *in vitro* PAI with Arsenazo-III. Passive *in vitro* characterisation in HL-1 cadiac myocytes was used for cellular imaging target because cells exhibit a spontaneous deporalisation and seem ideal for imaging calcium transients. There are many limitations to using Arsenazo-III as CAs in general, including stoichiometry which depends on its concentration, multicomponent response and relatively modest affinity to

Ca^{2+} under intracellular conditions.[43] Not only is Arsenazo-III cell-impermeant but its ability for binding to cellular proteins (common to all azo cores) and produce free radicals, affect cell viability. Quinoline-annulated phorphyrins, absorb light in the NIR with an unusually low ϕ as compared to normal phorphyrins. In the study carried out by Abuteen *et al.*[44], quinoline-annulated porphyrins embedded in tissue phantoms were shown to provide $\approx$ 2.5-fold contrast enhancement over that of ICG. PAI has the ability to also distinguish between monomers and dimers of methylene blue (MB), a fluorophore in which static quenching occurs upon its aggregation and its lifetime dramatically shortens to three orders of magnitute.[45] A heptamethine derivative, IC7-1-Bu was synthesised through classical method, as label for *in vivo* mouse model imaging. Like the quinoline-annulated phorphyrins, it was shown to have 2.5-fold higher PA signal intensity compared to ICG but also shows higher tumour fluorescence accumulation[46] using serum albumin as a carrier for tumor targeting. It was found that repeated laser irradiation impares PA signals dramatically and therefore high photostable derivatives were acquired in the following studies.[47] In order to understand how nonlinear absorption contributes to enhancing PA emission, derivatives of 4,4-difluoro-4-bora-3a,4a-diaza-s-indacene (BODIPY) were employed as agents.[30] CurcuminBF_2 in particular was chosen due to its structural similarity to bis-styryl $(MeOPh)_2$BODIPY sytem which contains π-conjugated styryl arms. Photoacoustic Z-scan techniques demonstrate that an excite-state absorption followed by $S_n \rightarrow S_1$ nonradiative decay is indeed responsible for the PA signal being detected. From the basis of these observations, we can conclude that efficient PA agents can be redefined as having a strong vis-NIR absorption, a long-lived S_1 excited state absorption, a large excited-state absorption ε and rapid $S_n \rightarrow S_1$ non-radiative decay. Organometallic compounds $Fe_3(CO)_{12}$, $Ru_3(CO)_{12}$ and $Os_3(CO)_{12}$ were also reported as safe, stable, reliable and high-absorbing CAs for PAI. *In vivo* PAI with $Os_3(CO)_{12}$ salt (30 μM) was administered showing greater image contrast as compared to single-walled nanotube (SWNT)s. The problem is that they have limited applications and efficacy because of their absorption in the visible region and therefore poor tissue penetration. To further investigate this and improve its applicability, molecular level understanding of organometallic compounds mentioned in the previous studies were referenced. New theoretical models were computationally calculated for various clusters $M_3(CO)_{12}$ (where M = Fe, Ru and Os).[48] More examples of new proof-of-concept dyes are continually demonstrated for photoacoustic imaging. For example,

new class of charge transfer NIR dyes were reported, accessed *via* cycloaddtion-cycloreversion reaction of alkynes with 2,3,5,6-tetrafluoro-7,7,8,8-tetracyanoquinodimethane.[49] Their PA signals were systematically studied, showing a positive correlation between molar ε and its PA effect. They were loaded into nano-sized liposomes and they were imaged in agarose gels, showing promising applications in biomedical PAI. Synthetic water-soluble melanin was introduced as high contrast PA agent, a simple linear polydopamine core synthesised *via* Kumada-coupling.[50]

To date, there are a number of classes of organic dyes that were investigated for photoacoustic imaging. Table 1.3 and Fig. 1.4 summarizes and includes all of the state-of-art investigation of absorbing agents reported for photoacoustic imaging.

Table 1.3: **Absorbing agents reported for photoacoustic tomography**[a] This is an exhaustive lists mostly on infrared chromophores. Abs = absorbance, SLN = sentinel lymh node

Cmpd	Absorbing agents	Abs (nm)	Conjugation to	ref
Cyanines and Heptamethines				
5	indocyanine-green**	805	-	37,38,51,52
14	IC7-n- Bu	830	-	46,46,47
	CDnir7	806	-	53
	IRDye 800cw- 2DG	774	2-deoxy glucose	54,55
	IRDye 800cw	780	NPR-1 peptide tag	56
	IRDye 800	792	peptide (c(KRGDf))	57
	IR-780	780	caspase inhibitor	58
	IR-780	776	NMDAR antagonist	59
Azo dyes				
7	evans blue	620	-	34,60
10	methylene blue	665	-	45,61–64
13	arsenazo-iii*	560 (native)		41,42
Alexa Fluor series dyes				
	alexa fluor 750	750	-	39

Continued on next page

Table 1.3 – *Continued from previous page*

Cmpd	Absorbing agents	Abs (nm)	Conjugation to	ref
	alexa fluor 750	750	peptide	11
	alexa fluor 750	749	Herceptin	32
	alexa fluor 647	647	Herceptin	32
Naphthalocyanines				
	SiNc[b]	770		65
	naphthalocyanine	860	PEG	66
Miscellaneous				
1, **2**, **3**	org. metallic clusters	230- 400	-	48,67
4	ppcy	730	-	40
6	polymer-based	400	linear dopamine	50
8	Porphyrin-based	721	-	44
9	mtt	550	formazan formation	68
11	ftq	800	-	49
12	violacein	590	bacteria targeting	69
15	bodipy	640- 687	-	30,70
	Hylite 750	750	V7 or K7 peptide	71
	SNARF-5F	564, 532	-	72,73
	CF-780	780	EGF peptide	74
	ATTO 740	740	GRPR	75–77

[a] see Fig. 1.4 for corresponding structures

[b] 2,3 napthalocyanine bi(trihexylsilyloxide)

[*] dynamic sensing in biological systems

[**]sensing with therapeutic applications in biological systems

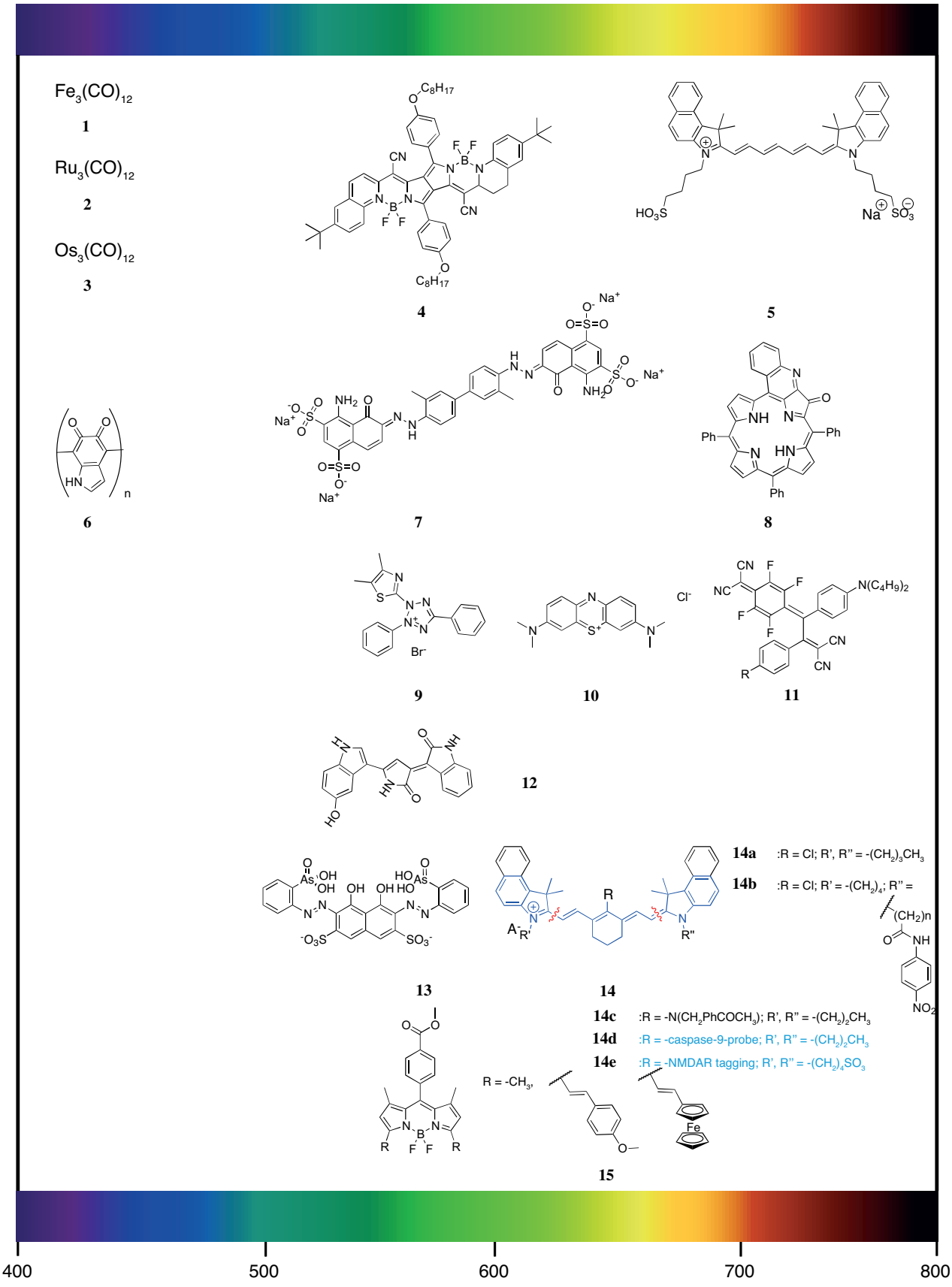

Figure 1.4: **Absorbing agents for photoacoustic imaging**. See Table 1.3 for corresponding information.

1.3.5 Nanostructured contrast agents for photoacoustic imaging

Nanoparticle (NP)s represents the largest class as photoacoustic agents for PAI.[1] They have superior chemical characteristics that are well-suited for molecular PAI. These include high chemical, physical and biochemical flexibilities. They possess substantially high extinction coefficients as compared to small molecule organic dyes. Their variable size, shapes and materials mean that their surface properties, reactivity and optical characteristics can be simply fine-tuned. A large number of targeting moieties or extra chemical properties can be attached to the particle.[1] While their large surface area is considered for gaining the right chemical properties, they do possess lower biocompatibility as they often accumulate in the reticuloendothelial systems for a long period of time.[1,78] They are often difficult to reproduce, purify and quantify homogeneous well-defined NPs. Details of all the nanoprobes that were reported for photoacoustic imaging can be found in Table 1.4.

Table 1.4: **A lists of currently investigated nanoprobes used for photoacoustic imaging.** The table is split based on the different family of nanoprobes, namely, organic, inorganic and hybrid nanoprobes. Each family are categorised on the variety of classes of nanoparticles and their corresponding absorbance. The table consist of references (*right*) where the study of materials are used for photoacoustic imaging. NP = nanoparticle, SWNT = single walled carbon nanotubes, FA = folic acid, ICG = indocyanine green, INDs = india ink nanodroplets, Au = Gold, GNPs= gold nanoparticles, MWNT = multi-walled carbon nanotubes, DNDs = radiation-damaged nanodiamonds, FND = fluorescent nanodiamonds, NDs = nanodiamonds, CNSs = carbonaceous nanospheres, CP = conjugated polymers, PFTTQ = poly[9,9-bis(4-(2-ethyl-hexyl)phenyl)fluorene-alt-co-6,7-bis(4-(hexyloxy)phenyl)-4,9-di-(thiophen-2-yl)thiadiazolo-quinoxaline], SPNs = semiconducting polymer nanoparticles, PANI = polyanaline, MBs = microbubbles, nanonaps = nanoformulated napthalocyanines, HA = hyaluronic acid, dPGS = Dendritic polyglycerol sulfates, HSA = human serum albumin, BPOx = benzo[*a*]phenoxazine, NR = nanorods, NTs = nanotubes

class	nanoprobe	absorbance (nm)	REF
organic nanoprobes[a]			
Graphene oxides	carbon NP	650	79
	Rbh, Cy5, Cy7	532, 675, 753	80
	ICG-GO,	808	81
	ICG-GO-FA		
	FGO	720	82

Continued on next page

Table 1.4 – *Continued from previous page*

class	nanoprobe	absorbance (nm)	REF
	ICG-PDA-rGO	780	83
SWNTs	SWNT-dye-RGD	1064	84
	INDs	820	85
	ICG-SWNT	790	86
	SWNT-RGD	690	87
Nanodiamonds	DNDs	820	88
	irradiated NDs	530, 565	89
	PEG-NDs,	820	90
	HER2-PEG-NDs glucose- CNSs	808	91
Polymer	G4-DOX-PEG-Tf-TAM*		92
nanoparticles	ICG-PEG*	540	37
	folate-CP dots	810	93
	polydopamine	445	50
	melanin NP	590	94
	PFTTQ	800	95
	SPNs	700, 735, 820	96,97
	FA- lipid PANI NPs	808	98
	PoP- upconversion NPs	-	99
	phorphyrin MBs	824	100,101
	J-aggregating NPs	824	102,103
	nanonaps	707, 860	104
	phorphyrin nanodroplets	705	105
	SiNc PNPs	780	106
	DiR encapsulated	780	107

Continued on next page

Table 1.4 – *Continued from previous page*

class	nanoprobe	absorbance (nm)	REF
	amphiphilic HA derivatives	790	108
	liposomal ICG	800	109,110
Miscellaneous	cellulose	700	111
	squaraines	532, 740	112
	nanocomplex dPGS	800	113
	C–HSA–BPOx–IR825	680	114
	Porphysomes*	680	115
	PFC-based nanodroplets*	790	116,117
	PDI nanoparticles*	700	118
inorganic nanoprobes[b]			
nanoparticle	Au-nanoparticle	620, 680	14,119–126
nanorod	Au-NR	520 - 780	12,127–142
nanostar	Au- nanostars	767	143–145
nanotripods	Au- nanotripods	700	146
nanoprism	Au- nanoprisms		147
nanocube	Au-cubic nano	808	78
nanoplate	Au- nanoplates	490	148
nanocage	Au- nanocage	760, 820	88,149–154
nanoshells	Au- NPs	528, 662	155,156
nanotubes	Au- NTs		157
hybrid nanoprobes[c]			
	Au-plated SWNTs	850	158
	Au-plated CN core	639, 900	159
	CNTR@AuNPs	808	160

Continued on next page

Table 1.4 – *Continued from previous page*

class	nanoprobe	absorbance (nm)	REF
	sGNR/MWNTs	715	161
	FND- GNP	500- 620	162
	TaO_x@PPy	700- 900	163
	HANPC	670	164

[a] chemical binding or self-assembly formation

[b] metal-containing NPs

[c] mixture of inorganic and organic NP components

[*] use in neuroimaging of the brain

1.4 Calcium imaging with photoacoustics

Calcium plays a major role in biological processes such as heart muscle contraction, regulations of the entire cell cycle, cell proliferation to cell death.[165,166] In the nervous system, calcium acts as an essential second messenger in neuronal signalling. During neuronal activation, action potential arrives in the pre-synaptic terminal and opens up calcium channels. The influx of calcium triggers vesicles containing neurotransmitters to move towards the cell's surface membrane, releasing their contents into the synaptic cleft. Each neuron is highly specific in the sense that they contain a specific neurotransmitter with well defined sub-cellular compartments for calcium regulations. At rest, neurons have on average 50- 100 nM calcium concentration that transiently increases during electrical activity to 10-100 fold.[35,166] These changes in concentration dynamics is being exploited for detection and the basis of calcium imaging technique.

1.5 Contrast agents for calcium imaging

Fluorescent calcium sensors are used widely in optical imaging. Since the discovery of the first synthetic calcium indicator prototyped by Tsien[167] in 1980, various variants of synthetic fluorescent calcium sensors stemming from a number of different commercially available dyes

(See Appendix B, Fig. B.1 and B.2). The first generation of these dyes is Quin-2, excited by ultraviolet (UV) light (339 nm) and the first to be used in biological experiments.[168,169] Because of its low brightness, large intracellular concentrations of Quin-2 were required to overcome autofluorescence.[170] In many ways, the second generation, fura-2, is superior to quin-2. It is normally excited at 350 and/or 380 nm and shows fluorescence changes that are significantly larger than quin-2. It is also ratiometric, allowing quantitative calcium measurements. As a result, Fura-2 quickly became a popular dye used by neuroscientists. Over time, many more calcium indicators with various excitation wavelengths and affinities for calcium emerged. These include indo-1, fluo-3 and the evolution of oregon green BAPTA-1 (OGB1) and fluo-4, the most popular and still currently the gold standard dye utilised to date.[171] asante calcium red (ACR) and asante calcium green (ACG) with absorption wavelengths at 537 and 515 respectively and 654 and 542 nm emission respectively[172,173] is the longest wavelength synthetic calcium dye. Refer to Appendix B, Fig. B.1 and B.2) for up-to-date details on the structural and photophysical characterisations of small calcium sensors. Historically, calcium imaging evolved *via* two parallel ways (1) the implementation of instrumentations and (2) the continuous development of calcium sensors.

1.6 State-of-the-art functional photoacoustic neuroimaging

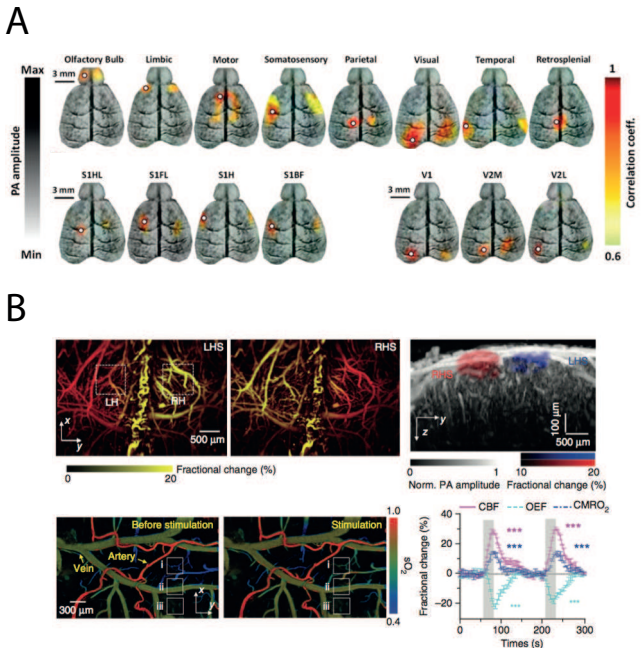

Figure 1.5: **State-of-the-art neuro functional photoacoustic imaging**. (A) Resting-state functional connectivity photoacoustic tomography.[174] (B) Photoacoustic microscopy to image blood oxygen, blood flow and oxygen metabolism in both resting and stimulated states.[175]

The most widely applied and well-established principle of *in vivo* neuroimaging methods have always been to use light for excitation in the near visible wavelength range (300-550 nm) in which naturally, photon emission occurs and its fluorescence detection is possible. Much of what we know about the brain is from studying neurons in an isolated form or another. Efforts are therefore now focused on studying single-cells in its natural physiological environment. An excellent demonstration of neuronal activity in an awake and freely moving animal were demonstrated by Kerr and Denk[176], Sawinski *et al.*[177]. This was possible because they have developed a mobile fibrescope, light and robust enough for rats to be carried, enabling stable recording $\geq$5 min per trial, recording 20 neurons. Conventionally, calcium dynamics are always tracked with fluorescent probes. These calcium transients are normally visualised using OGB1 and sulforhodamine 101 (SR101) correlated with visual stimuli. Despite the availabilities of other superior calcium dyes, OGB1 is still the gold standard commercially available calcium dye used in such imaging setup.

Photoacoustic tomography continues to grow and show promises to provide better understanding of the brain via imaging for enhanced monitoring, diagnostics and therapeutic treatment. Since the first introduction of tumour brain imaging *in vivo* using PAT,[57] a few other studies have emerged. Endogenous CAs, namely haemoglobin and blood oxygenation variations, are currently the most widely exploited agents for photoacoustic neuroimaging. These include imaging haemodynamic oxy-/deoxygenation changes using rat forepaw electrical stimulation using the functional photoacoustic microscopy (fPAM) system.[6,175] A miniature version of the system has been reported for an awake, freely moving rat and allows noninvasive *in vivo* brain photoacoustic imaging.[178] Advances in photoacoustic tomography by the addition of time-resolved volumetric blood oxygenation capabilities carried out by Luis and Razansky[21] have led to the 5-D neuroimaging of cerebral blood haemodynamics in mouse brains.[3]

A more direct technique of imaging brain activations is to use genetically encoded calcium indicator (GECI) in combination with Functional optoacoustic neuro-tomography (FONT) method.[29] The study shows that with a more careful choice of agents, indeed some of these GECI members give photoacoustic contrasts that is dependent on calcium absorption changes and paves a new way to image with photoacoustic technologies.

A major challenge has been to develop satisfactory means for nondestructively measuring intracellular free Ca^{2+} with good time, spatial and depth resolution. Currently, from all the examples so far, the established imaging technology has been to use optical fluorescence microscopy using dyes or proteins for detecting calcium transients. To map spatiotemporal patterns of Ca^{2+} - signalling across whole organs in intact animals, it is desirable to complement optical microscopy with photoacoustic tomography (PAT).

1.7 Chemical Strategies

In order to construct small synthetic molecules for PAI, it is pertinent to place importance in understanding that the signal generation processes involves several distinct phases. The initial incident photons are absorbed (exogenous or endogenous CAs). Heat is produced causing in

small temperature rise, typically $\leq$0.1 K from fast non-radiative conversion.[1] On top of that, the degree of heat intensity also relies on understanding the optical and thermodynamic interactions of underlying signal transduction mechanisms that could well serve a good base for designing and selecting an effective PA agent.

From examples in literature, dyes which are primarily based on cyanines, rhodamines, BODIPYs, squaraines, porphyrins, phthalocyanines and indocyanine are used to aid PAI (Refer to Appendix B, Fig. B.1. NIR dyes gain intensive attention in biomedical imaging but only few of them are readily available owing to poor solubility, photostability and specifically, in heterogenous tissues *in vivo*. Several studies are on redesigning and trying to adapt NIR dyes to overcome these difficulties.

Chapter 2

Cyanine based smart contrast agents for photoacoustic imaging: a modular chemical platform

Objectives

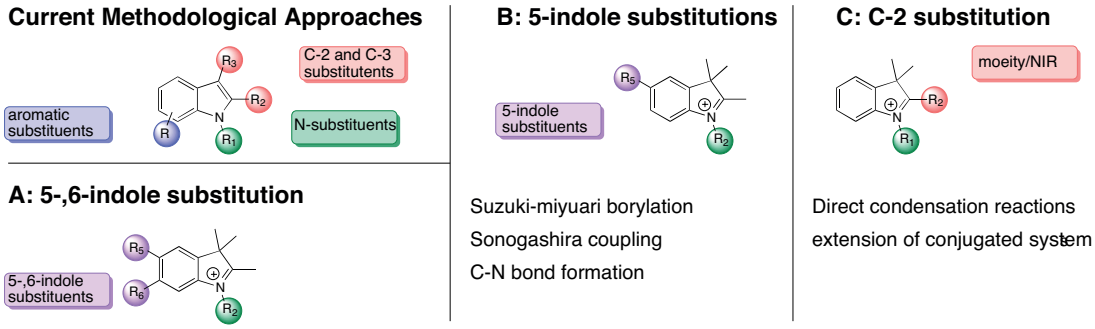

Figure 2.1: **The current state of indole research and strategies A, B and C.** There are numerous emerging methods that allow rapid access to simple functionalised indoles with differing substitutions at C-2, C-3 and N-1 atom and at aromatic R_1 (*top right*).[179–181] We contribute to the chemical diversity of indoles *via* functionalisations at 5,-6-indole positions (A), 5-indole position (B) and C-2 direct condensations (C). We investigate current catalytic methodologies that could subsequently give way to access new indole analogues of type A and B.

Synthetic methods are being investigated in terms of ease of synthesis and its applicability to the photoacoustic imaging technology in mind. Synthetic methods of group functionalisations at the pyrrole ring positions is the most common way for indole substitutions. There are plenty of literature papers explaining the well-established substitution reactions at these sites.[179–187] Details of the classical and more recently, green chemistries methods are well highlighted and detailed.[188]Traditional strategies in indole chemistry rarely allow for modifications at the 5,6-disubstituted indoles indicated in Fig. 2.1. This chapter (Chapter 2) explores the possibilities of 5,6- indole type modifications to achieve a number of *novel* calcium chelators highlighted in Fig. 2.1. C-2 substitutions *via* direct condensation reaction is expanded in more detail separately in Chapter 3.

2.1 Introduction

Chemists have been interested in the preparation of dyes for many centuries. The first record of their use was in China in 2600 BC. Their full history, from ancient times to the 20th century, is explored by Druding[189]. Textile industries are now a large scale market for natural dyes. Its important use extends to lasers, fabric dyes, contrast dyes, photography, food dyes, solvent and pigments. Although synthetic chemical dyes were discovered in the late 19th century, its exploration for medical applications has emerged only in the last few decades. Compounds with specific spectral properties have significant importance for developing the theory of organic colour chemistry as well as evolving practical use in areas such as optical recording, film industries, dye and pigment formulations and more recently, in biomedical imaging. Applications of NIR dyes are advantageous in bioanalytical methods because of their strong spectral properties in the desirable region of 700- 1000 nm wavelength range allowing minimal background from endogenous agents and thus higher sensitivity.

Identifying the core chemical structures which make the photophysical fingerprint different from one dye to another was my interest from the very beginning. In order to establish the necessary modular sensor platform, it was necessary to identify lead compounds that would match, as much as possible, the criteria for PAI. Therefore, chemical design was a critical part of this research. Structures of a variety of classes of organic dyes were investigated in terms of ease of synthesis and their suitability for optoacoustic imaging technology. Refer to Appendix B for more details on varying dyes that were initially under investigations. Amongst these were murexide (refer to Appendix B, Fig. B.15) and dyomics dyes (refer to Appendix B, Fig. B.6, B.7 and B.8). Our design study for NIR probes is based on two essential structural features: a target-binding moiety and a chromophore. At least one target-binding moiety is connected to at least one strong absorbing chromophore. To function as a dynamic sensor, the target-binding moiety must alter its electronic structure as a probe. Variation in the electronic structure (electron transfer and/or internal charge transfer) can lead to a change in absorption and/or emission properties.

We identified cyanines and heptamethines as our leading class of absorbers. They are subclasses

of dye family belonging to the polymethine group. Their core structure will serve as the main body of our chemical design (Scheme 2.4). Cyanines were and are widely used in industry and in recent years, more have been extensively used in biomedical technology. ICG **5**, an FDA approved dye, is the most common dye from this subclass. With extensive research into their its use as a static probe in biological imaging, very few researchers have shown it to be activatable[33,58,190–192] and none have shown it to be functional in response to biological processes. Therefore, developments and structural modifications, which can detect analytes are novel and highly attractive for medical and biotechnology applications. First, we will start with incorporating calcium ligands onto the indole scaffold to establish a chemical platform. Roger Tsien pioneered the work on calcium ligands (both synthetically and genetically) for a variety of biological purposes including sensing calcium transients in cells.[27,28,168,170,193] Appendix B, Fig. B.1 and Fig. B.2 is a summary of all the synthetic calcium sensors that are known and commercially available. They are mainly based on the 1,2-bis(o)-aminophenoxy)ethane-N,N,N',N'-tetraacetic acid (BAPTA) **16** core structure.

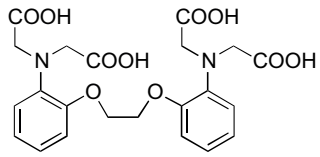

16

Figure 2.2: **The chemical structure of 1,2-bis(o)-(aminophenoxy)ethane-N,N,N',N'-tetraacetic acid (BAPTA).** BAPTA is a calcium (II) ion specific aminopolycarboxylic acid. Its scaffold is currently the synthetic ligand suitable for cytosolic intracellular dynamic imaging of calcium transients in the μM range. Absorption spectra of BAPTA varies depending on free Ca^{2+} and has less affinity to Mg^{2+} ions.

Spectral properties of dyes change as their absorption moves towards the NIR region. There are several drawbacks to this 1) spectral broadening 2) photoinstability 3) chemical instability 4) the tendency of dye molecules to aggregate due to hydrophobicity. We aim to synthesise probes that are in the long wavelength range, with a high ε value, ideally $\geq$200,000 M^{-1} cm^{-1}), a low ϕ at ≤ 0.1 that show dynamic absorption changes in response to a specific analyte. The specifications extend to probes being characteristically photostable, sensitive, cell-permeable, non-toxic, reversible and ideally able to cross the BBB.

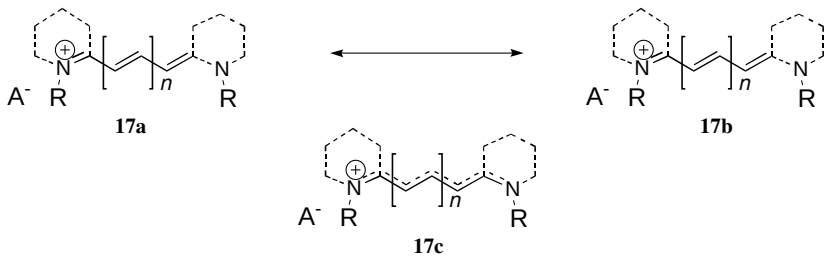

Scheme 2.1: **The resonance of cyanines**

The general structure of cyanines consists of two nitrogen centres of a *aza*-heterocyclic nature, one of a quaternary nature and its scaffold consists of an electron donors and acceptors of type **137**- **143** (See Appendix B, Fig. B.2). It is linked through a conjugated alkene chains of an odd number of carbon atoms extending to the other nitrogen atom. These single and odd numbers of methine groups in which (n+1) bi electrons are distributed over *n* atoms of delocalised cation can be characterised by three ideal states, the *aromatic state*, *the polyene state* and the *polymethine state*. This ”push-pull” mechanism is a prominent feature and forms the basis of the activity of the polymethine dye family of type **17c** in Scheme 2.1. Historically, its name class depends on the alkene length in the polyene chain with compound **17** of n = 0, 2 and 3 referred to as mono-, tri-, and penta-, and heptamethine cyanines respectively. Depending on the length of its methine chain, absorption in the visible and NIR region (400- 900 nm) can be achieved, a unique property only known to cyanines. Its narrow bands and high extinction coefficients are highly sought after characteristics that employ cyanines in wide variety of applications.

Several varieties of polymethine cyanine derivatives have been synthesised during the last decade. Their syntheses are achieved either through one pot (symmetric) or stepwise (asymmetric) condensation reactions of two nucleophilic *aza*-heterocycles containing an activated methyl group with a polyene chain precursor of an unsaturated bisaldehyde of type **40** as an example. Structural diversity is achieved through variations in the polyene chain, nitrogen substituents and the heterocycles. The general consensus is that synthetic methodologies are currently not compatible with a wide range of reactive groups located at *aza*-heterocycles. This makes it challenging to fine tune the reactivity and solubility of the polymethine cyanine derivtives by additing structural

motifs, in particular, incorporating decorative heterocycles.

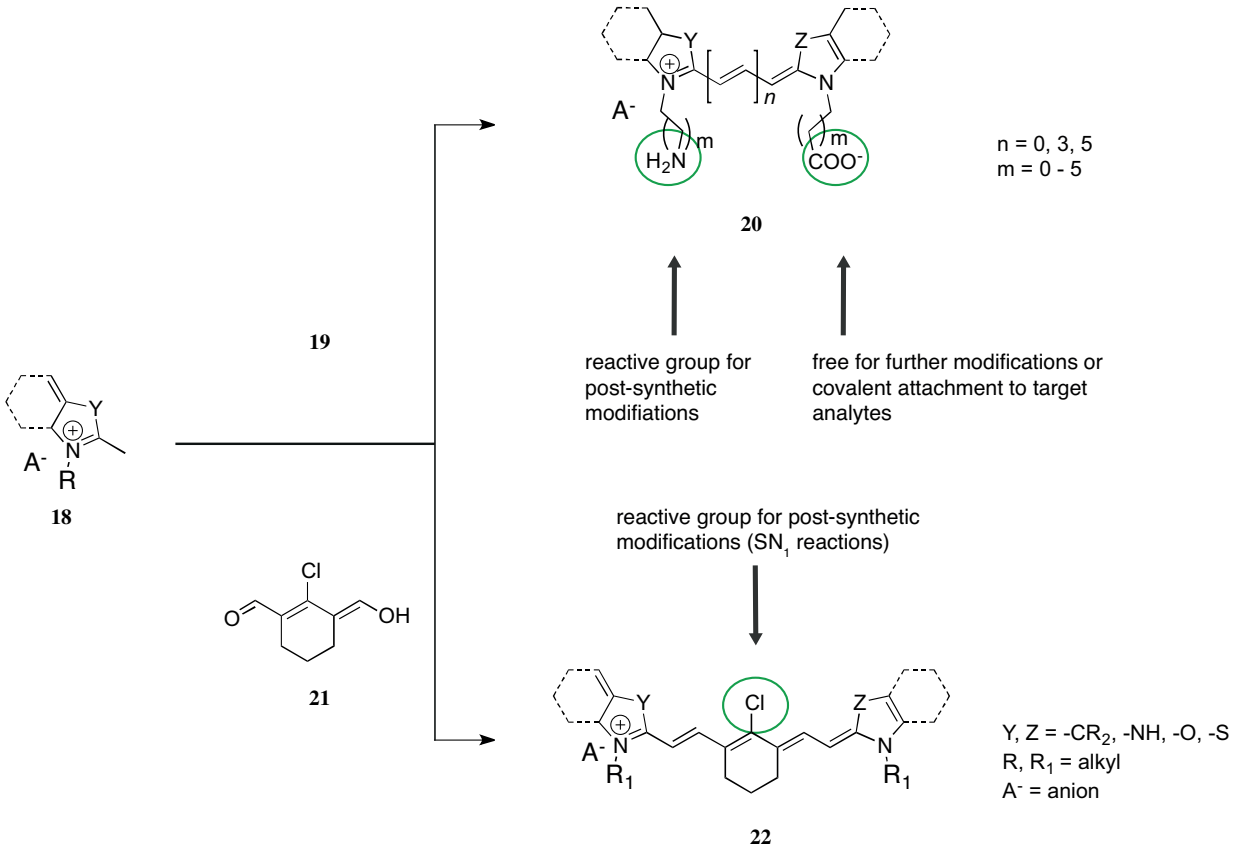

Figure 2.3: **Reactive groups for post-synthetic modifications**

Cyanines are divided into two different classes called merocyanines and heptamethines. Cyanines of formula **20** are prepared by heating a mixture of a heterocyclic base **18** containing an activated methyl and an unsaturated bisaldehyde **19**. The desired reactive group for post-synthetic modifications is installed before the condensation reaction. Much in the same way, heptamethine cyanine dyes of formula **22** are best synthesised by heating a mixture of quaternary salt of a heterocyclic base **18** containing an activated methyl and an unsaturated bisaldehyde 2-chloro-l-formyl-3-(hydroxymethylene)cyclohex-l-e **21** to reflux in a mixture of butanol and benzene (7:3) as solvents and without using any catalyst [194] as shown in Fig. 2.3. The purpose of using precursor **22** which has a chlorine at the *meso* position is that the chlorine can be substituted

with ease by various nucleophiles with hyroxy, amine and thiol groups via nucleophilic substitution (SN) reaction. The substitutuents attached to precursor **22** are important as NIR probes which are suitable for photoacoustic *in vivo* imaging as shown by Yang *et al.*[58] and Sim *et al.*[59] who has employed such strategy. Using both strategies produced IR-800cw NHS ester **23** in Fig. 2.4, where it was modified for at the *meso* position to increase solubility and employed an NHS ester crosslinker, located as an extension from the quaternary nitrogen of the indole, for post-synthetic modifications for various applications.

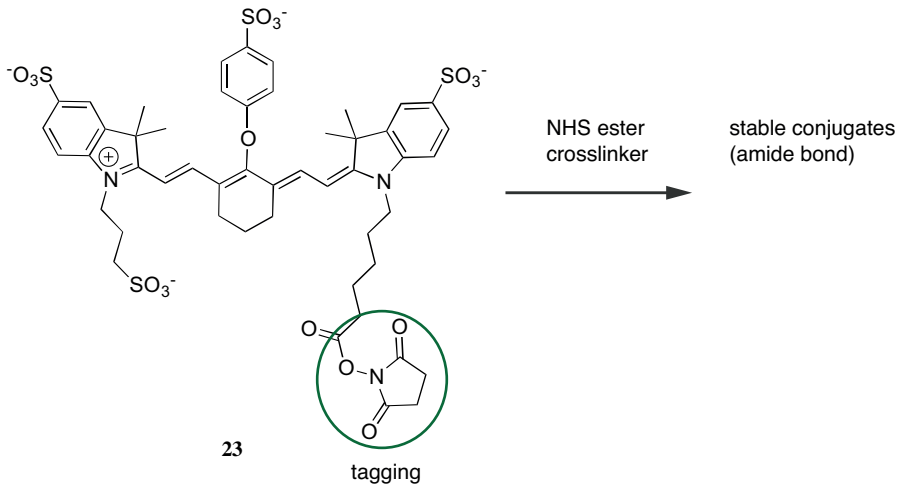

Figure 2.4: IR-800cw NHS ester conjugated used for peptide tagging

ICG is used in a variety of PAI studies either as a CAs on its own,[38,51] enabling sentinel lymph node (SLN)s mapping or in combination with PEG conjugated ICG to prolong its circulation in the blood allowing more time to image.[37] human serum albumin (HSA) conjugated to ICG shows increased uptake in tumours due to enhanced permeability and retention (EPR) effects.[52] Heptamines have been more often used for tagging *via* conjugation of peptides at the site indicated in Fig. 2.4, examples include for imaging of tumour specific molecular information.[54–57] See Table 1.3.

The indole scaffold is of upmost importance in our society and its motifs can be found in many natural products,[195] foods, perfume, dyestuffs, textiles and various other synthetic products. It has gained widespread attention due to its pharmacological activities, proving its most prominent use as therapeutic agents. Almost all the synthetic dyes features an indole core structure. Access to

highly- substituted indoles is desirable because they can provide a new and interesting set of NIR dyes with many useful applications across the biomedical fields. Our chemical design is based on modification of the aromatic chromophore, **20** and/or **22**. Upon interaction (co-ordination) of the probe to the analyte/target, the overall chromophoric structure will change its electronic distribution and we predict, will generate dynamic changes in absorption properties. Synthetic strategies and basic molecular design principles were investigated so as to achieve high absorbing molecules in the far red or even in the infrared region of the spectrum.[196] This design strategy to obtain compounds **37** is shown in Scheme 2.1.1, 2.1.2 and 2.1.3

It has also been shown that heptamethine dye series **38** is more photostable compared to its indocarbocyanine counterpart **37**. The fact that it has a high extinction coefficient and low quantum yield[197] prompts us to consider the commercial NIR core based on heptamethine precursor (IR-780). Commercially available heptamethine **22** could potentially be exchanged from a -Cl to a Ca^{2+}-chelator. This allows a one step reaction obtaining a potentially useful probe.

The summary of our NIR chemical platform is shown in Scheme 2.4, 2.7 and 3.1. We employ retrosynthetic approaches and use methodologies in organic chemistry for executing multi-synthetic pathways towards key targets. We propose three systems framework (see section 2.2.1, 2.2.3 and 2.2.4). We employ retrosynthesis models based on structure-goal (S-goal) strategies. This allows us to have bi-directional techniques to deduce several novel promising pathways for the synthesis of desired chemical probes.

2.1.1 Strategy A: Functionalisation of cyanines and heptamethines as near infrared calcium sensors

There are several ways in which an indole can be achieved. One of the oldest and widely used method is the *Fischer* indole synthesis. The aromatic heterocyclic indoles comes from a phenyhydrazine **24** and an aldehyde or ketone **25** under an acidic or thermal sigmatropic rearrangement to generate the indole skeleton with the elimination of ammonia as shown in Scheme 2.2.[198] Over 100 years after its initial discovery, the *Fischer* indole synthesis remains the most common method for indole preparations.[182] The method is efficient. It is possible to access less reactive benzene ring for electrophilic substitution as the synthetic methods are continually being developed. There are a variety of enolisable ketones commercially available for the substitution at the 2- and 3- positions of the indole nucleus. In contrast, there are limits to the number of arylhydrazines commercially available. Synthetic methods for the preparation of arylhydrazines involves arylamines as starting material which are reduced to its diazonium salts. The difficulties associated with the preparation of arylhydrazines often restricts the ability to readily prepare indoles which are substituted at 4-7 positions *via Fischer* indole methods.[199]

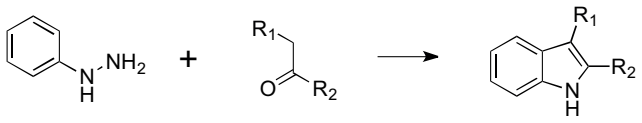

24 **25** **26**

Scheme 2.2: The **Fischer indole synthesis.** Aromatic heterocycle indole of type **26** is achieved using phenylhydrazine **24** and an aldehye of ketone **25** under acidic conditions.

Typically with indoles, compound **26**, structural diversity is achieved through variations in the nitrogen substituents and the pyrrole ring. It is highly reactive on the C-3 position. The pyrrole ring is the most reactive portion of the indole, with only electrophilic substition taking place at the pyrrole ring only after N-1, C-2 and C-3 are substituted. Simple cyanine based compounds with very little or unsubstituted rings have been shown to be synthesisable. Access to the 5-,6- indole positions are desirable because it can provide novel, interesting set of NIR dyes with many useful applications across fields. We set out to use the current synthetic procedures to synthesise indoles

of type **39**.

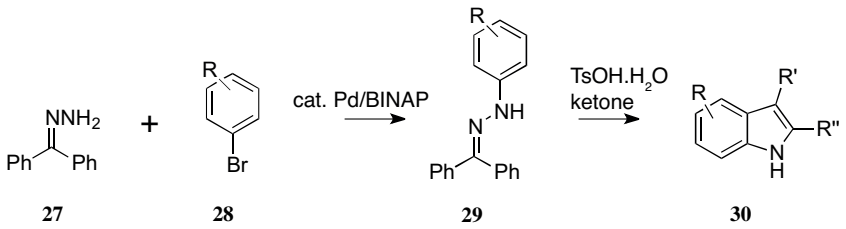

Figure 2.5: **Synthesis of N-aryl hydrazones and indoles *via* Buchwald modifications.**[199,200]

There are anticipated challenges in using *Fischer* indole synthesis. It prompted us to consider other ways to obtain indole of type **39**. Substitution reaction on the 5-,6-indole position can be challenged using Buchwald modification on the Fischer indole synthesis illustrated in Scheme 2.3. There are successful synthetic method using palladium-catalysed reactions by cross coupling of aryl halides (typically bromides) and hydrazones. These *N*-arylhydrazones undergo displacement with other ketones to promote cyclisations.[199,200] As such, various reports of palladium-catalysed procedures as alternatives to traditional methods such as Fischer indole have emerged in the past decade. These methods employ *o*-haloanilines precursors, which reacts with a variety of unsaturated segments, forming new C-C and C-N bonds to create the indole nucleus.[183–186] The introduction substituents on the 4-7 position of an indole ring presents a challenging task because the benzene ring of the indole nucleus is non-nucleophilic and considered unreactive. It is further complicated by the fact that there are competitive nucleophilicities at nitrogen and C3 positions. Pd-catalysed reactions for the cross-coupling of indoles and aryl halides have also been developed but it is relatively limited.[187] Pd-catalysed cross coupling of amines with aryl halides has been shown in several instances.[201] As shown in Scheme 2.3 shows an extension to the previous methodology for the preparation of arylhyrazones. It has been shown to be more convenient and a practical method as compared to Fischer indole synthesis.[199,200] We therefore considered it as part of our strategy, determining whether indole based pyro-EGTA variants can be synthesised. Palladium-catalysed reactions for the desired, highly functionalised aryl halides to indoles were reviewed and investigated.

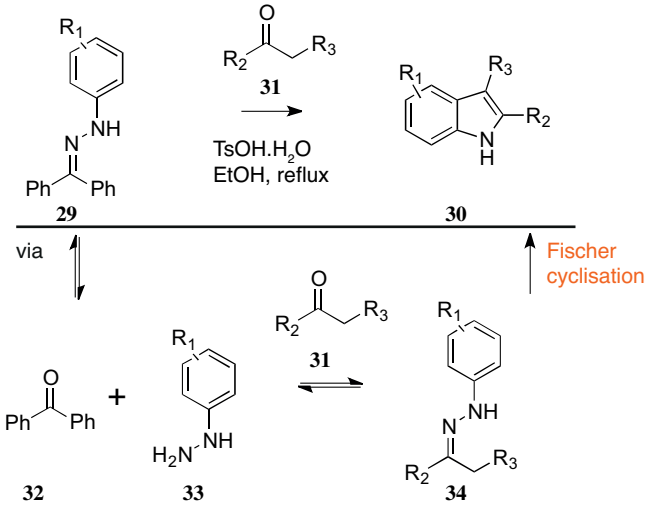

Scheme 2.3: **Palladium-catalysed cross coupling of amines with aryl halides allowing new method for the preparation of indoles.** The idea is that employing enolizable ketones **31** to the hydrolysis of N-aryl benzophenone hydrazones **29** would not only facilitate their hydrolysis but also directly provide the desired enolizable N-arylhydrazones **34** for Fischer cyclization to give indole **30**. The scheme shown here was adapted from Wagaw *et al.* [199].

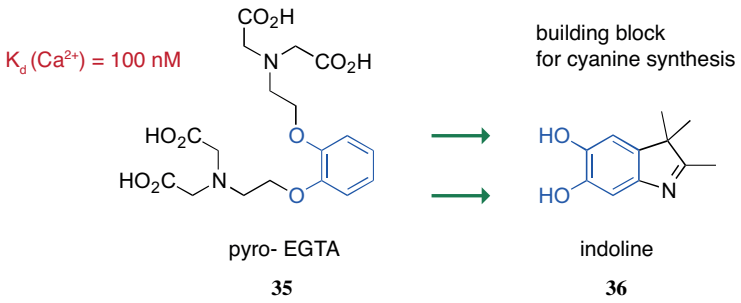

Figure 2.6: **Strategy A: An ideal ligand scaffold to be directly incorporated at the 5,6- indole ring position.** Pyro-EGTA **35** is reported to have K_d of 200 nM for binding of calcium ions.

Chemical diversity at 5-,6-indole position **39** (Fig. 2.6 and Scheme 2.4) through incorporation of ligand moieties are highly attractive new types of metal chelators. An indole nucleus prevalent in many natural products and the ligand directly positioned onto the indole scaffold is predicted to have shifts ideal for PAI. Ligand functionalities can pave way to dynamic NIR sensing of biological processes and sets it apart from static and label dyes. Cyanines of type **37** are valuable sensors for dynamic PA calcium sensing. However, highly decorative functionalisations

at 5- and/or 6- indole position using traditional strategies in indole chemistry does not allow high-yielding access to substitution reactions. So far, ligand functionalisations at these positions has not been achieved. In general, the benzene ring is inactive and simple functionalisations occur at N-1, C-2 and C-3 position of the pyrrole ring before any type of substitutions. There are several features in which ligand installation at 5-,6-indole position is attractive and versatile among other positions of the indole. For example, we can study the effect of direct functionalisations at the π-conjugated ring versus its photoacoustic signal as compared to ligands two or three bonds away. Changes in electronic configuration in the presence or absence of cations would spectroscopically influence dynamic absorption and in turn changes in PA.[202]

More importantly, we focus on a rational design of the ligand indole backbone based on ethylene glycol-bis(β-aminoethyl ether)-N,N,N',N'-tetraacetic acid (EGTA) and their derivatives pyro-EGTA **35**, a well known calcium chelator with affinities well- suited for intracellular biomedical imaging, shown in Fig. 2.6. The main limitation for achieving the new heterocyclic building blocks for the synthesis of cyanines is limited to a number of commercially available hydrazine hydrochlorides. Initially, the focus was on the traditional Fischer indole synthesis of indoles with suitable functionalities for covalent linking of ligands. The most suited initial precursor is 2,3,3-trimethyl-3H-indole-5,6-diol **36**. It is readily synthesisable and the presence of a reactive catechol at the 5-,6- position, it is reasoned that mild conditions *via* double alkylations would provide the best opportunity to access indole ligands of type **39** similar to chemical strategies employed by Tei *et al.*[203]. Thus, we set out to address the considerable challenge of whether 5-, 6-indole position functionalisation could be realised with complex ligand moieties to achieve type **39** indoles. Detailed strategies attempted during the course of this work will be elaborated and outlined in Scheme 2.4.

RATIONAL DESIGN

RETROSYNTHESIS APPROACH

Cyanine class

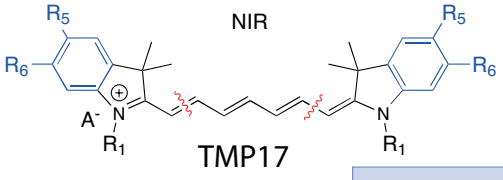

R_5/R_6 = Modular group for bio-conjugation of targeting moiety

R_1 = modification to alter cellular localisation and/or solubility

37a $R_5 = -N(CH_2CH_3)_2$, $R_6 = H$

37b $R_5 = -N(CH_2COOEt)_2$, $R_6 = H$

37c $R_5 = -N(CH_2COOMe)_2$, $R_6 = H$

37d $R_5 = -N(CH_2COOCH_2COOMe)_2$, $R_6 = H$

37e $R_5 = R_6 = -O(CH_2)_2N(COOH)_2$

37f $R_5 = R_6 = -(O(CH_2)_2N(COOMe)_2$

37g $R_5 = R_6 = -O(CH_2)_2N(COOCH_2COOMe)_2$

37h $R_1 = -CH_3$, $-CH_2CH_3$, $-(CH_2)_3SO_3^-$

A^- = counter ion

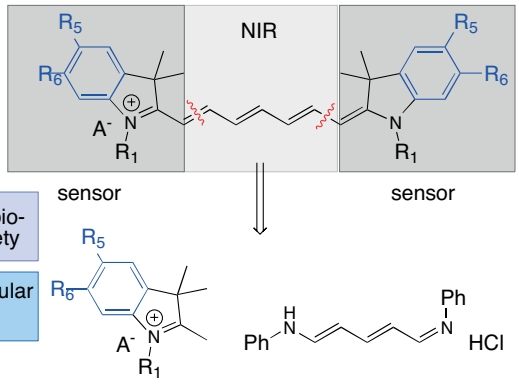

39 **40**

Heptamethine class

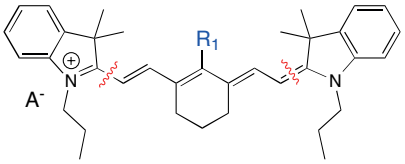

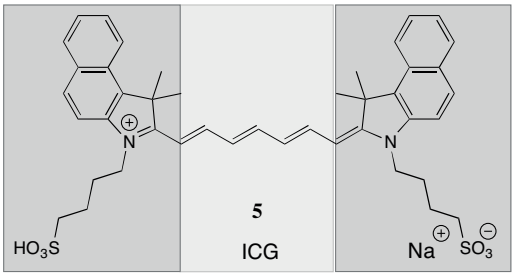

38 $R_1 = -Cl$, e.g. IR-780 iodide

38a - **38c** $R_1 =$ 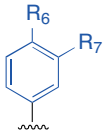

38a $R_6 = R_7 = -O(CH_2)_2N(COOH)_2$

38b $R_6 = R_7 = -O(CH_2)_2N(COOMe)_2$

38c $R_6 = R_7 = -O(CH_2)_2N(COOCH_2COOMe)_2$

A^- = counter ion

Scheme 2.4: **Strategy A- chemical design for the functionalisation of cyanines 37 and heptamethines 38 as near infrared calcium sensors for photoacoustic imaging.** We set out to investigate cyanines **37** and heptamethines **38** as the near infrared core. For cyanine scaffold, the Ca^{2+}-moiety is positioned at the 5-,6- indole position and at the cyclohexenyl ring of the heptamethine dye.

2.1.2 Strategy B: C-C cross couplings at substitution sites

Unlike Strategy A (refer to Fig. 2.4), we plan to use aryl pyro-EGTA of type **42** and indoles using direct C-C cross coupling reactions (Suzuki-miyaura borylation,[204] Sonogashira coupling and C-N bond formation on the 5-position of indoles) as shown in Scheme 2.5

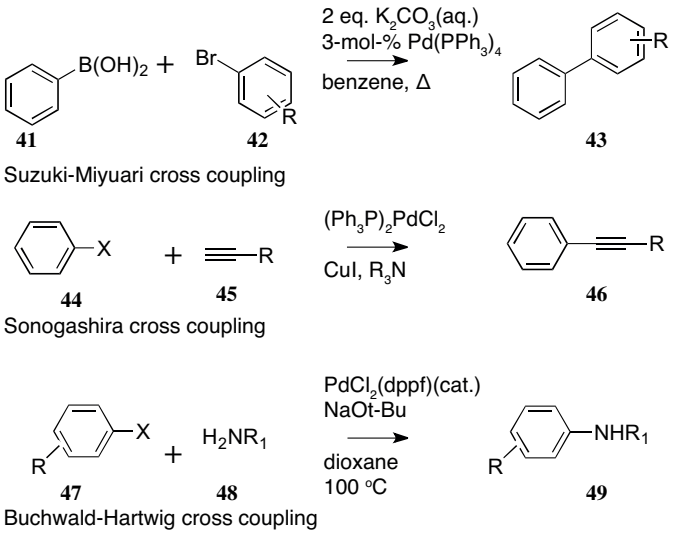

Scheme 2.5: **Pd-catalysed cross-coupling reactions.** Investigating Suzuki- Miyaura, sonogashira and Buchwald-Hartwig cross- coupling reaction towards the access of new type of calcium ligands.

In this part, the main focus is to explore the following possibilities to generate the following precursors **52** and **54** with C-C cross coupling at 5-position indole highlighted in Scheme 2.6 *via* previously described C-C cross coupling methods shown in Scheme 2.5. Suzuki coupling is a broad method and allows cross coupling between organoboronic acids and halides. It has already been employed in the synthesis of a few dyes used in the preparation of bridging squaraine units.[196]

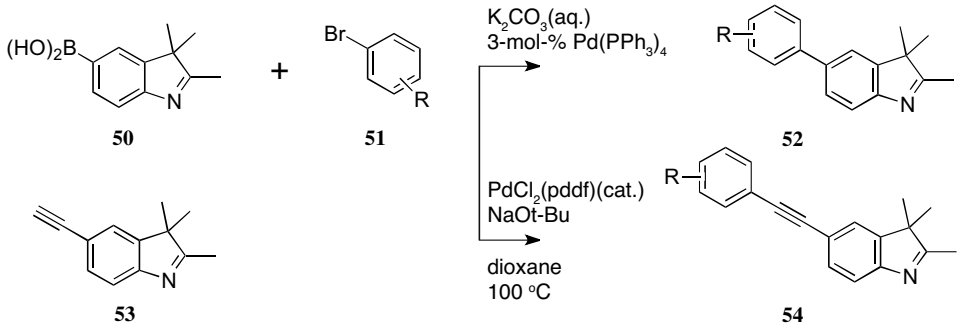

Scheme 2.6: We set out to use cross- coupling reactions to investigate the formation of indole of type **52** and **54**.

The main purpose of this work is to obtain NIR cyanine dyes of type **55** and to evaluate its photophysical and PA characteristics for intracellular calcium imaging. In contrast to Strategy A (Refer to subsection 2.1.1) in which the benzene part of indole is the pyro-EGTA scaffold, pyro-EGTA derivates are to be installed directly at 5-indole position. Using retrosynthetic approches lead us to the heterocyclic indole intermediates **56** from commercially available **40**. First, we attempt to functionalised indoles **56** using various palladium catalysed reaction for direct arylation of C-C and C-N bond formation. Using linkers to install pyro-EGTA that are one to three bonds away from indole might just be enough to maintain the π-conjugation throughout the scaffold during cation coordination. Hence, Suzuki, Sonogashira and C-N Pd-catalysed reactions were employed as synthetic approaches to access the appropriate linkers for pyro-EGTA installation.

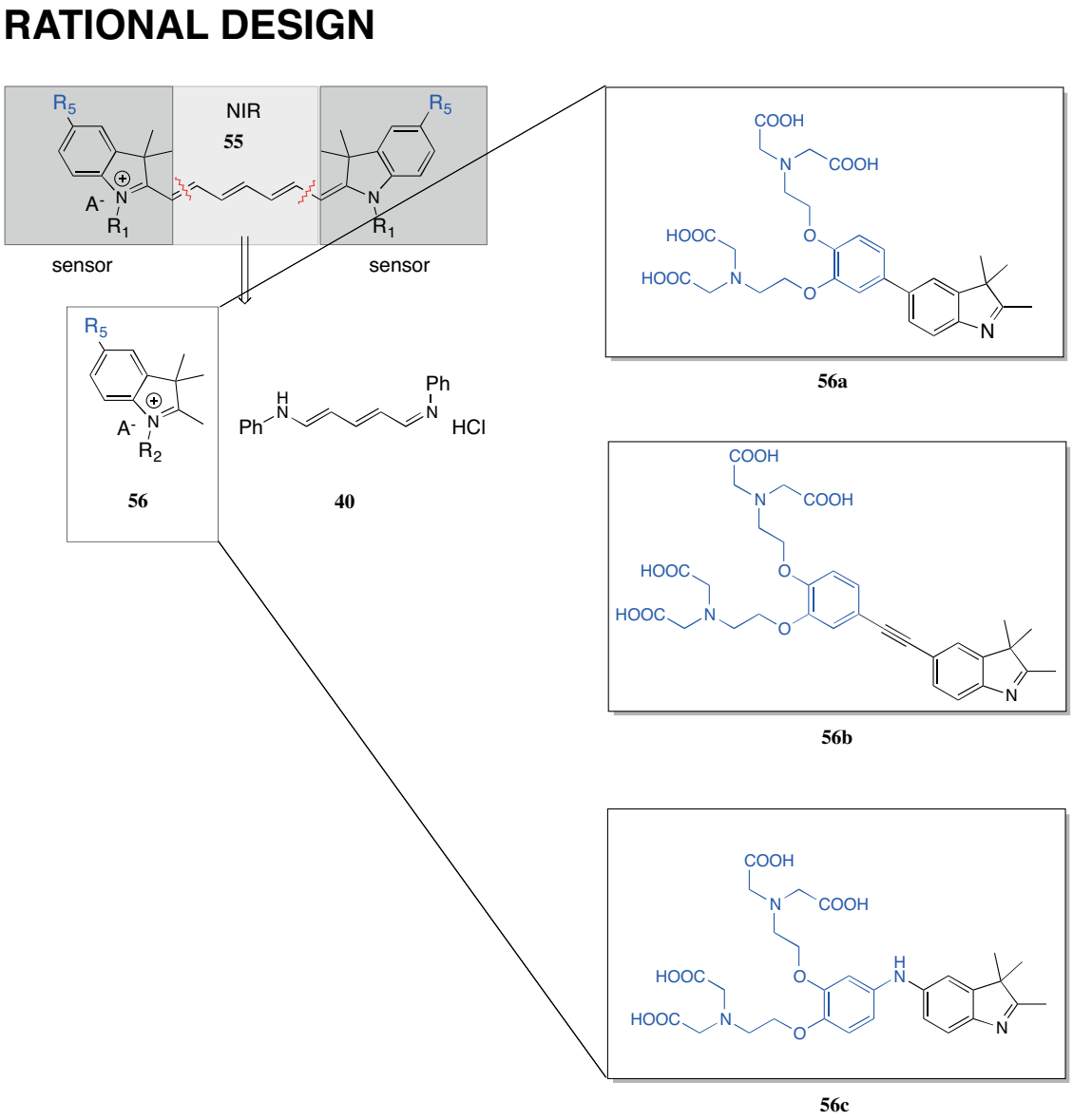

Figure 2.7: **Strategy B- palladium catalyzed (Pd-cat.) reactions at 5- position of the desired and highly functionalised indoles 56**. Synthetic methodologies including Suzuki-miyaura borylation,[196] Sonogashira coupling[205–207] and C-N bond formation[208] to access indole of type **56**.

2.1.3 Strategy C: Direct condensation reactions at C-2 position of indoles

Another way to access functionalised indoles is to use the strategies for the synthesis of styrylcyanines. The application of styrylcyanines as novel fluorescent probes has grown.[188,209] Herein, novel styrylcyanine-based metal sensors for photoacoustic imaging was achieved.

We set out to perform condensation reactions of simple indoles with the respective carbonyl components. The aim was to produce precursors **57** and **58** for the synthesis of styrylcyanine **59**. The success of this work is expanded in Chapter 3 with full *in vitro* and *in vivo* evaluations and applications.

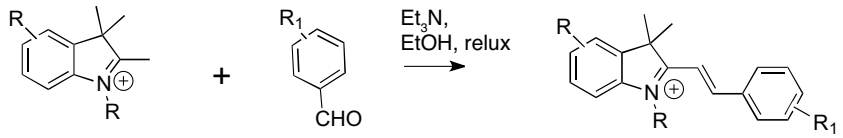

57 **58** **59**

Scheme 2.7: **The condensation of indole iodized salt 57 and arylaldehyde 58**. The pyrrole ring is the most reactive part of the heterocyclic ring. In particular the most reactive position on the indole for electrophilic substitution is N-1 and C-3. Indole of type **57** makes electrophilic substitution at 2-position, the next reactive position.

The main purpose of this is to obtain styrylcyanines **60** and its corresponding π-conjugation extension **61**, shown in Fig. 2.8. Scaffold **60** will serve as the core structure for our absorbers.[209] Approach A achieves chemical diversity through the condensation reactions of simple heterocyclic indoles with the corresponding aromatic aldehydes of a calcium ligand shown in a segment in Fig. 2.8 (*in blue*). Initial thoughts were to use pyro-EGTA ligand and to obtain an extended polyene chain of pyro-EGTA.

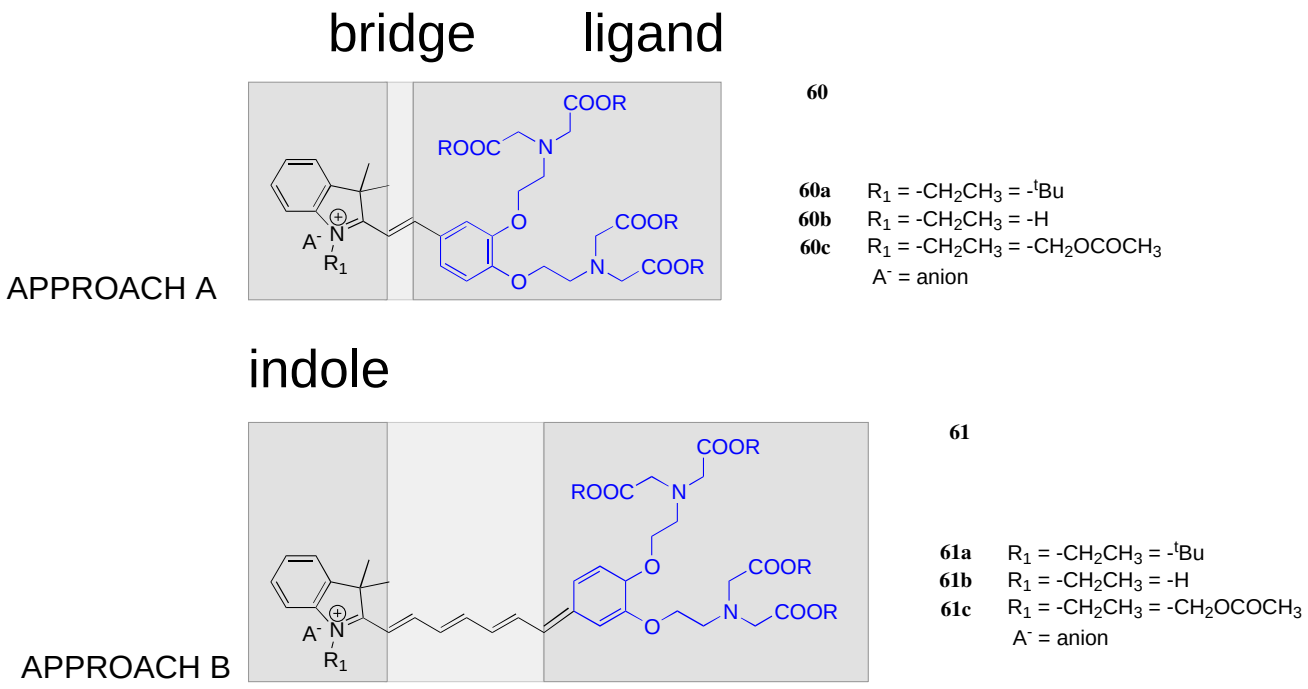

60

60a $R_1 = -CH_2CH_3 = -{}^tBu$
60b $R_1 = -CH_2CH_3 = -H$
60c $R_1 = -CH_2CH_3 = -CH_2OCOCH_3$
A^- = anion

61

61a $R_1 = -CH_2CH_3 = -{}^tBu$
61b $R_1 = -CH_2CH_3 = -H$
61c $R_1 = -CH_2CH_3 = -CH_2OCOCH_3$
A^- = anion

Figure 2.8: **Strategy C- Synthesis via direct condensation reaction of aromatic aldehydes and simple indoles.** Based on a semi-cyanine fluorophore 2-styrylindolium dyes **60**, several Zn^{2+} and Ca^{2+}- selective probes were designed. We would employ the same platform in Approach A to generate its corresponding NIR derivatives by extending the conjugated system (polymethine chain) to cy 7.

2.2 Results

2.2.1 Strategy A: Fischer Indole Syntheses/Buchwald Method

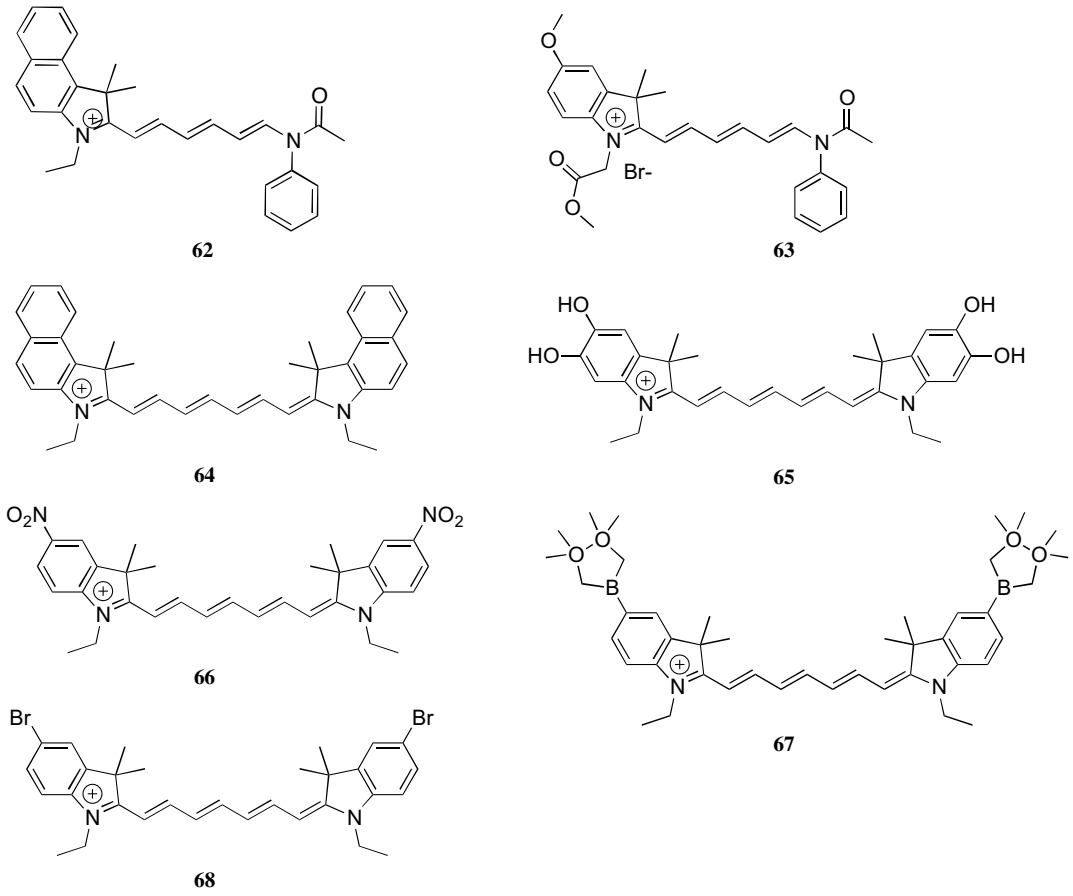

Figure 2.9: **Synthesised near-infrared cyanine dyes.** We have successfully synthesised the following selected near infrared chromophores using traditional synthetic methods.

Using the traditional way of synthesising cyanines,[47,188,194,210–213] we have taken simple corresponding indoles and it was alkylated with ethyl iodide in acetonitrile under reflux for 24h to afford the corresponding quaternary indole salt. The condensation reaction of quaternary salt with glutaconaldehyde dianilo hydrochloride **40** in acetic acid at 110 ^{o}C for 1h yielded near infrared cyanines. The selected cyanines, compounds **62**- **68**, were successfully synthesised and are shown in Fig. 2.9.

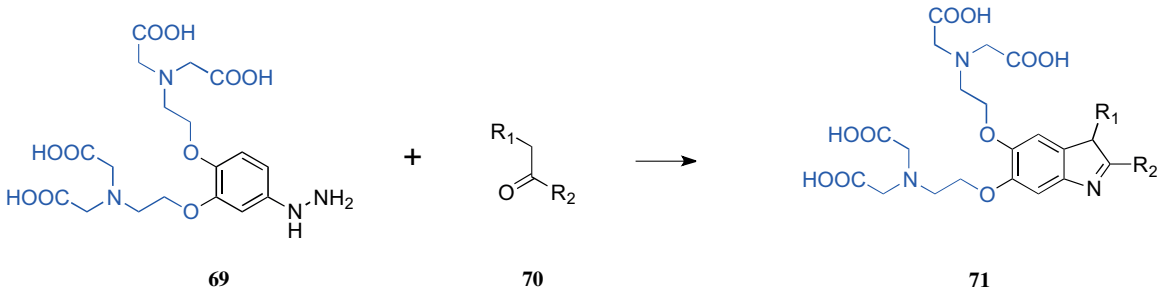

69 **70** **71**

Scheme 2.8: Synthetic scheme for the formation of precursor **71**, employing the *Fischer* indole reaction.

In order to test the reaction shown in Scheme 2.8, the first step was to generate the precursor **69**. The formation of compound **69** with 3-methyl-butan-2-ol **70** was carried out using the classical *Fischer* indole synthesis or the Buchwald modification. In an attempt to generate indole of type **71**, three synthetic approaches were employed, namely towards the synthesis of indolenine **80** as shown in Scheme 2.10 and 2.11. Commercially available 4-nitrobenzene-1,2-diol **71c** , 3,4-dimethoxyaniline **82** and 4-bromo-1,2-dimethoxybenzene **87** were the preferred starting materials for these syntheses. The first route was starting with 4-nitrobenzene-1,2-diol **71c** , outlined in Scheme 2.9. It relies on a multistep introduction of the aminomethyl group onto the catechol *via* elongation to cyanomethoxyphenoxyacetonitrile derivatives **74**. It was carried out *via* simple alkylation of chloroacetonitrile in anhydrous acetonitrile in the presence of potassium carbonate. The reaction was obtain in good yields (71-76%). Further selective reduction to diaminoethers **75** were carried out using borane dimethylsulfide refluxing in THF. *N*-alkylation of this compound using an excess of methyl bromoacetate in the presence of N,N-Diisopropylethylamine (DIPEA) in anhydrous acetonitrile gave the corresponding diaminoether **76c** . In Scheme 2.10, compound **76c** was nitro-reduced using Fe(0) and concentrated hydrochloric acid mixture in ethanol/water gave a aminoester **77**. One-pot diazotisation with sodium nitrite and concentrated hydrochloric acid (HCl) leads to formation of diazonium salt intermediate **78**. Reduction to arylhyrazine **79** using tin chloride (II) in concentrated HCl and direct one-pot reaction to corresponding **80** with corresponding 3-methyl-butan-2-one *via Fischer* indole synthesis under acidic condition was not observed. Indolium salt **81** to be synthesised *via* established methods with ethyl iodide. Several failed indolisation attempts prompt us to take another route.

The second route is outlined in Scheme 2.11. The synthesis of arylhydrazine **84** was adapted from Dougherty *et al.*[214]. It was prepared by oxidising 3,4-dimethoxyaniline **82** with sodium nitrite in the presence of hydrogen chloride to form the diazonium salt **83**.The reduction to (3,4-dimethoxyphenyl)hydrazine **84** using tin chloride (II) in HCl and direct *Fischer* indole synthesis using 3-methylbutan-2-one in acetic acid gave 5,6-dimethoxy-2,3,3-trimethyl-3H-indole **85** in sufficient yield. Here, I was able to obtain indole **85**, a simpler precursor. Demethylation using BBr_3- assisted cleavage of catechol dimethyl ether **85** in DCM, proceeds in a stepwise reaction (likely since a cyclic borate can form),[215] gave **86** in poor yields (20%). Here, I was able to at least obtain the indole **86**. At the time, we did not observe the corresponding product **81** using *O*-alkylation of the catechol with potassium carbonate.

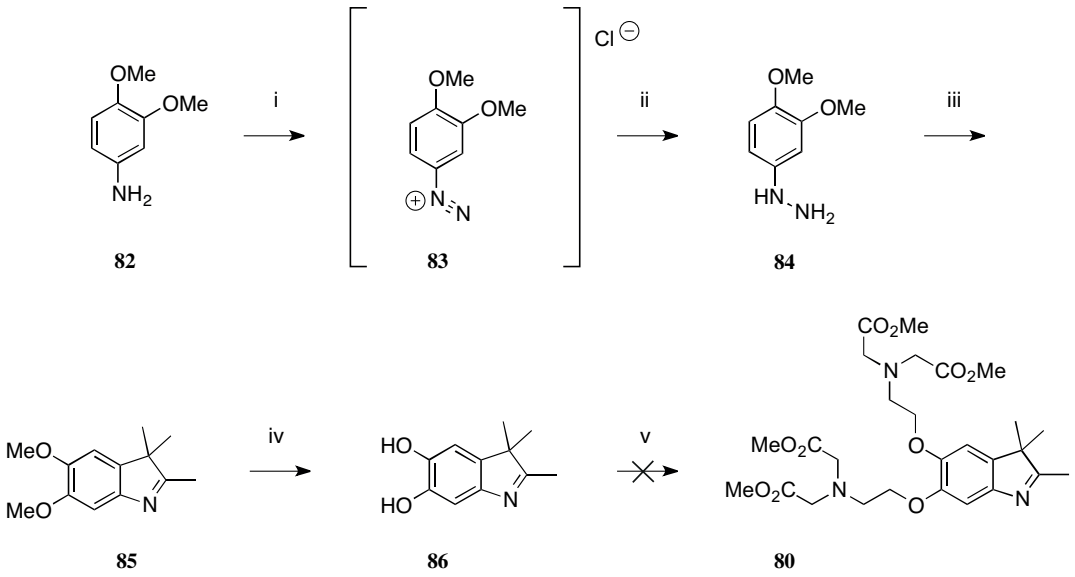

Scheme 2.11: **Route 2: Towards the synthesis of functionalised based on indolium salt** *Reactions and conditions:*. i) $NaNO_2$, HCl/H_2O (1:1), $\leq 0\ ^oC$, 30 min; ii) $SnCl_2$, HCl, $\leq 0\ ^oC$, 30 min; iii) 3-methyl-butan-2-one, acetic acid, r.t, overnight; iv) BBr_3, DCM, $0 \rightarrow$ r.t., 3 h; v) $Br(CH_2)_2(N(CH_2)_2COOMe)_2$, K_2CO_3, MeCN, r.t., 72 h

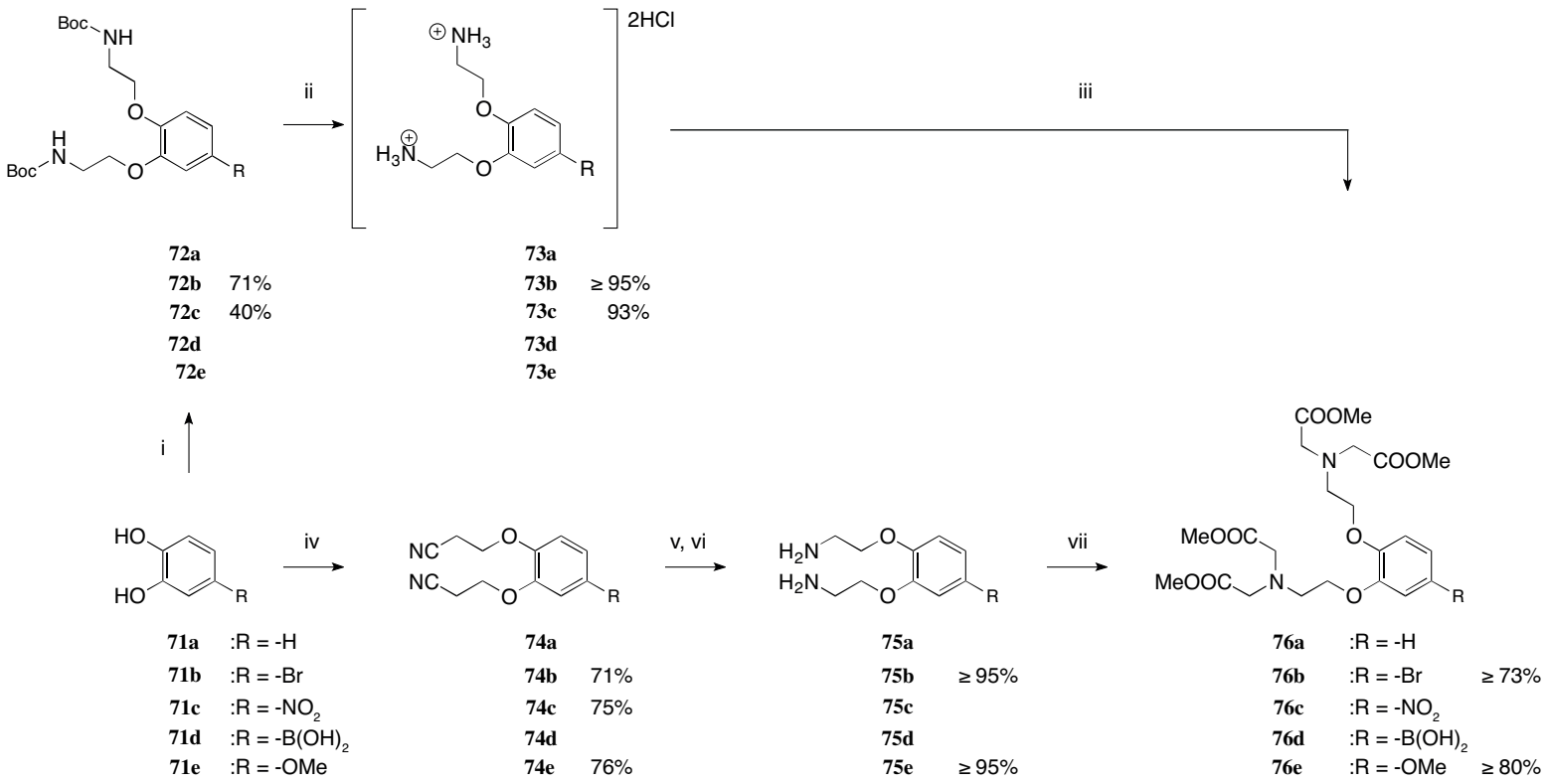

Scheme 2.9: **Syntheses of diaminoethers**. *Reagents and conditions:* i) *N*-Boc-2-bromoethyl-amine, K_2CO_3, MeCN, reflux, 3 h; ii) 4N HCl/dioxane, 0 ^{o}C, 3 h; iii) $BrCH_2CO_2Me$, DIPEA, reflux, 3 h; iv) $ClCH_2CN$, K_2CO_3, MeCN, r.t., 72 h; v) $BH_3 \cdot Me_2S$, THF, reflux, 4 h; vi) H^+/H_2O, reflux, 20 min; vii) $BrCH_2CO_2Me$, DIPEA, MeCN, reflux, 15 h.

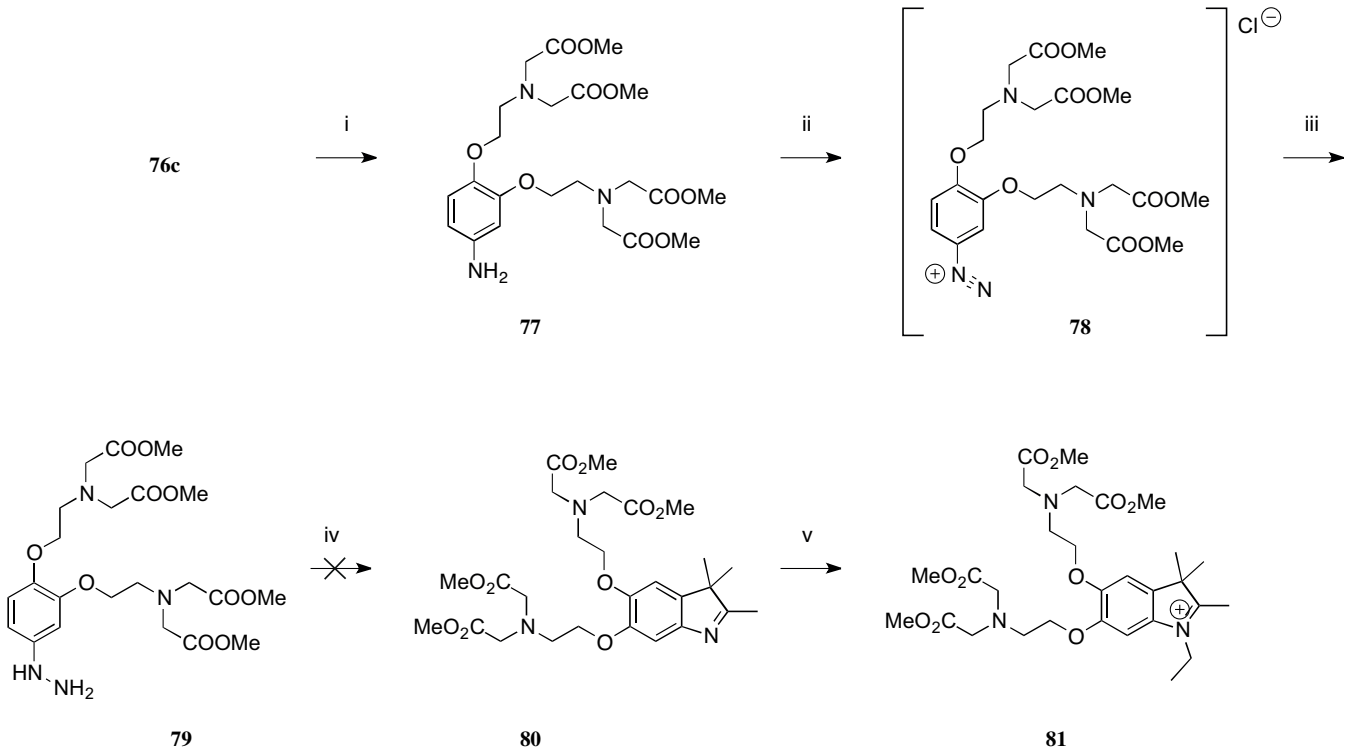

Scheme 2.10: **Route 1: Towards the synthesis of functionalised based on indolium salts 81** *Reactions and conditions:* i) Fe/HCl, EtOH:H_2O (7:3), reflux, 30 min; ii) $NaNO_2$, HCl, H_2O, 0 ^oC; iii) $SnCl_2$, HCl, 0 ^0C; iv) 3-methyl-butan-2-one, acetic acid, r.t, overnight; v) EtI, MeCN, reflux, overnight

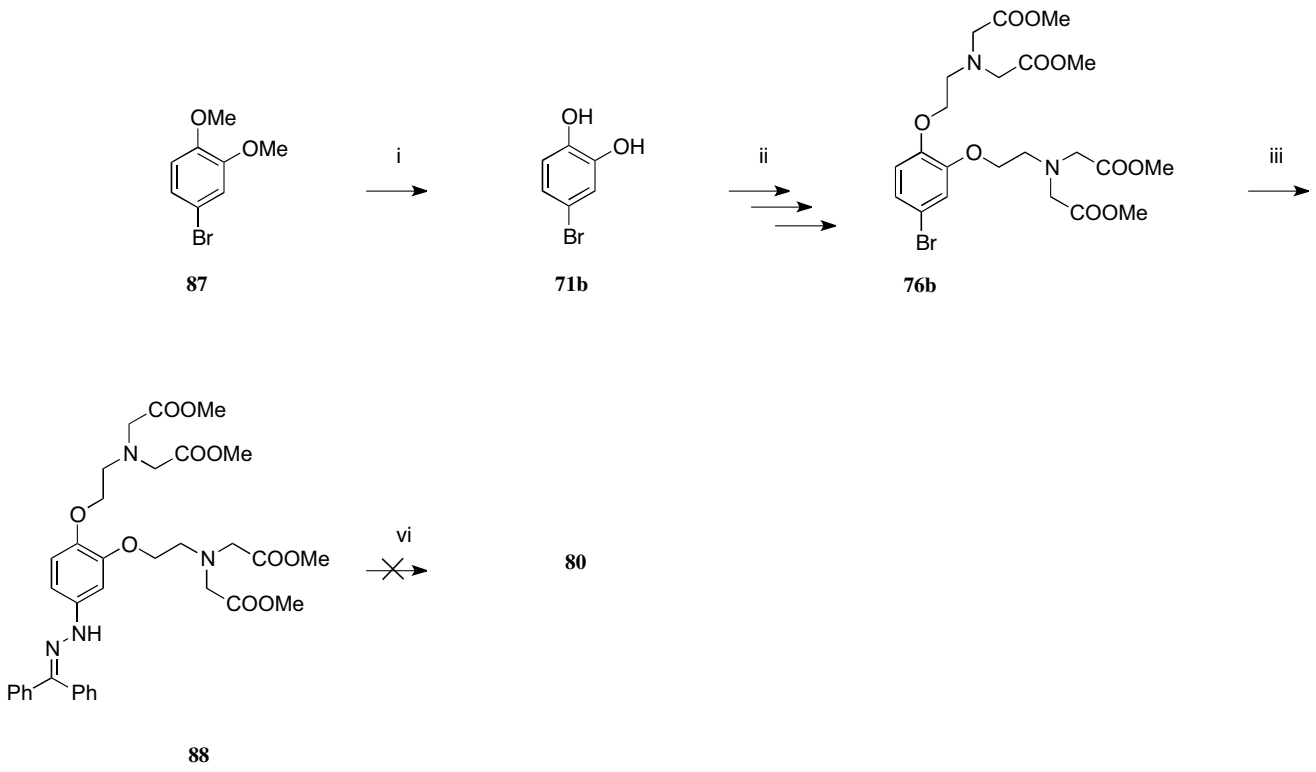

Scheme 2.12: **Route 3: Towards the synthesis of functionalised compounds based on indolium salt.** *Reactions and conditions:*. i) BBr_3, DCM, 0 $\rightarrow$ r.t., 3 h; ii) Ref. Scheme 2.9; iii) benzophenone hydrazone, $Pd(OAc)_2$ (5 mol %), $\pm$ BINAP (5 mol %), NaOt$-$Bu, toluene, 100 ^{o}C, 22 h; iv) 3, methyl-butan-2-one, $TsOH \cdot H_2O$, EtOH, reflux, 9 h.

The third route outlined in Scheme 2.12 starts with the demethylation of 4-bromo-1,2-dimethoxybenzene **87** using boron tribromide in dichloromethane (DCM) carried out below room temperature gave 4-bromobenzene-1,2-diol **71b** in excellent yield (95%). The synthesis of diaminoether **76b** as previously described in Scheme 2.9. Compound **76b** was converted to *N*-aryl benzophenone hydrozone **88** by reacting it with benzophenone hydrazone using $Pd(OAc_2)$/(S)-BINAP catalyst system in the presence of NaOt$-$Bu in toluene. We came to this point of the synthesis where benzophenone hydrozone **88** was successfully synthesised. However, further cyclisations to form the desired indole was unsuccessful.

2.2.2 Near infrared Calcium Sensor

This section of the work is now published and it was mainly carried out by Dr. Anurag Mishra.[216] We worked together on the initial design and synthesis of probe **89**. My contribution extended to

editing the manuscript, scientific discussions, the preparation of revised manuscript and contributed towards replying to the reviewer's comments. In short, this new NIR metallochromic contrast agent changes its photoacoustic signal in the presence of Ca^{2+} ions and can be used to reversibly measure calcium transients *via* photoacoustic imaging. The probe was synthesised using a commercial NIR dye core based on heptamethine dye. A known Ca^{2+}-chelating agent, APTRAmorpholinoamide (carboxymethyl) (4-hydroxy-2-[2- (morpholin-4-yl)-2-oxoethoxy]phenyl)amino]acetic acid), also known as APTRA was used to conjugate onto the cyclohexenyl ring of a heptamethine dye (IR-780). APTRA was synthesised in five synthetic steps.[216] The final PAI probe **89** was synthesized by *o*-alkylation of onto IR-780 [λ_{max} 780 nm] scaffold using NaH as base in anhydrous DMF/DMSO (90:10) with 5% yield and subsequently purified by reverse-phase HPLC.

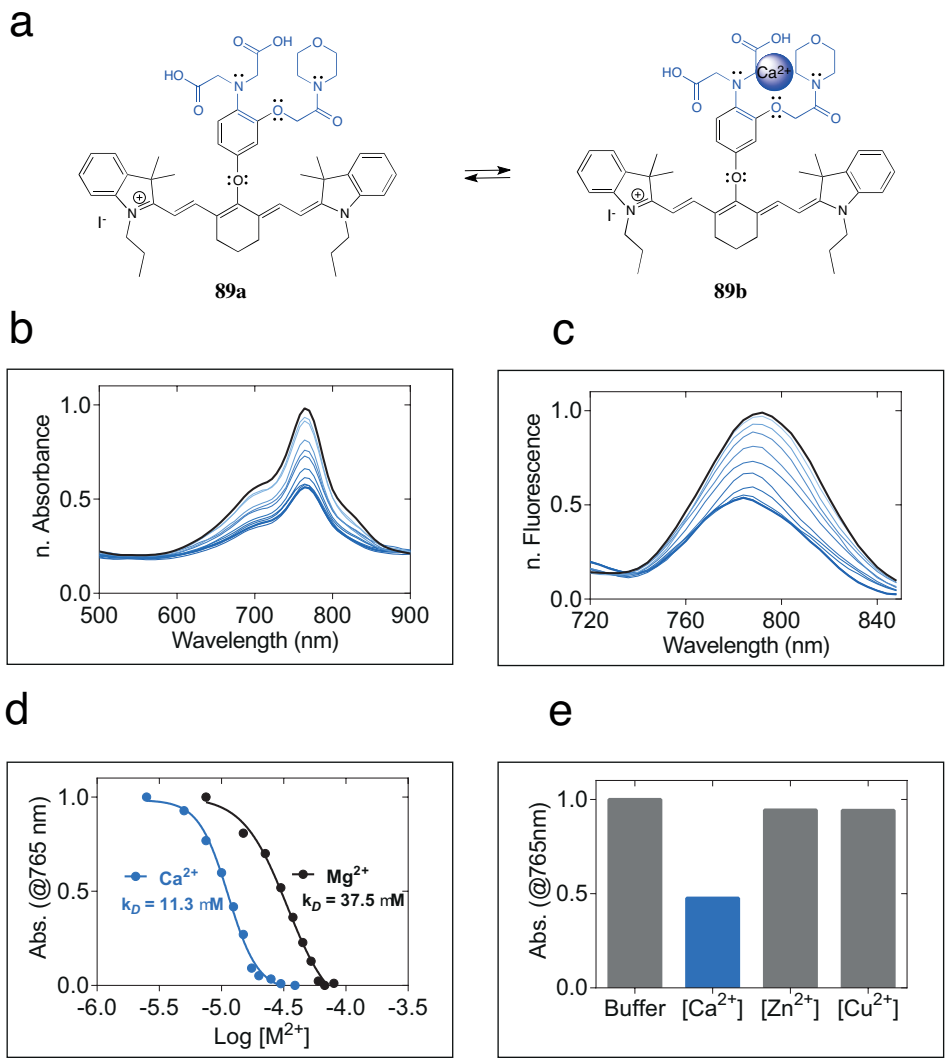

Figure 2.10: **Near-Infrared Photoacoustic Imaging Probe Responsive to Calcium.** (a) Schematic representation of the chemical structure of the NIR Ca^{2+} sensing PAI probe **89** in its unbound **89**a and Ca^{2+}-bound **89**b form.(b, c) Spectroscopic characterization of **89** to determine Ca^{2+} sensitivity and selectivity over other biologically relevant metals. Changes in absorbance (*left*) and fluorescence spectra (*right*) induced by various concentrations of free Ca^{2+} (0, 2.5, 5, 7.5, 10, 12.5, 15, 17.5, 20, 25, 30, and 39 μM) in 30 mM MOPS buffer containing 100 mM KCl (pH 7.2, 20 μM L) at 37 ^{o}C. The excitation wavelength was 680 nm. (d) IC50 values for Ca^{2+} and Mg^{2+} were determined from the peak absorbance value at 765 nm in 100 mM KCl, 30 mM MOPS (20 μM **89**, pH 7.2, 37 ^{o}C). The Ca^{2+} binding curve is shown in blue and the black curve shows the binding curve for Mg^{2+}. (e) Peak absorbance maxima (at 765 nm) measured from **89** (20 μM) upon addition of 50 μM [Ca^{2+}], [Zn^{2+}], and [Cu^{2+}] in 30 mM MOPS, 100 mM KCl (pH 7.2, 37 ^{o}C).This figure was adapted from Mishra *et al.* [216].

Due to the presence of four negative carboxylic acids, the calcium sensor **89** has less tendency to bind to endogenous proteins. It is soluble in water and therefore photophysical characterisations

of **89** was carried out in aqueous solution (pH 7.20, 21 ^{o}C). Upon exchanging -Cl on IR-780 to -0, λ_{max} hypsochromically shifted from 780 to 765 nm. The extinction coefficient ε of **89** at 765 nm was measured as 194 000 M^{-1} cm^{-1}, which is comparable to the λ of cyclicheptacyanine based NIR dyes with an intense $\pi \rightarrow \pi^*$(0 $\rightarrow$ 0 vibronic) transition. The shoulder at 695 nm is also $\pi \rightarrow \pi^*$ mode, relating to the 0 $\rightarrow$ 1 or 0 $\rightarrow$ 2 vibronic transitions. The emission spectra of **89** was measured following excitation at 680 nm and a weak emission band was obtained that centered at 790 nm, giving a Stokes shift of $\approx$25 nm (Fig. 2.10). Similar dye structures reported previously were shown to have quantum yields that fall in between 5 and 10%. The high extinction coefficient in the NIR makes **89** an excellent PAI sensor because the background absorbance (of oxygendependent photoacoustic changes due to hemoglobin) is relatively low in this wavelength range. Calcium response of **89** was conducted with various concentrations of free [Ca^{2+}] in 30 mM 3-(N-morpholino) propanesulfonic acid (MOPS) buffer containing 100 mM KCl and different ratios of K_2EGTA/CaEGTA (pH 7.2, 20 μM [**89**]) at 37 ^{o}C. The absorbance peak amplitude of **89** decreased to half with increasing [Ca^{2+}] (0 $\rightarrow$ 39 μM; Fig 1). Similarly, the fluorescence emission dropped to half upon excitation at 680 nm (Figure 1B). The IC50 values were determined from the Ca^{2+}-dependent change in the peak absorbance (765 nm) and fluorescence (790 nm) and calculated as 11.3 μM and 12.4 μM, respectively (Figure 1C (blue line) and Figure S4, Supporting Information). These values are lower than that of other APTRA (o-aminophenol-N,N,o-triacetic acid) based molecules (22 μM for Ca^{2+}), probably because we positioned the APTRA (donor) via a strong electron donating group (present on para position to $N(CH_2COOH)_2$) at the bulky chromophore (acceptor). We also observed a reduction of the molar extinction coefficient of **89**

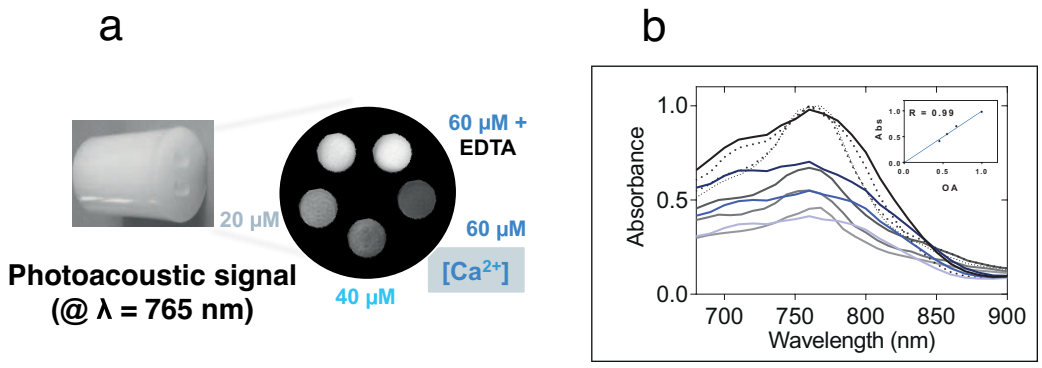

Figure 2.11: **Photoacoustic signal changes of probe 89 for varying Ca^{2+} and its subsequent reversibility upon addition of EDTA** (a) 40 μM in aqueous solution (30 mM MOPS, 100 mM KCl, pH 7.2, 37 ^{o}C) was mixed with 0 to 60 μM of Ca^{2+} ions and 60 μM Ca^{2+} ions + 80 μM EDTA and filled into 3 mm diameter tubes that were inserted in a 20 mm diameter phantom made of 1.3% agar. Photoacoustic images were acquired for different wavelengths (600- 900 nm in 10 steps, 9 ns laser pulses at a repetition rate of 10 Hz, 50 averages per image). (b) Corresponding photoacoustic spectra (solid lines) extracted from the average pixel intensities of circular region of interests (ROIs) covering the samples on the photoacoustic images are plotted together with absorbance spectra (broken lines) obtained for each of the Ca^{2+}. The inset shows the correlation between the absorbance and photoacoustic peak values. This figure was adapted from Mishra *et al.* [216].

Probe **89** was demonstrated as a Ca^{2+} sensing probe. It was detectable *via* photoacoustic imaging. We assessed probe **89** in the absence and presence of different [Ca^{2+}] concentration in 30 mM MOPS buffer [100 mM KCl, pH 7.20, 37 ^{o}C]. These experiments were conducted using a small animal PAI scanner (inVision 256-TF, iThera Medical GmbH, Munich, Germany). The measurements started with 40 μM of **89** mixed with varying [Ca^{2+}] concentrations [0 to 60 μM, (20 μM incremental points)] and the absorbance spectrum was measured. Each sample was then sequentially placed in a separate 3 mm diameter non-absorbing plastic tube together with a reference sample containing no calcium. This was inserted at a defined position in a 20 mm diameter phantom made of 1.3% agar mimicking tissue scattering. The images were reconstructed using model-based reconstruction method. The intensities are normalised to the reference. There is a gradual decrease in the signal intensity of the sample (imaged at 760 nm) as a function of increasing Ca^{2+} concentrations up to 60 μM. This correlates to what we have observed with the absorbance spectra. The addition of EDTA (80 μM) restores the signal to that of the metal-free probe by competing out Ca^{2+}. Fig. 2.11 shows the photoacoustic spectra plotted from the average pixel intensities obtained from a region of interest analysis of the photoacoustic images (solid

lines). Corresponding absorbance spectra of the identical samples are displayed as broken lines (Fig. 2.11); the inset shows the correlation of the peak signals from the absorbance and PA spectra (r = 0.99).

2.2.3 Strategy B: Pd-cat. reactions

Using this strategy, we deduce a novel and promising pathway via Pd-cat. reactions on the 5-indole position. This was based on the fact that we have successfully synthesised a number of analogues of compound **76**, specifically **76b** and **76d** derivatives.

I have explored several available synthetic pathways. The first challenge was to construct the terminal arylacetylenes **93** and **95**. Handling acetylenes directly is usually considered tedious and coupling is usually carried out using protected acetylene which is simpler to handle, followed by deprotection of protecting groups. The most commonly used monoprotected acetylene derivative is probably trimethylsilyl-acetylene. Removal of the protecting group was carried in the presence of fluoride ion or a base at ambient temperature and mild conditions. Another route that is more convenient for the preparation of acetylenes is to use 2-methyl-3-butyn-2-ol. It is low cost and the deprotection was the more favourable route.[217] We have tried to do several Pd-catalysed reactions of varying conditions either with C-C coupling with bromo indole **90** and aryl acetylene **95** or vice versa indole acetylenes **93** and bromo pyro EGTA. In all conditions, the desired products **56a** and **56b** were not observed. These reactions requires more direct monitoring.

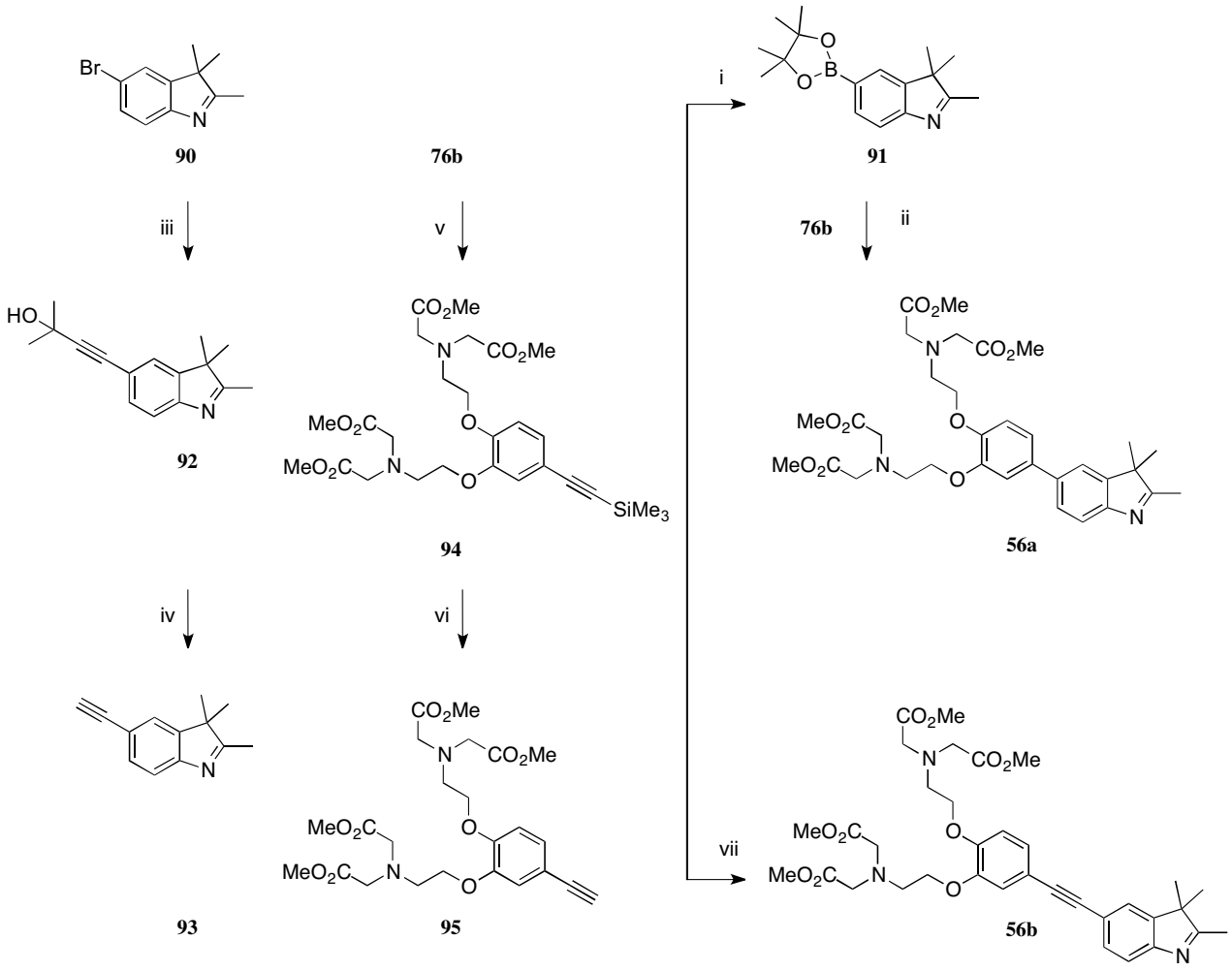

Scheme 2.13: **Strategy B: towards the synthesis of functionalised 5-indole position using Pd-cat.** *Reagents and conditions:* i) bis(pinacolato)-diboron, $Pd(dppf)Cl_2$ (5 mol- %), KOAc, dioxane, 85 ^{0}C, 2 h; ii); iii) 2-methyl-3-butyn-2-ol, $(Ph_3P)_2PdCl_2$ (2 mol- %), CuI (1 mol- %), Et_2NH, 50 ^{o}C, 9 h; iv) K_3PO_4-KOH, toluene, reflux, 1 h; v) trimethylsilylacetylene, $Pd(dppf)Cl_2$ (10 mol- %), CuI (10 mol- %), NEt_3, THF, 60 ^{o}C, 16 h; vi) TREAT-HF, THF, r.t., 5 h; vii)

2.2.4 Strategy C: Direct condensation reactions

The successful synthesis of cyanines **96**, **97** were observed. **96** and **97** were briefly evaluated as zinc sensors. The future syntheses of compounds **98** and **99** are desired for NIR properties. Products **96**, **97** were obtained by the condensation of 1,2,3,3-tetramethyl-3-H-indolium iodide with the respective carbonyl components in ethanol and triethyl amine as the reactive medium under reflux for 30 mins with 80 % yields. The compounds were verified by spectroscopic methods.

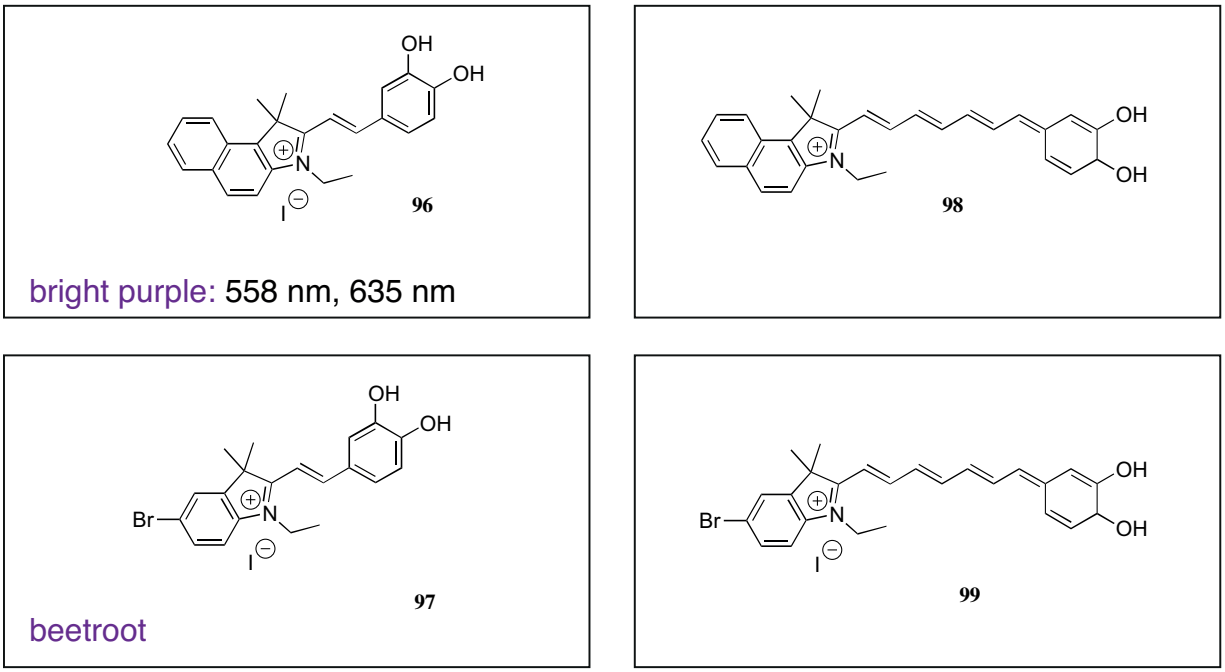

Figure 2.12: **Zinc sensor designs**. The condensation of 1,2,3,3-tetramethyl-3-H-indolium iodide and respective aryl carbonyl showing access to ligand chelators from the C-2 position

Successful synthesis of compounds **96** and **97** prompt us to investigate whether reaction of 1,2,3,3-tetramethyl-3-H-indolium iodide with the respective carbonyl components of BAPTA can be achieved using the same synthetic strategy. Indeed, Chapter 3 separately reveals and discusses the successful design and syntheses derivatives of **60** for the detection of calcium transients. Dynamic absorption changes in response to the metal cations, both using optical and optoacousic imaging techniques are shown showing the rational is successful. Full evident data is explored in Chapter 3 for its *in vitro* and *in vivo* biological applications.

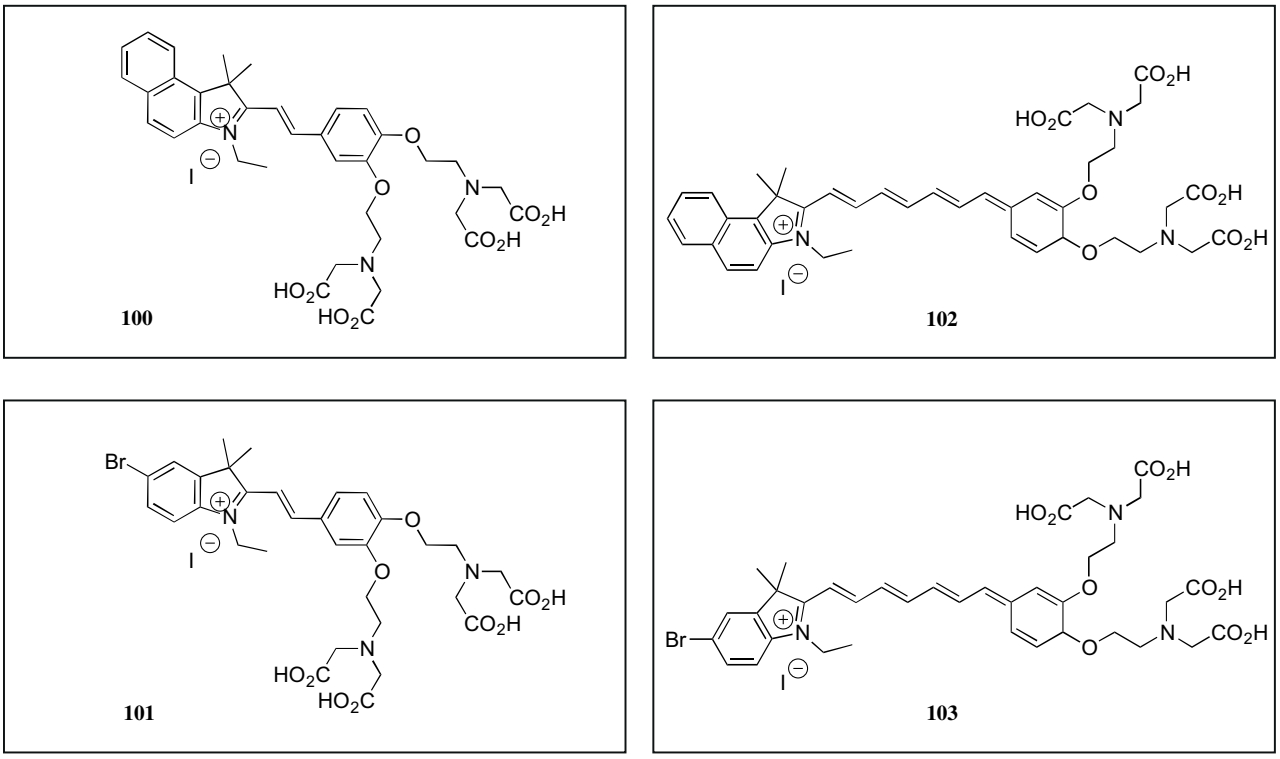

Figure 2.13: **The possible extension of semi-cyanines extends towards other calcium chelators.**

2.3 Discussion and conclusions

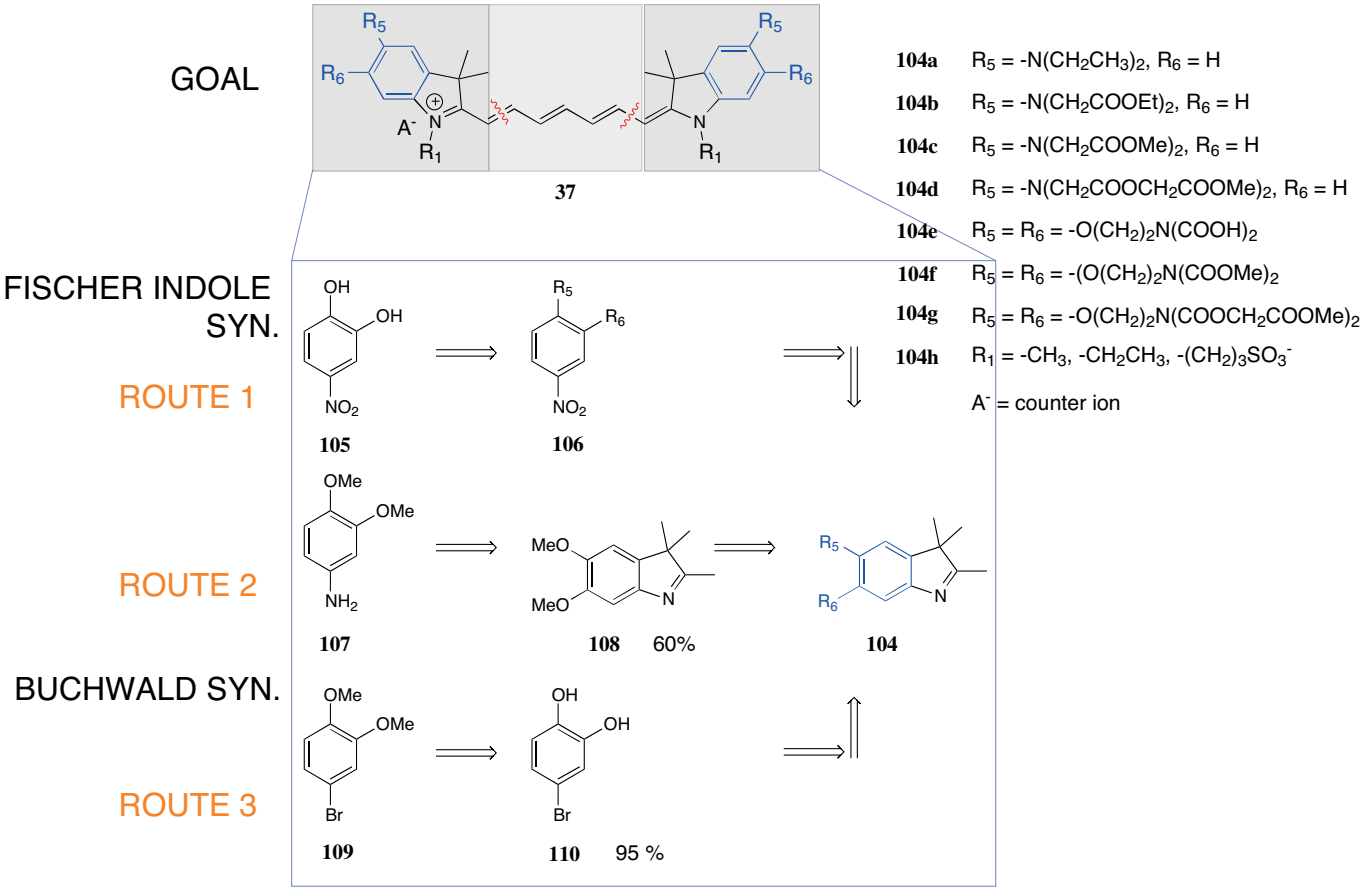

Scheme 2.14: Strategy A- Multi-synthetic pathways towards highly substituted indoles at 5-,6- position via Fischer indole synthesis[218] and Buchwald modification methods,[199,200] starting with commercially available compounds **105**, **107** and **109**.[203,219–222] Using the Fischer method, indoles are produced from the desired aromatichydrazines and ketones under acidic conditions. Buchwald method on the other hand, uses Pd-cat. reactions by cross coupling aryl halides (typically bromides) and hydrazones. palladium catalyst (Pd-cat.) are typically $PdCl_2$(dppf) and $Pd(OAc)_2$. These N-arylhydrazones then undergo displacement with other ketones to promote cyclisations.

The goal to synthesise derivatives of **37** was more challenging than we initially anticipated. We have reached major synthetic challenges in synthesising precursor **104**. We have synthesised up to precursor **106**, **108** and **110** in good yields. We did not observed the derivatives of **104** using the traditional *Fischer* indole syntheses shown as Route 1, 2 and Buchwald modification shown as Route 2 in Scheme 2.14 respectively. The nitro reduction of **106** for example was difficult to handle and quickly decomposes. *In situ* reaction of nitro reduction followed by condensation reaction was unsuccessful. Therefore, we took the second route, the cyclisations of **108** before

methyl protection. Route 2 proved the opposite result, we were able to do the Fisher indole synthesis, obtaining **108** in good yields but it proved difficult to deprotect. We have expanded this route using Buchwald modifications. The palladium-catalysed cross coupling of amines with aryl halides has proven to be successful for this system. In an initial experiment, we found that due to the success of synthesising the substrate, we hoped that this methodology would provide a complimentary synthesis towards indole **80**. We were able to observe N-aryl-benzophenone **88** in decent yields. The corresponding indolisations via hydrolysis of of hydrazines with an excess ketone was unsuccessful. The expectation was that in the presence of a ketone **70**, it could produce an enolisable hydrazone that would undergo Fischer indolisations under acidic reactions.

Routes one and two *via* Fischer indole synthesis using *N-arylhydrazines* precursor described above proved to be synthetically challenging. It has been proven that *N,N*-disubstituted hydrazones undergo Fischer cyclisations to afford its corresponding indole products,[223,224] the synthesis of *N,N*-disubstituted hydrazines are typically complicated due to the presence of two reactive nitrogens and its instability. To circumvent the need to prepare *N*-arylhydrazines, a Pd-catalysed method was employed for the preparation of *N*-arylhydrazones **88** for the Fischer indole synthesis of indole **80**.[199,200] I have conducted *Fischer* indolisation, outlined in Scheme 2.12. It was carried out under acidic hydrolysis in the presence of 3-methyl-butan-2-one, a reaction that should have irreversibly undergone a *Fischer* indolisation to completion. In all cases, we were not able to observe the desired indole **104** that we initially set out to synthesise. A more thorough monitoring of the reaction could benefit future evaluation of this synthetic method.

We have successfully synthesised, evaluated and demostrated that probe **89**[216] as a near infrared photoacoustic imaging agent that is reversible and suitable for dynamic imaging. The engineered probe strongly absorbed light in the NIR range, 765 nm, which is ideal for PAI methods since the background absorbance and signal changes due to hemodynamics are relatively low in this wavelength range. The compound showed a robust reduction in absorbance upon addition of Ca^{2+} that translated into a strong decrease in the PA signal. The sensor showed a three-times higher affinity for Ca^{2+} over Mg^{2+} which can be further tuned by changing the chelating moiety and/or altering its positioning on the chromophore, e.g., via cyclohexene-oxygen or directly on the

cyclohexene. The near infrared IR-780 core we introduced could be used to generate other series of NIR metallochromic sensors for molecular imaging of specific divalent cations in deep tissue via photoacoustic tomography. See relevant publication (click here) for more details of its use and photoacoustic application.[216]

Strategy A was conceived at the early stages of my PhD work. Its associated developments led to spin-offs described as the second and third strategies. The third strategy proved successful in providing us a lead compound. We focused our efforts to prioritise and fully characterised our lead compound, **111** and extended the study for MSOT calcium imaging, thus establishing the first new platform for dynamic MSOT imaging. The successful chemical structural diversity has been achieved through strategy 3.

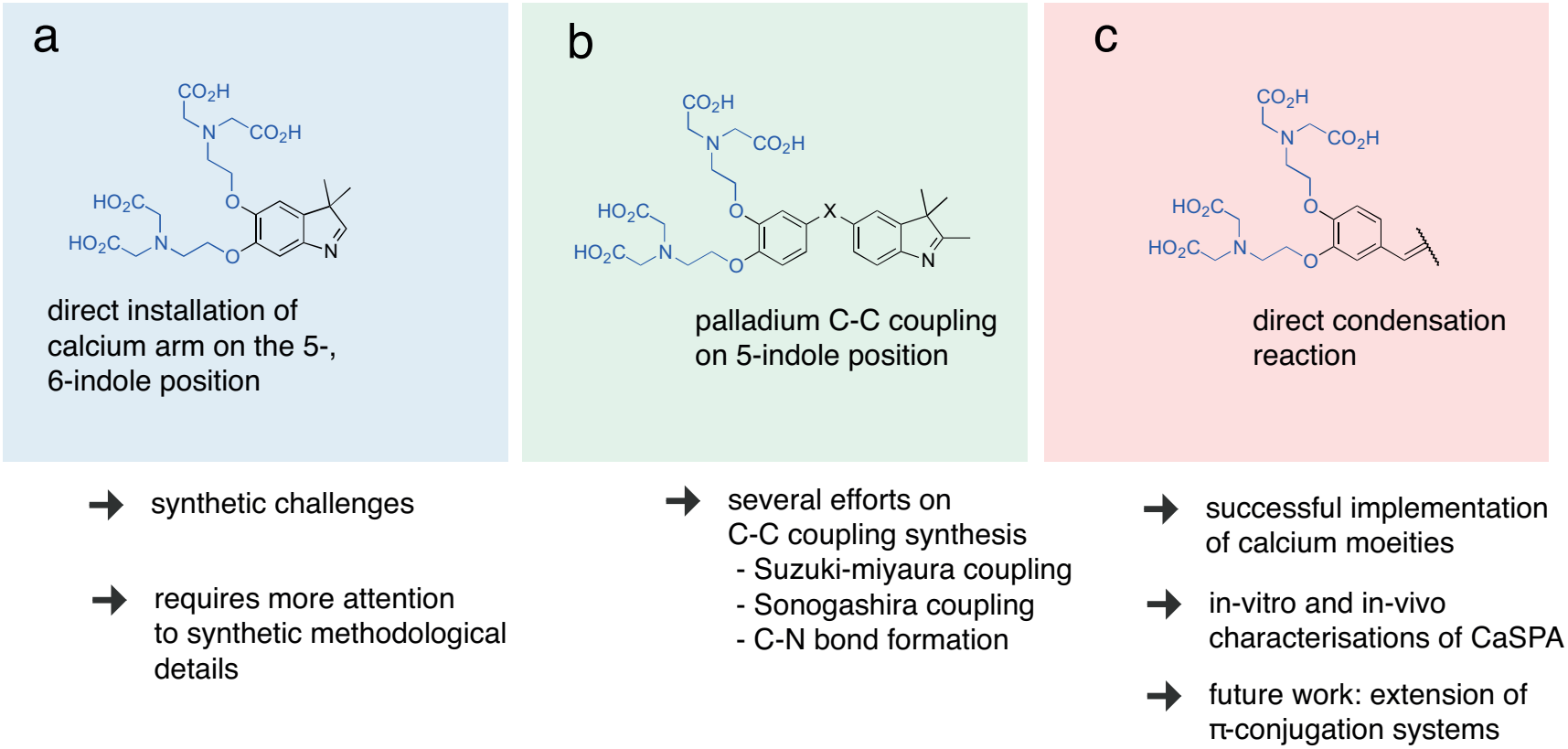

Figure 2.14: **Summary of our strategic design towards the formation of functionalised contrast agents** (A) access to substituted indoles at 5-,6-indole position via *Fischer* indoles synthesis and Buchwald modification methods (B) Employing Pd- cat. reactions at 5-position using Suzuki-miyaura borylation, Sonogashira coupling and C-N bond formation. (C) Facile synthesis via direct condensation reaction of aromatic aldehydes and simple indoles.

Chapter 3

Calcium selective photoacoustic agent (CaSPA series)

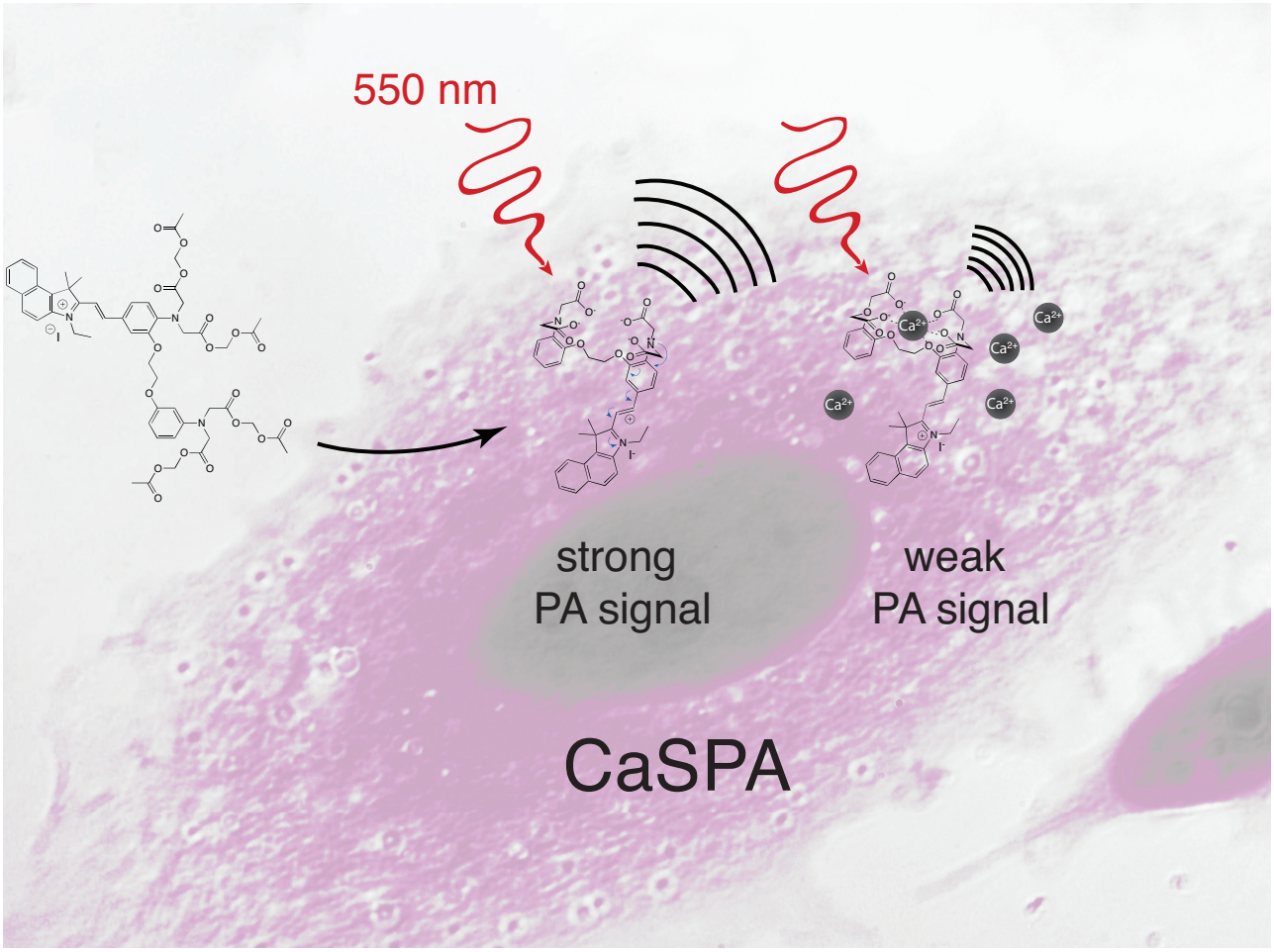

Objectives

The objective was to create chemical diversity of ligands at C-2 indole positions.

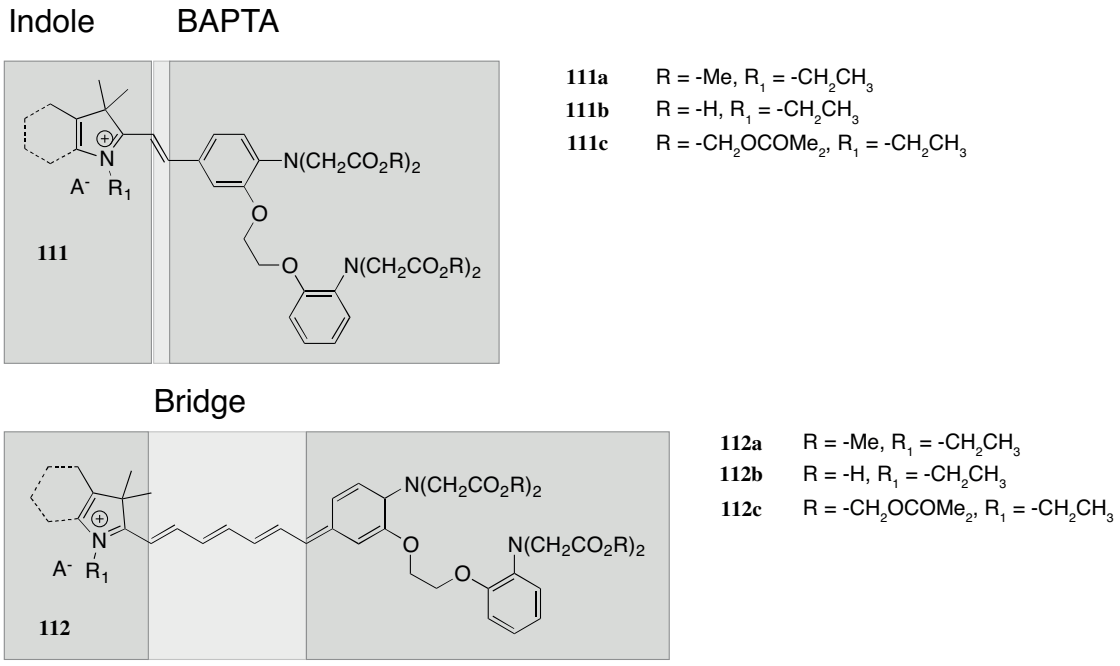

111a R = -Me, R_1 = $-CH_2CH_3$
111b R = -H, R_1 = $-CH_2CH_3$
111c R = $-CH_2OCOMe_2$, R_1 = $-CH_2CH_3$

112a R = -Me, R_1 = $-CH_2CH_3$
112b R = -H, R_1 = $-CH_2CH_3$
112c R = $-CH_2OCOMe_2$, R_1 = $-CH_2CH_3$

Figure 3.1: **The structure of calcium selective photoacoustic agent.** Based on a semi-cyanine scaffold (2-styrylindolium dyes), reactions of appropriate functionalised aromatic aldehydes to the C-2 indole terminal produces compounds **111** and **112**.

This work is under currently revision (Roberts et. al. *Calcium Sensor for Photoacoustic Imaging*, 2017).

3.1 Introduction

To design a reversible sensor for photoacoustics based on the appropriate prerequisites (refer to Chapter 1), one may search for functionalisations that alter its ε as a function of analyte or environmental parameter of interests. A photoacoustic sensor for Ca^{2+} should be highly selective for the target analyte over other biologically relevant divalent metals (Zn^{2+}, Mg^{2+}, Cu^{2+}). Magnesium is present in higher intracellular concentrations than Ca^{2+}.[225] Selectivity against zinc (Zn^{2+}) is also desirable as neurons containing zinc are all glutamatergic, but only some of the glutamatergic neurons actually contains zinc.[226] It is co-packaged with insulin in vesicles that are released from β-cells in a Ca^{2+}-dependent manner.[227] Furthermore, transmembrane delivery of the Ca^{2+} sensor should be efficient in order to load the majority of cells in a PAI voxel and minimize partial volume effects.

To date, cyanines such as ICG, a subclass of polymethine family dyes, are one of highest class of absorbers with ε above $\geq 200,000\ cm^{-1}\ M^{-1}$ with a low 0.1 QY constantly being reported.[228] Our initial assessment of the theoretical PA properties of cyanines makes it an ideal candidate for further group functionalisations. For a given absorber, smart CAs have to alter their ε as a function of the analytes concentration. While neurovascular coupling also occurs during neuronal activation, changes in oxygen-dependent hemoglobin is prominent and it is actually exploited for optoacoustic detection.[229] Well designed probes have maximum absorption peaks either at isosbestos points of oxy-and deoxy-haemoglobin or NIR regions away from this event. These set of specifications is however not fulfilled by most current calcum sensors used for fluorescence microscopy as these fluorophores, such as oregon green BAPTA-1 operate mainly via a change in its QY.[230]

There are two studies that have been performed: a) studying fast hemodynamic changes in deep mouse brain[3] and b) tracking neural calcium dynamics in zebrafish brain labelled with GECI, GCaMP5G.[29] Moreover, recent studies have shown PA imaging of biologically relevant analyte, this time though with copper(II). Based on Cu^{2+}-triggered cleavage of a 2-picolinic ester bond that derives to a shift in its absorption spectrum and therefore its photoacoustic signal

response. However, the system is irreversible and has not been shown its forward potential *in-vitro*.[4] 3-(4,5-dimethylthiazol-2-yl)-2,5-diphenyltetrazolium bromide (MTT) formazan was the very first and recent attempt to evaluate small molecules in cells using PA, however the cells were stained and fixed samples on agar.[68] Some well-known chromophores that change their absorbance in response to metal binding (metallochromic substances), such as Arsenazo-III and cholorophosphonazo-III (CPZ-III), exhibit specific absorbance changes in response to Ca^{2+}.[231] We have carried out these experiments to check their suitability as PAI agents. See Appendix B, Fig. B.10, Fig. B.11, Fig. B.13 and Fig. B.14.

However, Arsenazo-III and CPZ-III compounds exhibit lower selectivity for Ca^{2+} as compared with BAPTA. The Ca^{2+}-binding cavity cannot be easily modified to achieve efficient delivery into cells. We have attempted several modifications but we were not successful. Changing the cavity too much will likely deviate from its function. These probes are furthermore known to form complexes with two dye molecules per Ca^{2+}. Photoacoustic signals were measured from Arsenazo-III when packaged into liposomes and more recently, from cells into which the highly concentrated 200 μM Arsenazo-III were loaded. The result is measurable toxicity[42,232] and inherent stoichiometry problems which results in uncertain calibration.[43]

Because of the direct condensation reaction described in Chapter 2, section 2.2.4 was showing promising results, we have continued to pursue this route. We wanted to design metallochromic compounds that are expected to undergo a photoinduced charge transfer (PCT) as described for e.g. fura-2,[170] in which a Ca^{2+} sensitive donor (aniline in BAPTA) is conjugated to an acceptor molecule in the fluorophore (amino group) leading to a spectral blue shift upon calcium binding.[202,233] We reasoned that semi-cyanine chromophore could maintain the PCT mechanism and shift its wavelength to longer wavelengths more suitable for photoacoustics. In this chapter, we demonstrate the design strategy and results for *in vitro* and *in vivo* photoacoustic applications

3.2 Results

The semi-cyanine chromophore of CaSPA-550 tetramethyl ester (**117**, Scheme 3.1) was synthesised *via* condensation reaction of 3-ethyl-1,1,2-trimethyl-1H-benzo[e]indol-3-ium iodide salt **114**, containing activated methyl group with an appropriate unsaturated *p*-aldehyde 1,2-bis(*o*-aminophenoxy)-N,N,N',N'-tetramethyl ester) (BAPTA methyl ester **116**) gave deep purple crystals in 85% yield (Scheme 3.1). Subsequent demethylation using NaOH(aq) was carried out, dried as solid free acids gave erratic yields and purity to yellow oil **118** at $\leq$5%. Initial saponification of esters with tetrabutylammonium hydroxide in search for better yields and solubility in polar organic solvents for further esterification gave better yields of up to $\geq$ 20%.

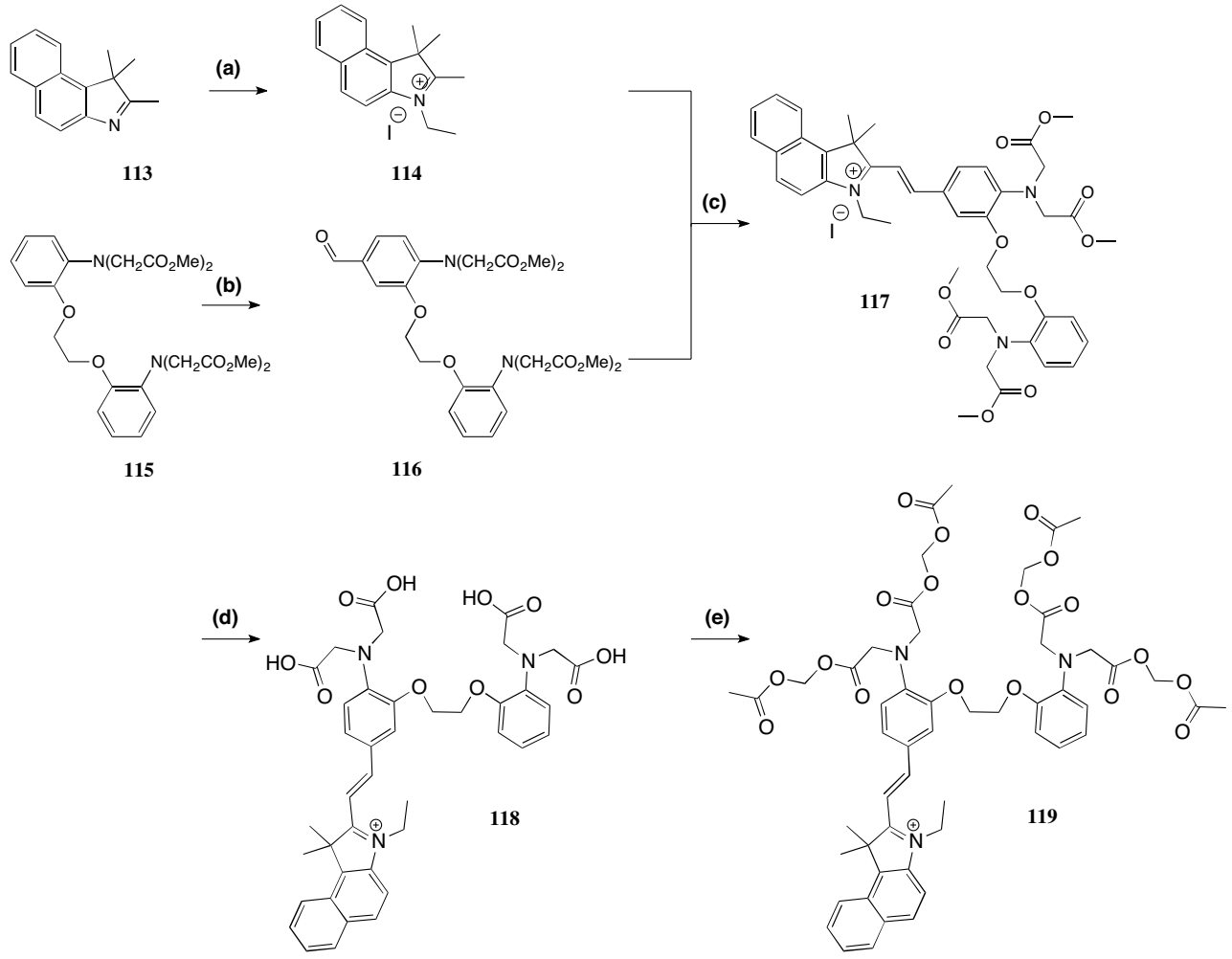

Scheme 3.1: **Synthesis and characterization of CaSPA-550 and CaSPA-550 AM.** *Reagents and conditions:* (i) EtI, anhydrous MeCN, reflux, 3 h, 89%; (ii) $POCl_3$, Et_3N, DMF, r.t., overnight, 40%; (iii) EtOH, Et_3N, reflux, 30 min, 90%; (iv) NaOH(aq), MeOH, r.t., 2 h; (v) $BrCH_2OCOCH_3$, DIPEA, MeCN, r.t., overnight, 10%.

In the absence of Ca^{2+}, photophysical characterisation of CaSPA-550, **118** reveals its maximum absorption band at 550 nm characterised by a high ε, ε_{550} = 77, 745 M^{-1} cm^{-1}. CaSPA-550 exhibits a reduction of its absorbance at maximum peak intensity of 550 nm as a function of increasing Ca^{2+} concentrations (0-39 μM). A second blueshifted peak at 455 nm appears as a function of increasing Ca^{2+} concentrations. The resulting maximum signal decrease of 550 nm was 50 %; the amplitude change at 455 nm was 65 % (Fig. 3.2). The peak fluorescence emission measured at 634 nm also decreased to half of the intensity as a function of increasing concentrations of Ca^{2+} (Fig. 3.2c). However, we observed no change in QY upon binding of

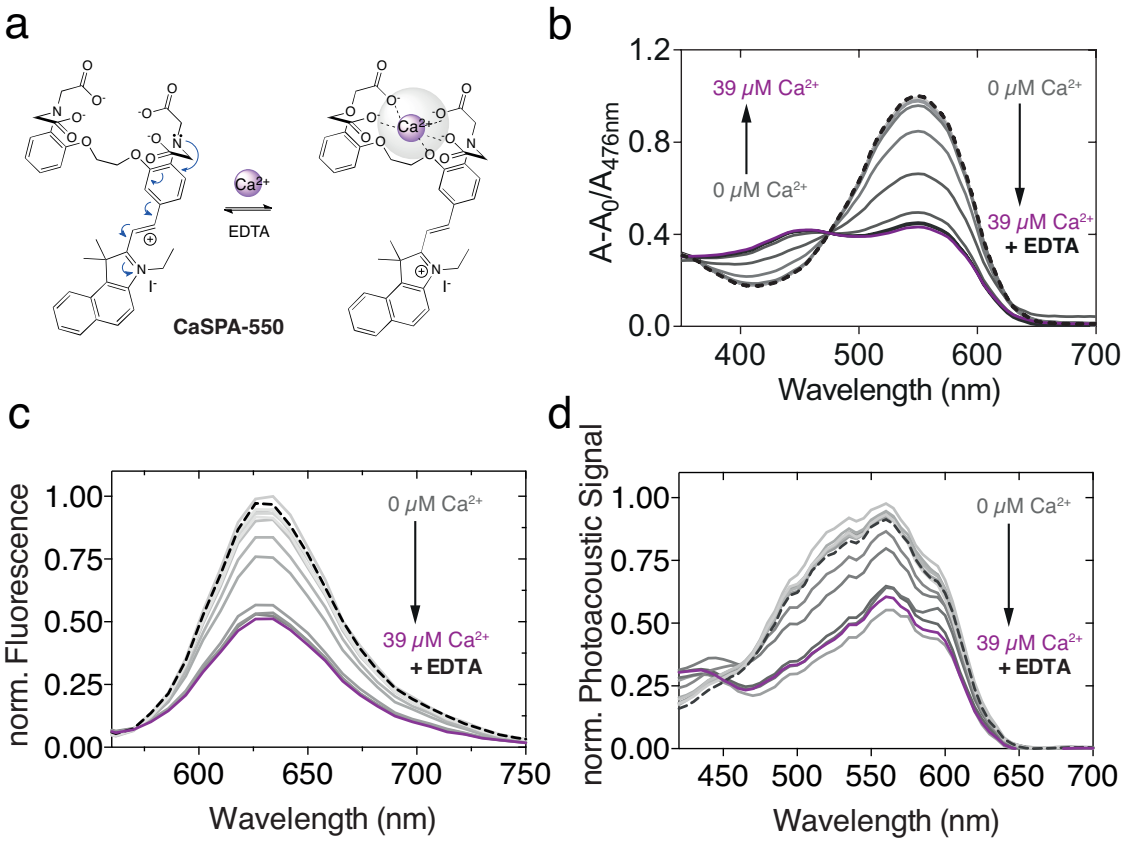

Figure 3.2: **Photophysical characterisation of CaSPA-550 in response to Ca^{2+} ions and its reversibility.** (a) Chemical structure of CaSPA-550 in its unbound (left) and Ca^{2+}-bound (right) state (b-d) Spectroscopic analysis of CaSPA-550 (25 μM) in MOPS (30 mM, 100 mM KCl, pH 7.20 at 25 ^{o}) with free $[Ca^{2+}]_f$ ions ranging from 0-39 μM. Spectra were obtained for absorbance (b), fluorescence, excitation at 540 nm (c) and its corresponding photoacoustic readout (d). The addition of tight chelator EDTA competes out Ca^{2+} from CaSPA-550 and reverts back to the original signal amplitudes (dash lines in b, c and d).

Ca^{2+}, which was low as desired for photoacoustics (QY_{noCa2+}= 0.01; QY_{+Ca2+}= 0.009; a relative measurement against rhodamine 101 yielded: QY_{noCa2+}= 0.007 $\pm$ 0.0003; Q_{+Ca2+} = 0.008 $\pm$ 0.0008). In addition, an isosbestic point at 470 nm was apparent as shown in Fig. 3.3 that could be used for ratiometric measurements correcting for differences in concentrations of the sensor. The binding curve was plotted between the ratio of the absorbance peak at 550 nm and normalised by the isosbestic point at 470 nm. The result shows the IC_{50} values of 4.3 μM (3.6 to 4.7 μM 95% CI) and 4.3 μM (4.2 to 4.5 μM 95% CI) measured from 10 μM and 25 μM of CaSPA-550 respectively. The absorbance of CaSPA-550 was not strongly affected when the pH was lowered to values that may be present in endosomes and synaptic vesicles but showed a substantial blueshift

and drop in absorbance when the pH was lowered to very acidic (pH 3.1) values.

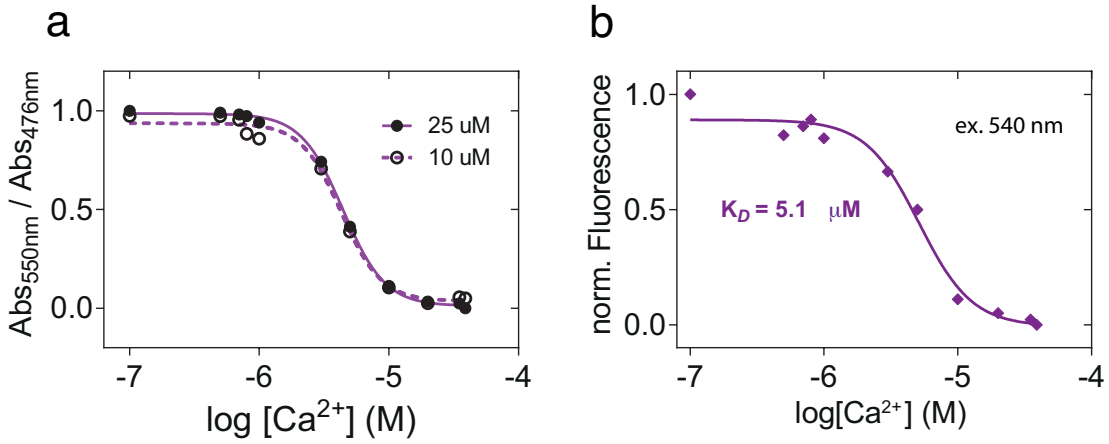

Figure 3.3: **Ratiometric measurements of Ca^{2+} binding** (a) Absorption spectra were taken as a function of varying concentrations of [Ca^{2+}] (0-39 μM) obtained for two differing concentrations of CaSPA-550 (10 and 25 μM). From this, binding curves are plotted from the ratio of its maximum absorbance peak at 550 nm normalised using the isosbestic point at 470 nm. The IC_{50} values obtained were 4.3 (95% CI: 3.6- 4.7 μM) and 4.3 (95% CI: 4.2- 4.5 μM) μM respectively. (b) Ca^{2+} binding curve obtained from its corresponding fluorescence emission. The IC_{50} value was 5.1 μM (95% CI: 3.9- 6.8 μM). Refer to Figure C.2 for detailed evaluation of results

Since we saw the dynamic changes of CaSPA-550 **117**, we subsequently measured the photoacoustic spectra of the identical samples on a custom-built photoacoustic spectrometer. The observed photoacoustic signal was at 550 nm and decreased by a factor of about two in response to 39 μM of Ca^{2+}. The peak intensity changes in absorbance spectra were found to be significantly correlated with the changes of the peak photoacoustic signal (R^2 = 0.99) as well as the peak fluorescence signal (R^2 = 0.99). From all three readouts, we determined the IC_{50} values for calcium to be ≈5 μM (Fig. 3.2a). The selectivity for Ca^{2+} over Mg^{2+}, Zn^{2+}, and Cu^{2+} was high. It is expected from BAPTA as previously reported[170] and none of these divalent metals induced any reduction in the absorbance (Fig. 3.4b). Furthermore, the compound also proved to be photobleaching resistant as shown in Appendix C, Fig. C.9.

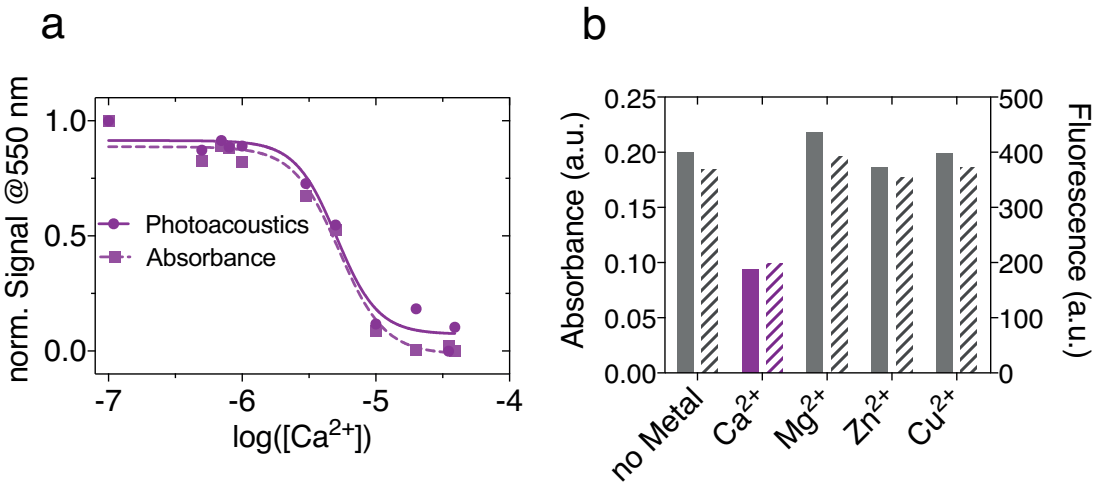

Figure 3.4: **Sensitivity and selectivity of CaSPA-550 for Ca^{2+}.** (a) The IC_{50} of CaSPA-550 were determine by photoacoustics (5.1 μ)M; 95 % CI: 3.9- 6.6 μM), absorbance (5.3 μ)M; 95 % CI: 4.1- 6.8 μM) and fluorescence (5.1 μ)M; 95 % CI: 3.9- 6.8 μM) (b) Selectivity of CaSPA-550 was tested by plotting the peak of the absorbance (filled bars) and fluorescence spectra (stripped bars) for several divalent metals added at 50 μM to MOPS (30 mM, 100 mM KCl, pH 7.20 at 25 ^{o}).

The observed photophysical properties of CaSPA-550 was desirable. In order to test the calcium sensor in *in vitro* biological system models, we sought a non-disruptive chemical technique for loading CaSPA-550 into cells. To do this, I generated the acetoxymethoxy (AM) variant CaSPA-550 AM **119**. We used a technique by temporarily masking the four carboxylic acids into ester groups.[193] Inside the cytoplasm of the cell, the ester variant should hydrolyse and at the same time trap the carboxylic variant. To do this, I have carried out the esterification of **118** by dissolving the free acid, 5 equivalents of DIPEA and 6 equivalents of acetoxymethyl bromide in anhydrous acetonitrile. The purification yielded deep pink crystals of CaSPA-550 AM **119**. Its high concentrate stock solution was prepared in dimethyl sulfoxide, aliquoted and stored at -20 ^{o}C.

The acetoxymethyl ester CaSPA-550 AM **119** was efficiently taken up by Chinese Hamster Ovary (CHO) cells as well as Human Embryonic Kidney Cells (HEK293) after incubation with low micromolar concentrations (see Fig. C.13 and Fig. C.15). Fig. 3.7 shows fluorescence signal trajectories obtained from CaSPA-550 AM loaded CHO cells in which calcium influx was triggered by a calcium-specific ionophore (Br-A23187) which lead to a ≈50% signal decrease as compared to vehicle control. Corresponding data from HEK cells are shown in Fig. C.13 in

Appendix C.

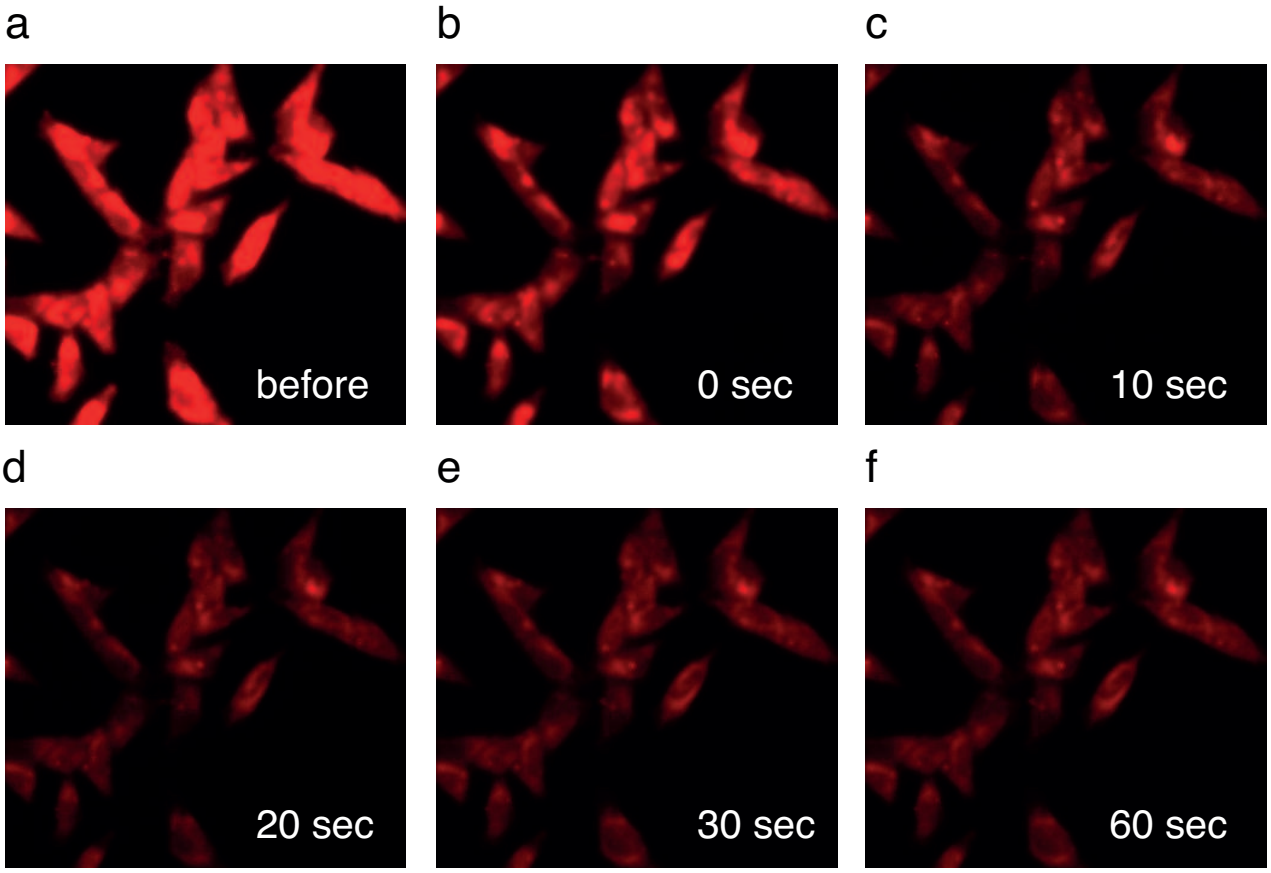

Figure 3.5: **Intracellular calcium transient imaging in Chinese hamster ovarian (CHO) cells loaded with CaSPA-550 AM by EVOS microscopy.** A basal level calcium image of CaSPA-550 AM (1 μM, pH 7.20, 30 min, 37 ^{o}C) labelled CHO cells was taken (a). An image of the same field of cells were stimulated with calcium ionophore (10 μM, Br-A23187) and imaged at various times after stimulation as shown in (b-f), interval of 10 seconds. As the intracellular calcium concentration increases, the intensity decreases by $\approx$ 50%. The results of a representative experiment are shown and were verified in at least three independent experiments. The corresponding quantitative fluorescence analysis can be found in Fig. C.16.

This substantial signal decrease in cells prompted us to conduct corresponding experiments on a custom-built optical resolution photoacoustic microscope (OR-PAM) that achieves $\approx$1 μm axial and $\approx$5 μm lateral at a maximum penetration depth of $\approx$300 μm.[193,234] Fig. 3.6 shows the CaSPA-550 AM loaded cells generated robust photoacoustic contrast (as compared with non-loaded cells) and the addition of the Ca^{2+} ionophore again lead to a $\approx$50% signal decrease.3.7,

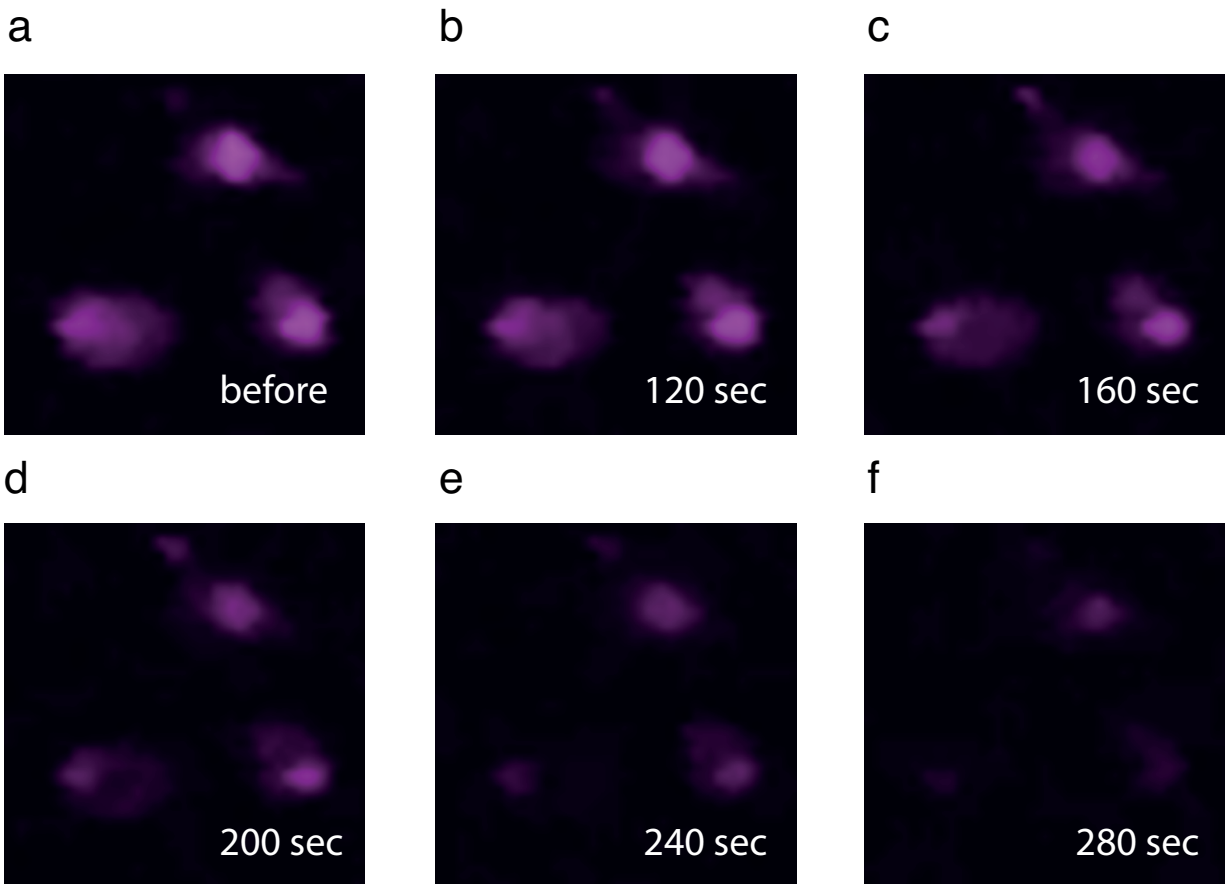

Figure 3.6: **Photoacoustic imaging of calcium fluxes in cells by CaSPA-550.** The optical resolution photoacoustic microscopy (OR-PAM) in HEK cells shows signal trajectories incubated with CaSPA-550 (2 μM, pH 7.20, 30 min, 37 ^{o}C) in response to Ca^{2+} influx triggered by addition of a Ca^{2+} ionophore (Br-A23187, 10 μM in HBSS with Ca^{2+} and Mg^{2+}) at timepoint between 120-160s. Vehicle control was 0.5% DMSO was added from at 0 timepoint. The average intensities were extracted by manual segmentation and plotted normalized to the intensity of each cellular ROI before addition of the ionophore or vehicle control. Photoacoustic signal time courses were recorded after addition of vehicle control (0.5% DMSO) followed by Ca^{2+} ionophore (Br-A23187, 10 μM). The images show FOVs (Scale bar 20 μm.

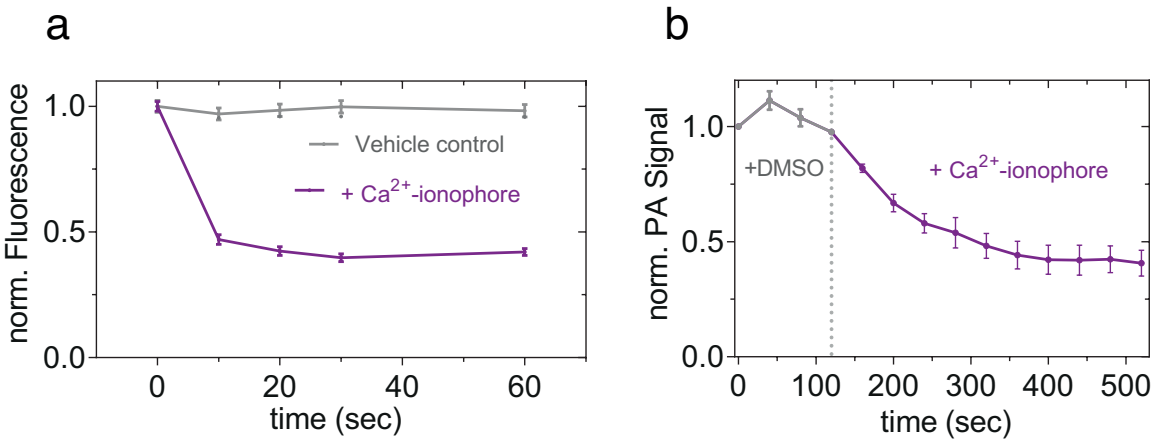

Figure 3.7: **Imaging of calcium transient in cells using CaSPA-550 by fluorescent and photoacoustic microscopy** (a) A basal level fluorescent calcium image of CaSPA-550 labelled CHO cells. Recording were taken after addition of (0.5% DMSO) control, followed by stimulation with Ca^{2+}- ionophore (Br-A23187, 10 μM). Images were taken at timepoints before stimulation, 30s and 60s after stimulation. (b) Analogous experiment conducted with optical resolution photoacoustic microscopy (OR-PAM) in HEK cells. Photoacoustic signal time courses were recorded after addition of vehicle control (0.5% DMSO) followed by Ca^{2+} ionophore (Br-A23187, 10 μM). Images of the same field of cells is shown at various time points before and after stimulation.

To further test CaSPA-550 AM for dynamic calcium transient photoacoustic imaging, we cultured heart organoids. Hear organoids are source of Ca^{2+} to spontaneously generate transients. We loaded them with CaSPA-550 AM. Via epifluorescence microscopy, we observe fluorescent signal decreases throughout a large stationary region of interest (ROI) that were clearly time-locked to small contractions on the outer ring of the organoid (gray shaded time intervals in Fig. C.19a) as expected for a Ca^{2+} response of the weakly fluorescent metallochromic sensor. When we loaded organoids with the commonly used green fluorescent calcium indicator Fluo-4 AM, we observed increases of the fluorescent signal associated with small contractions detected at the outer rim of the heart tissue (gray shaded bars in Fig. C.19b). Heart organoids loaded with CaSPA-550 AM were imaged in a custom-built hybrid 2-photon and optical resolution photoacoustic microscope (OR-PAM). Fig. 3.8 shows the optoacoustic signal (magenta) overlaid on a 2-photon imaging volume (gray) showing cellular fluorescent signals from CaSPA-550. It revealed the 3 dimensional structure of the organoid (Fig. 3.8). We sampled at the maximum imaging frame rate of 1 Hz, where we could observed photoacoustic signal decreasing in the ROI of up to 10% in a freqency range. This is the same frequency in which we also observed with the standard Fluo-4 AM in

fluorescence microscopy at a comparable sampling rate (Fig. 3.8b, C.19b).

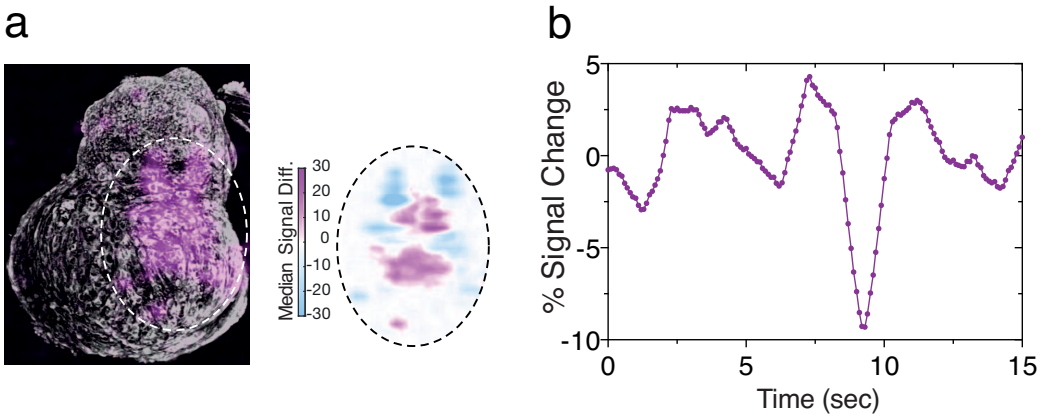

Figure 3.8: Co-registered overlay of maximum signal projection of a OR-PAM image time series (magenta) and a maximum signal projection of a two-photon excitation fluorescence volume (TPEF) (gray) of heart organoids loaded with CaSPA-550 AM with the corresponding median signal difference shown on the map (*right*). PA signal change of the region of interest (ROI) indicated (*dashed lines*)

We sought to work with the CaSPA-550 AM sensor *in vivo.* For this we used larval zebrafish and medaka fish for brain imaging. We delivered CaSPA-550 AM **119** using a standard intracranial injection procedure. We observed that the compound distributed from the intraventricular injection point one day post-injection. It was taken up well by cells as shown in Fig. 3.9 and Fig. 3.10.

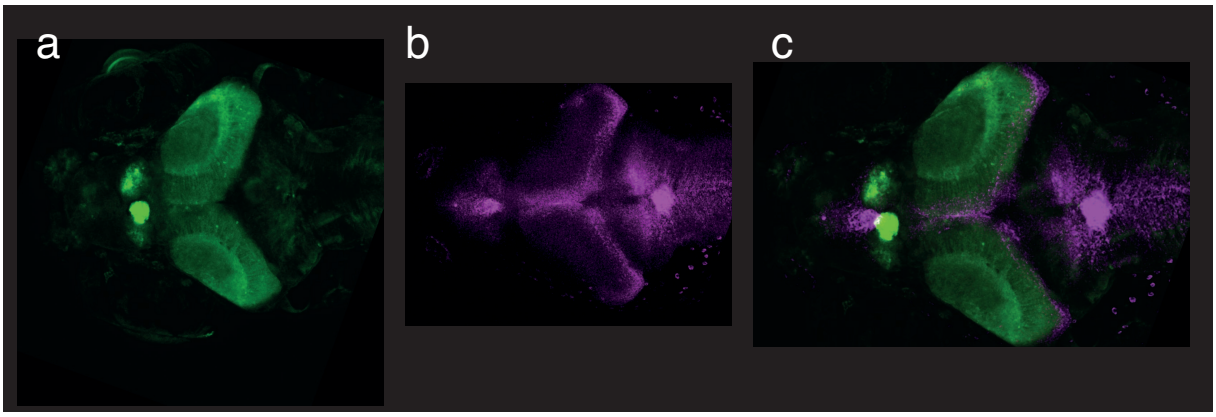

Figure 3.9: **In vivo zebrafish brain imaging of CaSPA-550 AM and its cellular distribution uptake** (a) Genetically encoded calcium indicator, GcAMP7a (b) Confocal fluorescence imaging after 4 h post- injection of CaSPA-550 AM excited at 560 nm, detection at 610- 680 nm. Intracranial injection in femtolitres of CaSPA-550 AM (10 μ)M in HBSS shows the distribution of the compound as well as cellular cytosolic uptake.

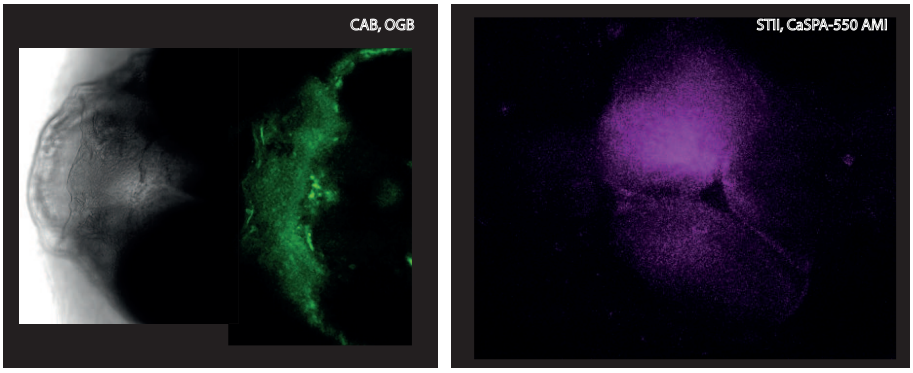

Figure 3.10: **In vivo medaka brain imaging of CaSPA-550 AM and its cellular distribution uptake** Image of medaka snout bathed in Oregon Green BAPTA AM (10 μ)M in HBSS) (*left*). Confocal fluorescence imaging after 20 h post- injection of CaSPA-550 AM excited at 560 nm, detection at 610- 680 nm. Intracranial injection in femtolitres of already prepared CaSPA-550 AM (10 μ)M in HBSS shows the distribution of the compound as well as cellular cytosolic uptake (*right*).

Excellent tissue distribution of CaSPA-550 AM sensor led us to imaging of CaSPA-550 AM for multispectral photoacoustic imaging. This was in collaboration with Dr Xosè Luis Deàn Ben from the Razansky's laboratory. We embedded a CaSPA-injected zebrafish larva next to a non-injected control fish in agar and positioned it in a multispectral photoacoustic imaging device. The system

is capable of fast acquistion of photoacoustic spectra in imaging volumes over time via the use of a tunable laser. At the same time the photoacoustic signal time courses were obtained, we also recorded fluorescence signal changes with a camera mounted on the opposite side from the photacoustic sensor array. As displayed in Fig. 3.11a, the brain of the CaSPA-injected fish showed a strong fluorescent signal when excited at 550 nm that was rather constant during 7 minutes of baseline observation. There was no fluorescent signal was detected from the brain of the control fish. When we then applied a low concentration of ethanol (1% in fish water), a neurostimulant with fast cellular diffusion, to both agar-embedded fish, we observed more spread in the fluorescent signals over a second 7 minute window with a transient signal dip (Fig. 3.11b). Subsequently we superfused the potent neurostimulant pentylenetetrazole (PTZ, 5 mM in fish water) that is commonly used to induce strong Ca^{2+} signaling in the brain and observed an overall fluorescent signal decrease in the brain region of the CaSPA injected fish.

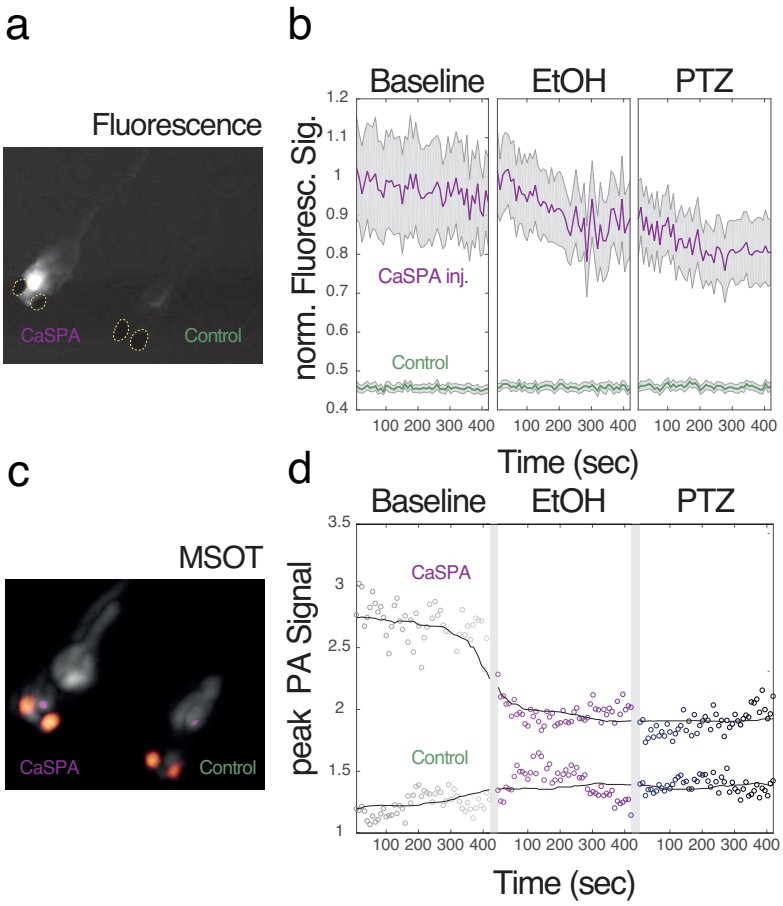

Figure 3.11: **Combined Multispectral photoacoustic tomography and fluorescence imaging of CaSPA-injected zebrafish larva.** (a) Single imaging frame of the epifluorescence time series showing fluorescence signal of the brain ROI of the CaSPA-injected zebrafish (550 nm excitation, absorbing eyes highlighted with dashed lines) as well as the non-injected control. (b) Fluorescence signal time course of an ROI placed over the peak absorbance (circle with magenta broken lines) during 7 minute baseline recording followed by two observational periods after stimulations with ethanol (EtOH) and the neurostimulant pentylenetetrazole (PTZ). The fluorescence signal time course (errobars represent standard deviation) of the corresponding brain region in the non-injected control fish is shown in green. (c) Simultanously acquired photacoustic imaging data with eyes shown in orange and the body of the animal shown in grayscale. In each of the 7-minute observational blocks, 50 photoacoustics spectra (from 430-630 nm) were acquired each 8.4 seconds. The magenta overlay represents the voxel time courses during the baseline recording that matched the CasPA-550 spectrum. The melanin containing eyes that give a broad PA spectrum are overlaid in orange. An anatomical reference is shown in gray (d) Photoacoustic signal time courses at the peak around 550 nm during baseline and after stimulation with EtOH and PTZ. The signal trajectory of the control fish is shown on the bottom.

Overall, the experiments mentioned above demonstrates that the metallochromic Ca^{2+} sensor for photocoustics (CaSPA-550) possesses optimized photophysical properties for photoacoustic

detection, namely a high extinction coefficient, a high photobleaching resistance, as well as a low QY. In addition, CaSPA-550-AM is cell-permeable that allows us to image Ca^{2+} transients with photoacoustics in cells, organotypic tissue culture and *in vivo* in zebrafish larvae. This is the first time to our knowledge that a dynamic and reversible calcium sensor, CaSPA-550 have been shown in genetically unmodified tissue for photoacoustic imaging.

We have chosen an efficient synthesis of CaSPA-550 and CaSPA-550-AM to obtain a semi-cyanine metallochromic compound based on PCT. It is cell-permeable. The signal of CaSPA-550 decreases in a Ca^{2+}-dependent manner (as opposed to a signal increase). It is irrelevant for the information that can be obtained from detecting dynamic Ca^{2+} fluxes and is beneficial in many experimental settings as it facilitates determining the distribution of CaSPA-550 in biological samples. The future synthesis of red-shifted variants in which to do incremental increase in the alkene chain lengths should give rise to a series of related metallochromic CaSPAs covering the 550-750 nm region of the spectrum while maintaining the affinity and selectivity for Ca^{2+} ions. The photophysical properties of these derivatives with increasing alkene chain lengths will very likely decrease photostability. The larger variants might also show less favorable biodistribution as compared with the highly cell-permeable CaSPA-550 AM. It could however potentially be overcome by several techniques including introduction of sulfonated residues. The new semi-cyanine metallochromic calcium sensor could be extended to generate different metallochromic sensors selective for other biologically relevant (such as Zn^{2+}, Cu^{2+}, or Mg^{2+}) or toxic metals.

Table 3.1: **Photophysical properties of CaSPA-550 in MOPS buffer** a) Quantum efficiencies determined in MOPS buffer according to the calcium calibration kit and b) MOPS buffer(pH 7.25, prepared from chelex-100 treated H_2O

Compound	ε **(M^{-1} cm^{-1})**	λ_{abs} **(nm)**	**QY**
CaSPA-550 + 0 $[Ca^{2+}]_f$	77, 745	550	0.01[a]
CaSPA-550 + 39 $[Ca^{2+}]_f$	27, 463	550	0.01[a]
CaSPA-550 AM	116, 000	590	[b]

3.3 Discussions and conclusions

The new CaSPA design aims at dynamic absorption changes in the presence of [Ca^{2+}] ions over other divalent metals. It has a higher extinction coefficient in combination with longer absorbance wavelengths than any other previous calcium indicators such as fluoresceins, rhodamines and fura series. Asante calcium green absorbing at 515 nm (Ca^{2+}-free) to 519 nm (Ca^{2+}-saturated) and asante calcium red absorbing at 537 nm (Ca^{2+}-free) to 542 nm (Ca^{2+}-saturated) are the latest commercially available dyes absorbing at the longest wavelength of the spectrum. Semi-cyanines **117**- **119** were prepared as model compounds in which long-wavelength absorption of an extended chromophore was deliberately sacrificed to make the synthesis as short as possible and allow quick test of the basic design principles of dynamic photoacoustic imaging.

In summary, CaSPA-550 possesses a high extinction coefficient, a high photobleaching resistance, as well as a low QY. These photophysical properties make CaSPA-550 a very attractive photoabsorber for PAI compared to other chromophores with similar spectral properties. In addition, CaSPA-550 AM is readily cell-permeable and offers a reversible and selective 50% photoacoustic signal change in response to Ca^{2+} which for the first time allows for specific photoacoustic imaging of calcium.

Using Strategy C gives us access to our calcium sensors which is short and efficient in synthesis of CaSPA-550 and CaSPA-550 AM. The semi-cyanine metallochromic compound with a considerably red-shifted absorbance peak as compared to the currently commercially available dyes such as fura-2 while maintaining the photoinduced charge transfer (PCT) mechanism. Incremental increase in the alkene chain lengths should give a series of related metallochromic CaSPAs covering the 550-750 nm region of the spectrum while maintaining the affinity and selectivity for Ca^{2+} ions.

In conclusion, CaSPA-550 AM constitutes the first member of a semi-cyanine class of cell-permeable, selective calcium sensors optimized for photoacoustic detection, enabling molecular imaging of calcium cell signaling in deep tissue with photoscattering-independent

resolution.

3.4 Future work: Extension of CaSPA π- conjugation

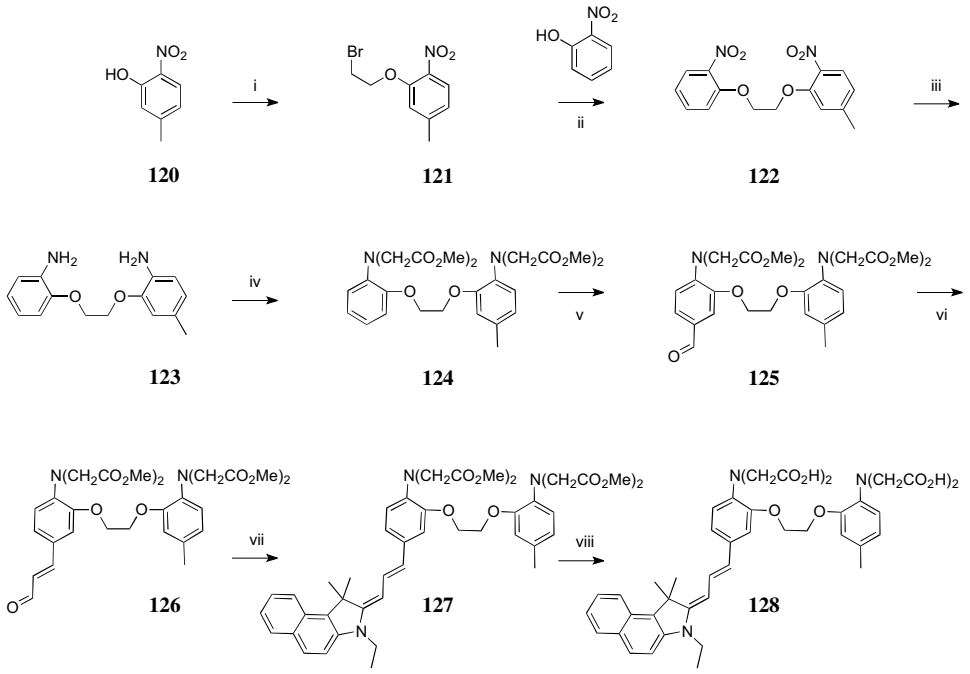

Scheme 3.2: (i) 1,2-dibromoethane, K_2CO_3, DMF, reflux, 2h (ii) 2-nitrophenol, K_2CO_3, DMF, 120 ^oC, 1 h. (iii) Fe, HCl iv) $BrCH_2CO_2Me$ v) $POCl_3$, DMF/pyridine (10:1), 60 ^oC (1 h) $\rightarrow$ r.t. (overnight) vi) Wittig reaction, $HCOCH{=}P(C_6H_5)_3$ vii) 3-ethyl-1,1,2-trimethyl-1H-benzo[e]indol-3-ium iodide salt, EtOH, Et_3N, reflux, 30 mins viii) deprotection; $NaOH(aq)$, MeOH

Several projects with regard to extending the polyene chain of the CaSPA-550 is on-going. One of the route that is being considered is shown in 3.2.

Summary

The understanding and investigation of synthetic designs and syntheses of ”smart” probes which can be fine tuned towards photoacoustic imaging have majorly contributed to delivering useful leading compounds, namely probe **89** and **111** series. Probe **89** allows us photoacoustic imaging in the near infrared but lacks the specificity towards Ca^{2+} ions. Probe **111** is specific towards Ca^{2+} but could benefit from extension of its π-conjugation towards near infrared. Through these strategies, we achieve chemical diversity of cyanines. In particular, this doctoral work has led us to successfully arrive at our **Ca**lcium **S**ensitive **P**hotoacoustic **A**gent with a maximum absorption at 550 nm (CaSPA-550). Its dynamic responses in the presence of differing concentration of Ca^{2+} in both UV/Vis spectrometer and photoacoustic techniques were extensively shown in Chapter 3. The work provides the first biological *in-vitro* and *in-vivo* characterisation attempts in zebrafish and medaka fish models, thus gaining insights into the biological applications of our dyes and its associated technical demands for a successful photoacoustic imaging. With the experiments, we significantly contribute to the research that provides the very first functional and dynamic molecule for optoacoustic imaging enabling analyte detection, specifically Ca^{2+} ions. Calcium imaging is significant in biological processes and in combination with photoacoustic technology. In the near future, it can have potential impact in *non-invasive* clinical settings. First, near infrared chromophores in combination with intracellular specificity towards Ca^{2+} can be use for neuroscience applications using photoacoustic technology.

This interdisciplinary project provides chemical platform for dynamic photoacoustic imaging. The continued success of design probes will one day enable real-time imaging of the brain. These probes have the potential application as preclinical agents for high temporal and spatial resolution imaging of neuronal activations. Furthermore, the introduction of new chemical constructs can be

use to extend brain imaging detection to other relevant biological processes in other organs like the heart, kidney, liver etc.

Appendices

Appendix A

Materials and Methods

A.1 General synthetic procedures

The commercially available chemicals were purchased from the following providers: Acros, Aldrich, Fluka, Merck, Strem and VWR or Life Tech. All reagents were obtained from commercial suppliers, and were used without further purification unless otherwise stated. Dry solvents for anhydrous reactions were purchased directly from Sigma-Aldrich or were dried over 3 $\AA$ molecular sieves activated *via* microwave heating (50W, 3 $\times$ 5 mins) or flame dried using a heat gun (several times), then cooled in a vacuum disiccator for 2-4 h. All glassware used for anhydrous reactions were flame-dried and/or heated overnight in an oven at 60 ^{o}C and cooled prior to use. Unless and otherwise mentioned, all the reactions were carried out under nitrogen atmosphere and the reaction flasks were pre-dried by heat gun under vacuum. All the chemicals, which were air or water sensitive, were stored under inert atmosphere. Pure water (18 MΩ cm^{-1}, 25 ^{o}C) was used throughout. All glassware was washed with a mixed acid solution and thoroughly rinsed with deionized, distilled water. Compound that are described in the experimental part were synthesised according the previously described literature. Organic extracts were dried using magnesium sulfate ($MgSO_4$) unless otherwise stated. room temperature (RT) refers to 20-25 ^{0}C. Degasification refers to bubbling a solution with inert nitrogen gas, stirred vigorously and bubbled for at least 15 min. All reactions requiring anhydrous conditions were otained using an oil bath equipped with a temperature sensor. *In vacuo* referes to the use of Büchi Rotavapor R-300 rotary evaporator using the vacuum pump V-710. All reactions were magnetically stirred and thin layer chromatography (TLC) was performed on aluminium TLC plates pre-coated with silica gel 60 containing an UV254 fluorescent indicator (Merck Millipore). Compounds were visualised with a 254 nm, handheld UV lamp (VL-206G, 155 $\times$ 70 mm, 2 $\times$ 6W). flash chromatography (FC) was performed using 230-400 mesh silica gel (Sigma-Aldrich) in the solvent system stated. Small scale FC was performed on corning Pasteur pipette (L 5 3/4 in. (146 mm), Macherey-Nagel) loaded with silica gel 60.

A.2 Reverse phase high-performance liquid chromatography

High performance liquid chromatography (HPLC) was performed at room temperature on Waters 2767 Autosampler, Waters 600 Multisolvent Delivery System with an analytical pump head (100 μL); Waters 600 Controller; Waters 2525 Binary Gradient Module with preparative pump heads (500 μL). At column-dilution, solvent-1, MeCN:H_2O 70:30 (v/v); flow rate 5 mL/min. Autosampler 2767 with 10 mL syringe and 10 mL Sample loop. Column 6-position valve Flom 401 with Waters X-bridge prep OBD 5 μm, 19 $\times$ 150 mm with X-Bridge RP18 guard cartridge 5 μm, 19 $\times$ 10 mm used at flow rate 20 mL/min. Eluent A, H_2O containing 0.1 % (v/v) HCO_2H; eluent B, MeCN. Different linear gradients, individually adapted to sample. Injection volume was 9 mL. Make-up solvent, MeOH- MeCN - H_2O- HCO_2H [80: 15: 4.95:0.05 (v/v/v/v)]. Make-up pump, Waters reagent manager, flow rate 0.5 mL/min. Waters ZQ single quadrupole mass spectrometer with electrospray source. Positive or negative ion mode scanning m/z 105- 950 or 300- 1200 in 1 s; capillary, 3.6 kV; cone voltage 45 V; multiplier voltage, 700 V; probe and desolvation gas temperature, 120 ^{o}C and 250 ^{o}C, respectively. Waters Fraction Collector 2767 with a mass or UV-triggered fraction collection. Waters 2487 Dual λ absorbance detector, set to 254 nm. Software, waters masslynx V 4.0 SP4.

Analytical reverse phase HPLC was carried out on a Perkin Elmer system at 22 ^{o}C using a 150 $\times$ 4.66 mm 4 μ Phenomenex Synergi Fusion-RP 80i column using method: 95% solvent A (H_2O, 0.1% HCOOH) and 5% solvent B (MeCN, 0.1% HCOOH) isocratic for 2 min, 5% B to 100% solvent B in 15 min and then running isochratic for 1.0 min and then back to 5% solvent B in the next 2 min.

A.3 Photophysical characterisations

All samples for spectrometric characterisation were contained in 96 well-plates with path lengths 0.231 cm and 0.30 cm for volume 75 μL and 100 μL, respectively. Measurements were recorded at 298 K and 310 K. UV/Vis absorbance spectra and Emission spectra were measured on SpectraMax

M5 Multi-Mode Microplate Readers (UV/Vis/NIR spectrometer). Samples were measured relative to a reference of pure solvent contained in a matched well and volume. An integration time of 0.5 seconds, increment of 8 nm, excitation and emission slit widths of 2.5 and 1.5 nm, respectively, were used throughout. Free [Ca^{2+}] was controlled by a commercial buffer kit (30 mM MOPS, 100 mM KCl, pH 7.2) to generate different ratios of K2EGTA/CaEGTA (Calcium Calibration Buffer Kit, Life Technologies). Binding curves were fitted to a variable slope model using Prism 6 (GraphPad Software, La Jolla, California, USA).

A.4 NMR-Spectroscopy

^{1}H NMR spectra were recorded on AV Bruker 250, 300, or 500 MHz at 25 ^{o}C. ^{1}H NMR data are reported as follows: chemical shifts are in parts per million (ppm, δ) relative and are referenced to residual protic peaks. The coupling constants, *J*, are quoted in Hz and its multiplicities by s (singlet) d (doublet), t (triplet), q (quartet) m (multiplet) and br (broadened). ^{13}C NMR AV Bruker are reported in parts per million (ppm) relative to the solvent.

A.5 Mass Spectroscopy

Electrospray mass spectra (ESI-MS) were recorded on SL 1100 system (Agilent, Germany) with ion-trap detection in positive and negative ion mode.

Preparative Reverse phase HPLC-MS was performed at 25 ^{o} on Waters 2767 Autosampler, Waters 600 Multisolvent Delivery System with analytical pump heads (100 μL); Waters 600 Controller; Waters 2525 Binary Gradient Module with preparative pump heads (500 μL). At column-dilution, solvent-1, MeCN:H_2O 70:30 (v/v); flow rate, 5 mL/min. Autosampler 2767 with 10 mL syringe and 10 mL sample loop. Column 6-position valve Flom 401 with Waters X-Bridge Prep OBD 5 μm, 19x150 mm with X-Bridge RP18 guard cartridge 5 μm, 19x10 mm used at flow rate 20 mL/min. Eluent A, H_2O containing 0.1% (v/v) HCO_2H; eluent B, MeCN. Different linear gradients, individually adapted to sample. Injection volume was 9 mL. Make-up solvent, MeOH - MeCN - H2O - HCO2H [80: 15: 4.95: 0.05 (v/v/v/v)]. Make-up pump, Waters Reagent Manager,

flow rate 0.5 mL/min. Waters ZQ single S-4 quadrupole mass spectrometer with electrospray source. Positive or negative ion mode scanning m/z 105 - 950 or 300 – 1200 in 1 s; capillary, 3,6 kV; cone voltage, 45 V; multiplier voltage, 700 V; probe and desolvation gas temperature, 120 ^{o}C and 250 ^{o}C, respectively. Waters Fraction Collector 2767 with mass or UV-triggered fraction collection. Waters 2487 Dual λ Absorbance Detector, set to 254 nm. Software, Waters MassLynx V 4.0 SP4.

A.6 Chemicals and solutions

Chelex-treated Ultrapure H_2O were used before preparing all the buffers. It is prepared as follows: Milli Q (500 cm^3) and Chelex 100 resin (6 g, sodium form, 50-100 mesh) were mixed and stirred for at least 18h. Resins were allowed to settle to the bottom for an hour before filtering to remove the Chelex from the water. All buffers for pH titrations were prepared by mixing 30 mM 3-(N-morpholino)propanesulfonic acid (MOPS) and 100 KCl (potassium chloride) in deionised H_2O. Fine adjustments were made to the pH by 0.1 M HCl($_{aq}$) or 0.1 M NaOH($_{aq}$). The pH values were determined using an InLab423 combination pH micro electrode (Mettler Toledo, 3 mm diameter shaft) calibrated at 4.0, 7.0 and 10.0 standard buffers at 25 ^{o}C. For photophysical characterisations of chelators as a function of $[Ca^{2+}]_f$, the Calcium Calibration Kit 3 # (Life Technologies, Darmstadt, Germany) (pH 7.2, ∂ = 22 ^{o}C, I = 0.1) was used to prepare 13 solutions of varying concentrations from 0 - 39 $[Ca^{2+}]_{free}$ (0, 0.1, 0.5, 0.7, 0.8, 1.0, 3.0, 5.0, 10.0, 20.0, 35.0, 39), including 5 mM $[Ca^{2+}]$. According to[168] , a $[Ca^{2+}]_{free}$ stock solution of 0.5 M K_2H_2EGTA and a $[Ca^{2+}]$-saturated stock solution (SS) of 1 M K_2H_2EGTAH were prepared by potentiometric back titration for *in-situ* calibration experiments. These SS were then diluted in a buffer solution (160 mM NaCl and 10 mM MOPS) to the final concentration of 10 mM EGTA and 10 mM CaEGTA calibration buffer solutions (pH 7.40, adjusted with HCl). By mixing the K_2H_2EGTA and K_2CaEGTA, various calcium concentrations $[Ca^{2+}]_{free}$ could be achieved according to Equation (A.1). The given EGTA dissociation constant $K_d{}^{EGTA}$ depends on temperature, ionic strength and pH and under recent conditions (pH 7.40, ∂ = 20 ^{o}C, I = 0.16). For investigating protein-dye interactions, porcine liver esterase (PLE) and either 0 and 39 μM $[Ca^{2+}]$-free or 5 mM Ca^{2+}-saturated buffer solutions were used. phosphate-bufferred saline (PBS)

contained 137 NaCl, 2.7 KCl, 10 Na_2HPO_4, 1.8 KH_2PO_4, pH 7.40.

$$[Ca^{2+}]_{free} = K_d^{EGTA} \times \frac{[\text{CaEGTA}]}{\text{EGTA}} \tag{A.1}$$

A.7 Determinations of Quantum Yield

The ϕ of CaSPA was determined according to the literature and based on the Equation A.2.

$$\theta = \frac{\theta_B I A_B \lambda^B \eta^1}{I A_1 \lambda^1 \eta^B} \tag{A.2}$$

Where θ is the ϕ; I is the integrated area under the corrected emission spectra; A is the absorbance at the excitation wavelenght λ; η is the refractive index of the solution; the subscripts 1 and B refer to the unknown and the standard, respectively. The emission photoluminescence spectra were recorded on a Horiba Jobin Yvon SPEX Fluorolog 3-22 spectrofluorometer in quartz cuvettes with a path length 10 mm. Quantum yield values of all samples were determined by comparative method relative to rhodamine 101 as a standard (ϕF= 1 in EtOH/ 0.01% HCl) following the literature method. Absolute QY measurements were obtained on a Quantaurus-QY (Hamamatsu).[209]**?**

A.8 Quantum chemistry

Electronic structure optimizations and frontier orbital analysis of the Ca^{2+} complexed and uncomplexed forms of the Calcium sensor were performed using density functional theory (DFT) and the B3LYP/6-31G** basis set as implemented in Schrödinger Jaguar (Schrödinger). HOMO and LUMO were plotted as isosurfaces with Schrödinger Maestro (Schrödinger).

A.9 Cell culture, seeding and loading

CHO and HEK293 cells were maintained in Advanced Dulbecco's Modified Eagle Medium (DMEM, Invitrogen) containing 10% FBS and according to vendor's instructions at 37 ^0C and 10% CO_2 and passaged weekly. For *time-dependent cellular uptake*, cells were plated on a Greiner black clear-bottom 96 well plate and allowed to grow for 2-3 days. CaSPA-550 AM stock solution

was prepared in DMSO at concentration of 2 mM, then diluted into medium to final working concentrations containing probeneacid (2.5 mM) and 1X Powerload concentrate (2.5 mM). Cells were exposed to CaSPA-550 AM for 0, 1, 2, 3, 8 and 24 h. At the end of incubation time, the loading medium was removed and the cells were washed with 250 μL PBS (2x). For *fluorescence imaging*, cells were seeded between 70-75% confluency onto 8-well ibidi chips (μ-Slide 8 well, Collagen IV, polymer coverslip, sterilised, IBIDI, Martinsried, Germany). Cells were incubated with CaSPA-550 AM **119**(2 μM) in a freshly prepared loading buffer composed of Probeneacid (2.5 mM) and Powerload concentrate 100X (2.5 mM) in growth media with a total volume (V_tot) of 150 μL for 30 mins at 37 ^{o}C. After incubation period, loading buffer was carefully aspirated, the cells were washed with PBS (2x) and loaded with the final imaging buffer, Hank's Balanced Salt Solution (HBSS contains $CaCl_2$ (12.61 mM), $MgCl_2 \cdot 6H_2O$ (4.93 mM) and $MgSO_4 \cdot 7H_2O$ (4.07 mM), without phenol red). These combination of concentration and incubation parameters were used in all fluorescent experiments unless otherwise stated.

A.10 Fluorescence microscopy

Fluorescence images during Ca^{2+} stimulation were acquired on an EVOS FL Auto Imaging System equipped with GFP (Ex: 470/22 Em: 525/50) and RFP (Ex: 531/40 Em: 593/40) light cube. Confocal Microscopy was conducted on a Leica SP5. CaSPA-550 was excited by a 561 nm laser; transmission images were obtained with a 488 nm laser. Region of interest (ROI) analysis was conducted by manually segmenting 50 cells per condition and plotting their signal trajectories over time (normalized to the average ROI signal before addition of vehicle control (DMSO) or 20 μM Ca^{2+}-ionophore Br-A23187 (Sigma). Heart organoids were imaged on an upright Leica MZ16 microscope with a Texas Red filter set (540-580 ex, 610LP) and a Neo 5.5 sCMOS camera (Andor) operating at an imaging frame rate of 5 Hz. Fluo-4 imaging in heart organoids was performed on an EVOS FL Auto Imaging using the GFP filter set and image series were recorded a 0.33 Hz. Confocal microscopy of CaSPA-injected zebrafish larva was conducted on a Leica SP5 (with at a voxel size of 0.7576 x 0.7576 x 9.9869 micron∧3) using 561 nm excitation.

A.11 Photoacoustic spectroscopy

Photoacoustic spectra were acquired on a custom-built photoacoustic spectrometer. Disposable cell culture chips with optically transparent bottoms (μ-Slide I 0.2 Luer, hydrophobic, uncoated, sterile, IBIDI, Martinsried, Germany) were filled with the samples (dyes in solution and positioned in a plastic holder with the flow channel containing the sample in the acoustic focus of the ultrasound detector (V382-SU, 3.5 MHz Immersion Transducer, Olympus, Hamburg, Germany). The device was placed on an optical table within a water basin to ensure acoustic coupling between the sample and the ultrasound detector. The output of a tunable visible laser (SpitLight DPSS 250, Innolas, Krailling, Germany) was guided via mirrors to illuminate the flow channel. Photoacoustic data were recorded by a high speed PCI digitizer (CS121G2, DynamicSignals LLC, Lockport, USA) connected to a standard computer. A laser photodiode was used to measure the laser power as a function of wavelength to normalize the photoacoustic signal amplitude for each wavelength applying custom routines implemented in MATLAB (Mathworks, Natick, USA).

A.12 Photoacoustic microscopy

Photoacoustic microscopy was carried out on a custom-built transmission mode optical resolution photoacoustic microscope (OR-PAM). The system equipped an active Q-switched 532 nm laser with a repetition rate of 50 kHz (SPOT-10-100-532 Elforlight Ltd., Daventry, UK) which was guided over a set of galvanometric mirrors (6215H, Cambridge Technology, Bedford, MA, USA), enlarged by a telescopic arrangement of plan-convex lenses, and focused by a microscopic objective lens (PLN 10X, Olympus, Hamburg, Germany; NA 0.25, WD 10.6 mm) into the sample. The sample is positioned by high-precision xyz-stages (MLS203-2 & MZS500, Thorlabs, New Jersey, USA) mounted on an inverted microscope (AxioObserver. D1, Zeiss, Jena, Germany). For acoustic signal detection, a spherically focused 100 MHz transducer (SONAXIS, Besancon, France) was co-axially adjusted by high-precision xyz-stages (M-683.2U4 & M-501.1DG, Physik Instrumente GmbH & Co. KG, Karlsruhe, Germany) to a positive defocus in transmission mode matching the scanned area, and acoustically coupled to the sample by a droplet of the sample buffer. For image generation, the optical excitation was raster scanned across the sample synchronized to

the laser repetition. The raw photoacoustic signals detected by the transducer were amplified by 63 dB (AU 1291, Miteq, New York, USA) and digitized by a high-speed 12 bit data acquisition card (ADQ412, SP Devices, Linköping, Sweden) whereas the control as well as the synchronization of the galvanometric mirrors and the laser was enabled by a 16 bit data acquisition card (PCIe 6363, National Instruments, Austin, USA). The signals were further bandpass filtered in the range of 10-180 MHz and their maximum amplitude was extracted for image generation. Control of the custom-built OR-PAM as well as the data acquisition was performed in Matlab (Matlab 2014a, Mathworks, Natick, USA) whereas final image processing was carried out using ImageJ (ImageJ 1.50e, Wayne Rasband). The photoacoustic images (100 x 100 pixels) were acquired at 50 kHz with 20 pixel-averaging leading to an imaging framerate of 1 Hz. The TPEF images were acquired with 800 x 800 pixels and a scanning speed at 320 kHz with an image-average of 20 in a stacked imaging manner with a z-step of 10 μm over a full depth of 260 μm. The overlay of OR-PAM and TPEF data was achieved by referencing to a suture-cross and translating the images accordingly (raw offset 8 μm in x, 6 μm in y, 25 μm in z). Final images are processed in a normalized 8-bit scale, gamma corrected with a value of 0.7, gaussian filtered with a 0.7 pixel-size, interpolated to 800 x 800 pixels and contrast/and brightness adjusted to improve visibility.

A.13 Generation and dye-loading of cardiac organoids

The differentiation of cardiac organoids was adapted from Lian et al.6 hiPSCs grown on Geltrex in mTeSR1 medium (StemCell Technologies) were dissociated for 15 min at 37 ^{o}C in Accutase (Sigma-Aldrich). 6x104 cells per cm were subsequently cultured in RPMI/B27 medium w/o insulin (Gibco), in the presence of CHIR99021 (12 μM) in low attachment plates for the formation of embryoid bodies. At day 3, the medium was changed to RPMI/B27 medium w/o insulin and w/ IWP2 (5 μM) and at day 5 to RPMI/B27 medium w/ insulin and vitamin A, until day 15 when the cardiac organoids generally start beating and can be used for recording. Medium was changed every two days. The Fluo-4 (Fluo-4 Direct Calcium Assay Kits; # F10471) dye was used at 1:2 in RPMI/B27 medium in 37 ^{o}C for 15 min as positive control to assess Calcium flux. CaSPA-550 AM was loaded at 2 μM with 2.5 mM Powerload.

A.14 Photoacoustic Mesoscopy

CaSPA-550 AM (500 μM with 2.5 mM Probenecid, 1x PowerLoad (molecular probes), 1 fL total volume) were injected into the diencephalic ventricles of 5 day-old Zebrafish larvae (casper). The fish were embedded in agar and positioned in the photoacoustic imaging system (10 MHz central frequency and 140^o (1.3 pi solid angle) angular coverage) with a semi-spherical transducer array positioned underneath and a scientific camera focused (bandpass emission filter with 630 nm central wavelength and 69 nm bandwidth) from above. The 512-element spherical ultrasound array (10 MHz central frequency and 140^o (1.3pi solid angle) delivers $\approx$75 microns spatial resolution and $\approx$200 mm^3 field of view. By using a tunable pulsed laser, we acquired photoacoustic volumes (from 430 nm to 630 nm in steps of 10 nm) at 2.5 Hz while epifluorescence images were taken at 5 Hz. Spectral unmixing was performed by vertex component analysis7. To extract signal time courses, ROIs (5x5x5 voxels) were placed over the brain region as indicated in the figure and the normalized photoacoustic signal peaks (520-560 nm) were extracted from the spectrum over time.

A.15 Supporting information

A.15.1 Syntheses of precursors

Syntheses towards diaminoethers **76**, methods as previously described in the literature.[235,236]

General synthesis of Compounds 72 To a solution of **35** (1.0 equiv.) and K_2CO_3 (6.0 equiv.) in anhydrous MeCN under N_2 was added *N*-Boc-2-bromoethyl-amine (3.0 equiv.). The reaction mixture was refluxed for 3 h. It was allowed to cool to room temperature, diluted with EtOAc and filtered. The organic layer was washed with $NaHCO_3$, dried with $MgSO_4$ and evaporated *in vacuo*. Gave product **72** in good yields.

Compound **72b**

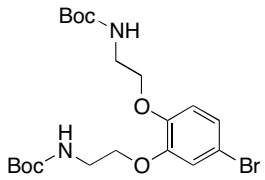

72b

Prepared in 71% yield starting from **71b** . ^{1}H NMR ($CDCl_3$, 250MHz): δ (ppm) 6.94- 7.20 (m, 2H, ArH), 6.78 (d, *J*= 9.2 Hz, 1H, ArH), 5.30 (br. s., 2H, -NH), 3.91- 4.22 (m, 4H, -$(OCH_2)_2$), 3.51 (d, *J*= 4.3 Hz, 4H, $(OCH_2)_2$), 1.34- 1.77 ppm (m, 18H, -Boc). ^{13}C NMR (63 MHz, $CDCl_3$) δ 155.87, 149.67, 148.03, 124.84, 118.67, 116.86, 113.96, 79.63, 69.47, 40.11, 28.33, 14.12. ESI-MS (ES^+) calculated for $C_{20}H_{31}BrN_2O_6$ [M^{+2}] *m/z* 476.14, found 476.78.

Compound **72c**

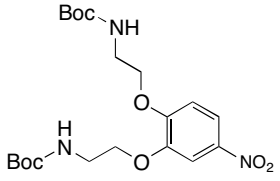

72c

Prepared in 40% yield starting from **71c** . ^{1}H NMR ($CDCl_3$, 250MHz): δ (ppm) 7.93 (dd, *J*= 8.9, 2.6 Hz, 1H), 7.79 (d, *J*= 2.7 Hz, 1H), 6.95 (d, *J*= 9.0 Hz, 1H), 5.05- 5.27 (m, 2H), 4.09- 4.24 (m, 4H), 3.51- 3.69 (m, 4H), 1.47 (d, *J*= 1.7 Hz, 18H)

General Syntheses of **73**

To a solution of **72** (1.0 equiv.) in dioxane stirred at 0 ^{o}C under nitrogen atmosphere was added 4N HCl/dioxane (equiv.). The reaction mixture was TLC monitored and stirred for 3 h until the reaction completed and formed amorphous white solid **73** in good yields.

Compound **73b**

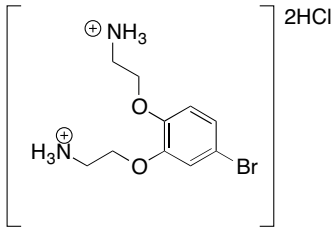

73b

Prepared in $\geq$95% yield starting from **72**b. Amorphous white solid. ^{1}H NMR (D_2O, 250MHz): δ (ppm) 7.25 (d, *J*= 2.2 Hz, 1H), 7.16 (s, 1H), 6.97 (d, *J*= 8.7 Hz, 1H), 4.23- 4.36 (m, 4H), 3.72 (s, 8H), 3.40- 3.51 (m, 4H). ^{13}C NMR (63 MHz, D_2O) δ 147.77, 146.40, 124.93, 117.09, 115.39, 113.60, 66.55, 65.28, 38.78. ESI-MS (ES^+) calculated for $C_{10}H_{17}BrN_2O_2^{2+}$ [M^+H^+] *m/z* 276.05, found 276.89.

Compound **73c**

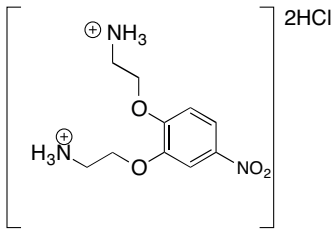

73c

Prepared in $\geq$ 95% yield starting from **35**c. ^{1}H NMR (D_2O, 250MHz): δ (ppm) 7.97 (d, *J*= 9.0 Hz, 1H), 7.87 (d, *J*= 2.7 Hz, 1H), 7.15 (d, *J*= 9.0 Hz, 1H), 4.34- 4.50 (m, 4H), 3.70 (s, 6H), 3.44- 3.53 (m, 4H).

*General syntheses of compounds **76** starting from compounds **73***

To a solution of **73** (1.0 equiv.) in anhydrous acetonitrile under nitrogen atmosphere was added DIPEA (6.0 equiv.), followed by the addition of methyl bromoacetate (8.0 equiv.). The reaction was refluxed for 3 h, allowed to cool to room temperature and dried *in vacuo*. It was extracted with DCM and washed with $NaHCO_3$ and water. Organic layer was dried with $MgSO_4$ and evaporated *in vacuo*. Purification (silica gel, MeOH: DCM 5:95).

Compound **76b**

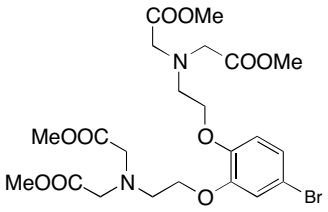

76b

Prepared in 88% yield starting from **73b** . Pale yellow oil **76b** . ^{1}H NMR ($CDCl_3$, 250MHz): δ (ppm) 6.93- 7.03 (m, 2H), 6.73 (d, *J*= 8.2 Hz, 1H), 4.09 (td, *J*= 5.6, 1.8 Hz, 4H), 3.66- 3.73 (m, 20H), 3.19 (td, *J*= 5.6, 2.7 Hz, 4H). ^{13}C NMR (63 MHz, $CDCl_3$) δ 171.75, 149.27, 147.76, 123.73, 116.56, 114.49, 112.99, 68.50, 55.80, 53.40, 51.54, 28.37. ESI-MS (ES^+) calculated for $C_{21}H_{29}BrN_2O_{10}$ [M+2] *m/z* 562.12, found 564.78.

Compound **76c**

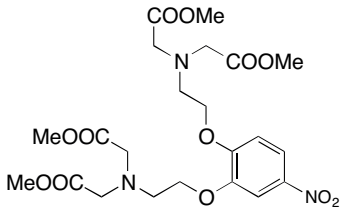

76c

Prepared in 93% yield starting from **73c** . ^{1}H NMR ($CDCl_3$, 250MHz): δ (ppm) 7.87 (dd, *J*= 8.9, 2.6 Hz, 1H), 7.72 (d, *J*= 2.7 Hz, 1H), 6.89 (d, *J*= 9.0 Hz, 1H), 4.13- 4.25 (m, 4H), 3.64- 3.75 (m, 20H), 3.23 (t, *J*= 5.6 Hz, 4H).

*General syntheses of cyanoethers **74***

To a solution of appropriate dihydroxy derivative **35** (1.0 equiv.) in anhydrous MeCN were added K_2CO_3 (4.0 equiv.) and chloroacetonitrile (5.0 equiv.). The resulting mixture was stirred for 72h at RT. After filtration through Celite, the filtrate was evaporated and the residue was purified by column chromatography (silica gel, n-hexane: EtOAc 70:30).

Compound **74b**

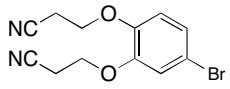

74b

Prepared in 71% yield starting from 4-bromobenzene-1,2-diol **71b** . Yellow solid. lit. m.p. 103.2-106.2 ^{o}C. ^{1}H NMR (MeOD, 300MHz): δ (ppm) 7.36 (d, *J*= 2.2 Hz, 1H), 7.24- 7.29 (m, 1H), 7.11 (d, *J*= 8.8 Hz, 1H), 5.03 (s, 2H), 4.98- 5.01 (m, 2H), 3.21 (p, *J* = 1.6 Hz, 4H). ^{13}C NMR (75 MHz, MeOD) δ 149.36, 147.98, 127.76, 120.65, 119.01, 116.73, 116.69, 116.57, 56.18. ESI-MS (ES^+) calculated for $C_{10}H_7BrN_2O_2$ [M^+H^+] *m/z* 265.97, found 279.20

Compound **74c**

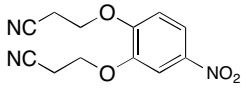

74c

Prepared in 75 % yield starting from 4-nitrobenzene-1,2-diol **71c** . Yellow solid. ^{1}H NMR (MeOH-d_4,300MHz): δ (ppm) 8.09- 8.12 (m, 1H), 7.36- 7.39 (m, 1H), 7.33- 7.36 (m, 1H), 5.18 (s, 4H). ^{13}C NMR (75 MHz, MeOD) δ 153.59, 147.95, 144.31, 120.80, 116.83, 116.35, 116.16, 115.14, 112.04, 56.15, 55.64, 25.70. ESI-MS (ES^+) calculated for $C_{10}H_7N_3O_4$ [M^+H^+] *m/z*

233.04, found 234.20

Compound **74e**

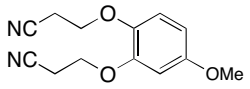

74e

Prepared in 76% yield, starting from 4-methoxybenzene-1,2-diol **71e** . ^{1}H NMR ($CDCl_3$, 300MHz): δ (ppm) 7.06 (d, *J*= 8.8 Hz, 1H), 6.62- 6.66 (m, 1H), 6.57- 6.62 (m, 1H), 4.79 (s, 2H), 4.72 (s, 2H), 3.78 (s, 3H). ^{13}C NMR (75 MHz, $CDCl_3$) δ 171.28, 157.04, 148.41, 140.86, 119.80, 115.44, 107.90, 104.00, 60.50, 55.93, 24.81, 21.15, 14.30, 1.12.

*General syntheses of cyanoethers **75***

To a solution of nitrile **74** (1.0 equiv.) in anhydrous THF was added BMS (4.0 equiv.). The resulting mixture was stirred under reflux under N_2 atmosphere for 4h. After cooling, to reaction was added cautiously solution (20 cm^3 water and 20 cm^3 THF) and mixture was evaporated. To residue was added solution HCl conc.:H_2O, 1:1 (50 cm^3) and stirred under reflux for 20 mins. After cooling ,mixture was alkalized by 20% NaOH and extracted with $CHCl_3$. The organic layers were combined, washed with brine, dried over $MgSO_4$, and evaporated to give **75**.

Compound **75b**

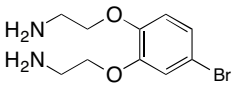

75b

Prepared in $\geq$ 95% yield, starting from **74b** . ^{1}H NMR ($CDCl_3$, 300MHz): δ (ppm) 6.96- 7.09 (m, 2H), 6.77 (d, *J*= 8.4 Hz, 1H), 4.33 (br. s., 4H), 3.97- 4.17 (m, 4H), 2.97- 3.25 (m, 4H). ^{13}C NMR (75 MHz, $CDCl_3$) δ 149.63, 148.05, 124.74, 117.93, 116.23, 113.91, 70.33, 51.04, 41.01, 30.72.

Compound **75e**

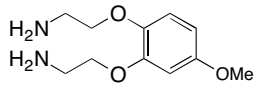

75e

Prepared in % yield starting from **74e** . White amorphous solid. ^{1}H NMR ($CDCl_3$, 300MHz): δ (ppm) 6.79 (dd, *J*= 8.8, 3.3 Hz, 1H), 6.48 (d, *J*= 2.9 Hz, 1H), 6.37 (dd, *J*= 8.7, 2.8 Hz, 1H), 4.01-4.13 (m, 4H), 3.73- 3.75 (m, 3H), 3.64- 3.72 (m, 4H), 3.17 (dt, *J*= 9.4, 5.7 Hz, 4H). ^{13}C NMR (75 MHz, $CDCl_3$) δ 172.08, 154.86, 149.83, 143.01, 115.01, 104.13, 101.50, 55.99, 53.65, 51.77.

*General procedure syntheses of cyanoethers **76**, starting from **75***

To a solution of **75** (1.0 equiv.) in MeCN were added DIPEA and briefly followed by methyl bromoacetate (5.0 equiv.). The reaction mixture (RM) were bubbled through N_2 for 10-15 mins and it was stirred and refluxed overnight for 15 h. The RM were filtered through celite. The residue was purified by column chromatography [n-hexane: EtOAc].

Compound **76a**

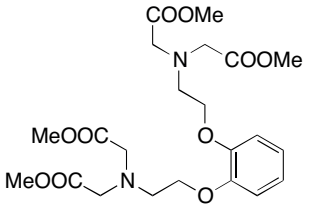

76a

Prepared in % yield, starting from **75a** . Pale yellow. ^{1}H NMR (300 MHz, $CDCl_3$) δ 6.80 (m, 4H), 4.04 (m, 4H), 3.80 – 3.39 (m, 18H), 3.13 (m, 4H). ^{13}C NMR (75 MHz, $CDCl_3$) δ 171.84, 148.49, 121.25, 113.40, 68.05, 55.79, 53.52, 51.56.

Compound **76b**

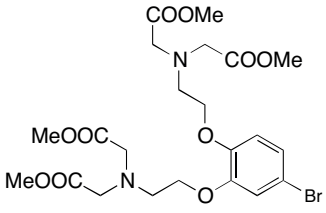

76b

Prepared in 73% yield, starting from **75b** . Pale yellow oil **76b** . ^{1}H NMR (300 MHz, $CDCl_3$) δ 6.95 – 6.87 (m, 2H), 6.65 (d, J = 8.3 Hz, 1H), 4.01 (td, J = 5.7, 2.3 Hz, 4H), 3.62 (dd, J = 4.7, 2.0 Hz, 20H), 3.11 (td, J = 5.6, 3.1 Hz, 4H). ^{13}C NMR (75 MHz, $CDCl_3$) δ 171.94, 162.68, 149.39, 147.89, 123.86, 116.60, 114.53, 113.10, 68.65, 60.77, 55.98, 53.55, 51.74, 36.65, 31.58, 25.71, 20.64.ESI-MS (ES^+) calculated for $C_{22}H_{31}BrN_2O_{10}$ $[M^+H^+]$*m/z* 562.12 found 565.20

Compound **76e**

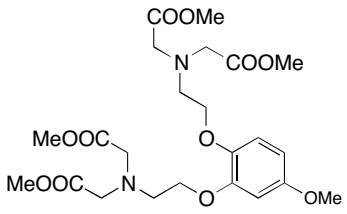

76e

Prepared in 80% yield, starting from **75e** . ^{1}H NMR ($CDCl_3$, 300MHz): δ (ppm) 6.91- 7.04 (m, 2H), 6.75 (dd, J= 19.3, 8.4 Hz, 1H), 4.02- 4.12 (m, 4H), 3.51- 3.86 (m, 23H), 3.14- 3.25 ppm (m, 4H). ^{13}C NMR (75 MHz, $CDCl_3$) δ 172.07, 148.16, 126.64, 123.98, 116.74, 68.27, 55.98, 53.55, 51.82, 29.89, 1.22, 0.22. ESI-MS (ES^+) calculated for $C_{23}H_{34}N_2O_{11}$ $[M^+H^+]$*m/z* 514.22 found 514.40.

Compound **85**

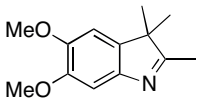

85

Synthesis based on previously described literature by Dougherty *et al.* [214]

3,4-dimethoxyaniline **82** (500 mg, 3.26 mmol, 1.0 equiv.) was dissolved in a mixture of HCl/H_2O (1:1), stirred under N_2 and cooled to -10 ^{o}C. A cooled solution of H_2O(aq) (4 cm^3) was added slowly added *via* syringe, ensuring that the reaction maintains a temperature below 0 ^{o}C. The reaction was stirred for 30 min, then added a solution of $SnCl_2$ (2.2 g, 9.78 mmol, 3.0 equiv.) in concentrated HCl. The addition of 3-methyl-2-butanone (842 mg, 9.78 mmol, 3.0 equiv.) followed.

The mixture was stirred for further 30 min, then quenched into a vigorously stirred solution of $NaHCO_3$(aq·) and EtOAc (4:6). After the extraction with EtOAc, the combined organics are dried with $MgSO_4$, filtered and concentrated *in vacuo*. The residue was taken up in AcOH (5 cm^3) and an additional 3-methyl-2-butanone was added. The reaction is stirred overnight at room temperature and concentrated *in vacuo*. Direct flashed chromatography of the crude (silica gel, n-hexane: EtOAc (6:4)) gave a brown oil product **85** (250 mg, 35%). ^{1}H NMR (250 MHz, $CDCl_3$) δ 7.06 (s, 1H), 6.73 (s, 1H), 3.79 (d, J = 0.9 Hz, 6H), 2.13 (d, J = 0.6 Hz, 3H), 1.21 – 1.11 (m, 6H). ^{13}C NMR (63 MHz, $CDCl_3$) δ 186.58, 173.48, 170.64, 148.66, 147.16, 146.43, 137.10, 105.03, 103.84, 60.00, 56.21, 55.89, 53.65, 22.96, 21.14, 20.66, 14.90, 13.91. R_f = 0.3

Compound **86**

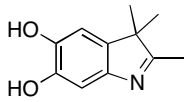

86

Synthesis based on previously described literature by Dougherty *et al.*[214]
Dimethoxyindolenine (230 mg, 1.14 mmol) was dissolved in dry DCM under N_2 and cooled to 0 ^{o}C. BBr_3 (2.50 cm^3, 2.28 mmol) was added dropwise over 15 min and the mixture was allowed to warm to room temperature. After stirring for 3 h., the reaction was diluted with H_2O and the pH was adjusted to pH 5.0 using sodium acetate. The mixture was extracted with DCM, and the combined organics were dried over Na_2SO_4, filtered and evaporated *in vacuo*. Flash chromatography of the crude (silica gel, MeOH: DCM (5:95) to obtain the desired product (43 mg, 20%). ^{1}H NMR (250 MHz, $CDCl_3$) δ 8.50 (s, 2H), 7.15 (s, 1H), 6.74 (s, 1H), 2.62 – 2.07 (m, 3H), 1.16 (s, 6H).

Compound **71b**

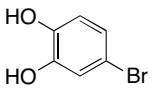

71b

4-bromo-1,2-dimethoxybenzene **87** (10 g, 46 mmol) in anhydrous DCM was cooled to 0 ^{o}C. BBr_3 in 1M DCM (25.4 g, 101.35 mmol) was added dropwise to the solution. Stirred under cooled condition for 15 min. It was further stirred at r.t. for 20 h. The reaction was slowly diluted with H_2O (5 cm ^{3}). The mixture was adjusted to pH 10 (3M KOH, 70 cm^3), stirred at r.t. for 20 min. The pH was adjusted back to to 1.0 with conc. HCl (13 cm^3) or until it turns yellow. Organic was extracted with DCM several times (3x 30 cm^3), combined organic layer dried with $MgSO_4$ and evaporated *in vacuo* yielding analytically pure 4-bromobenzene-1,2-diol **71b** (8.3 g, 95%).

Compound **88**

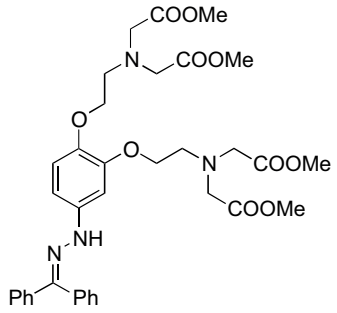

88

Benzophenone hydrazone (19.23 mg, 0.098 mmol, 1.1 equiv.), $Pd(OAc)_2$ (0.24 mg, 1.33×10^{-3} mmol, 1.5%) and (*S*)-BINAP (1.27 mg, 2.04×10^{-3} mmol, 2.3% mole) were dissolved in toluene (2 cm^3). The RM was purged with N_2 for at least 10 mins, heated briefly (3 mins) to 100 ^{o}C, then cooled to 25 ^{o}C. The resulting purple/dark orange solution was added compound **76b** (50 mg, 0.089 mmol, 1.0 equiv.), NaO−tBu (13.20 mg, 0.137 mmol, 1.40 equiv.) and toluene (500 μ)L. The RM was recapped with septum, purged briefly with N_2 and heated to 100 ^{o}C until the aryl bromide **76b** was consumed. It would be useful to monitor the reaction here. The RM was cooled to 25 ^{o}C, filtered through a short pad of silica gel and Celite and the silica cake was rinsed with ether (30 cm^3. The filtrated was concentrated and purified by flash column chromatography (MeOH: DCM [1:99]) to afford viscous yellow compound **88**. ^{1}H NMR (250 MHz, $CDCl_3$) δ 7.40 – 7.31 (m, 5H), 7.14- 7.20 (m, 5H), 6.84- 6.90 (m, 2H), 6.71 – 6.51 (m, 1H), 5.15 (s, 1H), 3.93-3.99 (m, 4H), 3.72 – 3.43 (m, 20H), 3.04- 3.10 (m, 4H). ^{13}C NMR (63 MHz, $CDCl_3$) δ 186.58, 173.48, 170.64, 148.66, 147.16, 146.43, 137.10, 105.03, 103.84, 60.00, 56.21, 55.89, 53.65, 22.96, 21.14,

20.66, 14.90, 13.91. ESI-MS (ES^+) calculated for $C_{35}H_{42}N_4O_{10}$ $[M^+H^+]$*m/z* 678.29 found 679.80

2,3,3-trimethyl-5-(4,4,5,5-tetramethyl-1,3,2-dioxaborolan-2-yl)-3H-indole **91**

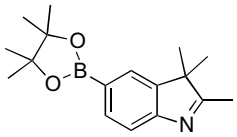

91

Synthesis based on previously described literature by Oriou *et al.* [237]

90 (1 g, 4.20 mmol), bis(pinacolato)-diboron (1.6 g, 6.30 mmol), anhydrous potassium acetate (1.24 g, 12.60 mmol) and [1,1'-bis(diphenylphosphino)ferrocene]dichloropalladium(II) (154 mg, 0.21 mmol) were dissolved in a mixture of dioxane (200 cm^3) and DMSO (5% v/v), stirred vigorously and degassed with nitrogen. It was connected to the rotary evaporator, reaction proceeded at bath temperature 85 ^oC and at 850 mbar, allowing rotation for 2 h. Reaction was evaporated *in vacuo*. The dark brown residue was diluted in EtOAc (50 cm^3), filtered over a thin silica layer and extracted. The organic layer was removed *in vacuo*. Flash chromatography (silica gel, *n*-hexane: EtOAc 25:75) obtained pink solid **91**. Prepared in 90% yield. Lit. m.p 121 ^oC. ^1H NMR ($CDCl_3$, 300MHz): δ (ppm) 7.40- 7.43 (m, 2H), 7.40 (d, J= 1.1 Hz, 1H), 2.26 (s, 3H), 1.21- 1.32 (m, 18H). ^{13}C NMR (75 MHz, $CDCl_3$) δ 188.51, 152.27, 147.61, 130.55, 124.73, 121.15, 119.22, 118.82, 82.45, 74.93, 53.99, 24.51, 22.80, 15.18. ESI-MS (ES^+) calculated for $C_{17}H_{24}BNO_2$ $[M+H^+]$ *m/z* 285.19, found 286.10.

2-methyl-4-(2,3,3-trimethyl-3H-indol-5-yl)but-3-yn-2-ol **92**

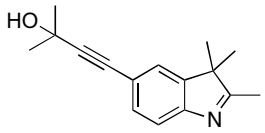

92

Synthesis based on previously described literature by Takase and Inouye [238].

To a solution of **90** (200 mg, 0.84 mmol), $(Ph_3P)_2PdCl_2$ (12 mg, 0.84 mmol) and CuI (1.6 mg, 8.4 μmol) in Et_2NH (10 cm^3) was added 2-methyl-3-butyn-2-ol (141 mg, 1.68 mmol) at room temperature. The reaction mixture was stirred at 50 ^oC for 9 h. The solvent was removed *in vacuo*,

the dark brown residue was poured into water and extracted with DCM. The solvent was dried *in vacuo*. Purification (silica gel, *n*-hexane: EtOAc 70:30) gave dark yellow solid **92**. Prepared in 90% yield. ^{1}H NMR ($CDCl_3$, 400MHz): δ (ppm) 7.43- 7.49 (m, 1H), 7.28- 7.35 (m, 2H), 2.23- 2.30 (m, 3H), 1.59- 1.65 (m, 6H), 1.25- 1.29 (m, 6H). ^{13}C NMR (101 MHz, $CDCl_3$) δ 189.28, 131.45, 130.58, 124.69, 121.22, 119.69, 119.40, 93.84, 82.32, 65.40, 31.55, 22.87, 19.22, 15.40, 13.84. ESI-MS (ES^+) calculated for $C_{16}H_{19}NO$ [M^+H^+] *m/z* 241.15, found 241.30.

5-ethynyl-2,3,3-trimethyl-3H-indole **93**

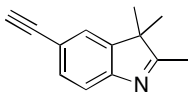

93

Synthesis based on previously described literature by Smeyanov and Schmidt[217]

92 (1 g, 4.1 mmol), K_3PO_4 (870 mg, 4.1 mmol) and KOH (230 mg, 4.1 mmol) were suspended in anhydrous toluene (10 cm^3). The suspension was stirred vigorously, refluxed for 1 h and monitored by TLC until completion. The mixture was allowed to cool to room temperature, filtered through a plug of Celite and washed with toluene (3x 10 cm^3). The solvent was dried *in vacuo* to obtain dark yellow solid **93**. Prepared in $\geq$ 95% yield. ^{1}H NMR ($CDCl_3$, 300MHz): δ (ppm) 7.46 (t, *J*= 1.0 Hz, 2H), 7.39- 7.42 (m, 1H), 3.08 (s, 1H), 2.28 (s, 3H), 1.27- 1.31 (m, 6H). ^{13}C NMR (75 MHz, $CDCl_3$) δ 189.57, 154.11, 145.71, 132.08, 125.15, 119.77, 118.53, 84.07, 76.80, 53.68, 22.90, 20.72, 15.49, 14.05. ESI-MS (ES^+) calculated for $C_{13}H_{13}N$ [M+H^+] *m/z* 183.10, found 183.2.

TMS-Alkyne **94**

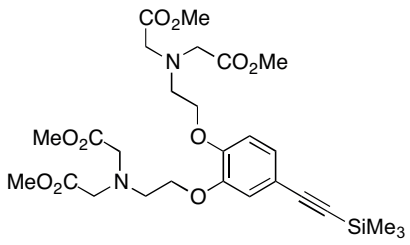

94

To a degassed suspension of $Pd(dppf)Cl_2$ (147 mg, 0.18 mmol), CuI (34 mg, 0.18 mmol) and NEt_3 (2.51 cm^3, 18 mmol) in anhydrous THF, was added **76b** (1 g, 1.8 mmol) and stirred at room temperature for 20 min under nitrogen atmosphere. Trimethylsilylacetylene (212 mg, 2.16 mmol) was added to the mixture and heated to 60 ^oC for addition 16 h. The mixture was extracted with DCM (3x 40 cm^3). The combined organic layers were dried with $MgSO_4$ and evaporated *in vacuo*. Flash chromatography (silica gel, MeOH: DCM 2:98) obtained dark brown **94**. Prepared compound **94** (1 g, 97% yield). ^1H NMR (500 MHz, $CDCl_3$) δ 7.04 – 6.84 (m, 2H), 6.67 (dd, J = 15.6, 8.4 Hz, 1H), 4.02 (dt, J = 9.6, 5.5 Hz, 4H), 3.71 – 3.54 (m, 20H), 3.12 (q, J = 5.5 Hz, 4H), 0.17 (s, 3H). ESI-MS (ES^+) calculated for $C_{27}H_{40}N_2O_{10}Si$ $[M^+H^+]$ *m/z* 580.25, found.

Compound **95**

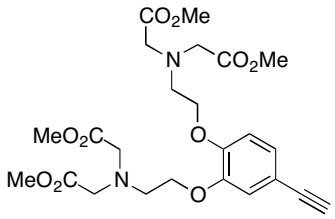

95

To a degassed solution of **94** (535 mg, 0.921 mmol, 1.0 equiv.) in anhydrous THF (6 cm^3) was added TREAT-HF (148 mg, 0.921 mmol, 1.0 equiv., 150 μL) at room temperature. The reaction mixture was stirred at ^{35}C, monitored by TLC and upon completion, the solvent was dried *in vacuo*. Flash chromatography (silica gel, MeOH: DCM 4:96) obtained dark yellow **95**. Prepared in $\geq$ 97% yield. ESI-MS (ES^+) calculated for $C_{24}H_{32}N_2O_{10}$ $[M^+H^+]$ *m/z* 508.21, found 508.30.

A.15.2 NMR characterisations

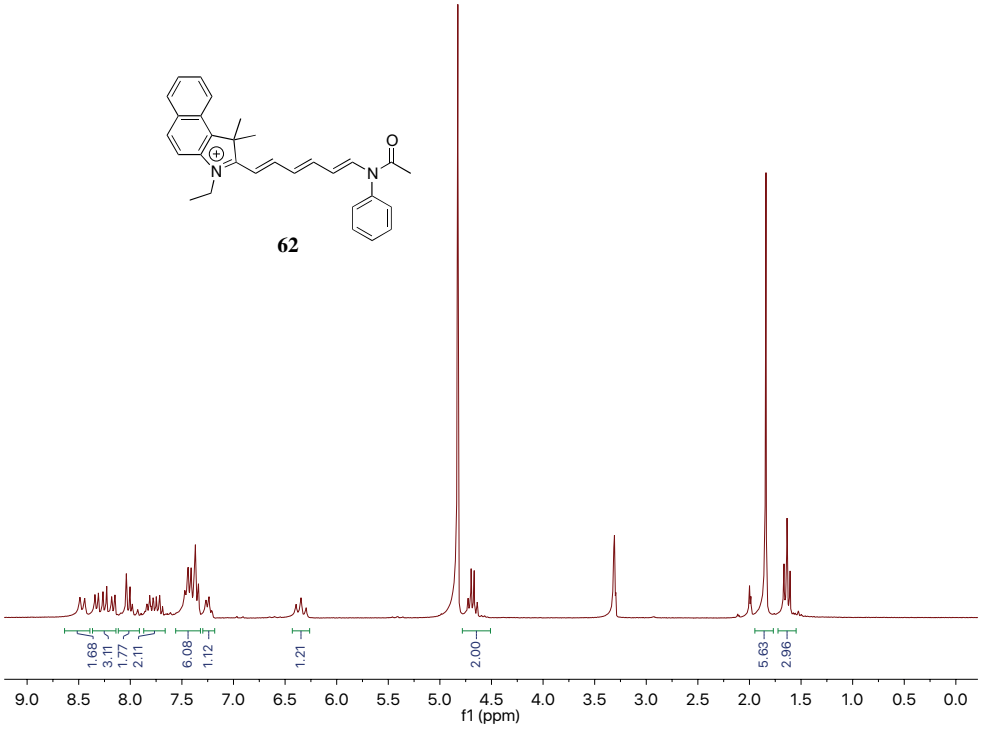

Figure A.1: ^{1}H NMR of compound **62**.

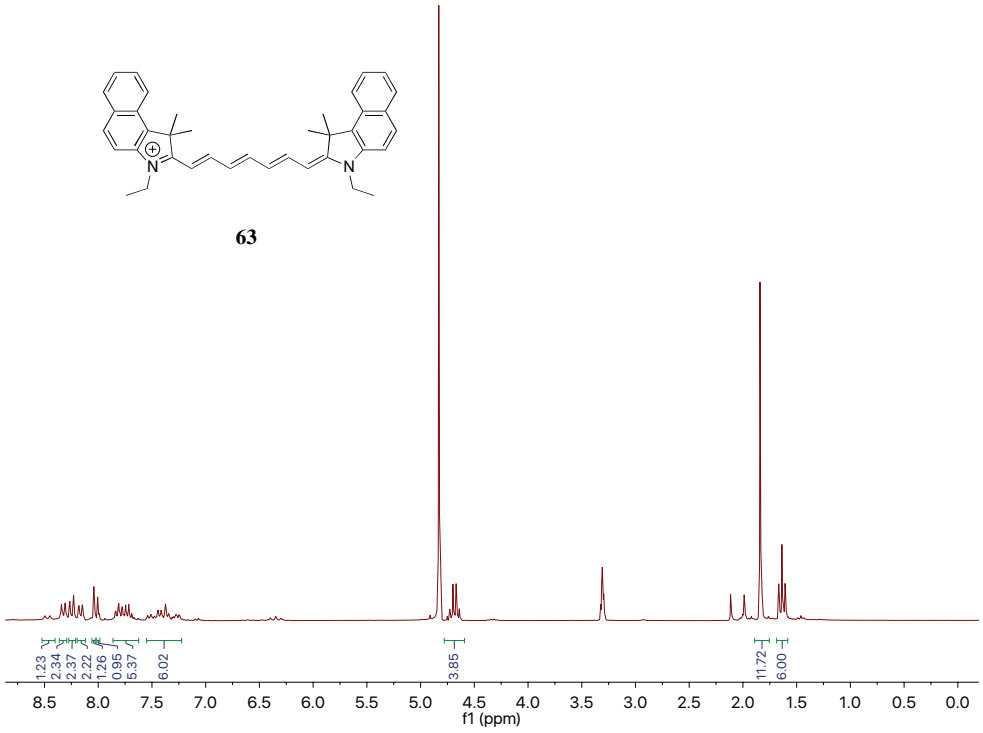

Figure A.2: ^{1}H NMR of compound **63**.

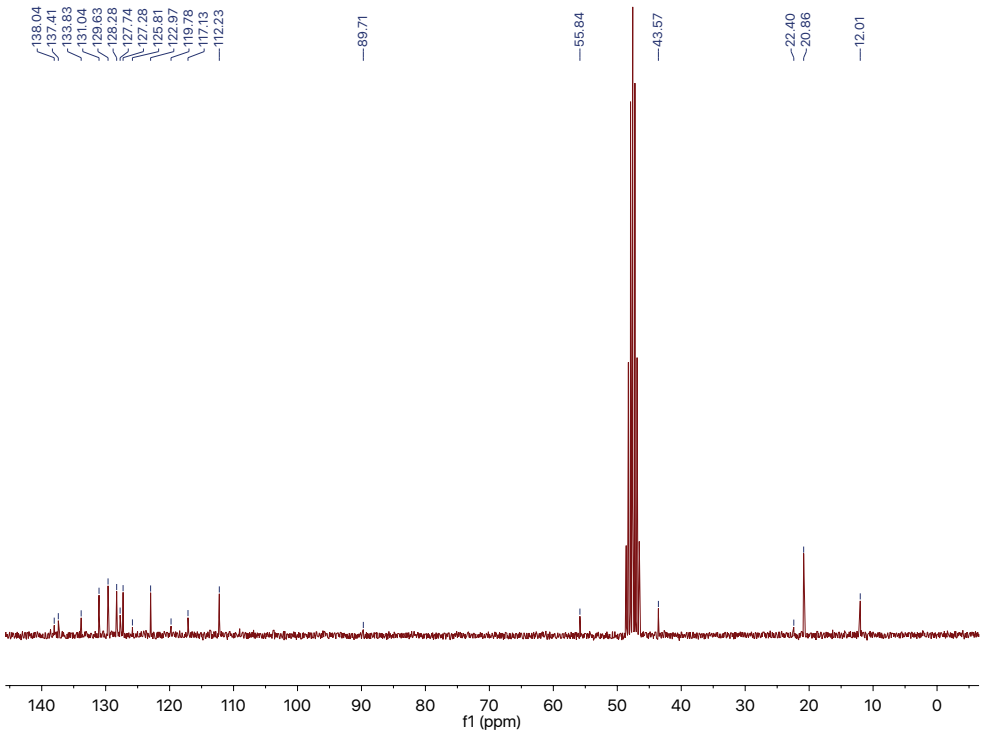

Figure A.3: ^{13}C NMR of compound **63**.

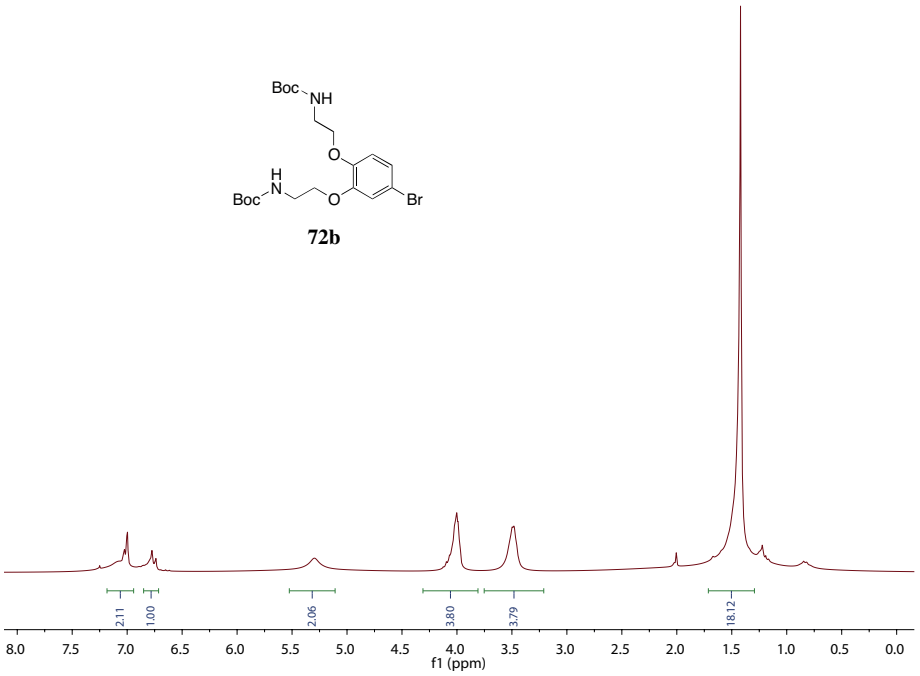

Figure A.4: ^{1}H NMR of compound **72**b.

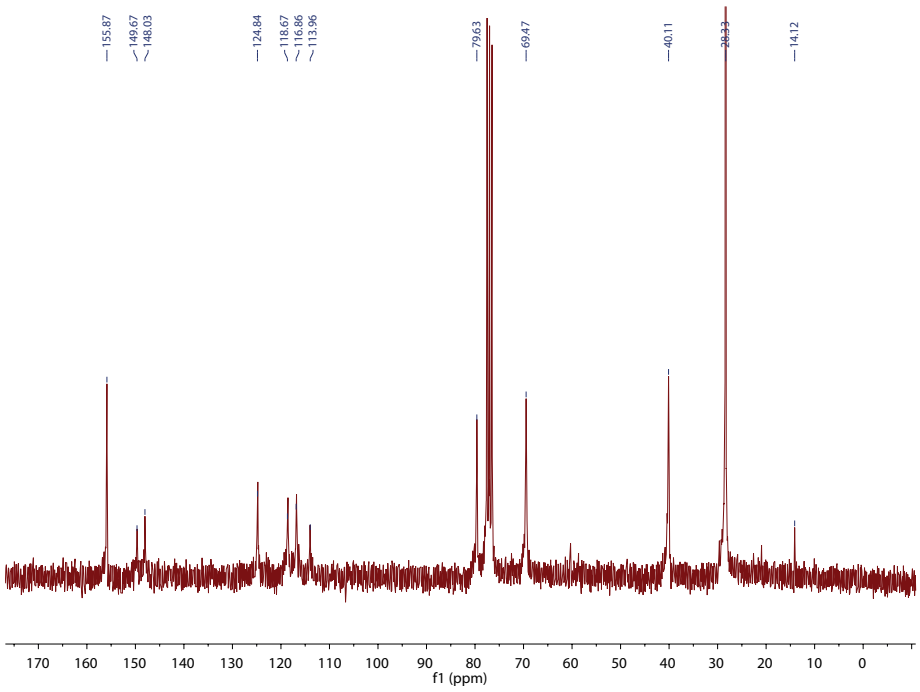

Figure A.5: ^{13}C NMR of compound **72**b.

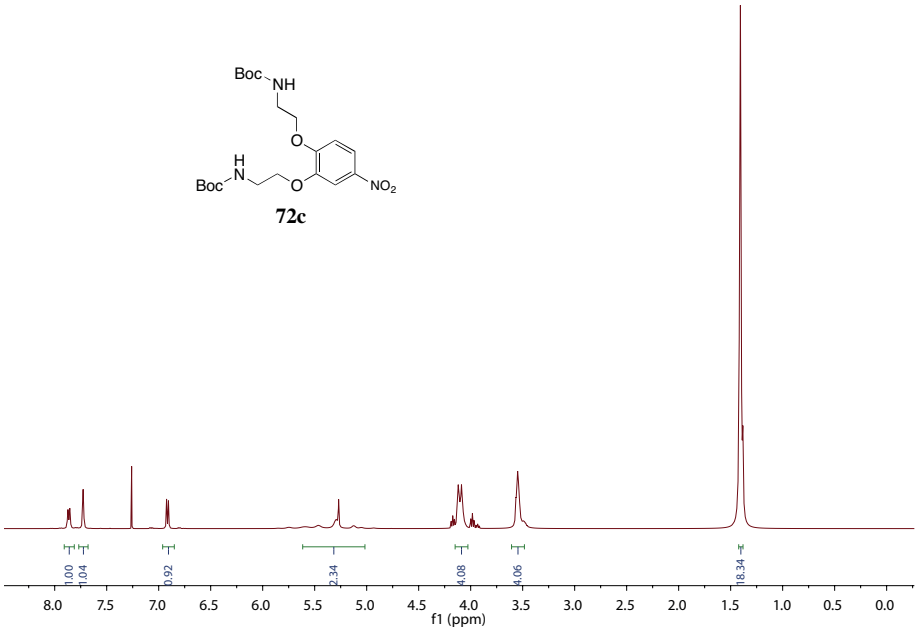

Figure A.6: ^{1}H NMR of compound **72**c.

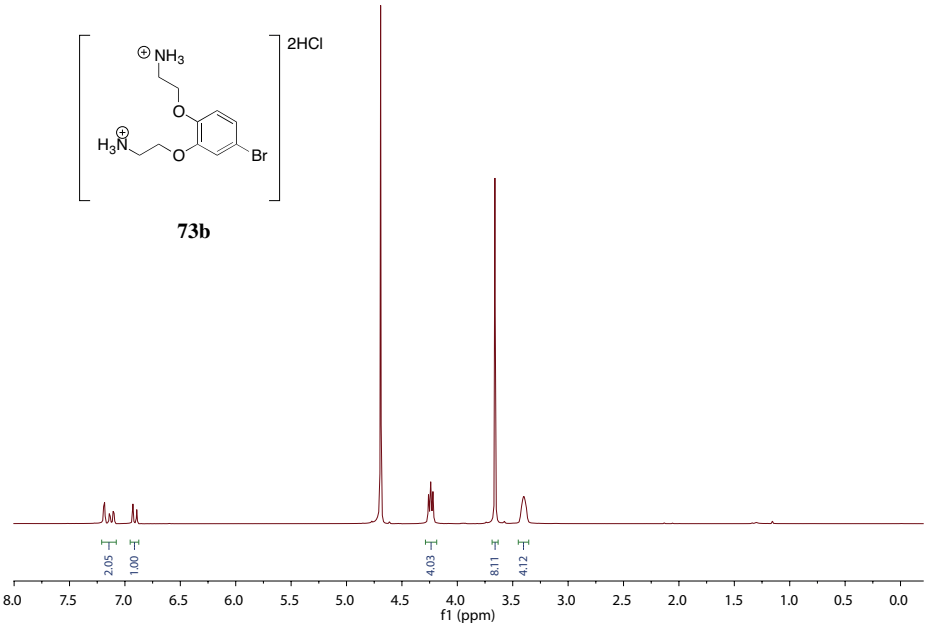

Figure A.7: ^{1}H NMR of compound **73**b.

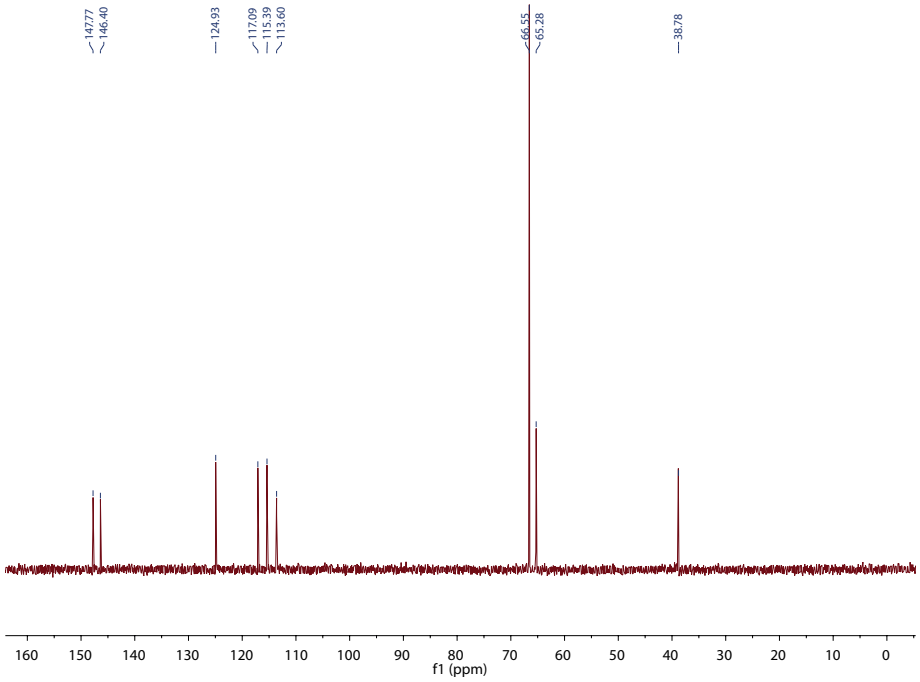

Figure A.8: ^{13}C NMR of compound **73**b.

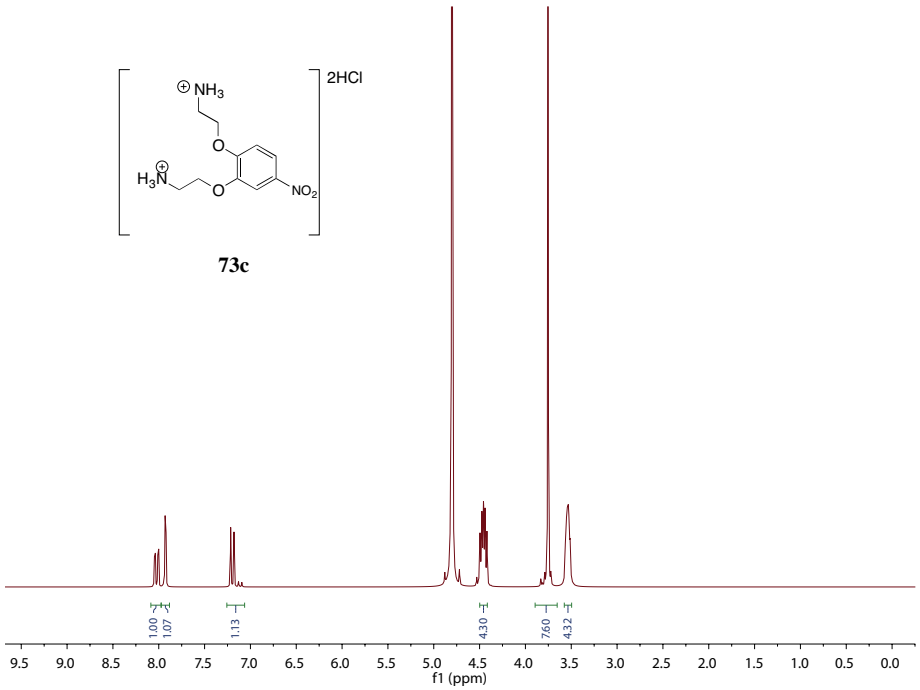

Figure A.9: ^{1}H NMR of compound **73**c.

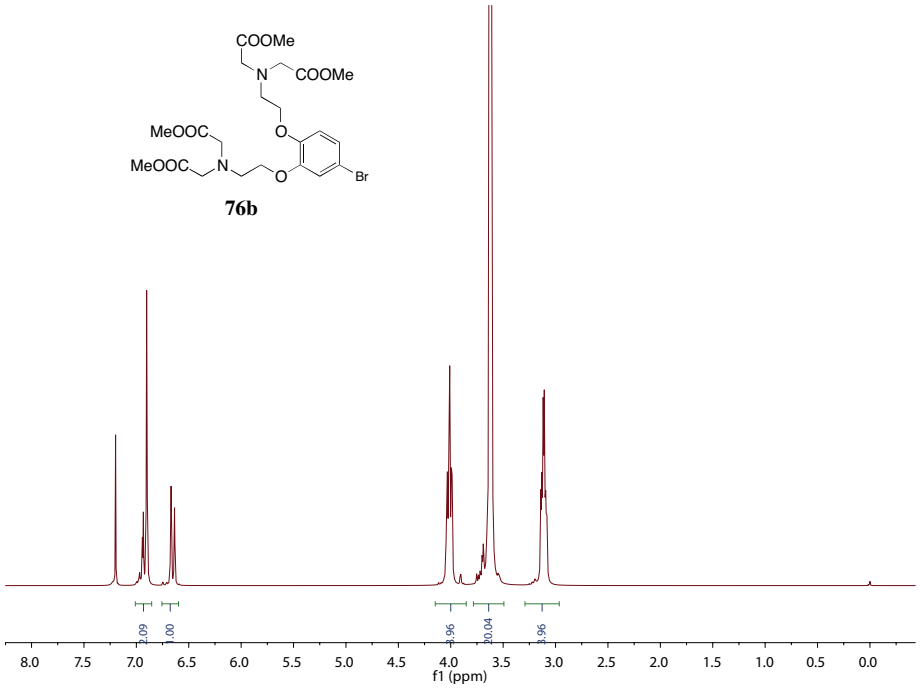

Figure A.10: ^{1}H NMR of compound **76**b.

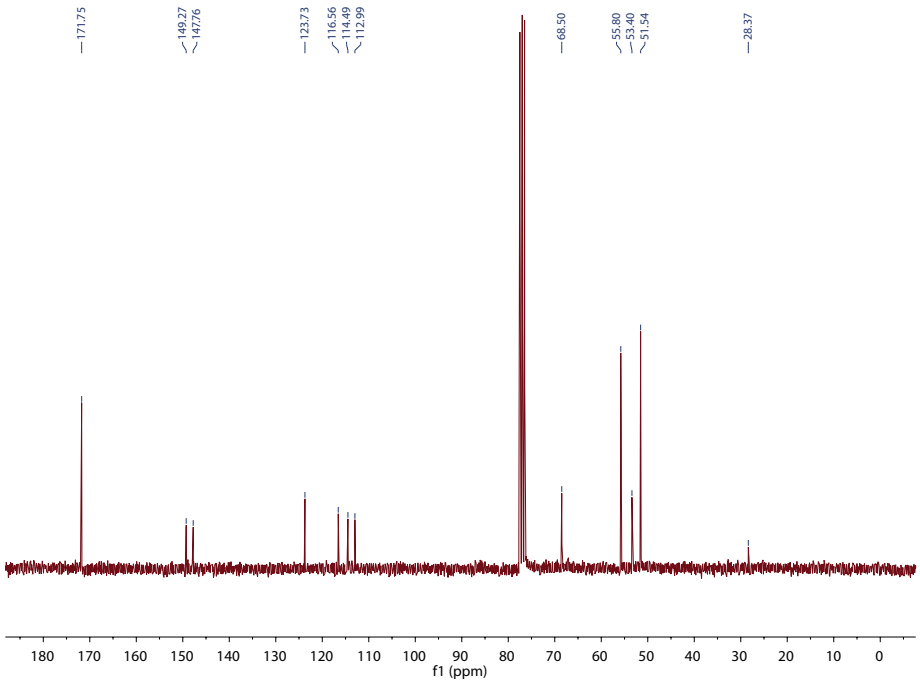

Figure A.11: ^{13}C NMR of compound **76**b.

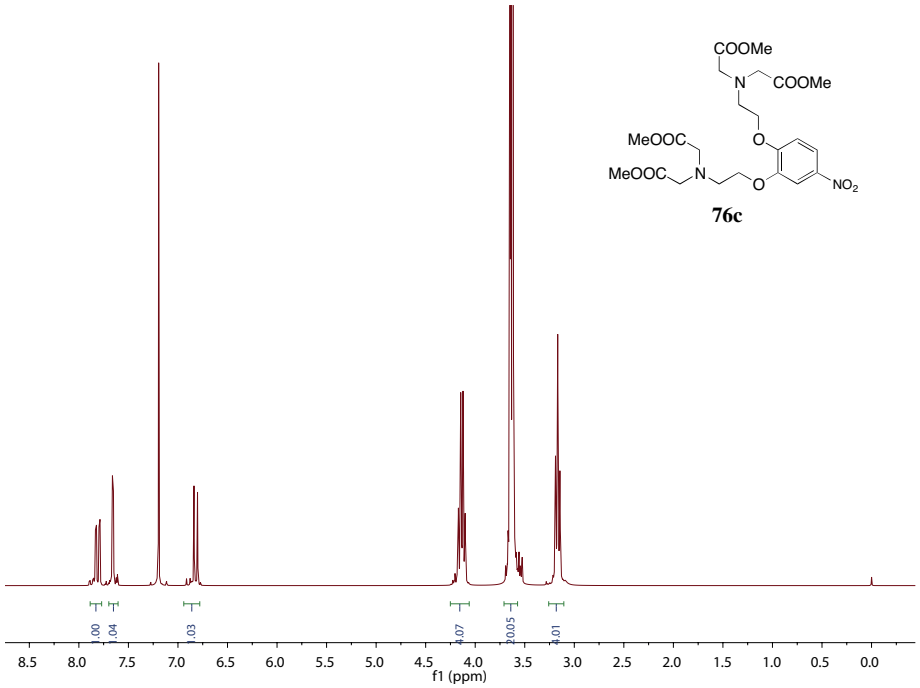

Figure A.12: ^{1}H NMR of compound **76**c.

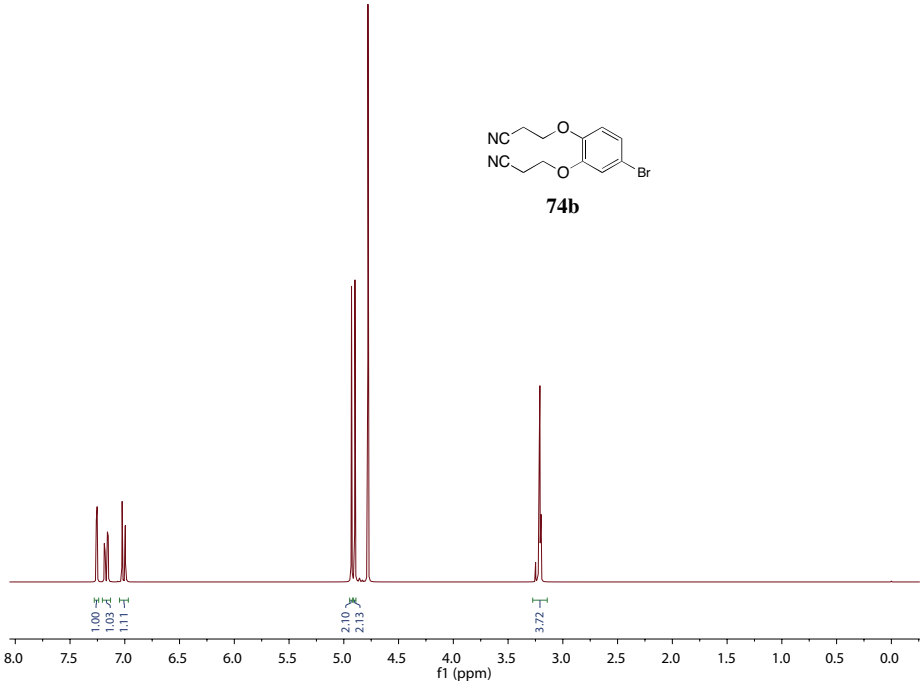

Figure A.13: ^{1}H NMR of compound **74**b.

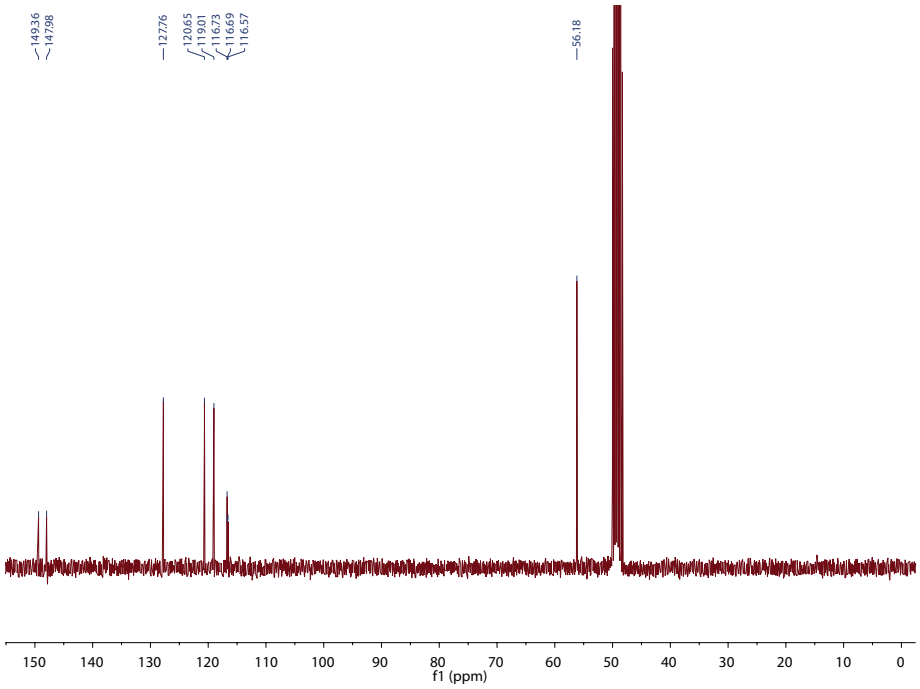

Figure A.14: ^{13}C NMR of compound **74**b.

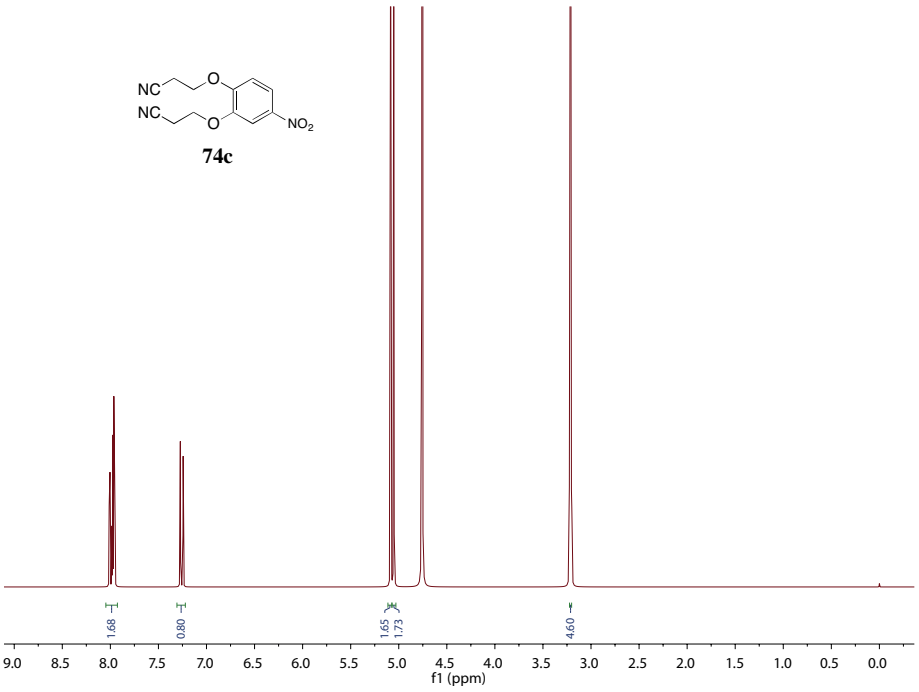

Figure A.15: ^{1}H NMR of compound **74**c.

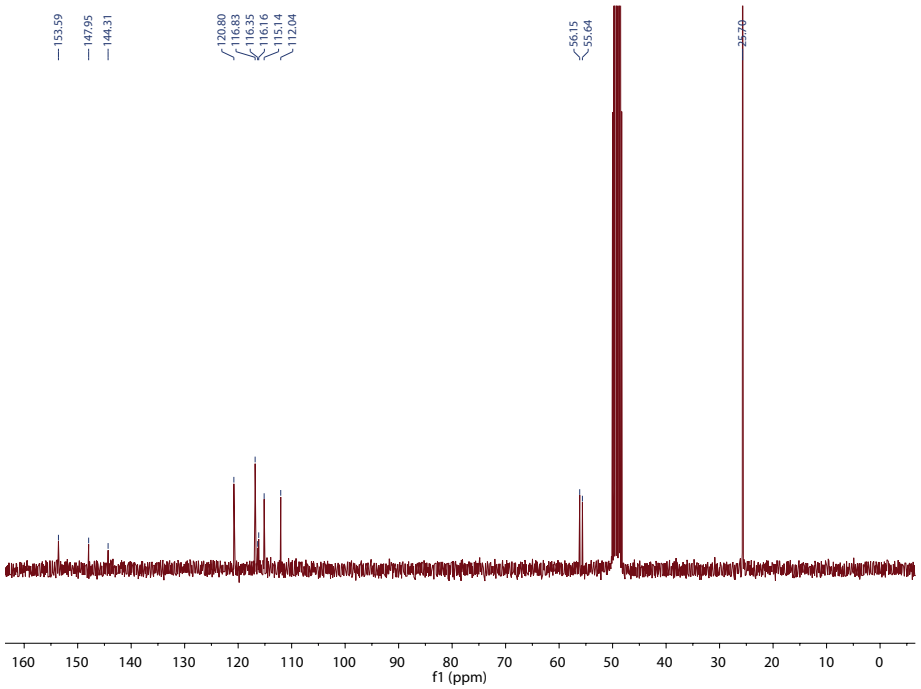

Figure A.16: ^{13}C NMR of compound **74**c.

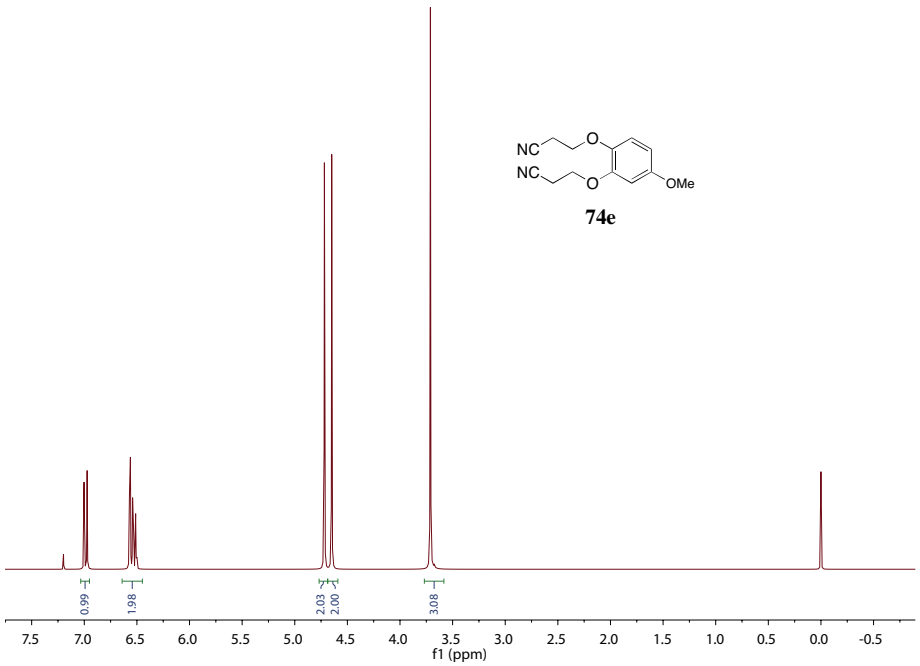

Figure A.17: ^{1}H NMR of compound **74**e.

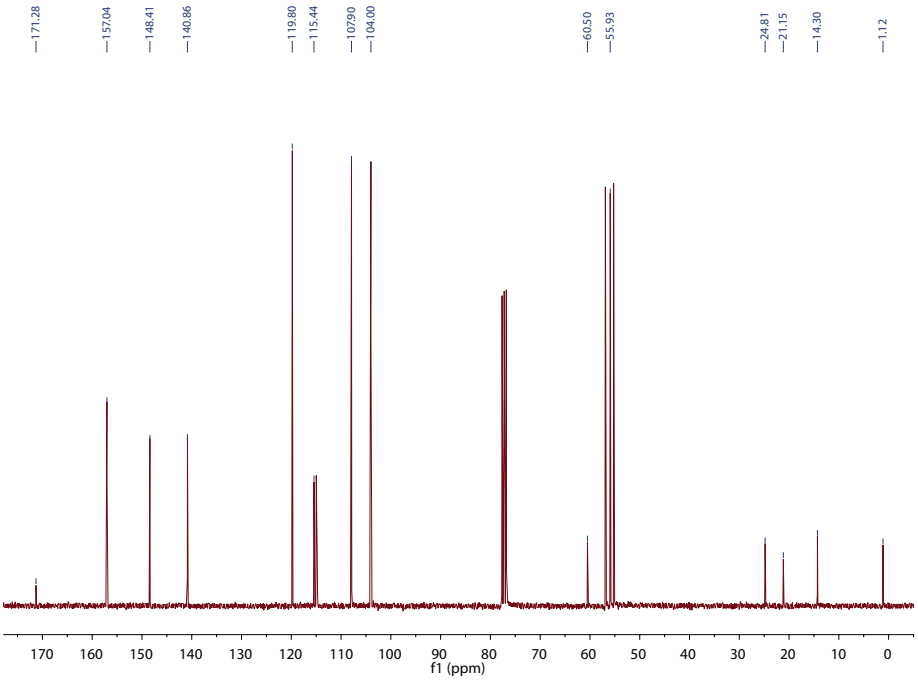

Figure A.18: ^{13}C NMR of compound **74**e.

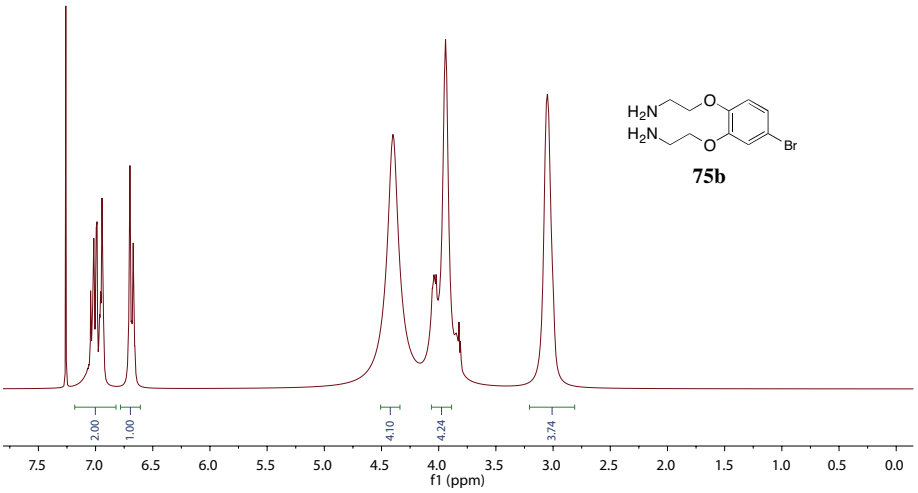

Figure A.19: ^{1}H NMR of compound **75**b.

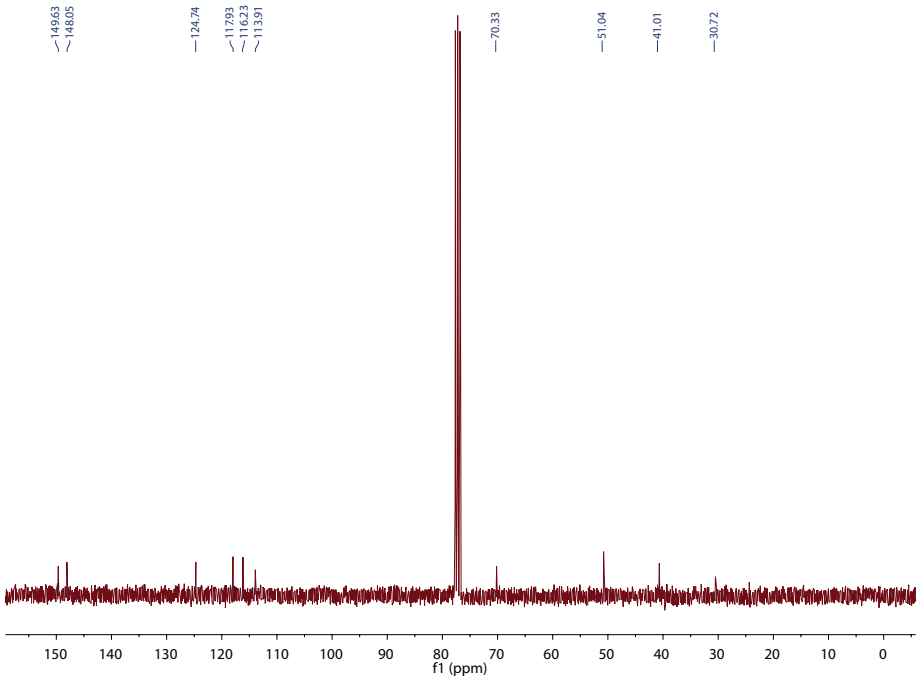

Figure A.20: ^{13}C NMR of compound **75**b.

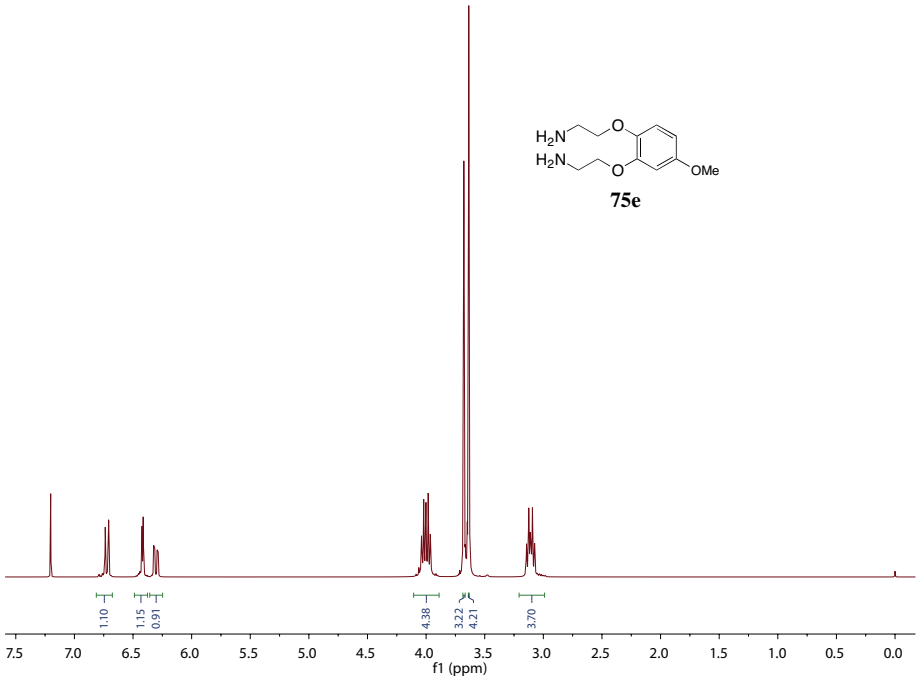

Figure A.21: ^{1}H NMR of compound **75**e.

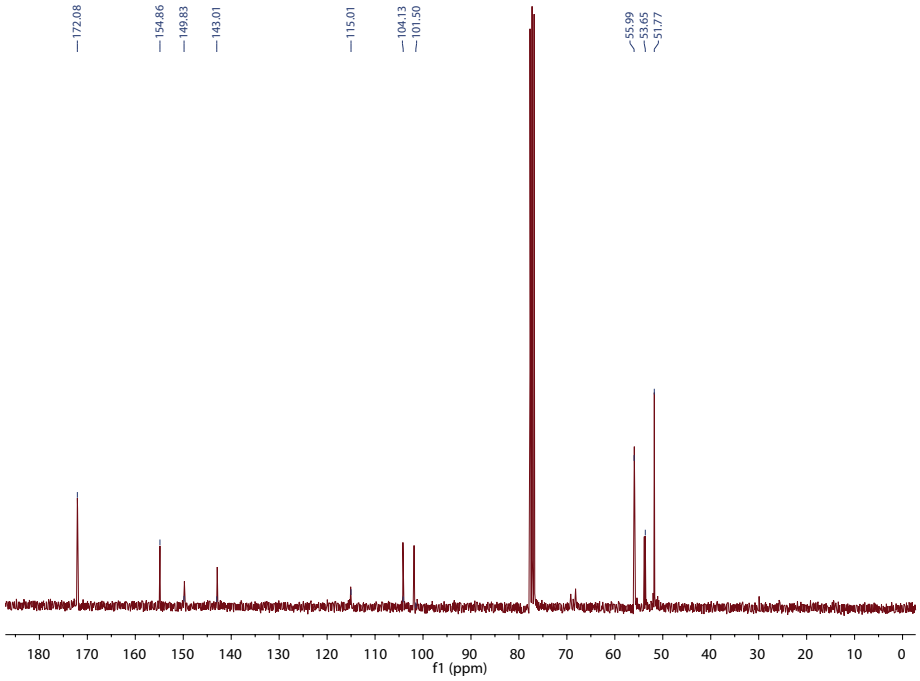

Figure A.22: ^{13}C NMR of compound **75**e.

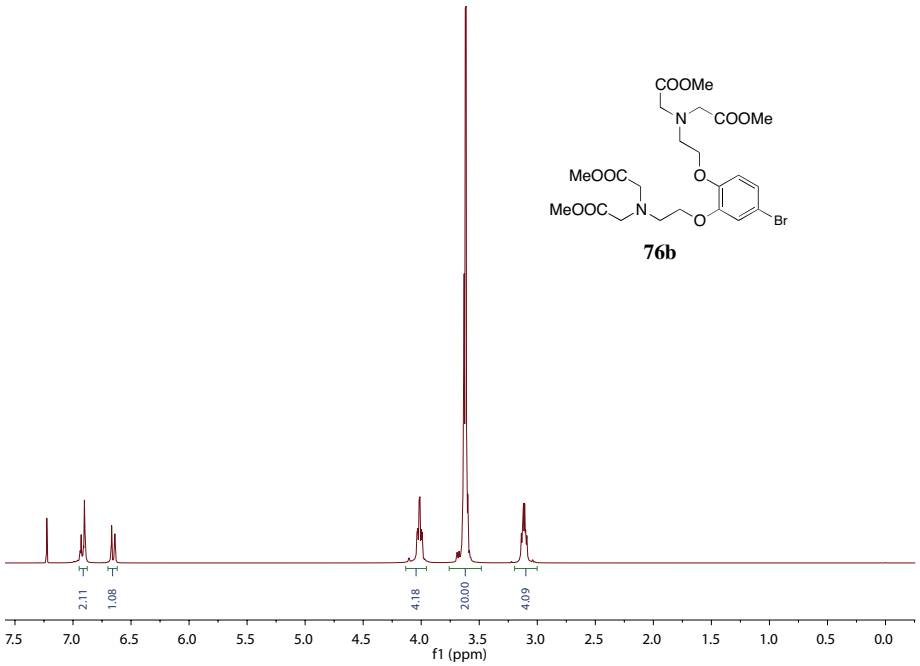

Figure A.23: ^{1}H NMR of compound **76**b.

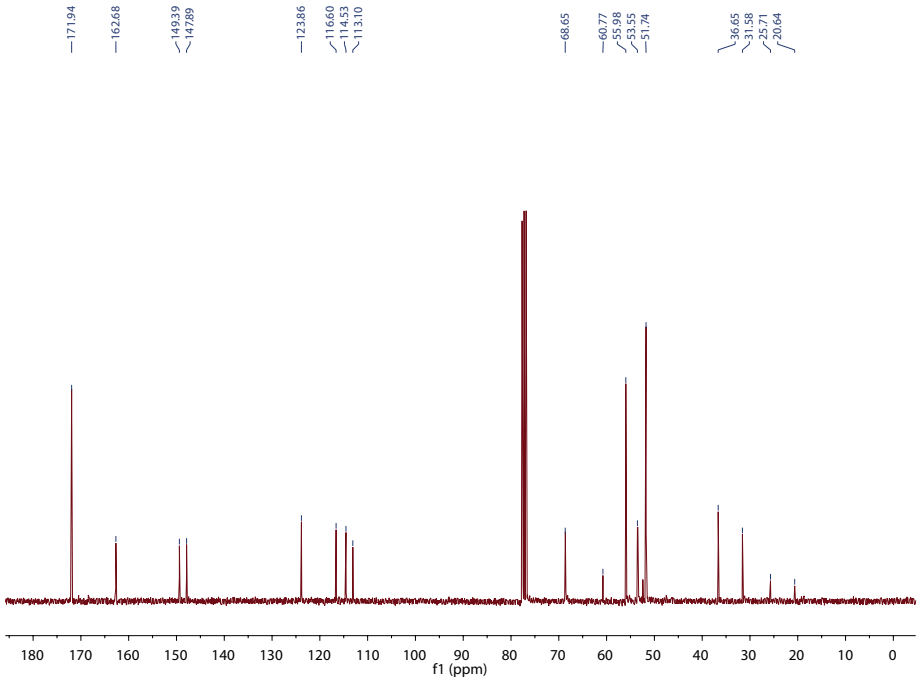

Figure A.24: ^{13}C NMR of compound **76**b.

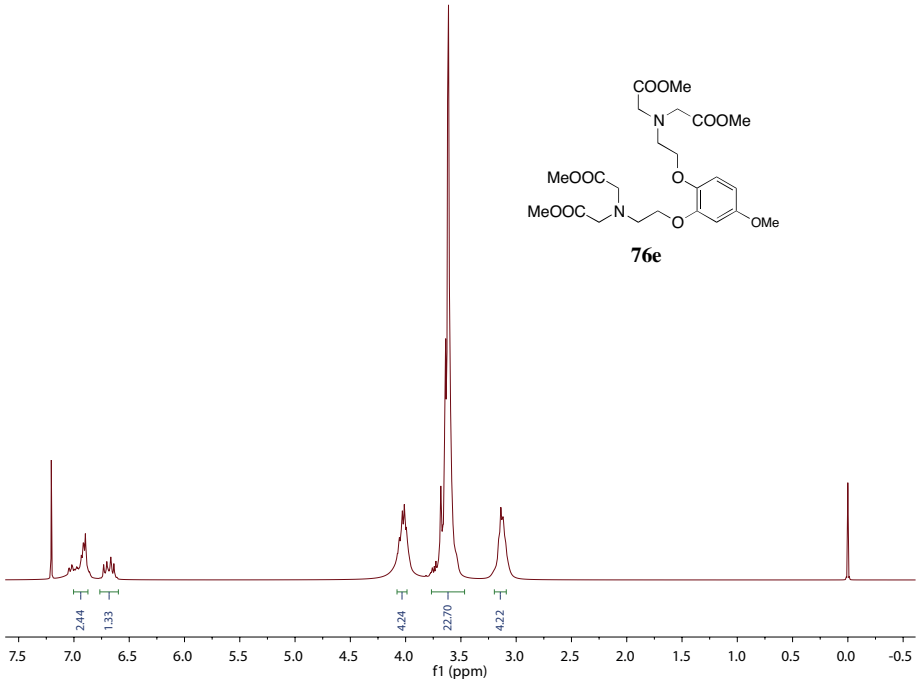

Figure A.25: ^{1}H NMR of compound **76**e.

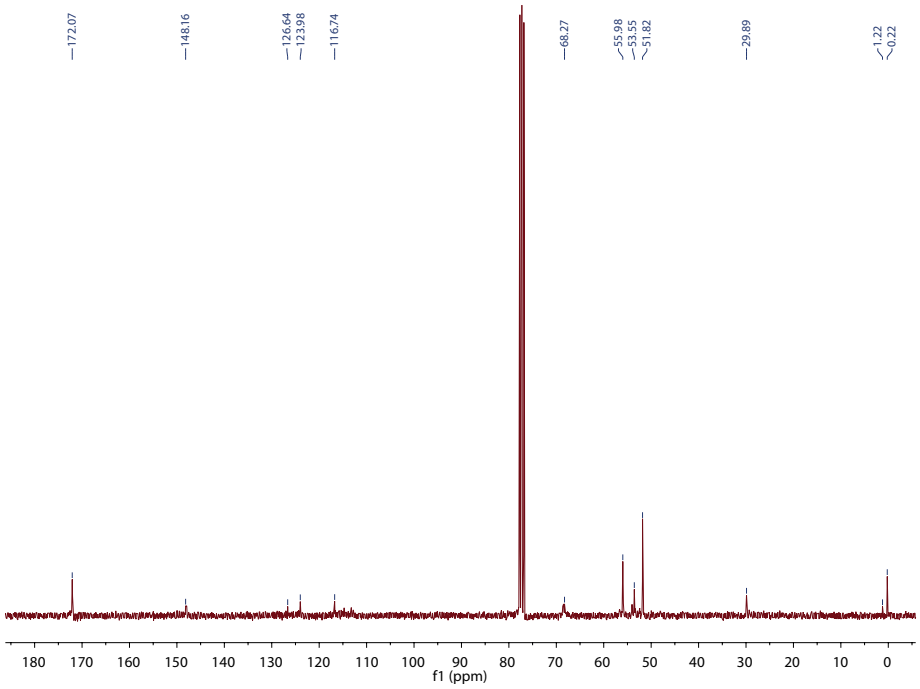

Figure A.26: ^{13}C NMR of compound **76**e.

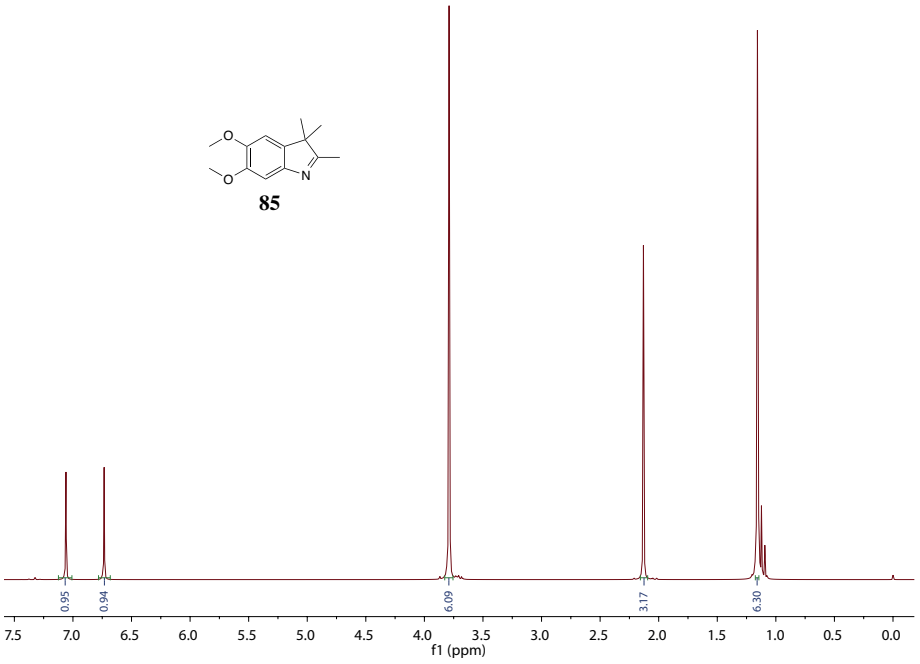

Figure A.27: ^{1}H NMR of compound **85**.

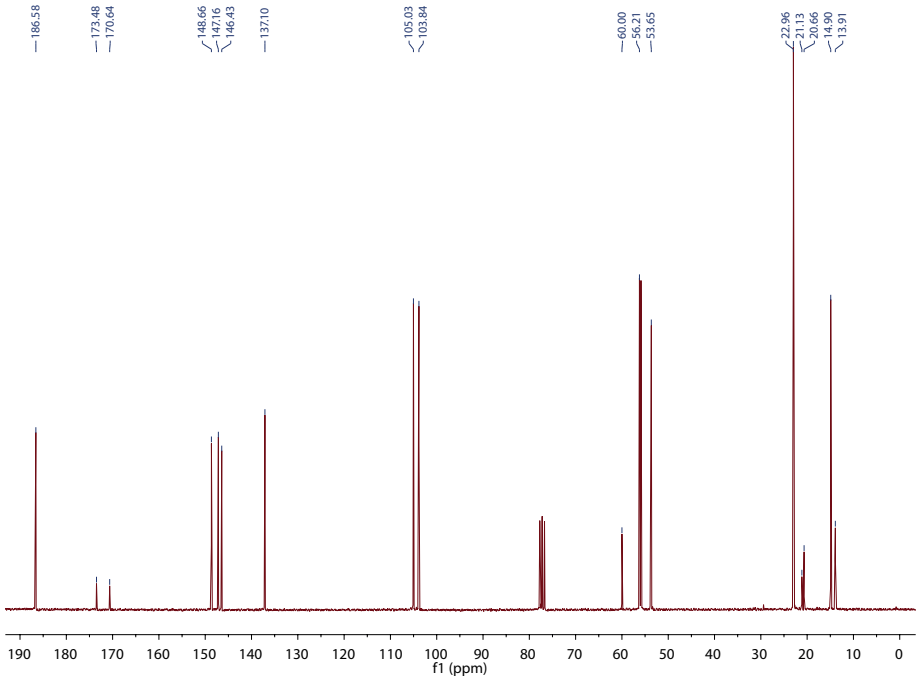

Figure A.28: ^{13}C NMR of compound **85**.

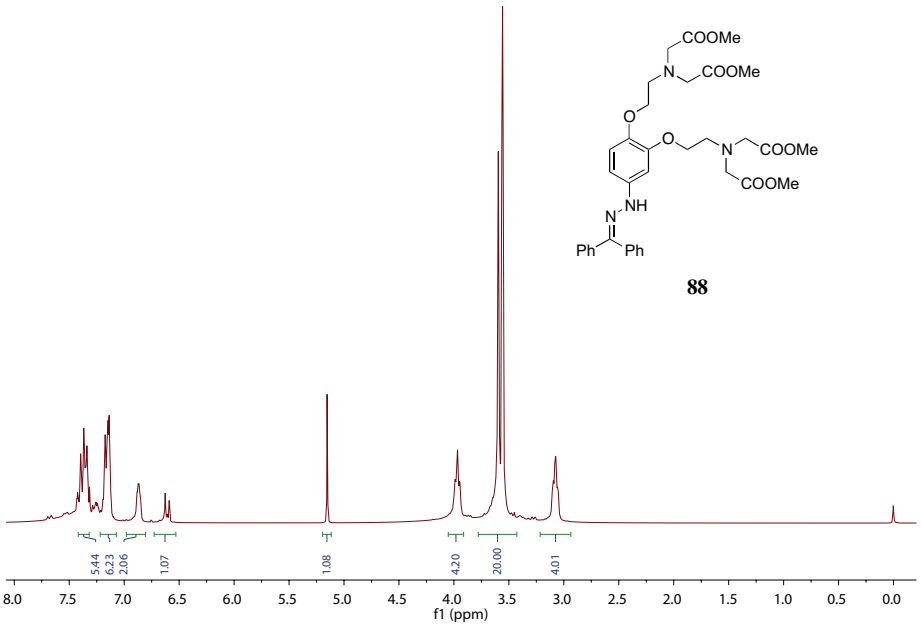

Figure A.29: ^{1}H NMR of compound **88**.

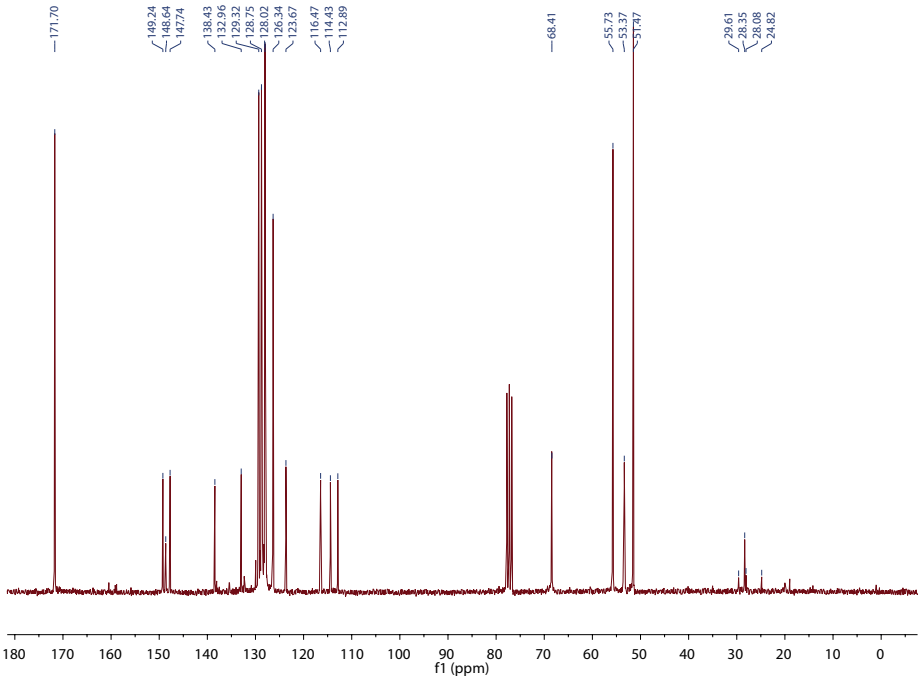

Figure A.30: ^{13}C NMR of compound **88**.

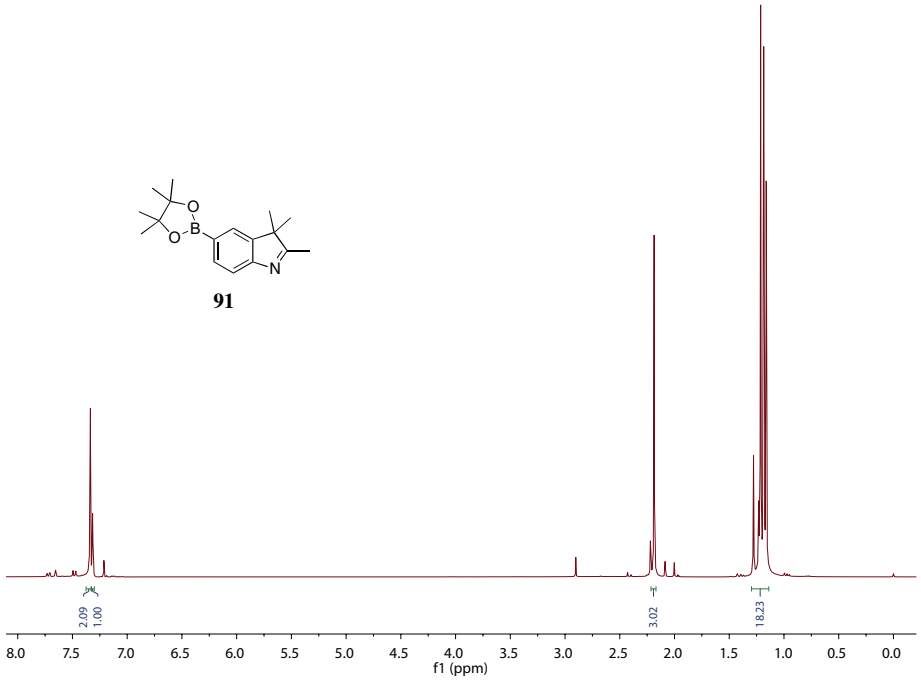

Figure A.31: ^{1}H NMR of compound **91**.

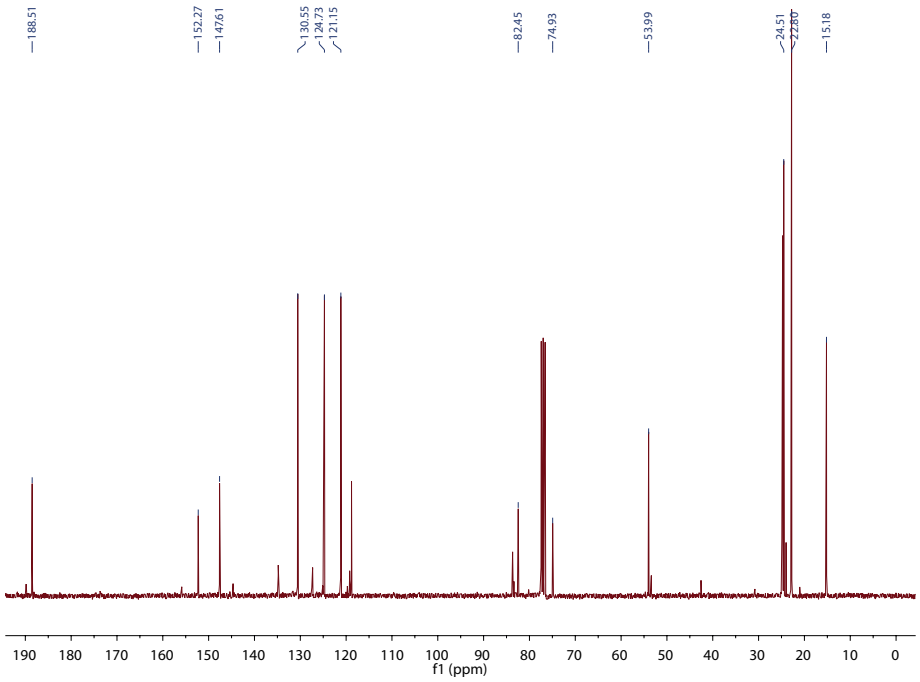

Figure A.32: ^{13}C NMR of compound **91**.

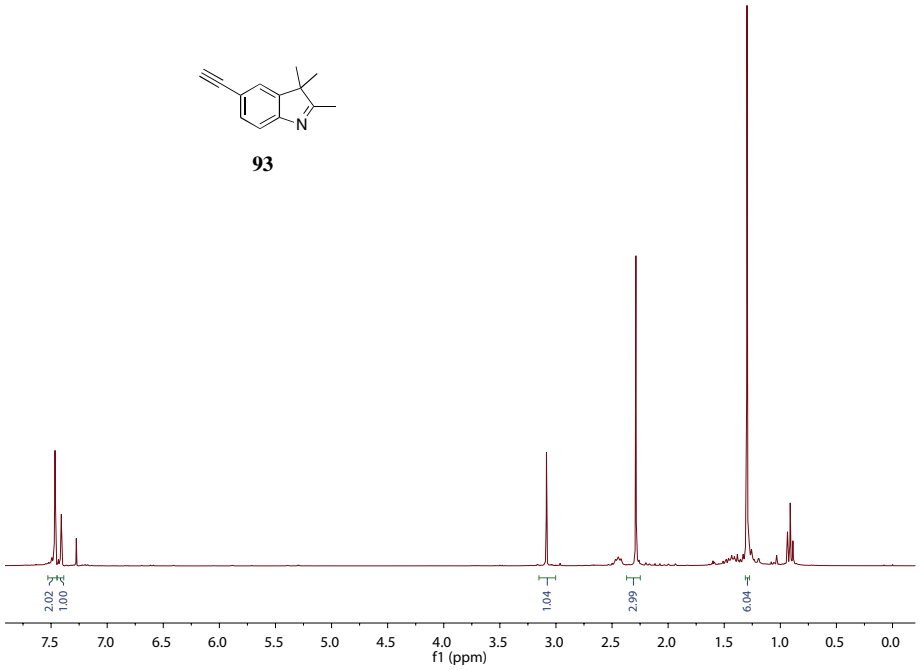

Figure A.33: ^{1}H NMR of compound **93**.

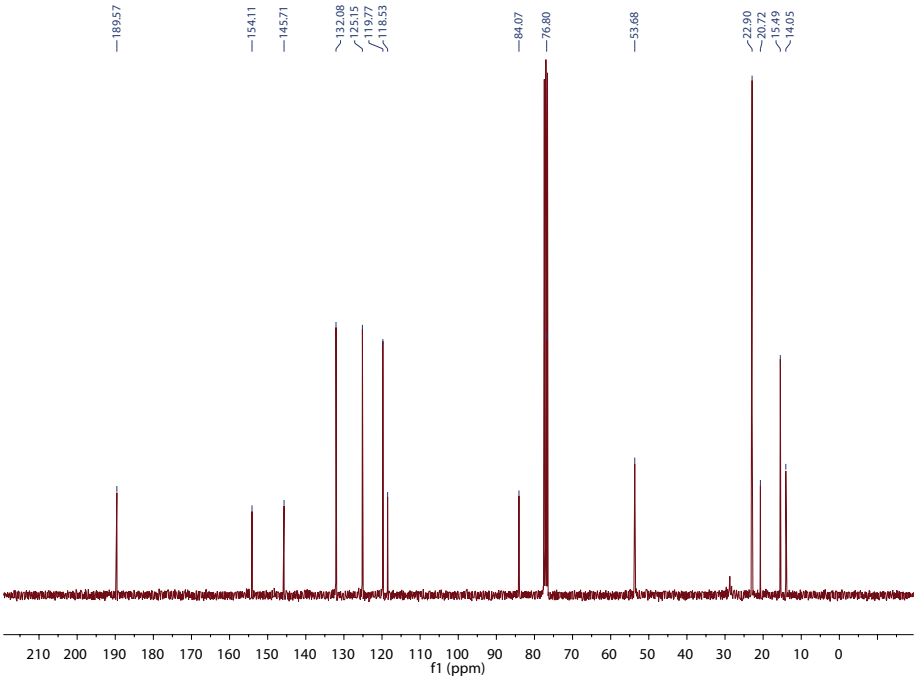

Figure A.34: ^{13}C NMR of compound **93**.

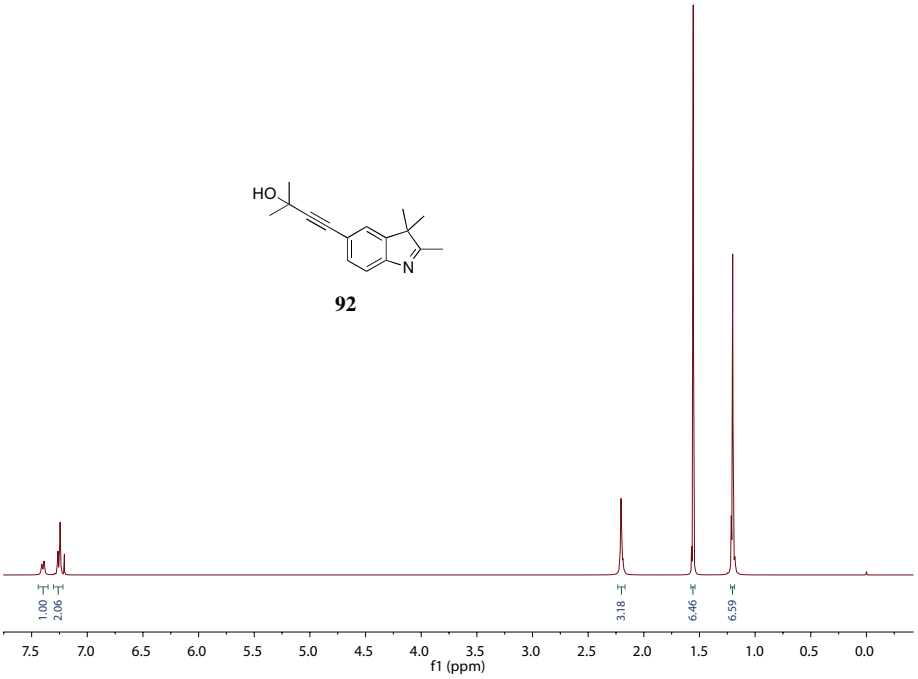

Figure A.35: ^{1}H NMR of compound **92**.

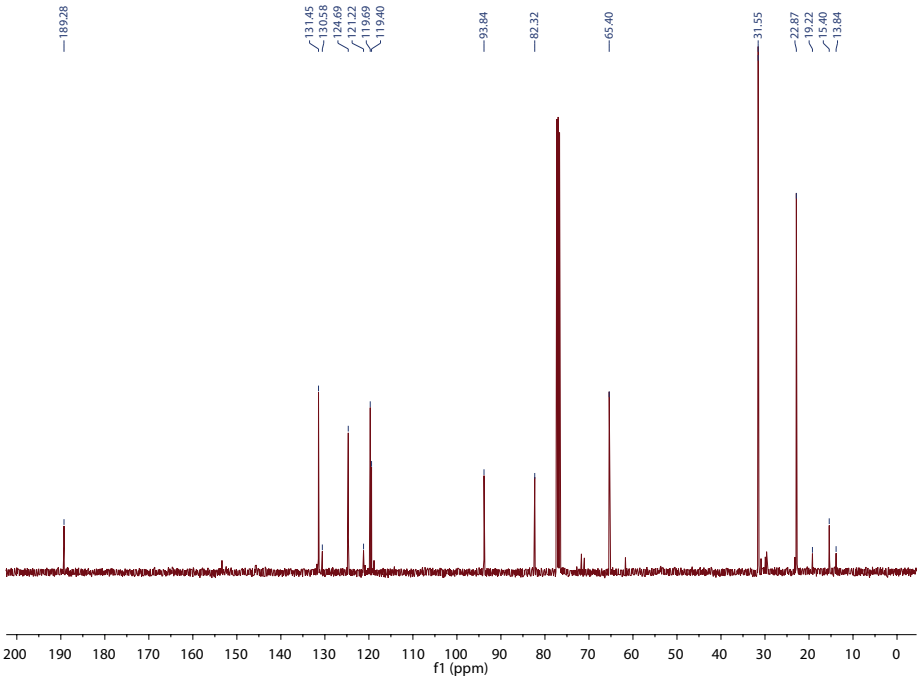

Figure A.36: ^{13}C NMR of compound **92**.

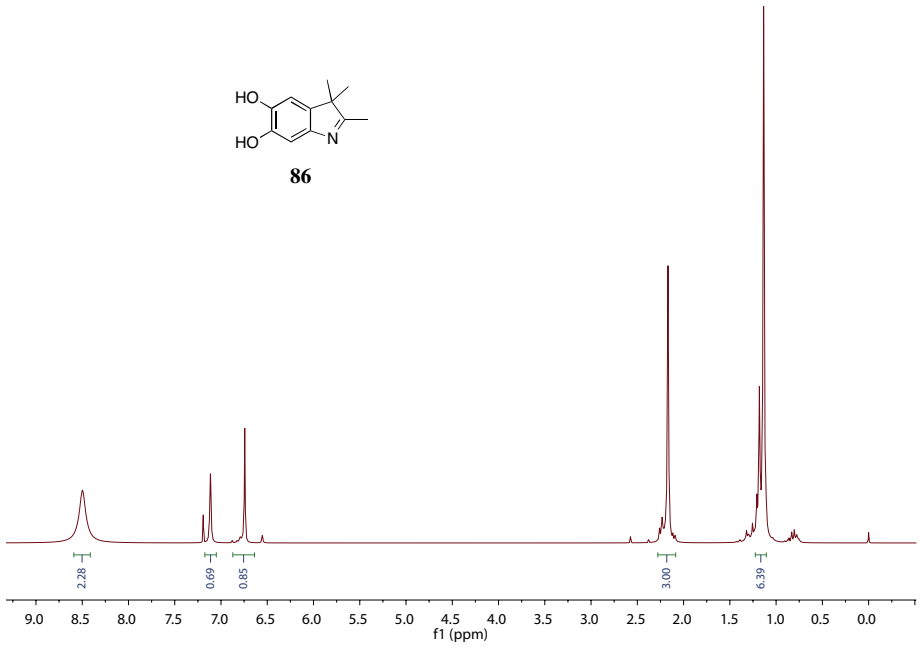

Figure A.37: ^{1}H NMR of compound **86**.

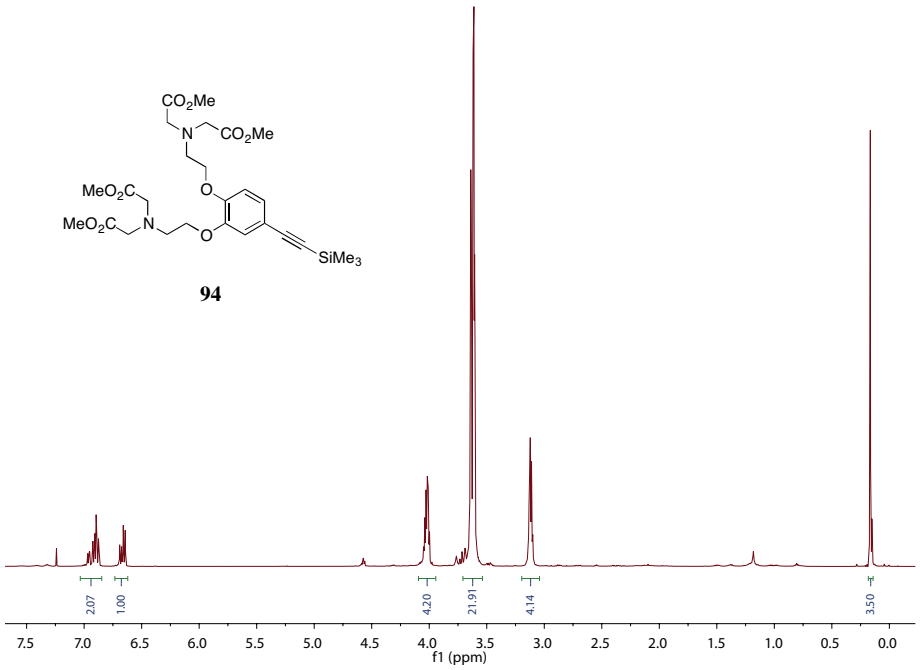

Figure A.38: ^{1}H NMR of compound **94**.

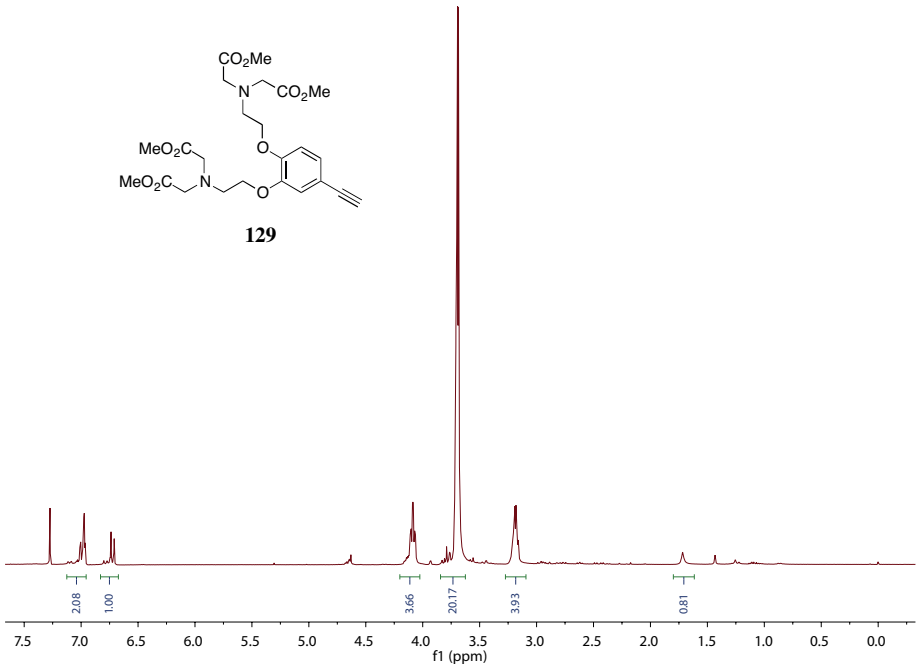

Figure A.39: ^{1}H NMR of compound **129**.

Appendix B

Contrast agents for photoacoustic tomography

B.1 Near infrared dyes

Table B.1: **Potential absorbing agents for photoacoustic imaging.** Classes of highly absorbing dyes that were explored in details as potential photoacoustic agents. Evaluated their photophysical properties and ease of syntheses.

Absorbing agents	Structure	**Abs (nm)**	ε ($\times 10^3$ **cm**$^{-1}$ **M**$^{-1}$)	**ref**
Cyanines	**130**			104
Perylenes	**131**	385 - 945	-	239
Rhodamines	**132**	494 - 554	31 - 87	240,241
Squaraines	**133**	54- 328	-	196,237,242,243
Porphyrin	**8**			44,99–101,105,115,244
Fluoresceins	**134**	450- 540	50 - 56	172
BODIPYs	**135**	500- 687	251 - 545	30,70
Squaraines	**136**	54- 328	-	196,237,242,243

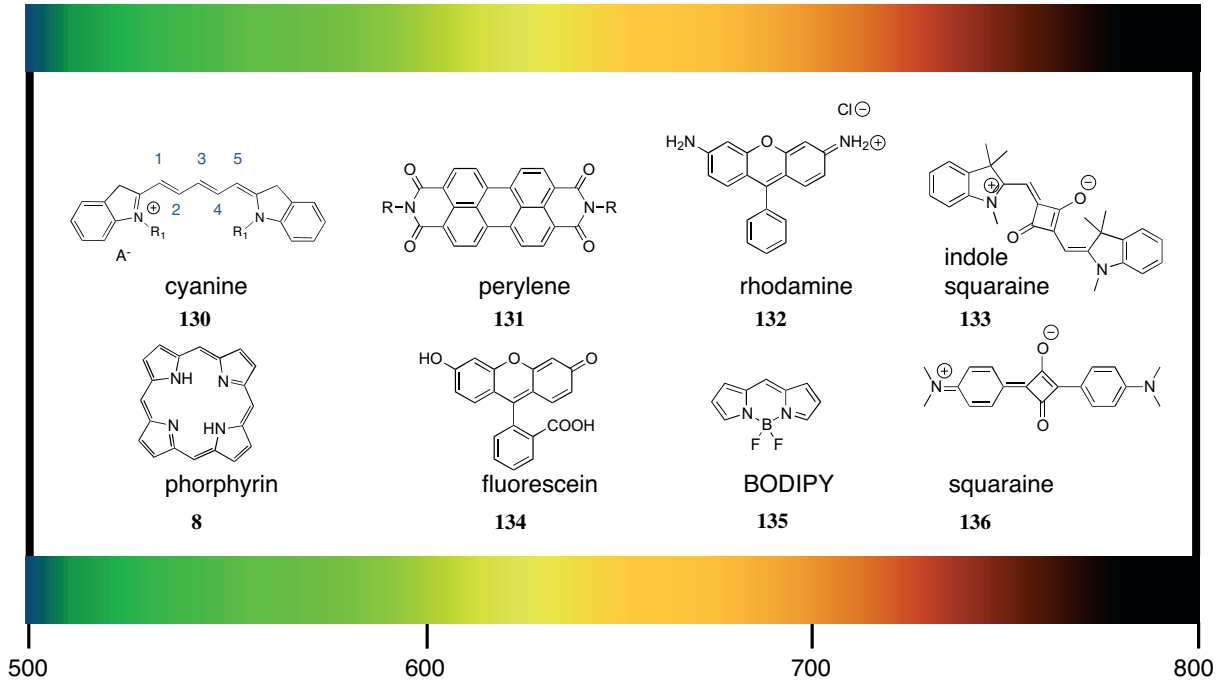

Figure B.1: **Basic chemical structures of near-infrared dyes.** Shown here are the general chemical structure of cyanines **130**, perylenes **131**, rhodamines **132**, indole squaraines **133**, phorphyrins **8**, fluoresceins **134**, bodipys **135** and squaraines **136**. We decided with cyanines as our starting core for the design of optoacoustic agents.

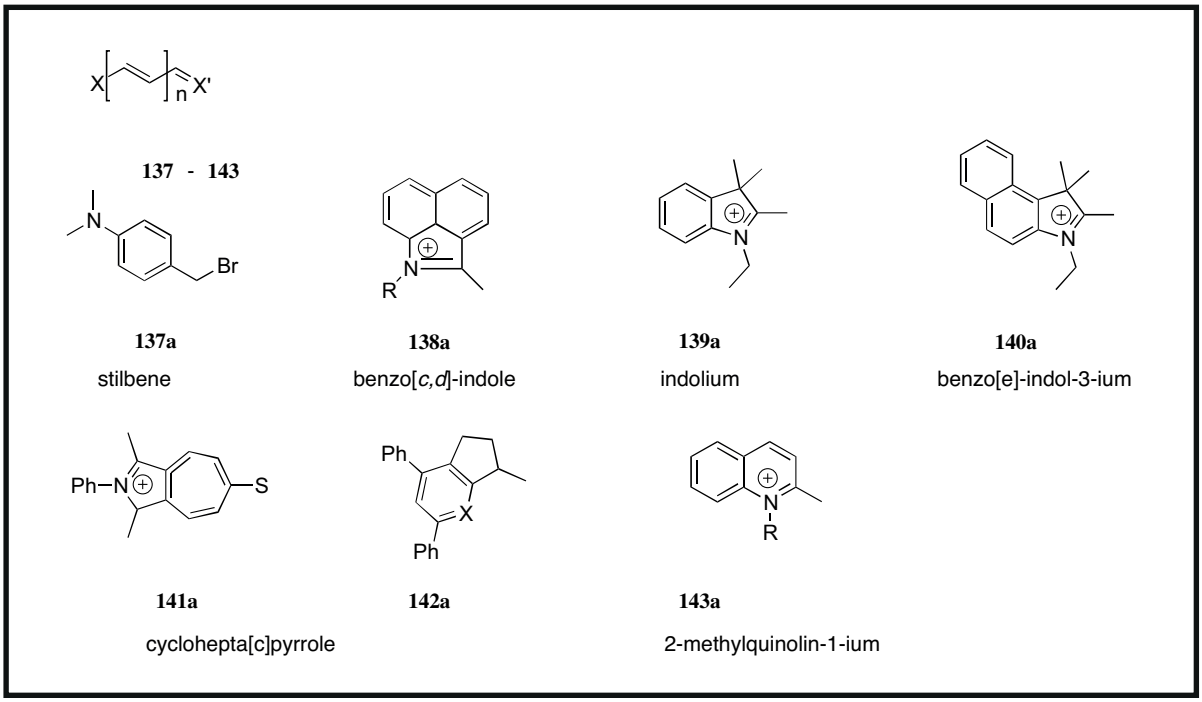

Figure B.2: **Common merocyanines and heptamethines.** Chemical representation of heterocycles for the synthesis of the cyanines.

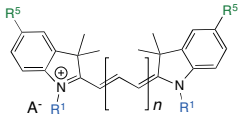

144a Cy3: n = 1, R^1 = -$C_nH_{(2n+1)}$, R^5 = -H
144b sulfo-Cy3: n = 1, R^1 = -$C_nH_{(2n+1)}$, R^5 = -SO_3^-
144c Cy5: n = 2, R^1 = -$C_nH_{(2n+1)}$, R^5 = -H
144d sulfo-Cy5: n = 2, R^1 = -$C_nH_{(2n+1)}$, R^5 = -SO_3^-
144e Cy7: n = 3, R^1 = -$C_nH_{(2n+1)}$, R^5 = -H
A^- = counter ion

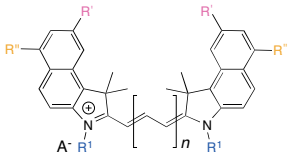

145a Cy3.5: n = 1, R^1 = -$C_nH_{(2n+1)}$, R' = -H, R'' = -H
145b Cy5.5: n = 2, R^1 = -$C_nH_{(2n+1)}$, R' = -H, R'' = -H
145c sulfo-Cy5.5: n = 2, R^1 = -$C_nH_{(2n+1)}$, R' = -SO_3^-, R'' = -SO_3^-
145d Cy7.5: n = 3, R^1 = -$C_nH_{(2n+1)}$, R' = -H, R'' = -H
A^- = counter ion

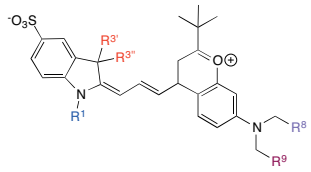

146a DY-630: R^1 = -conj. , $R^{3'}/R^{3''}$ = -CH_3, R^8/R^9 = -CH_3
146b DY-631: R^1 = -$C_3H_6SO_3^-$, $R^{3'}$ = -CH_3, $R^{3''}$ = -conj., R^8/R^9 = -CH_3
146c DY-632: R^1 = -$C_3H_6SO_3^-$, $R^{3'}$ = -CH_3, $R^{3''}$ = -conj., R^8 = -CH_3, R^9 = -$CH_2SO_3^-$
146d DY-633: R^1 = -conj. , $R^{3'}/R^{3''}$ = -CH_3, R^8 = -CH_3, R^9 = -$C_2H_4SO_3^-$
146e DY-634: R^1 = -$C_3H_6SO_3^-$, $R^{3'}$ = -CH_3, $R^{3''}$ = -conj., R^8/R^9 = -$CH_2SO_3^-$
A^- = counter ion

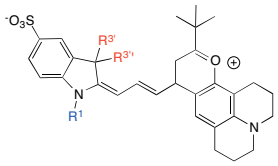

147a DY-635: R^1 = -conj., $R^{3'}/R^{3''}$ = -CH_3
147b DY-636: R^1 = -$C_3H_6SO_3^-$, $R^{3'}$ = -CH_3, $R^{3''}$ = -conj.
A^- = counter ion

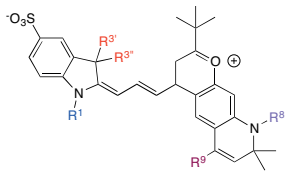

148a DY-650: R^1 = -conj., $R^{3'}/R^{3''}$ = -CH_3, R^8 = -C_2H_5, R^9 = -CH_3
148b DY-651: R^1 = -$C_3H_6SO_3^-$, $R^{3'}$ = -CH_3, $R^{3''}$ = -conj., R^8 = -C_2H_5, R^9 = -CH_3
148c DY-652: R^1 = -$C_3H_6SO_3^-$, $R^{3'}$ = -CH_3, $R^{3''}$ = -conj., R^8 = -$C_3H_6SO_3^-$, R^9 = -CH_3
148d DY-654: R^1 = -$C_3H_6SO_3^-$, $R^{3'}$ = -CH_3, $R^{3''}$ = -conj., R^8 = -C_2H_5, R^9 = -$CH_2SO_3^-$
A^- = counter ion

Figure B.3: **Commercially available fluorescent dyes.**

Table B.2: **Near-infrared dyes from Dyomics that were briefly characterised.** Evaluated their photophysical properties and suitability as photoacoustic agents

Absorbing agents	**Abs (nm)**	**Emm. (nm)**	ε **(cm^{-1} M^{-1})**	**ref**
DYQ-4[a]	742	786	59, 500	
DY-781[b]	762	792	-	
DY-800 carboxylic acid[a]	765	785	151, 666	
DY-800 biotin	765	785	-	
DY-831 carboxylic acid[a]	814	-	51, 733	
DY-840-S[c]	831	-	286, 667	

[a] HEPES [30 mM, 100 KCl, pH 7.40, RT 20 ^{o}C]

[b] MOPS [30 mM, 100 KCl, pH 7.40, RT 20 ^{o}C]

[c] MeOH, RT 20 ^{o}C]

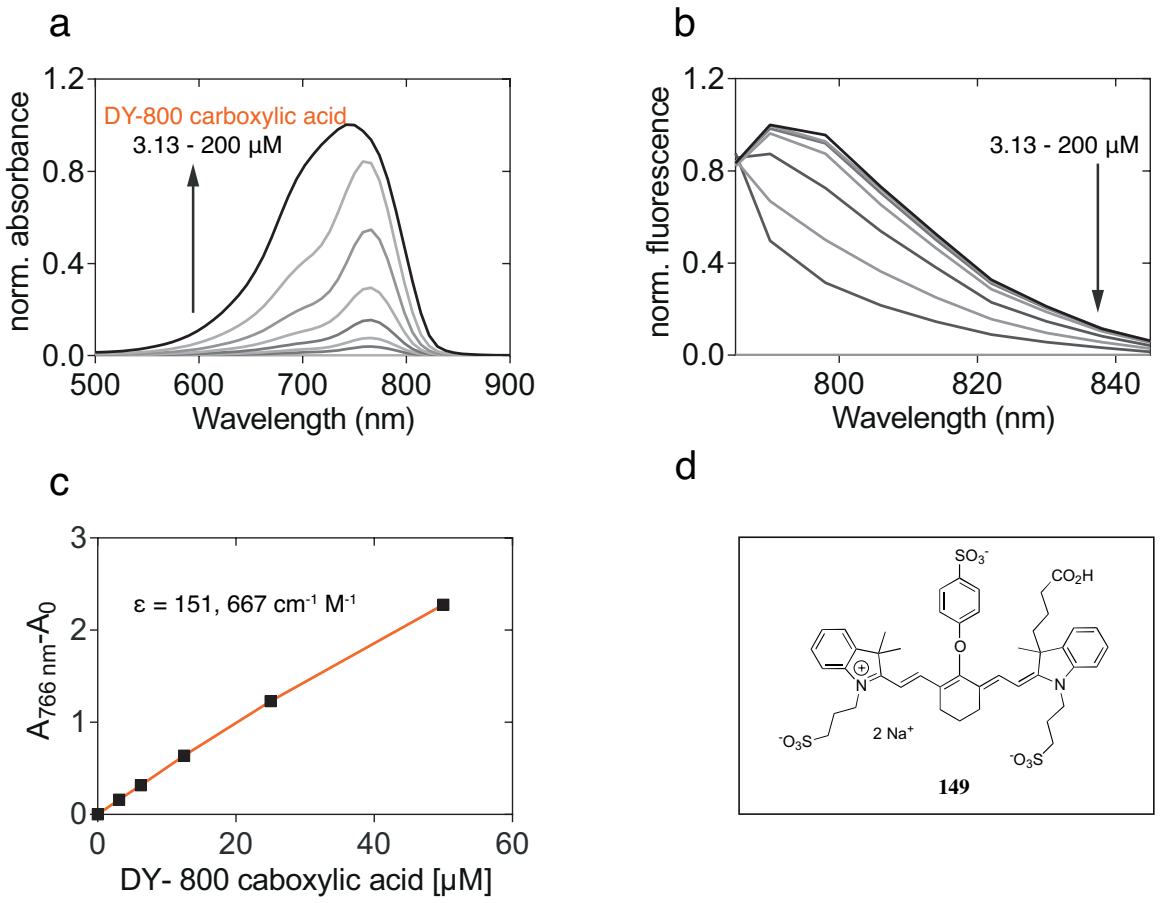

Figure B.4: **Spectroscopic characterisations of DY-800 carboxylic acid.** (a/b) the absorption and fluorescent spectra of DY-800 carboxylic acid (3.13, 6.25, 12.5, 25, 50, 100 and 200 μM) in HEPES buffer (30 mM HEPES, 100 mM KCl, pH 7.40). The data were background corrected (HEPES). Then, it was normalised using the highest concentration (200 μM) as 100 % value at the maximum intensity for absorption and fluorescent spectra (755 nm and 790 nm respectively); (c) the extinction coefficient of DY-800 carboxylic acid was calculated by plotting its absorbance at a various concentrations; (d) the chemical structure of DY-800 carboxylic acid.

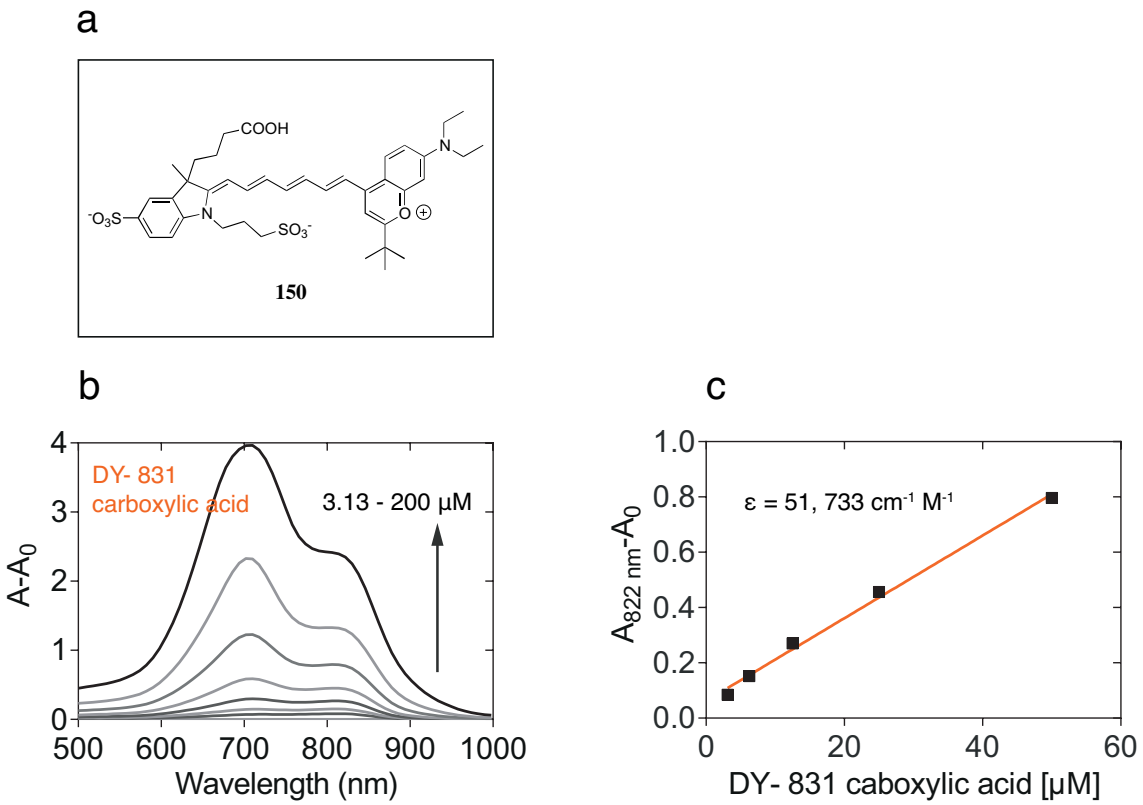

Figure B.5: **Spectroscopic characterisations of DY-831 carboxylic acid.** (a) the chemical structure of DY-831 carboxylic acid; (b) the absorption spectra of DY-831 carboxylic acid (3.13, 6.25, 12.5, 25, 50, 100 and 200 μM) in HEPES buffer (30 mM HEPES, 100 mM KCl, pH 7.40). The data were background corrected (HEPES). (c) the extinction coefficient of DY-831 carboxylic acid was calculated by plotting its absorbance at a various concentrations. DYQ-4 is non-fluorescent.

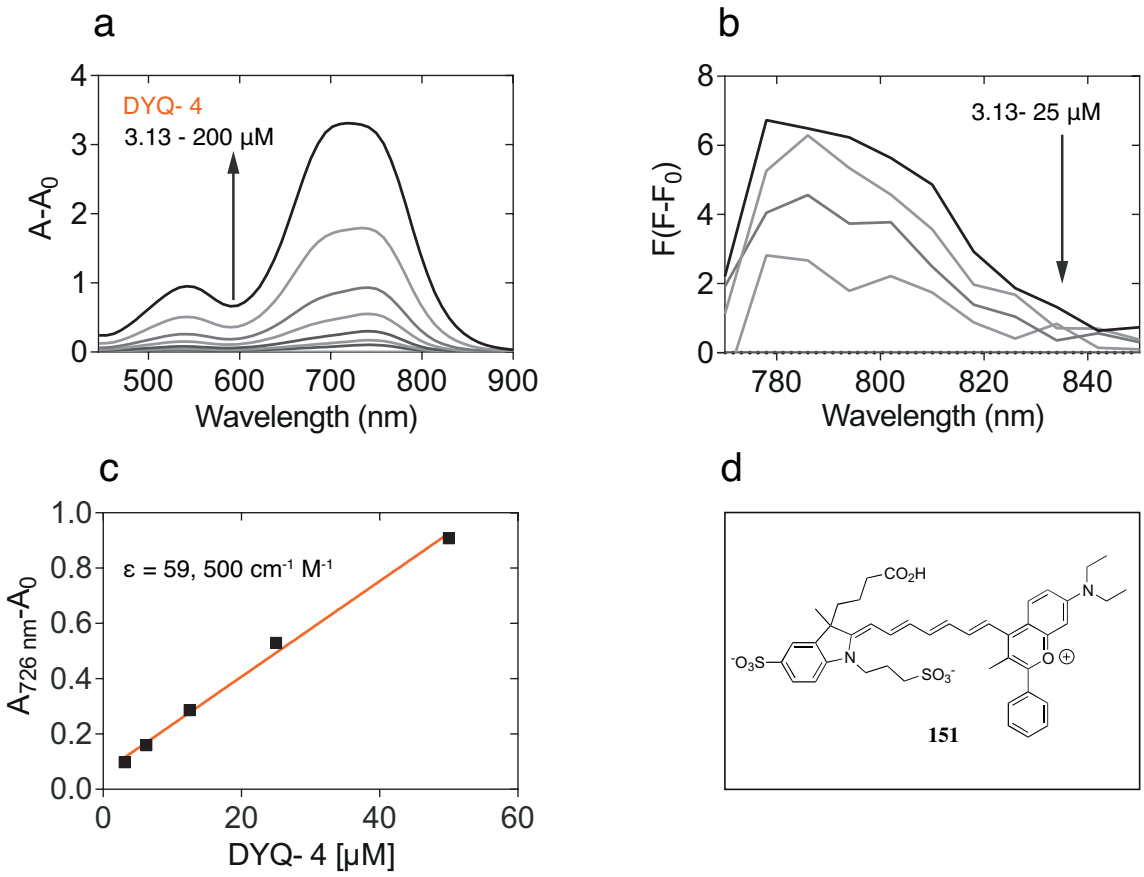

Figure B.6: **Spectroscopic characterisations of DYQ-4 carboxylic acid.** (a) the absorption spectra of DYQ-4 carboxylic acid (3.13, 6.25, 12.5, 25, 50, 100 and 200 μM) in HEPES buffer (30 mM, 100 mM KCl, pH 7.40). The data were background corrected (HEPES). (b) the fluorescent spectra of DYQ-4 carboxylic acid (3.13, 6.25, 12.5, 25 μM) in HEPES buffer (30 mM, 100 mM KCl, pH 7.40). (c) the extinction coefficient of DYQ-4 carboxylic acid was calculated by plotting its absorbance at a various concentrations (3.13, 6.25, 12.5, 25 μM). (d) the chemical structure of DYQ-4.

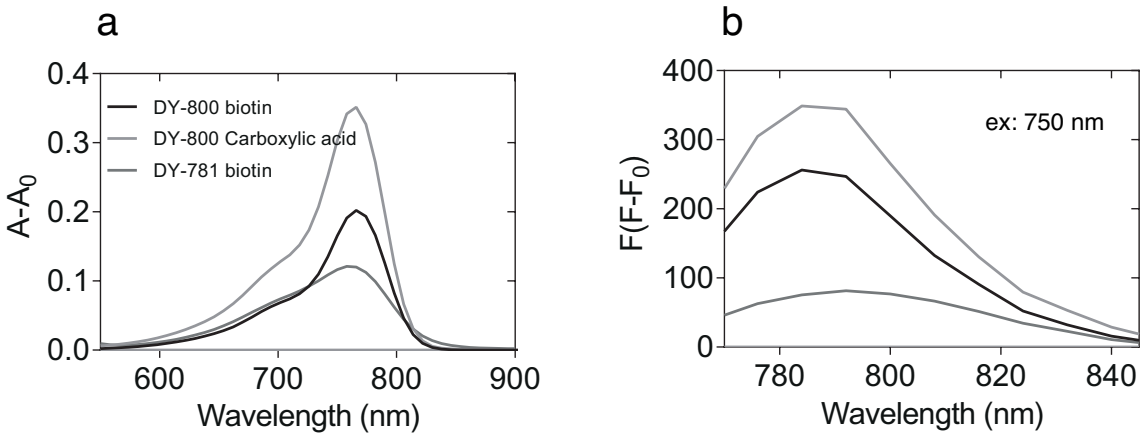

Figure B.7: **Photophysical characterisations of DY-800 biotin, DY-800 carboxylic acid and DY-781.** a) absorption of DY-800 biotin, DY-800 carboxylic acid and DY-781 (5 μM) in MOPS buffer (30 mM, 100 mM KCl, pH 7.40) b) Corresponding fluorescence using excitation at 750 nm.

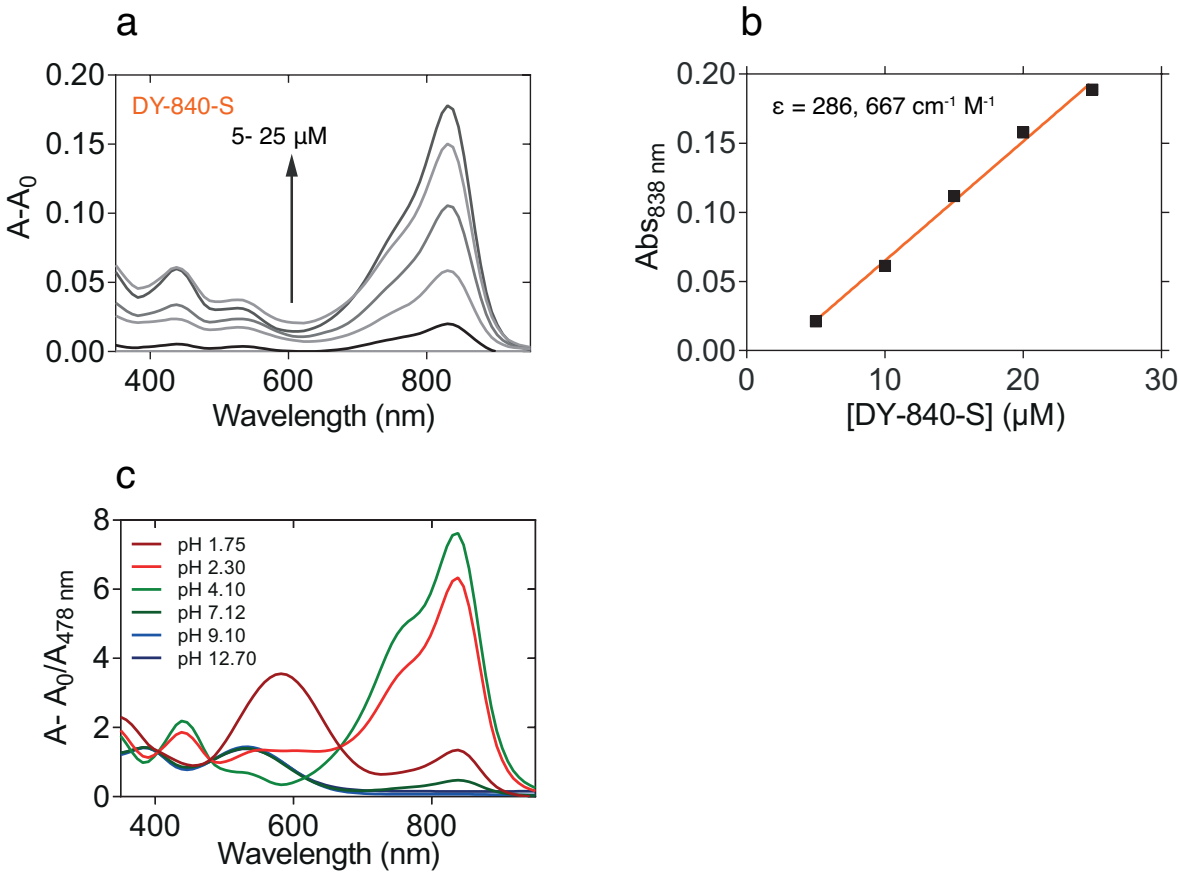

Figure B.8: **Spectroscopic characterisations of DY-840-S.** (a) the absorption spectra of DY-840-S carboxylic acid (5-25 μM) in HEPES buffer (30 mM, 100 mM KCl, pH 7.40). The data were background corrected (HEPES). (b) the extinction coefficient of DY-840-S carboxylic acid was calculated by plotting its absorbance at a various concentrations (5-25 μM). (c) The absorbance of DY-840-S at different pHs (1.75, 2.30, 4.10, 7.12, 9.10, 12.70) varies as shown here. An interesting molecule as a pH sensor for photoacoustic imaging.

B.2 Calcium sensors

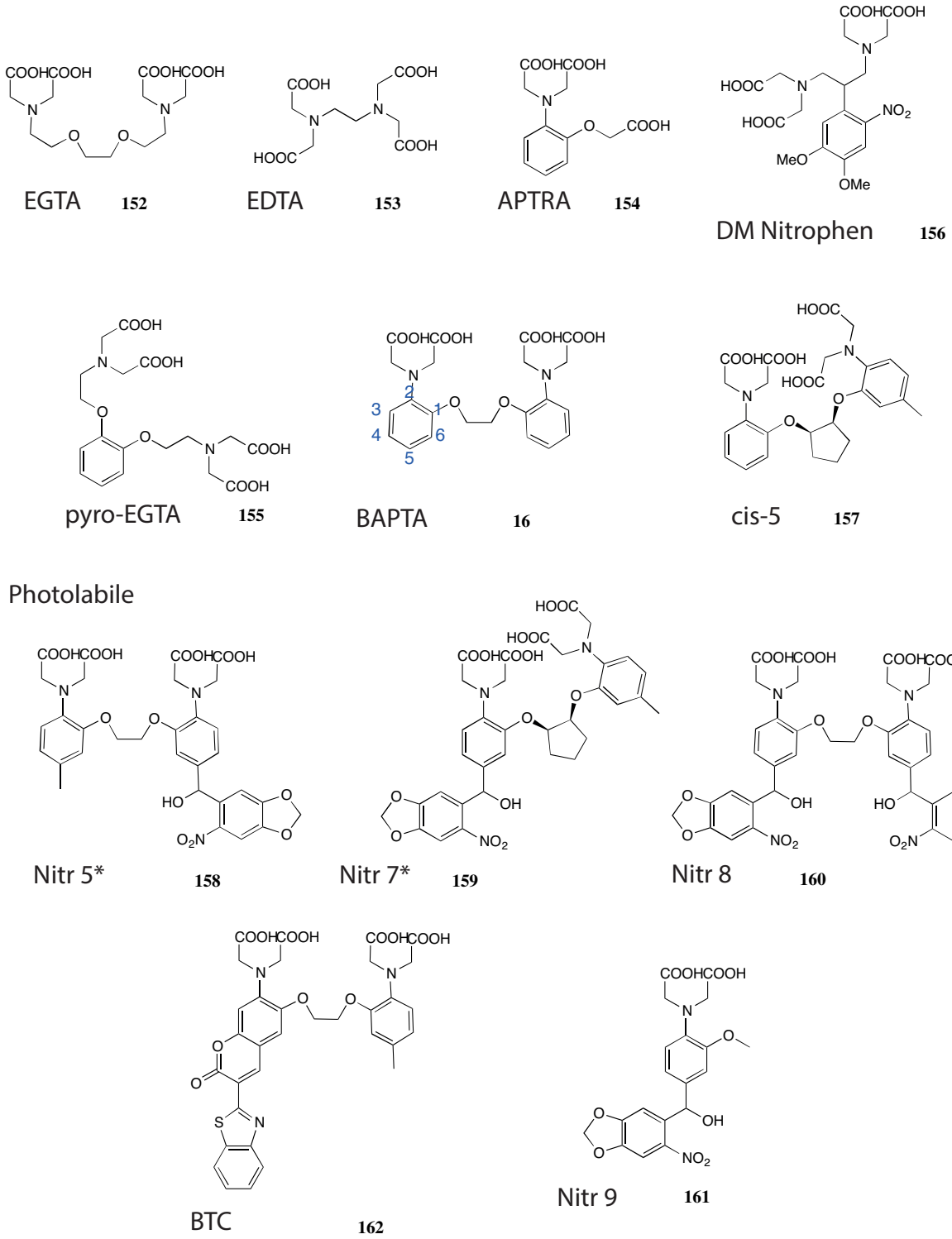

Figure B.9: Small molecule calcium chelators

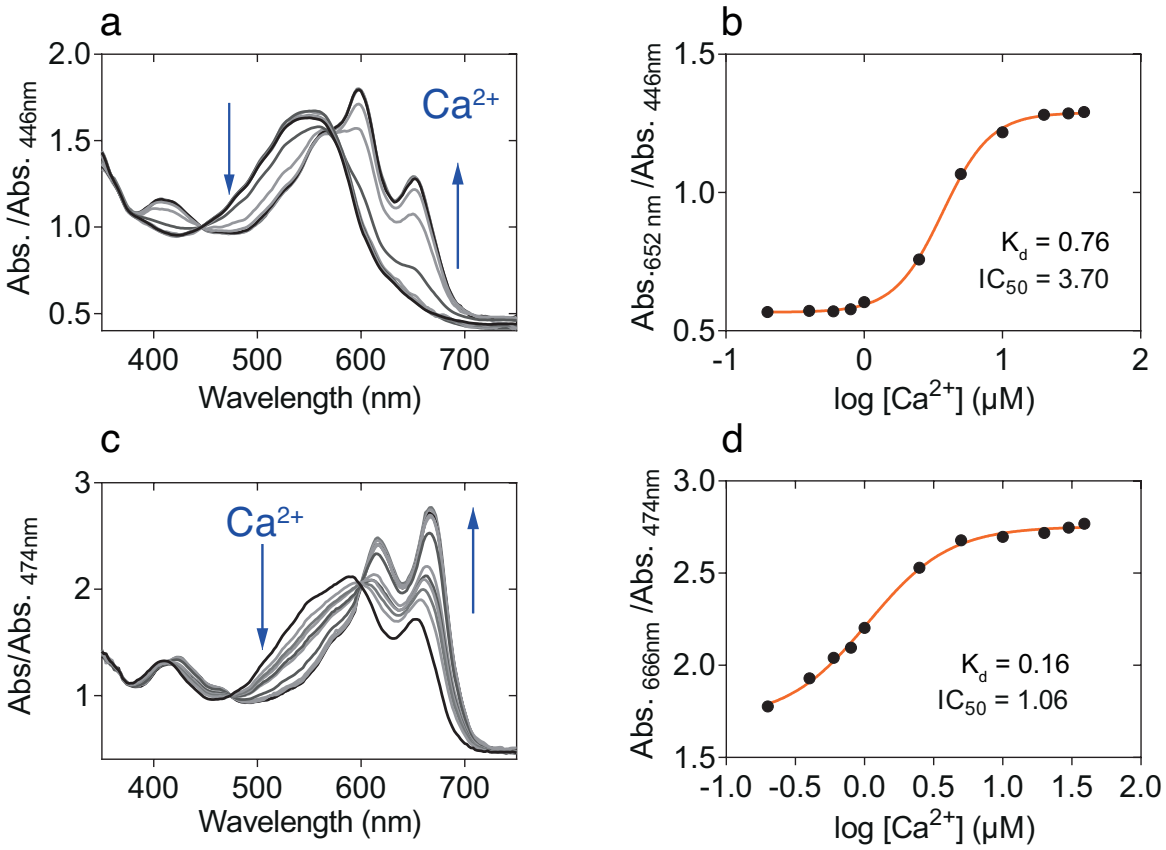

Figure B.10: **Photophysical properties of Arsenazo-III and CPZ-III in the presence of various $[Ca^{2+}]_{free}$ ions.** (a) absorbance change of Arsenazo-III from 350 to 750 nm and increasing calcium ion concentrations (0, 0.2, 0.4, 0.6, 0.8, 1.0, 2.5, 5.0, 10.0, 20.0, 30.0 and 39.0 μM). (b) absorbance response plot of Arsenazo-III at 652 nm, extrapolated IC_{50} (3.70 μM; 95% CI: 0.57- 1.39) and K_d (0.76 μM; 95% CI: 0.07- 1.45). (c) absorbance change of CPZ-III (25 μM) in the presence of increasing $[Ca^{2+}]_{free}$ ions (0, 0.2, 0.4, 0.6, 0.8, 1.0, 2.5, 5.0, 10.0, 20.0, 30.0 and 39.0 μM) (d) absorbance response of CPZ-III plot at 666 nm, extrapolated IC_{50} (1.06 μM; 95% CI: 1.71- 2.75) and K_d (0.82 μM; 95% CI: 0.61- 1.02) values.

High Affinity Ratiometric

Fura Series

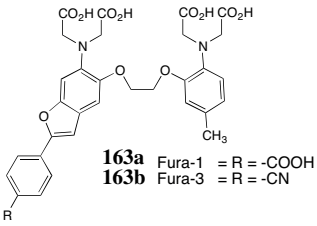

163a Fura-1 = R = -COOH
163b Fura-3 = R = -CN

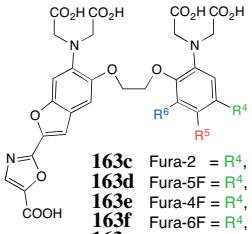

163c Fura-2 = R^4, R^5, R^6 = -H, $-CH_3$, -H
163d Fura-5F = R^4, R^5, R^6 = -H, -F, -H
163e Fura-4F = R^4, R^5, R^6 = -F, -H, -H
163f Fura-6F = R^4, R^5, R^6 = -H, -H, -F
163g Fura-FF = R^4, R^5, R^6 = -H, -F, -F

Fura- Red

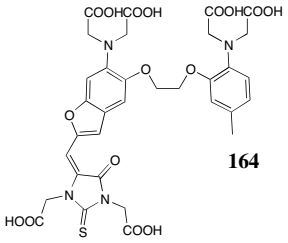

164

High Affinity non-ratiometric

FLUORESCEINS

Fluo Series

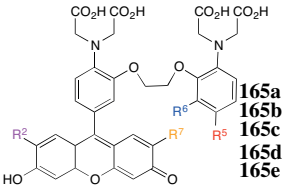

165a Fluo-3 = R^2, R^7, R^5, R^6 = -Cl, -Cl, $-CH_3$, -H
165b Fluo-4 = R^2, R^7, R^5, R^6 = -F, -F, $-CH_3$, -H
165c Fluo-5F = R^2, R^7, R^5, R^6 = -F, -F, -F, -H
165d Fura-5N = R^2, R^7, R^5, R^6 = -F, -F, $-NO_2$, -H
165e Fura-4FF = R^2, R^7, R^5, R^6 = -F, -F, -F, -F

Calcium Green & Oregon Green BAPTA Series

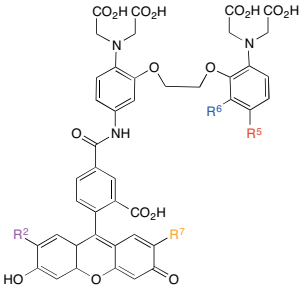

166a Calcium Green-1 = R^2, R^7, R^5, R^6 = -Cl, -Cl, -H, -H
166b Calcium Green-5N = R^2, R^7, R^5, R^6 = -Cl, -Cl, $-NO_2$, -H
167a Oregon Green BAPTA-1 = R^2, R^7, R^5, R^6 = -F, -F, -H, -H
167b Oregon Green BAPTA-6F = R^2, R^7, R^5, R^6 = -F, -F, -H, -F
167c Oregon Green BAPTA-5N = R^2, R^7, R^5, R^6 = -F, -F, $-NO_2$, -H

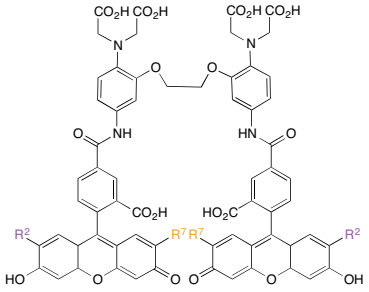

166c Calcium Green-2 = R^2, R^7 = -Cl, -Cl
167d Oregon Green BAPTA-2 = R^2, R^7 = -F, -F

RHODAMINES

Rhodamines

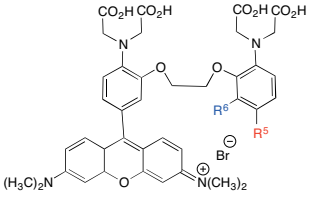

168a Rhod-2 = R^5, R^6 = $-CH_3$, -H
168b Rhod-FF = R^5, R^6 = -F, -F
168c Rhod-5N = R^5, R^6 = $-NO_2$, -H
168d RhoCa-I = R^5, R^6 = -I, -H

X-Rhod-1

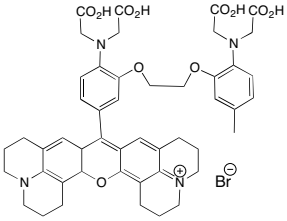

169

Calcium Orange

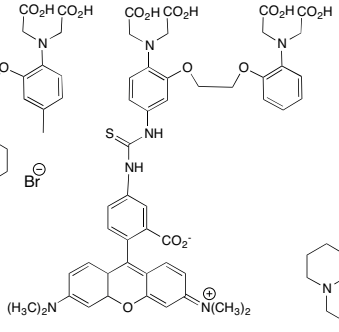

170

Calcium Crimson

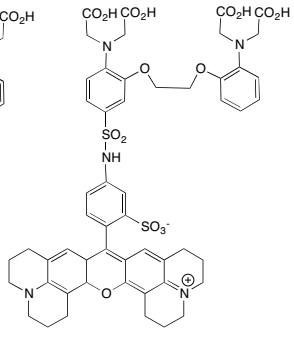

171

Scheme B.1: High ratiometric and non- ratiometric calcium indicators

Low Affinity

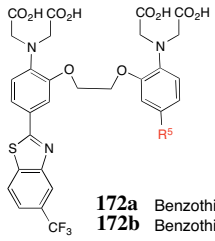

172a Benzothiaza-1 = R^5 = -CH_3
172b Benzothiaza-2 = R^5 = -F

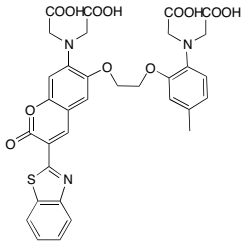

BTC **173**

Symmetric

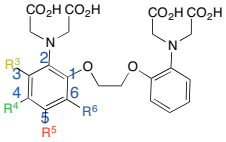

173a BAPTA = -R^3, R^4, R^5, R^6 = -H, -H, -H, -H
173b 3F-BAPTA = -R^3, R^4, R^5, R^6 = -F, -H, -H, -H
173c 4F-BAPTA = -R^3, R^4, R^5, R^6 = -H, -F, -H, -H
173d 5F-BAPTA = -R^3, R^4, R^5, R^6 = -H, -H, -F, -H
173e 5Cl-BAPTA = -R^3, R^4, R^5, R^6 = -H, -H, -Cl, -H
173f 6F-BAPTA = -R^3, R^4, R^5, R^6 = -H, -H, -H, -F
173g FF-BAPTA = -R^3, R^4, R^5, R^6 = -H, -H, -F, -F
173h Br-BAPTA = -R^3, R^4, R^5, R^6 = -H, -H, -Br, -H
173i CH_3-BAPTA = -R^3, R^4, R^5, R^6 = -H, -H, -CH_3, -H

Scheme B.2: Low affinity calcium indicators

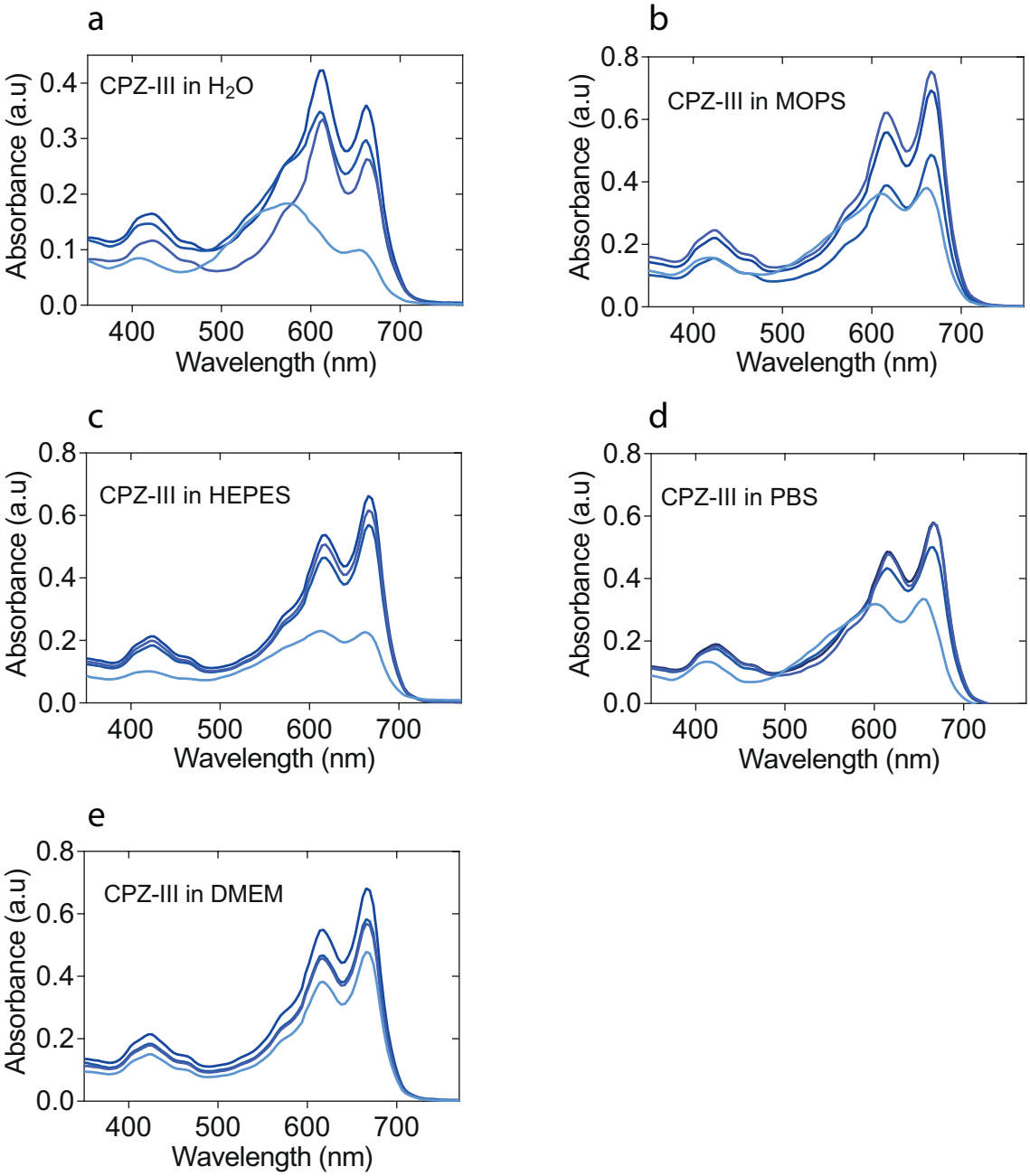

Figure B.11: **Photophysical characterisation of CPZ-III in various biological buffers.** CPZ-III (25 μM) in H_2O and various relevant biological buffers (MOPS, HEPES, PBS and DMEM) in the presence of various Ca^{2+} (0, 25, 50 and 500 μM)

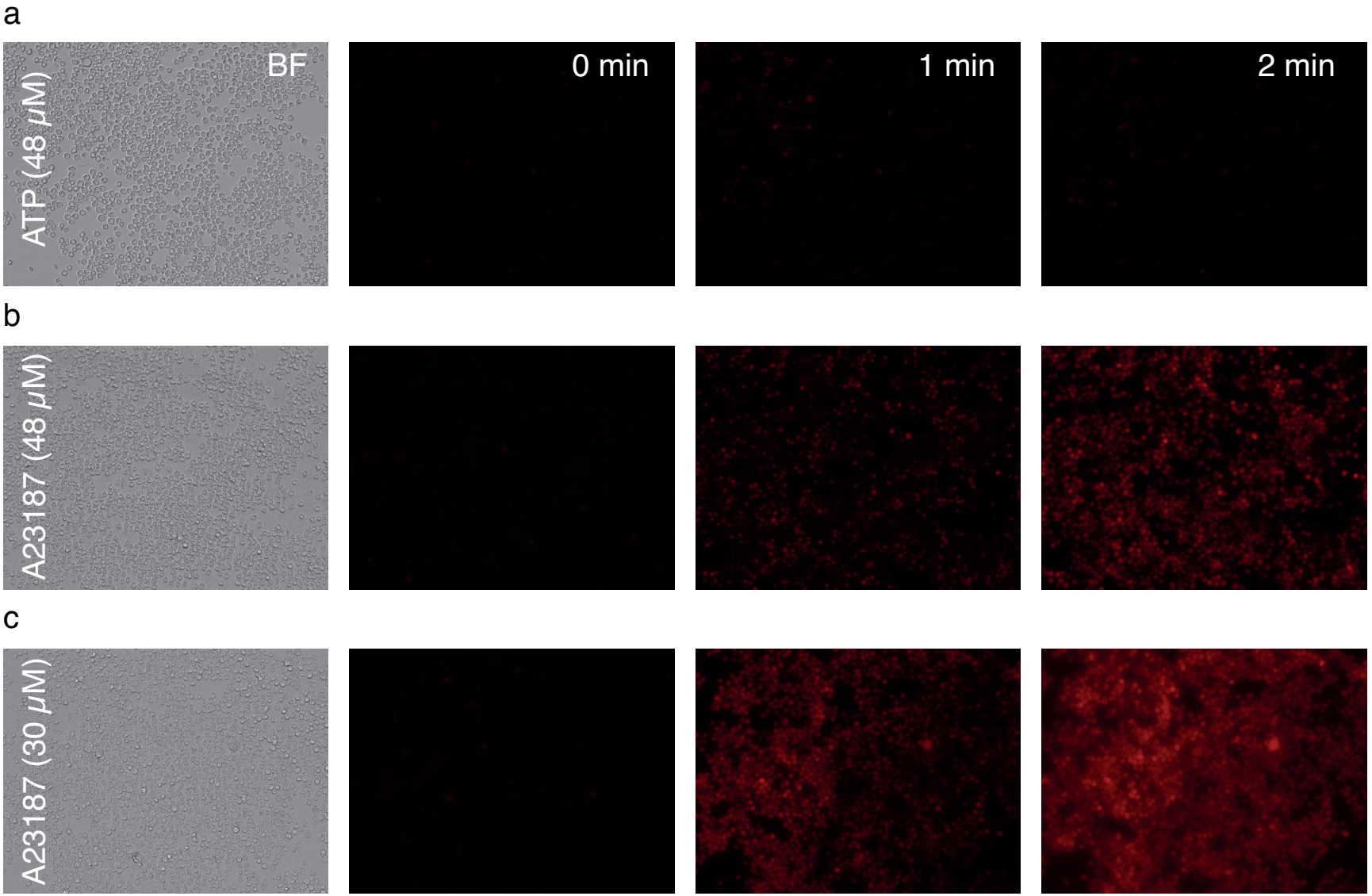

Figure B.12: **Increase intracellular calcium transients in Rhod-3 AM labelled ANA-1 macrophages.** A basal level calcium image of Rhod-3 AM labelled ANA-1 was taken at 0 timepoint. ANA-1 was stimulated with 48 μM ATP (a), 48 μM (b) and 30 μ (c) calcium ionohore, A23187. An image of the same field of cells is shown at various times after stimulation. The signal intensity increases as the intracellular calcium concentration increases. This was to show we could use A23187 ionophore and ATP (known calcium stimulants) to trigger calcium influxes.

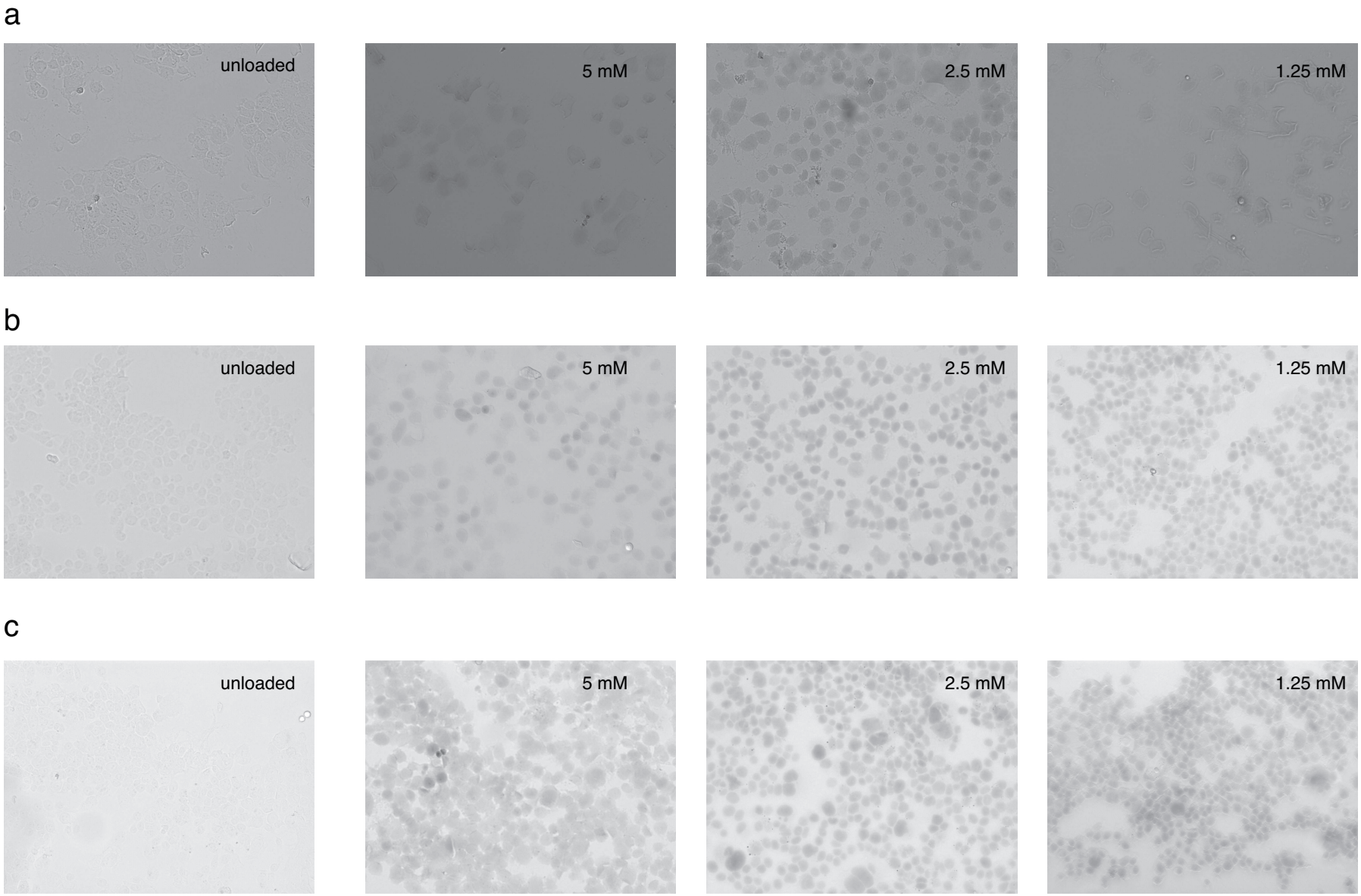

Figure B.13: **HEK293 cells incubated with CPZ-III.** The concentrations used for incubating HEK293 cells with CPZ-III are 5 mM, 2.5 mM and 1.25 mM for (a) 10 mins (b) 20 mins (c) 30 mins. A clear CPZ-III staining were observed even after 10 mins of incubation time.

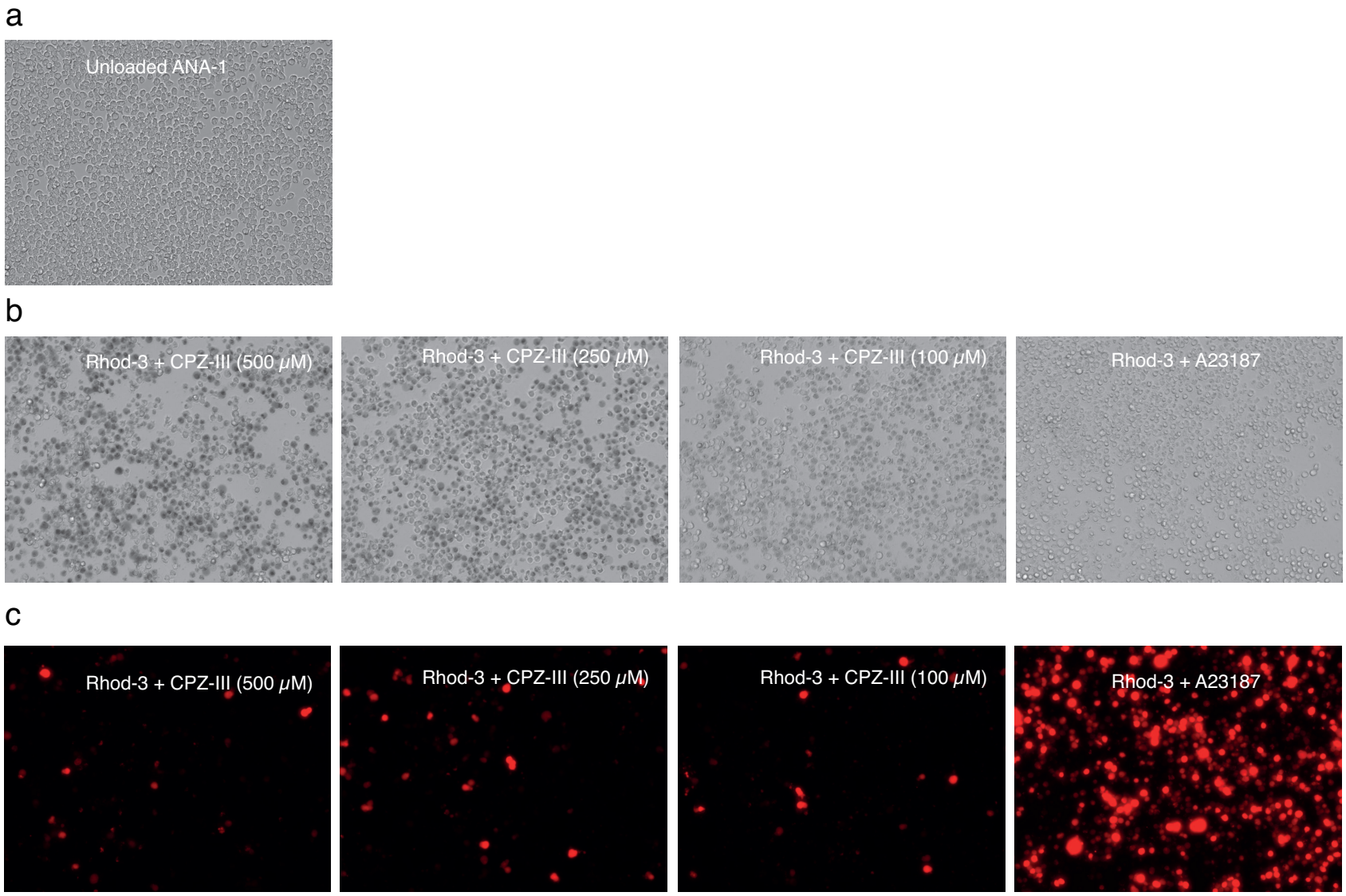

Figure B.14: **ANA-1 macrophages incubated with CPZ-III.** (a) control, unloaded ANA-1 macrophages. (b) ANA-1 macrophages were incubated with varying amounts of CPZ-III (500 μM, 250 μM, 100 μM and *left to right*) together with calcium indicator Rhod-3 AM (10 μ)M for 18 h. We have similar data for 6 h incubation time period.

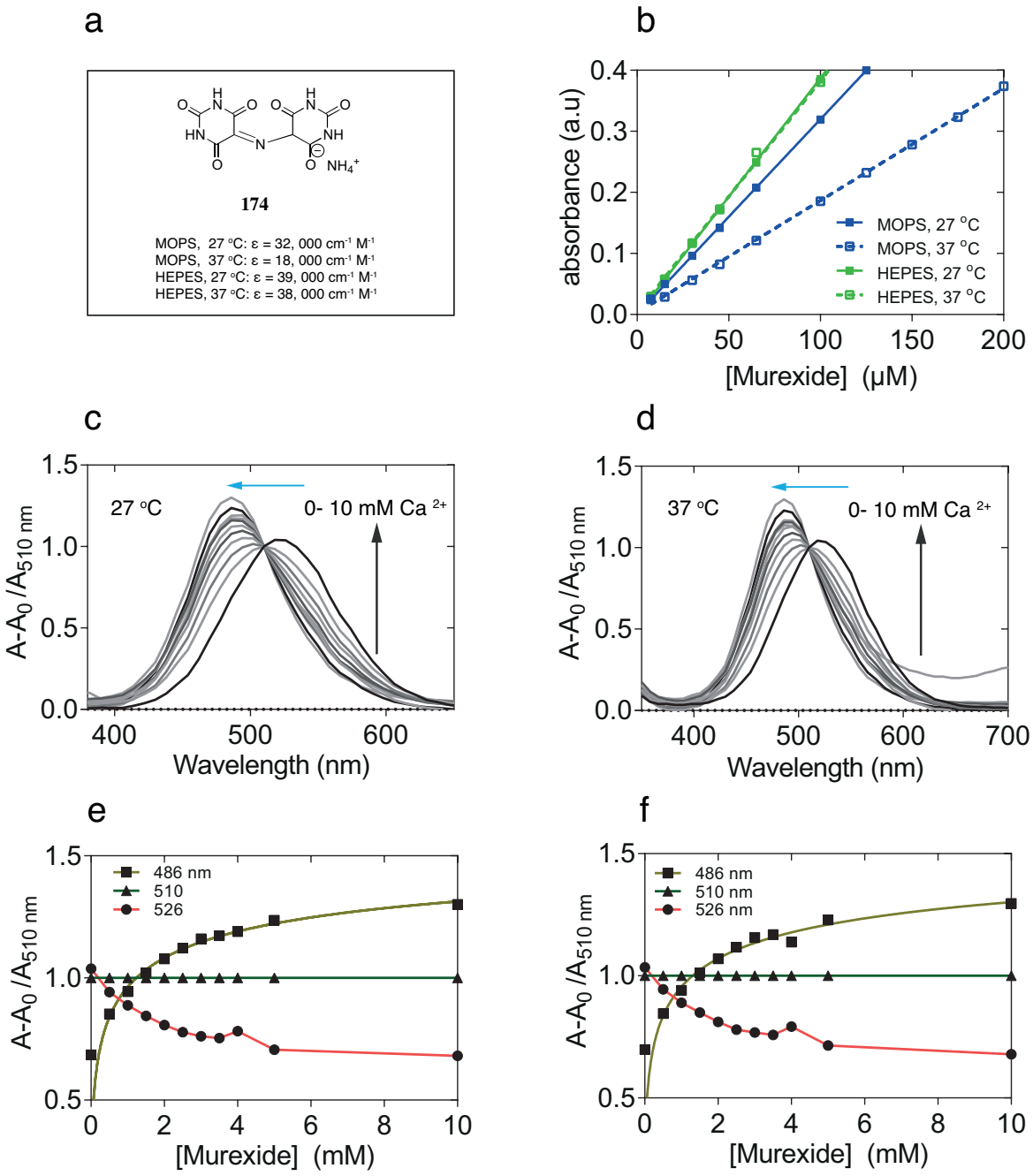

Figure B.15: **Spectroscopic characterisations of Murexide.** (a) the chemical structure of murexide; (b) molar extinction coefficient of murexide at two different temperatures, 27 ^{o}C (solid lines) and 37 ^{o}C (broken lines) in either HEPES (green lines) or MOPS (blue lines) buffer. Absorbance at 525 nm was obtained and plotted with a dilution series of murexide (7.5, 15.0, 30.0, 45.0, 65.0, 100.0, 125.0, 150.0, 175.0 and 200.0 μM). In all series, volume and path length were 100 μM and 0.30 cm respectively; (c/d) Absorption spectra of murexide (15 μM, pH 7.20, 27 ^{o}C (c) and 37 ^{o}C (d)) and its response in the presence of various calcium concentrations (0-10 mM). The data were background corrected and normalised at 510 nm; (e/f) Selectivity of murexide towards calcium.

Appendix C

Calcium Selective Photoacoustic Agent (CaSPA-550)

C.1 Supporting Information

[h]

Table C.1: **Photophysical properties of CaSPA-550 in MOPS buffer**

Compound	ε (M^{-1} cm^{-1})	λ_{abs} (nm)	**QY**
CaSPA-550 + 0 $[Ca^{2+}]_f$	77, 745	550	0.01[a]
CaSPA-550 + 39 $[Ca^{2+}]_f$	27, 463	550	0.01[a]
CaSPA-550 AM	116, 000	590	[b]

[a] Quantum efficiencies determined in MOPS buffer according to the calcium calibration kit

[b] MOPS buffer (pH 7.25), prepared from chelex-100 treated

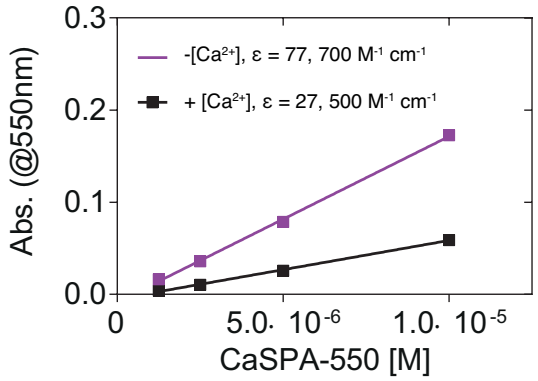

Figure C.1: **Molar extinction coefficient of CaSPA-550 with and without Ca^{2+}. Purple line:** Absorbance obtained at 550 nm with the dilution series of CaSPA-550 (pH 7.40, 296 K) measured without calcium ions. **Black line:** Absorbance obtained at 550 nm with the dilution series of CaSPA-550 (μM, pH 7.40, 294 K) measured with calcium ions. In all series, volume and path lengths were 100 μL and 0.3 cm respectively.

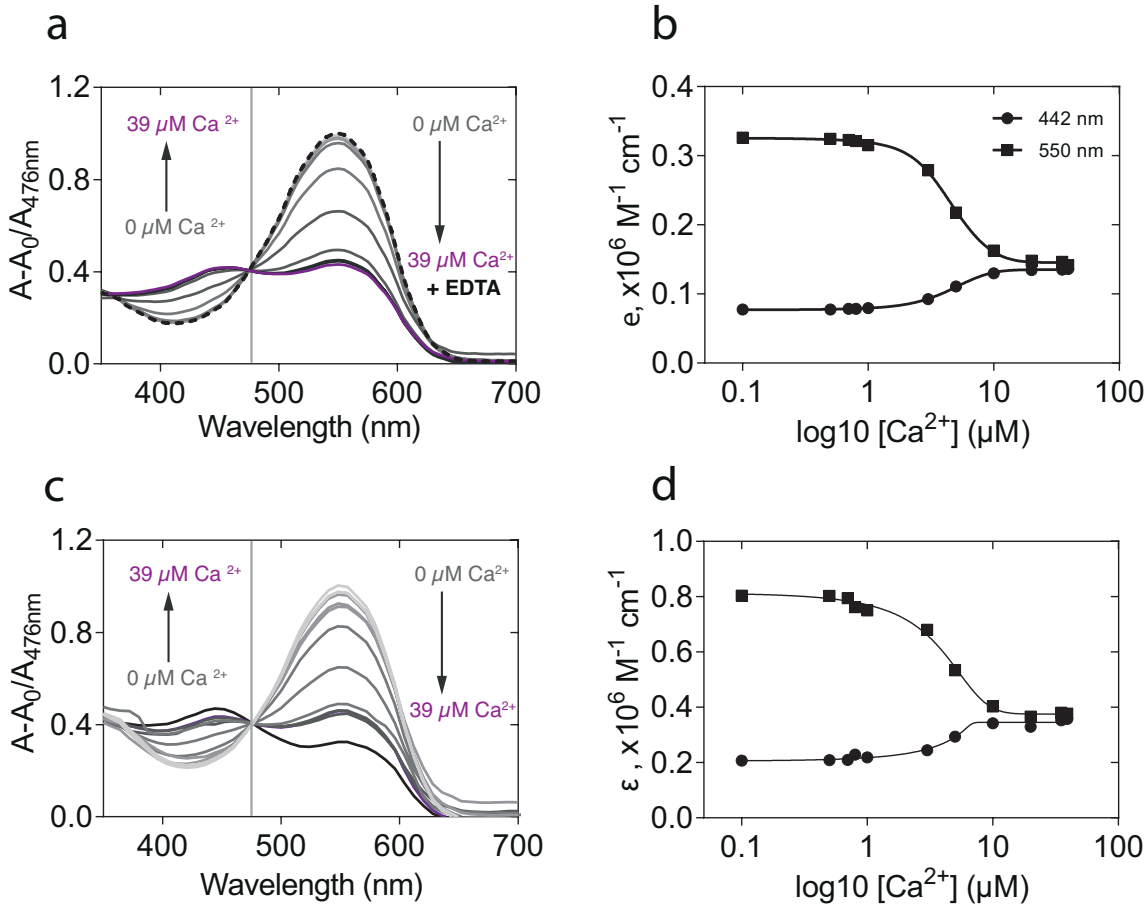

Figure C.2: **Spectroscopic characterisation of CaSPA-550 in 30 mM MOPS solutions.** Representative absorption and emission spectra of CaSPA-550 (10 μM and 25 μM) in the absence and presence of various concentrations of calcium ions to determine Ca^{2+} sensitivity (0, 0.1, 0.5, 0.7, 0.8, 1.0, 3.0, 5.0, 10.0, 20.0, 35.0, 39 μM free calcium ions and 5 mM calcium ions). The addition of 10 mM EDTA competes out the 39 μM Ca^{2+} from CaSPA-550 and reverts back to the original signal intensity comparable to 0 Ca^{2+}-free (broken black line in spectra a). Spectra a and c were background corrected (A-$A_{MOPSonly}$) and normalised at isosbestic point (475 nm) intensity, then represented as a scale from 0-1 using absorption spectra maxima intensity at 0 Ca^{2+}-free indicator after (100%).

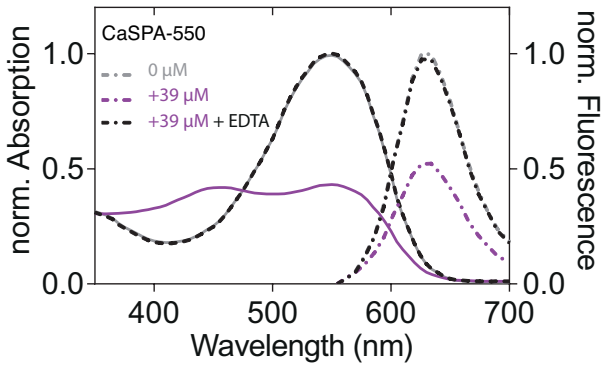

Figure C.3: **Absorbance and fluorescence of CaSPA-550 in 30 mM MOPS solutions.** Absorbance and fluorescence spectra of CaSPA-550, **118** (25 μM, pH 7.40, 294 K) were obtained at 0 and 39 μM Ca^{2+}-free ions. The absorption maxima was obtained at 550 nm and fluorescence maxima at 630 nm (excitation: 540 nm). The Stokes shift is 80 nm. Absorbance data were background corrected (A-$A_{MOPSonly}$) and normalised at isosbestic point (475 nm), then represented as a scale from 0-1 using the absorption spectra maxima intensity at 0 Ca^{2+}-free indicator as 100% value. Fluorescence data were background corrected (F-$F_{MOPSonly}$) and normalised at 780 nm (0 fluorescence), then represented as a scale from 0-1 using the fluorescence spectra maxima intensity at 0 Ca^{2+}-free indicator as 100% value.

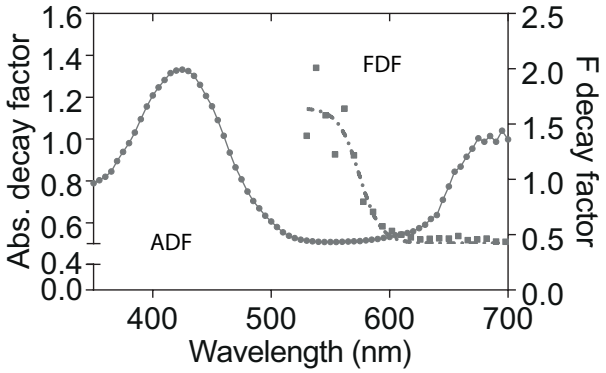

Figure C.4: **Absorption and fluorescence decay factor (ADF and FDF respectively) of CaSPA-550 as a function of its excitation wavelength.** The ADF the ratio of absorption intensities of the excitation spectra under Ca^{2+}-saturation and Ca^{2+}-free conditions. The FDF is the ratio of fluorescence intensities of the excitation spectra under Ca^{2+}-saturation and Ca^{2+}-free conditions. The maximum ADF and FDF achieved for CaSPA-550. ADF and FSF were analysed from Fig. C.3 data.

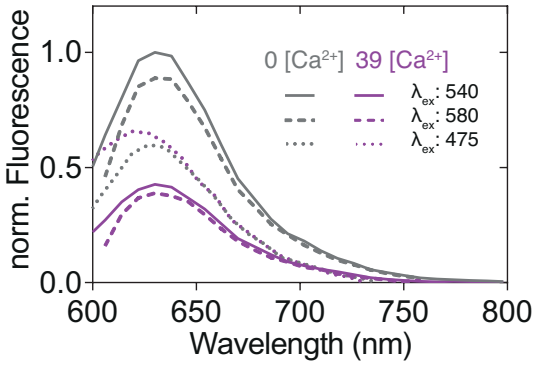

Figure C.5: **Emission spectra of CaSPA-550 at varying excitation wavelengths.** Representative emission spectra of Ca^{2+}-free (grey lines) and Ca^{2+}-bound (purple lines) of CaSPA-550 in calibration buffers containing either 0 or 39 μM $[Ca^{2+}]_{free}$ ions. The fluorescence were collected at 630 nm at various excitation wavelengths: 474 (dotted lines), 540 (solid lines) and 580 nm (dash lines). The spectra were background corrected (F-F_{MOPS}) and normalised to the maximum emission of Ca^{2+}-free CaSPA-550 excited at 540 nm.

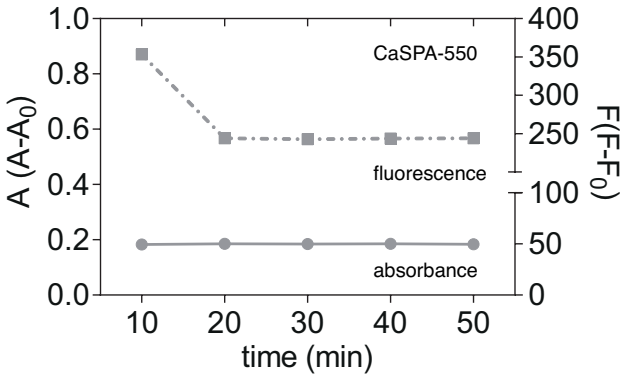

Figure C.6: **Stability studies of CaSPA-550 in MOPS buffer with time.** Absorbance and fluorescence at 550 nm and 630 nm in 30 mM MOPS buffer (20 μM CaSPA-550, pH 7.20, 294 K). The sample was irradiated repeatedly (5x) at time intervals of 10 mins with x% light intensity. The absorbance and fluorescence signal change over time (50 min) was $\leq$ 1% and 31% respectively.

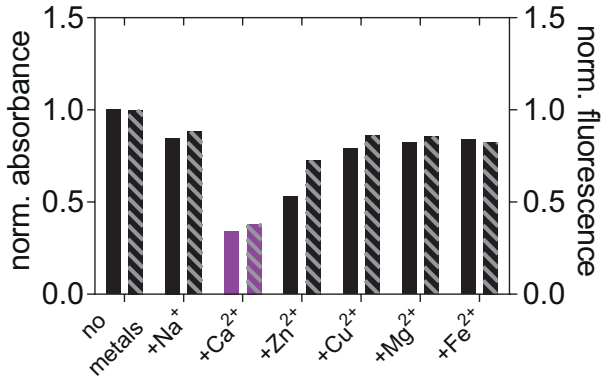

Figure C.7: **Spectroscopic determination of CaSPA-550 to determine its selectivity for Ca^{2+} over other biologically relevant mono-, di- and tri-valent cations.** Peak absorption (550 nm, filled bars) and fluorescent maxima (630 nm, striped bars) measured from CaSPA-550 (20 μM) with no metals and upon addition of 50 μM [Na^{+}], [Ca^{2+}], [Zn^{2+}], [Cu^{2+}], [Mg^{2+}] and [Fe^{3+}] in 30 mM MOPS buffer (100 mM KCl, pH 7.80, 310 K). The data were normalised as a scale from 0-1 using the absorption maxima intensity and fluorescence maxima intensity at no metals as 100% value.

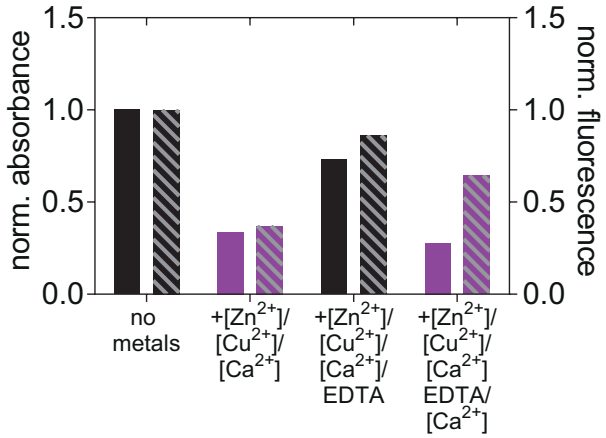

Figure C.8: **Spectroscopic determination of CaSPA-550 to determine its selectivity in the presence of biologically relevant divalent metal mixtures.** Peak absorption (550 nm, filled bars) and fluorescent maxima (630 nm, striped bars) measured from CaSPA-550 (20 μM) in 30 mM MOPS (100 mM KCl, pH 7.80, 310 K) with no metals and upon addition of 50 μM (2.5 equiv.) each of [Zn^{2+}]/[Cu^{2+}]/[Ca^{2+}] mixtures, after subsequent addition of 300 μM EDTA. Absorption was further measured from an exact sample preparations with a subsequent addition of 100 mM [Ca^{2+}]. Data were normalised as a scale from 0-1 using the absorption maxima intensity and fluorescence spectra intensity at no metals as 100% value.

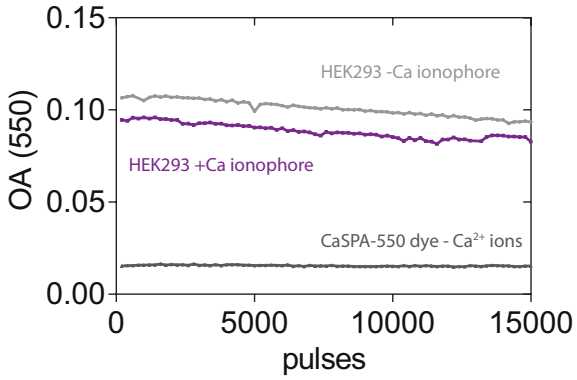

Figure C.9: **Photobleaching assessment of CaSPA-550 and CaSPA-550 loaded HEK293 cells in photoacoustic system.** CaSPA-550 in MOPS solution (2 μM, pH 7.20, 310 K) and CaSPA-550 AM (2 μM, pH 7.20, 310 K, 30 mins incubation at 5% CO_2) loaded HEK293 cells subjected to 15,000 laser pulses (550 nm).

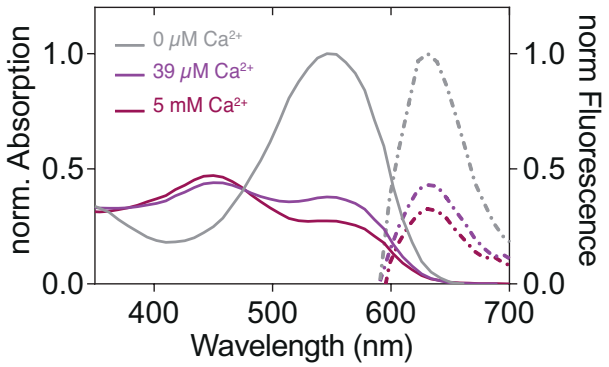

Figure C.10: **Absorbance and fluorescence of CaSPA-550 in 30 mM MOPS solutions with excess Ca^{2+} ions.** Absorbance and fluorescence spectra of CaSPA-550, **118** (25 μM, pH 7.40, 294 K) were obtained at 0 (25 μM CaSPA-550, 30 mM MOPS, 100 KCl, 10 mM EGTA, pH 7.20, 294 K), 39 μM Ca^{2+}-free ions (25 μM CaSPA-550, 30 mM, 100 KCl, 10 mM CaEGTA, pH 7.20, 294 K) and 5 mM Ca^{2+} ions (25 μM CaSPA-550, 30 mM MOPS, chelex-treated H_2O, 100 mM KCl, pH 7.25, 294K). The absorption maxima was obtained at 550 nm and fluorescence maxima at 630 nm (excitation: 540 nm). The Stokes shift is 80 nm. Absorbance data were background corrected (A-$A_{MOPSonly}$) and normalised at isosbestic point (475 nm), then represented as a scale from 0-1 using the absorption spectra maxima intensity at 0 Ca^{2+}-free indicator as 100% value. Fluorescence data were background corrected (F-$F_{MOPSonly}$) and normalised at 780 nm (0 fluorescence), then represented as a scale from 0-1 using the fluorescence spectra maxima intensity at 0 Ca^{2+}-free indicator as 100% value.

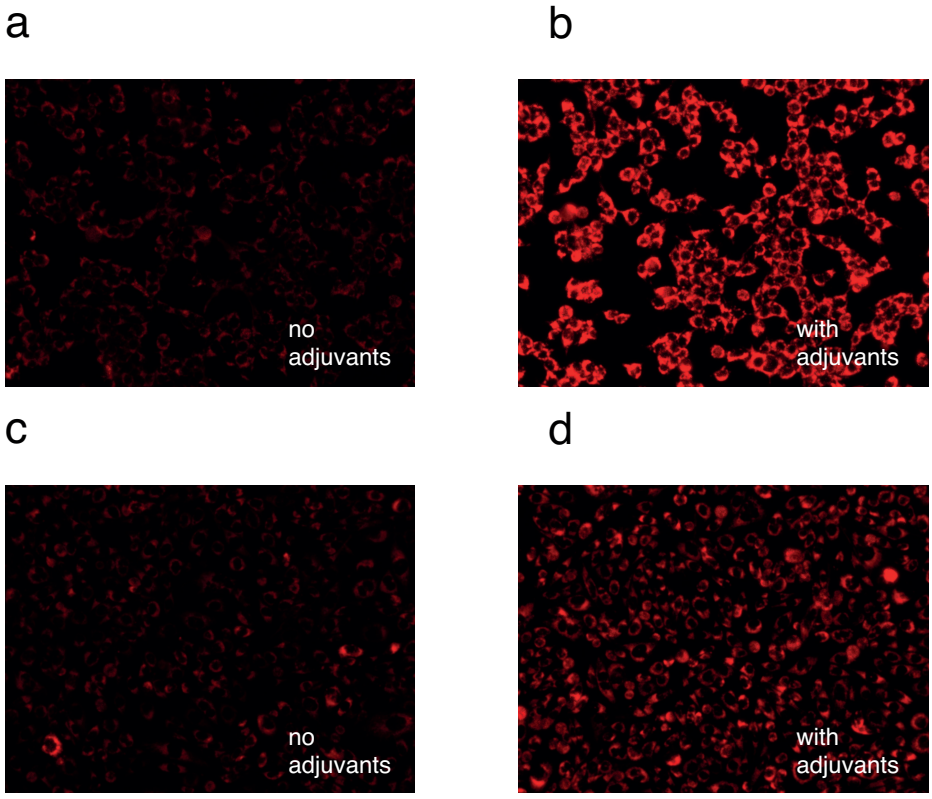

Figure C.11: **Fluorescent images of HEK293 and Chinese hamster ovarian (CHO) cells incubated with CaSPA-550 AM without and without adjuvants.** HEK293 cells were incubated with CaSPA-550 AM (1 μM, 30 min, pH 7.20, 37 ^{o}C) in HBSS formulation without adjuvants (a) and with adjuvants (2.5 mM Probeneacid and 2.5 mM Powerload concentrate) (b). CHO cells were loaded with CaSPA-550 AM (1 μM, 30 min, pH 7.20, 37 ^{o}C) in HBSS formulation with adjuvants (c) and with adjuvants (2.5 mM Probeneacid and 2.5 mM Powerload concentrate) (d). All cells were excited using the EVOS RFP light cube (593/40 nm) and were taken in optical windows (red filter) between 593 - 643 nm.

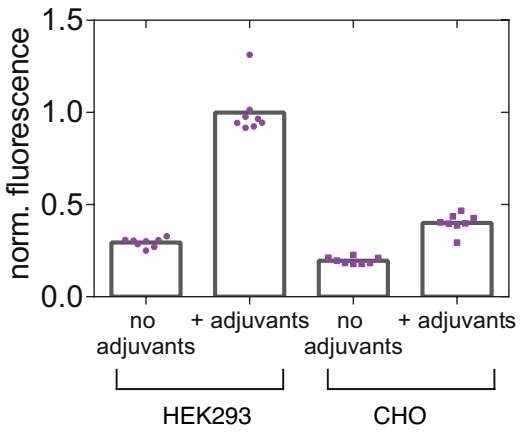

Figure C.12: **Quantitative fluorescence analysis of HEK293 and chinese hamster ovarian (CHO) cells incubated with CaSPA-550 AM with and without adjuvants.** From a fluorescent image, eight cell cluster regions were taken. Each dot plot is the mean of four independent experiments (background corrected). The box plot represents the overall mean of the clusters (8x). Fluorescence is 71% greater in the presence of adjuvants in HEK293 loaded cells as compared to its absence. Fluorescence is 50% greater in the presence of adjuvants in CHO loaded cells as compared to its absence. Representative and selected images with described loading procedure of cells are shown and described in Fig. C.11.

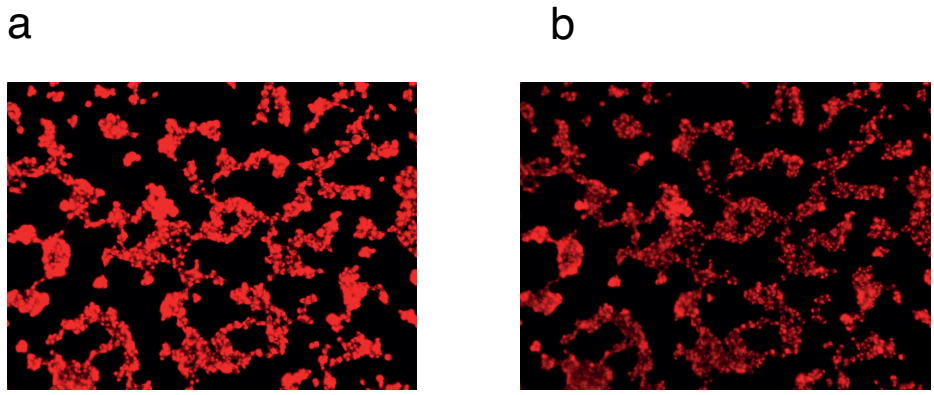

Figure C.13: **Fluorescent images of HEK293 cells incubated with CaSPA-550 AM before and after addition of calcium ionophore.** HEK293 cells were incubated with CaSPA-550 AM (2 μM, pH 7.20, 30 min, 37 ^{o}C) in HBSS buffer. (a) HEK293 cells were imaged before (0 sec. timepoint) and (b) after the addition (60 sec. timepoint) of calcium ionophore (10 μM, Br-A23187). Quantitative fluorescence analysis is found in Fig. C.14

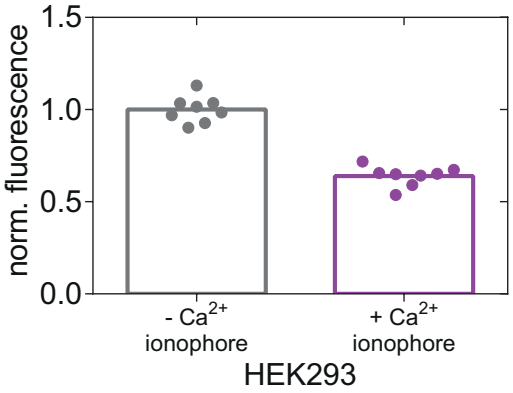

Figure C.14: **Quantitative fluorescence of HEK293 cell clusters before and after the addition of calcium ionophore.** There are eight HEK293 cell cluster regions taken from a fluorescent image. Each dot plot is the mean of three independent experiments (background corrected). The box plot represents the mean of the clusters (8x). Data were taken from before (0 timepoint) and after (60 sec timepoint) the addition of calcium ionophore (Br-A23187) with a mean decrease in fluorescence of 36%. Data were normalised to the box plot mean at -Ca^{2+} ionophore as 100% value. Representative and selected images with described loading procedure of cells are shown in Fig. C.13

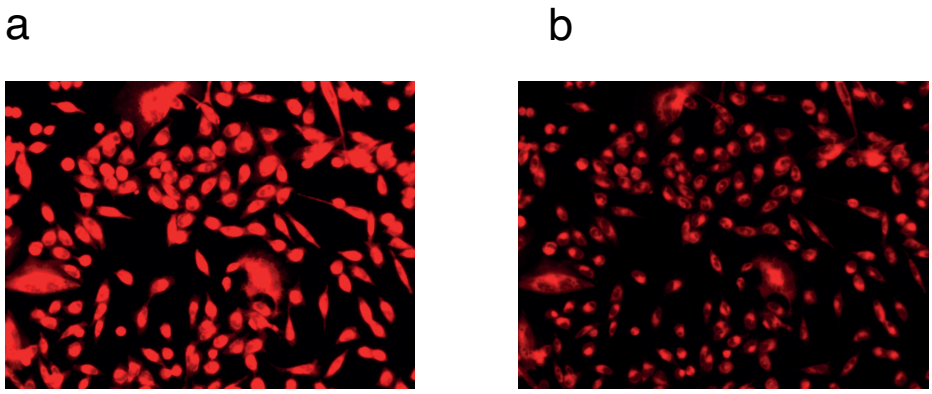

Figure C.15: **Fluorescent images of Chinese hamster ovarian cells (CHO) incubated with CaSPA-550 AM before and after addition of calcium ionophore.** CHO cells were incubated with CaSPA-550 AM (2 μM, pH 7.20, 30 min, 37 ^{o}C) in HBSS buffer. (a) CHO cells were imaged before (0 sec. timepoint) and (b) after the addition (60 sec. timepoint) of calcium ionophore (10 μM, Br-A23187). Quantitative fluorescence analysis is found in Fig. C.16

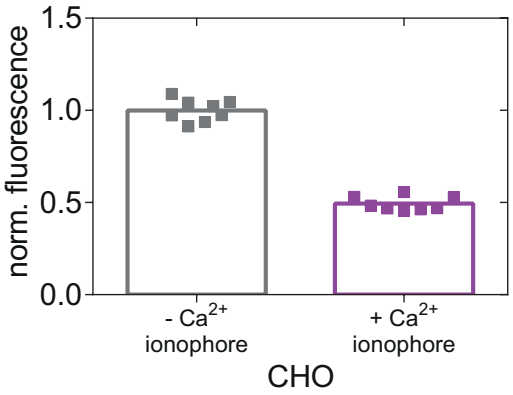

Figure C.16: **Quantitative fluorescence of chinese hamster ovarian (CHO) cell clusters before and after the addition of calcium ionophore.** There are eight CHO cell cluster regions taken from a fluorescent image. Each dot plot is the mean of three independent experiments (background corrected). The box plot represents the mean of the clusters (8x). Data were taken from before (0 timepoint) and after (60 sec timepoint) the addition of calcium ionophore (Br-A23187) with a mean decrease in fluorescence of 51%. Data were normalised to the box plot mean at -Ca^{2+} ionophore at 100% value. Representative and selected images with described loading procedure of cells are shown in Fig. C.15

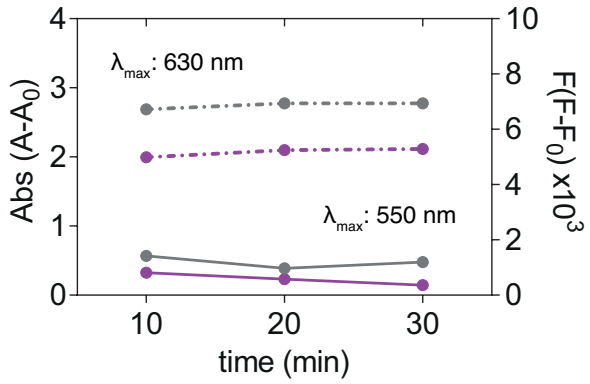

Figure C.17: ***In cellulo* stability studies of CaSPA-550 in HEK293 cells.** Absorbance (solid lines) and fluorescence emission (broken lines) of HEK293 cells loaded with CaSPA-550 AM in HBSS buffer (2 μM CaSPA-550 AM, pH 7.20, 30 min, 37 ^{o}C) without (grey lines) and with calcium ionophore (10 μM Br-A23187, purple lines). The sample was irradiated repeatedly (3x) at time intervals of 10 mins. The absorption signal change over time (30 min) with no calcium ionophore was 16% and 55% with calcium ionophore. There was no fluorescence signal change over time (30 min) with no calcium ionophore nor in the presence of calcium ionophore.

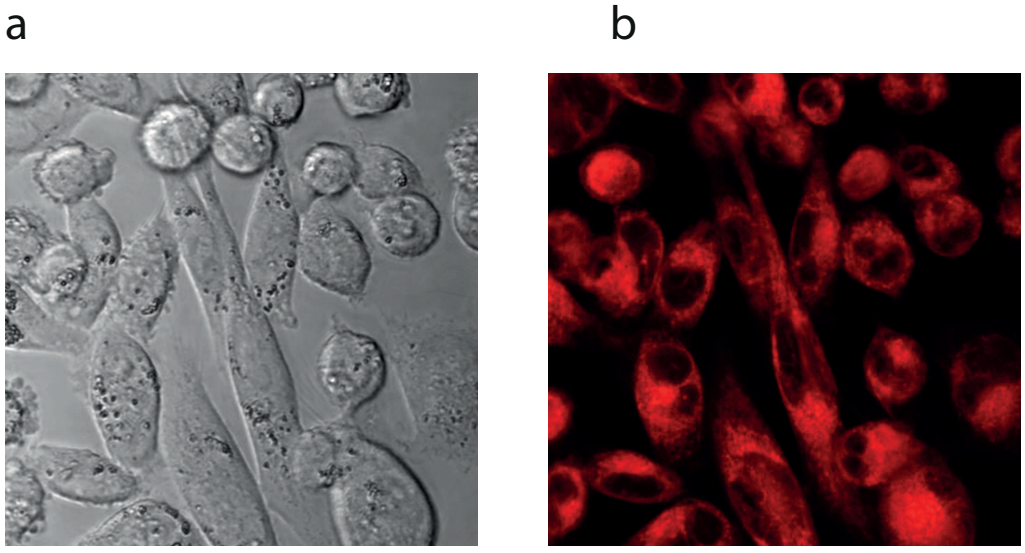

Figure C.18: **Representative confocal microscopy image of Chinese hamster ovarian (CHO) cells loaded with CaSPA-550 AM.** CHO cells were incubated with CaSPA-550 AM (2 μM, pH 7.40, 3 h, 37 ^{o}C, 5% CO_2). Phase-contrast as well as fluorescent images were taken on a confocal microscope (Leica SP5).

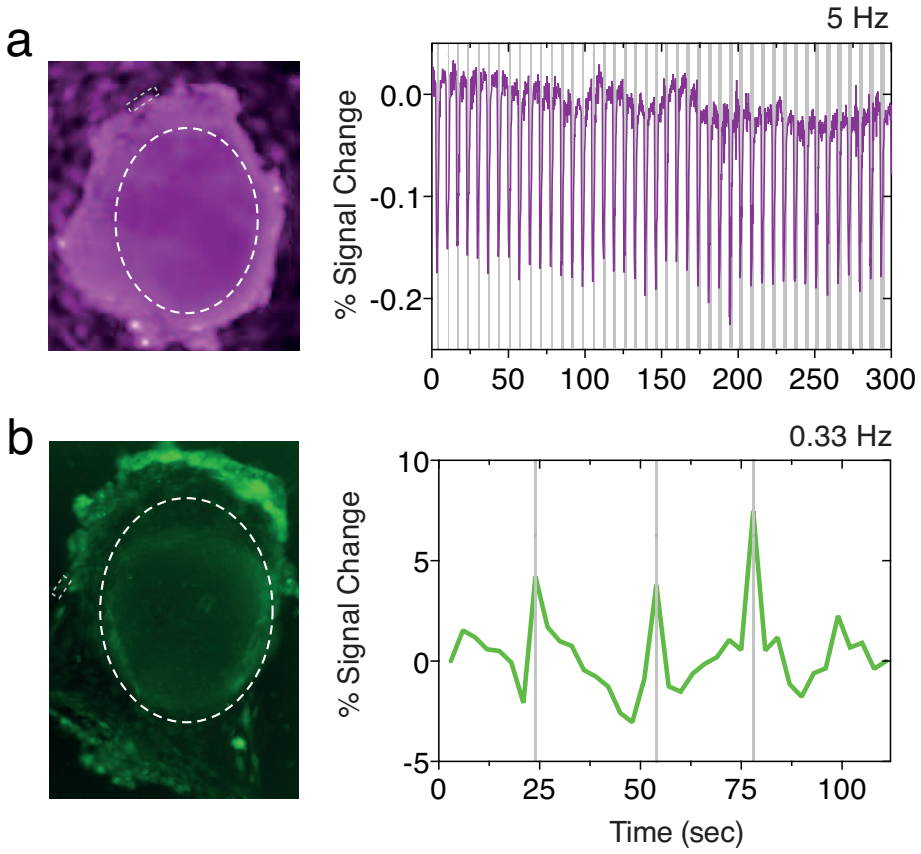

Figure C.19: **Fluorescence Ca^{2+} imaging of heart organoids.** (a) CaSPA-550 AM (2 μM) was loaded into heart organoids for 10 minutes before fluorescence microscopy on a Leica upright microscope operating at 5 Hz. Individual frames were co-registered and the % Signal change plotted over the stationary ROI depicted by the white dashed line. The gray-shaded time intervals indicate small contractions detected by binarizing the signal changes in rectangular ROI positioned directly at the upper edge of the organoid (gray dashed box). (b) Analogous experiment as in (a) but using the classical fluorescent probe Fluo-4 AM imaged at 0.33 Hz on an Evos microscope. Gray shaded time points again indicate small contractions that were detected by the rectangular grey box on the left.

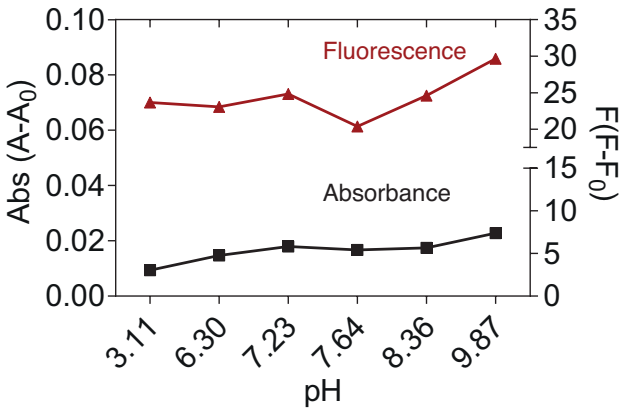

Figure C.20: **pH response of CaSPA-550.** Absorbance and fluorescence spectra of CaSPA-550 (1 μM, 25 ^{o}C) in MOPS (30 mM, 100 KCl) buffer at various pHs (3.11, 6.30, 7.23, 7.64, 8.36, 9.87). Little or no changes in absorption from 3.11-9.87, specifically at 6.30-7.64, within the desired physiological ranges

C.1.1 Syntheses

Compound **114**:[196] *3-ethyl-1,1,2-trimethyl-1H-benzo[e]indol-3-ium iodide*

Ethyl iodide (1.12 g, 7.20 mmol) was added to a solution of 1,1,2-trimethyl-1H-benzo[e]indole 1 (500 mg, 2.40 mmol) in anhydrous MeCN (50 cm^3). The resulting mixture was refluxed under N_2 overnight. A further 50% equiv. of ethyl-iodide was added and RM was refluxed for another 15 hrs. The RM was cooled and dried *in vacuo*. The residue was suspended in cold diethyl ether filtered and washed with cold diethyl ether several times. The precipitate was dissolved in minimum volume of hot MeOH and recrystallized by the addition of small amounts of diethyl ether gave **114** as pale blue powder. Yield: 777 mg, 89%, *Rf* = 0.25 (98:2 DCM/MeOH), lit. m.p. 228 ^{0}C. ^{1}H NMR (MeOD, 250 MHz): δ (ppm) 8.33 (d, J = 8.5 Hz, 1H, -C*H*Ar), 8.24 (d, J = 9.0 Hz, 1H, -C*H*Ar), 8.12-8.21 (m, 1H, -C*H*Ar), 8.04 (d, J = 9.0Hz, 1H, -C*H*Ar), 7.77 - 7.87 (m, 1H, -C*H*Ar), 7.66 - 7.77 (m, 1H, -C*H*Ar), 4.78 - 4.83 (m, 3H, -C^{In}CH_3), 4.70 (q, J = 7.4 Hz, 2H, CH_2CH$_3$), 1.82 - 1.92 (m, 6H, -C^{In}(CH_3)$_2$), 1.59 - 1.72 ppm (m, 3H, -CH$_2$CH_3). ^{13}C NMR (MeOD, 63 MHz): δ (ppm) 139.6, 138.9, 135.3, 132.6, 131.2, 129.8, 129.2, 128.8, 124.5, 113.9, 57.4, 45.3, 22.5, 13.7. ESI-MS (ES$^+$) calculated for $C_{17}H_{20}N^+$ [M$^+$H$^+$] *m/z* 238.16, found 238.36.

Compound **116**:[170]

1,2-bis(o-aminophenoxy)ethane-N,N,N',N'-tetramethyl ester **115** (100 mg, 0.19 mmol) was dissolved in anhydrous DMF (5 cm3) containing 10% v/v Et_3N under N_2. $POCl_3$ (69 mg, 0.451 mmol) was added slowly with stirring at 0 ^{o}C. After 30 min, the RM was allowed to cool to RT and stirred overnight at RT. The RM was neutralized with 1 M NaOH. It was then extracted with three portions (30 cm^3) of ethyl acetate, dried in $MgSO_4$ and dried *in vacuo*. Pale yellow oil of **116** was obtained. Yield: 42 mg, 40%, *Rf* = 0.40 (40:60 EtOAc: n-hexane). ^{1}H NMR (CDCl^3, 300 MHz): δ (ppm) 9.60 (s, 1H, -CHCO), 7.30-6.85 (m, 7H, -CHAr), 4.25-4.10 (m, 12H, -O(CH$_2$)$_2$ and –N(CH$_2$)), ,3.66- 3.55 (m, 12H, -OCH$_3$). ESI-MS (ES$^+$) calculated for $C_{27}H_{32}N_2O_{11}$ [M$^+$H$^+$] *m/z* 560.20, found 560.10.

Compound **117**:

Et_3N (50 μL, 0.36 mmol) was added in a mixture of **116** (10 mg, 0.018 mmol) and indole iodized

salt **114** (4.26 mg, 0.018 mmol) in EtOH (1 cm^3). The RM was heated to reflux for 30 mins, during which the solution turned deep purple. After cooling to RT, the solvent was dried *in vacuo*. The residue was recrystallized from cold MeOH and purification by column chromatography (silica gel, DCM: MeOH = 20:1, *Rf* = 0.45) yielded deep pink needle crystals **117** (5.60 mg, 40% yield). ^{1}H NMR ($CDCl_3$, 500 MHz) δ 8.15 – 7.97 (m, 1H, -CHAr), 7.94 – 7.27 (m, 4H, -CHAr), 7.08 – 6.90 (m, 3H, -CHAr), 6.86 (td, *J* = 6.6, 5.6, 3.2 Hz, 1H, -CHAr), 6.80 (td, *J* = 8.9, 8.1, 2.9 Hz, 3H, -CHAr), 6.76 – 6.70 (m, 1H, -CHAr), 4.25 (tq, *J* = 9.1, 4.5, 3.9 Hz, 4H, -$O(CH_2)_2O$), 4.18 – 4.04 (m, 8H, -$CH_2CO_2CH_3$), 3.99 (d, *J*) = 31.3 Hz, 2H, -ceCH2CH3), 3.54 – 3.49 (m, 12H, -OCH_3), 2.77 (dd, *J* = 9.4, 6.9 Hz, 1H, -CH=CH), 2.54 (dd, *J* = 9.3, 7.0 Hz, 1H, -CH=CH), 1.31 (s, 3H, -CH_2CH_3), 1.22 (s, 6H, -$Ar^{in}(CH_3)_2$). ^{13}C NMR ($CDCl^3$, 126 MHz) δ 172.63, 171.98, 154.11, 152.20, 151.49, 150.31, 150.21, 139.21, 136.02, 135.40, 135.35, 134.13, 130.82, 130.66, 129.37, 124.70, 124.43, 124.40, 122.40, 122.30, 121.50, 119.07, 118.57, 113.04, 111.72, 111.01, 67.15, 66.95, 62.24, 53.31, 51.64, 34.30, 34.20, 30.28, 29.69, 29.35, 22.68, 14.12. HRMS (ESI^+) calculated for $C_{40}H_{50}N_3O_{10}^+$ [M^+H^+] *m/z* 780.3489, found 780.3477.

Compound **118**:

Saponification was carried out by dissolving the methyl ester **117** (40 mg, 0.05 mmol) in a water miscible solvent MeOH (1.5 cm^3) and added an excess of NaOH (4.8 mg, 0.20 mmol). A brief warming of the solution was helpful to start the hydrolysis of esters that precipitated upon addition of aqueous solution. The deprotection requires a homogeneous solution containing at least 0.1 M excess of NaOH for several hours and was monitored by TLC (*Rf* = 0.30; 95:5 DCM:MeOH). The solution was evaporated and purified by RP-HPLC to give **118** solid (33 mg, 90%). ^{1}H NMR (MeOD, 500 MHz) δ 8.34 (d, *J* = 15.8 Hz, 1H, -CHAr), 8.28 (d, *J* = 8.6 Hz, 1H, -CHAr), 8.13 – 8.06 (m, 1H, -CHAr), 8.02 (d, *J* = 8.3 Hz, 1H, -CHAr), 7.89 (s, 2H, -CHAr), 7.80 (d, *J* = 9.6 Hz, 1H, -CHAr), 7.67 (t, *J* = 7.7 Hz, 1H, -CHAr), 7.60 – 7.48 (m, 1H, -CHAr), 7.40 (d, *J* = 15.9 Hz, 1H, -CHAr), 7.00 – 6.70 (m, 3H, -CHAr), 4.65 (s, 1H, -CH=CH), 4.39 (s, 1H, -CH=CH), 4.34 – 4.16 (m, 4H, -$O(CH_2)_2O$), 3.99 (s, 2H, -CH_2CH_3), 3.22 (s, 8H, -$CH_2CO_2CH_3$), 1.98 (s, 3H, -CH_2CH_3), 1.20 (s, 6H, -$Ar^{in}(CH_3)_2$). ^{13}C NMR (MeOD, 126 MHz) δ 181.34, 176.69, 175.02, 164.60, 163.47, 153.79, 145.58, 138.73, 138.08, 137.81, 133.49, 131.08, 129.87, 128.00, 127.43, 126.59, 122.59, 121.29, 111.80, 67.02, 57.48, 56.96, 53.44, 41.41, 35.56, 30.24, 29.33,

25.43, 12.68. HRMS (ES^+) calculated for $C_{40}H_{42}N_3O_{10}^+$ [M^+H^+] *m/z* 724.29, found 724.2857. Analytical HPLC; t_R = 5.80 min. λmax/ λem (MOPS) 550/634 nm.

Compound **119**:[170]

Esterification of the sodium salt of ligand **118** (20 mg, 0.028 mmol) was carried out in MeCN, followed by the addition of excess DIPEA (18 mg, 0.14 mmol) and acetoxymethyl bromide (26 mg, 16 μL, 0.17 mmol). The RM was stirred at RT overnight. The solution was dried *in vacuo*, re-suspended in CH_2Cl_2, filtered and re-evaporated. The product was purified by preparative RP-HPLC to give **119** as pink solid (6 mg, 20%). ^{1}H NMR ($CDCl_3$, 500 MHz) δ 8.13 (d, J = 9.9 Hz, 1H, -CHAr), 8.09 – 7.93 (m, 2H, -CHAr), 7.66 (d, J = 7.4 Hz, 1H, -CHAr), 7.58 (t, J = 7.4 Hz, 1H, -CHAr), 7.46 (d, J = 8.6 Hz, 1H, -CHAr), 7.29 (t, J = 2.2 Hz, 1H, -CHAr), 6.98 – 6.60 (m, 5H, -CHAr), 5.59 (s, 1H, -CH=CH), 5.51 (s, 1H, -CH=CH), 5.33- 5.15 (m, 2H, $-CH_2CH_3$), 5.06 – 4.57 (m, 4H, $-O(CH_2)_2O$), 4.36 – 3.92 (m, 8H, $-CH_2CO_2CH_3$), 2.13 – 1.75 (m, 20H, -AM group), 1.27 (s, 6H, $-Ar^{In}(CH_3)_2$), 1.21 (s, 3H, $-CH_2CH_3$). HRMS (ES^+) calculated for $C_{52}H_{58}N_3O_{18}^+$ [M^+H^+] *m/z* 1012.3724, found 1012.3695. Analytical HPLC; t_R = 4.90 min. λmax/ λem (MOPS) 590/609 nm

C.1.2 NMR characterisations

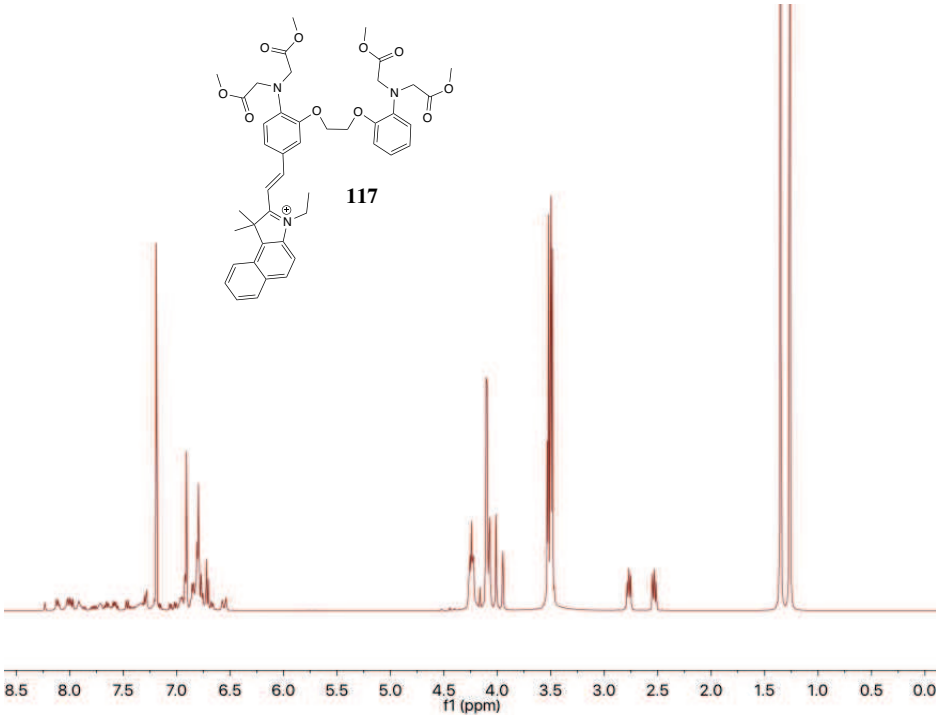

Figure C.21: ^{1}H NMR of CaSPA-550 tetramethyl esters **117**.

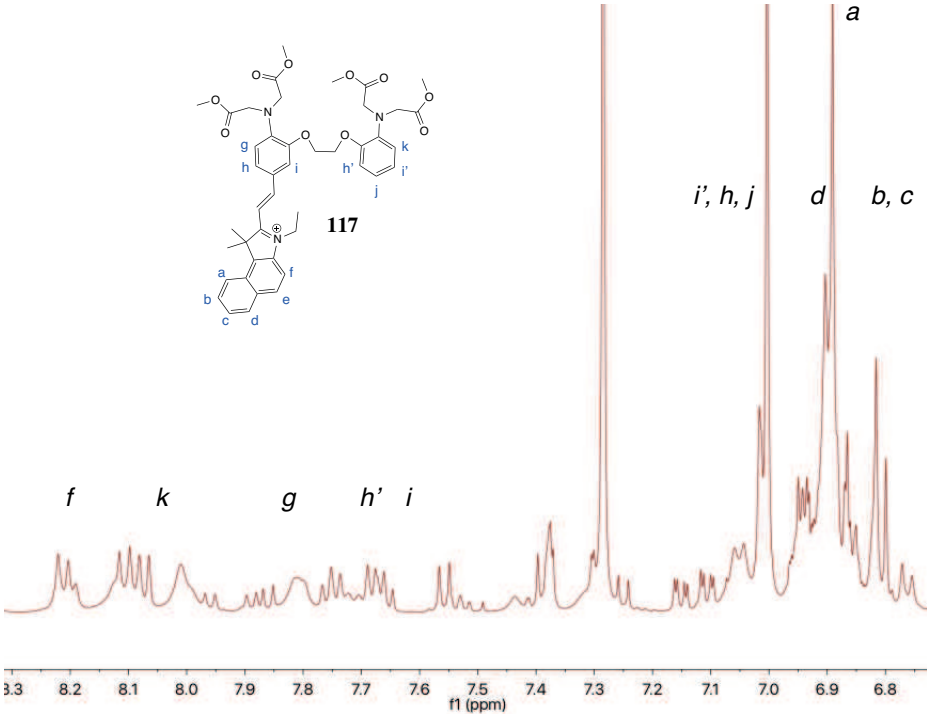

Figure C.22: ^{1}H NMR of CaSPA-550 tetramethyl esters **117** in the aromatic region.

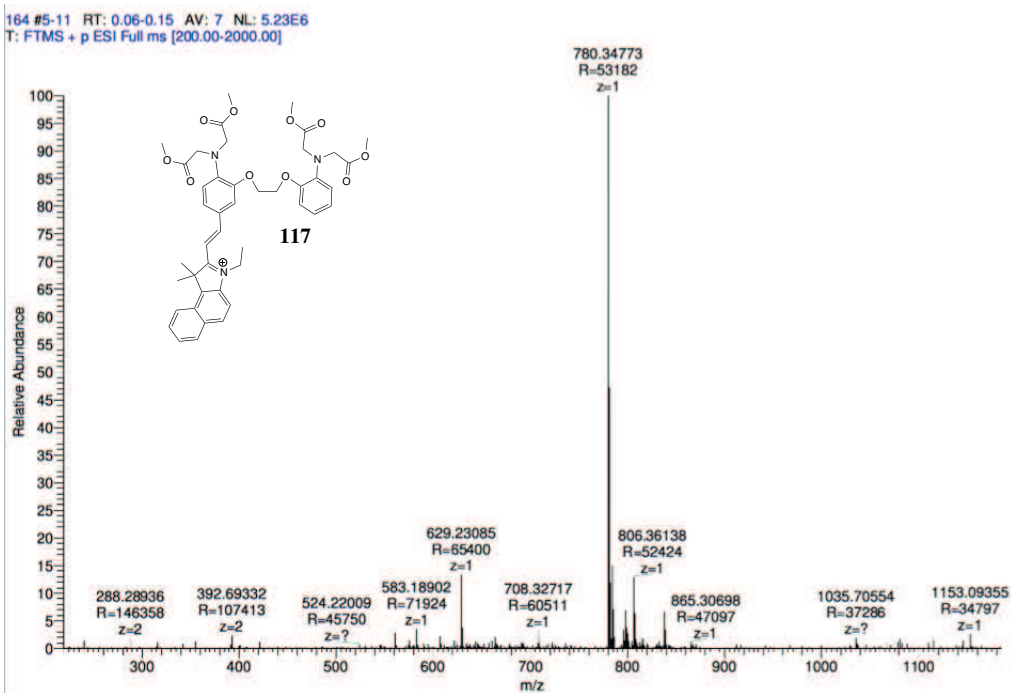

Figure C.23: High-resolution mass spectrometry (HRMS) of CaSPA-550 tetramethyl esters **117**.

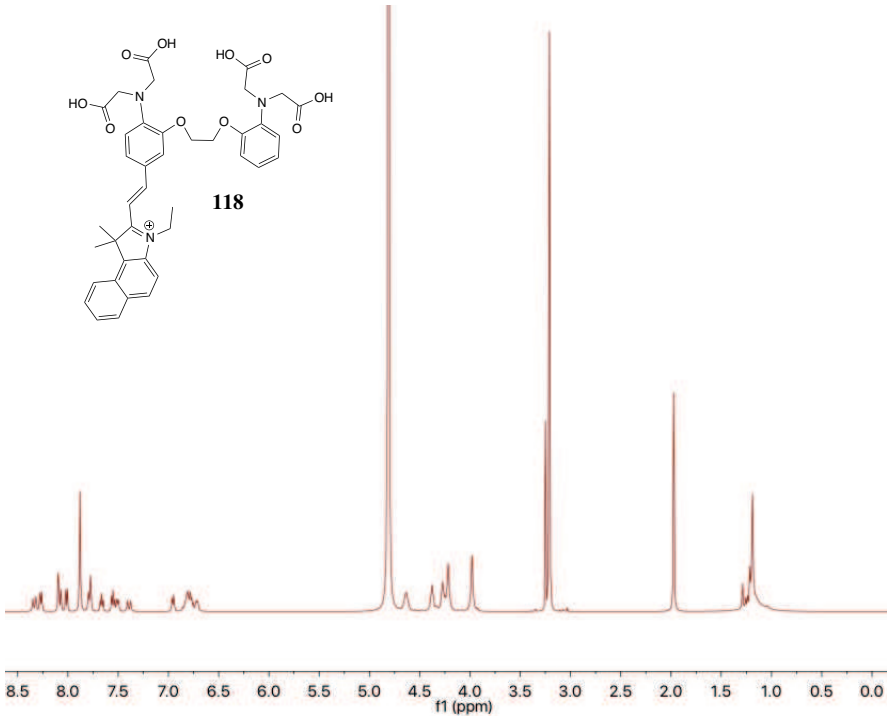

Figure C.24: ^{1}H NMR of CaSPA-550 carboxylic acid **118**.

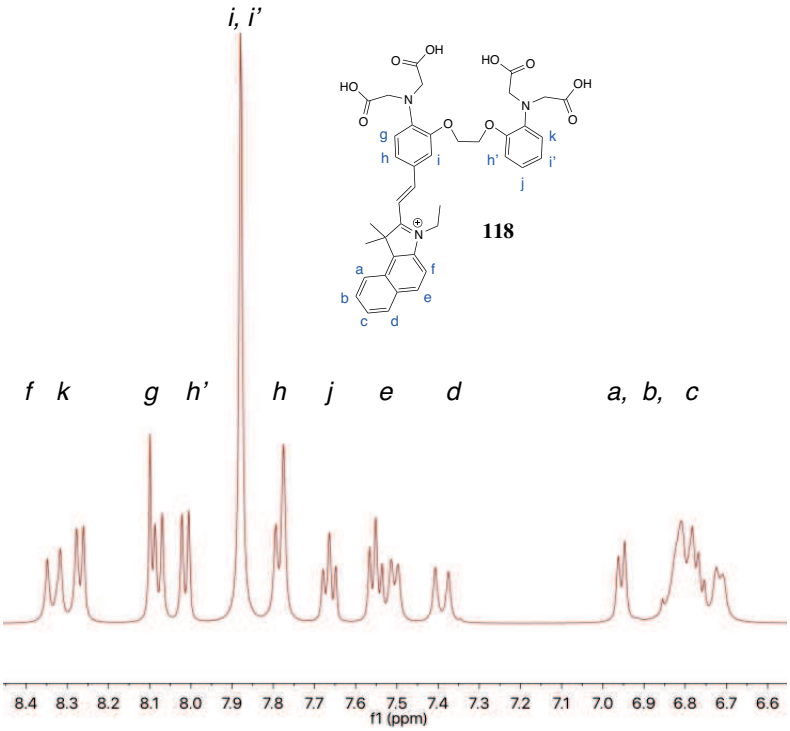

Figure C.25: ^{1}H NMR of CaSPA-550 carboxylic acid **118** in the aromatic region.

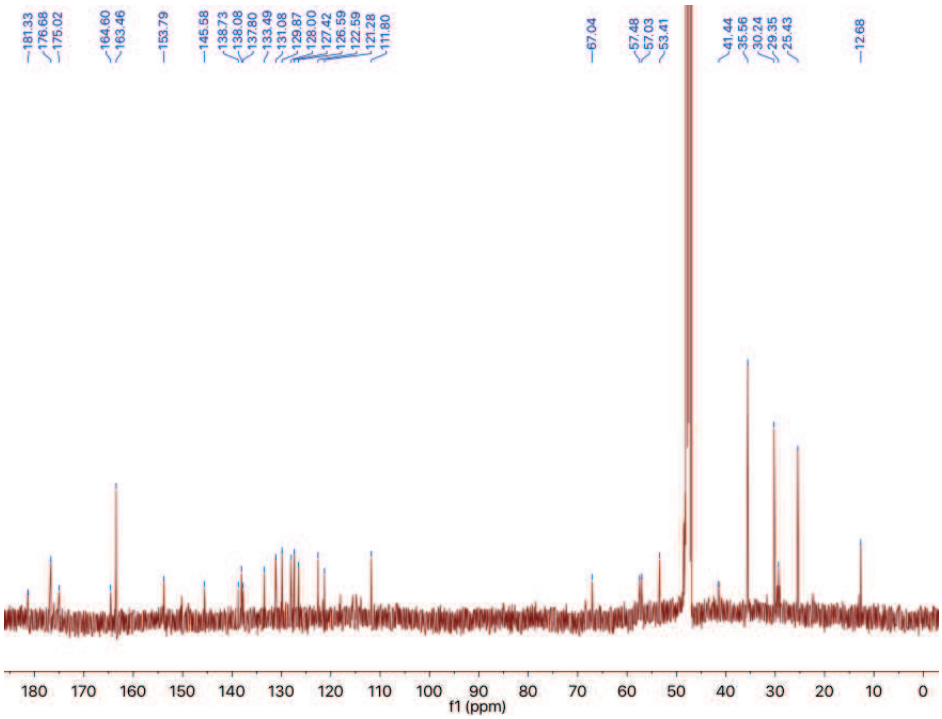

Figure C.26: ^{13}C NMR of CaSPA-550 carboxylic acid **118**.

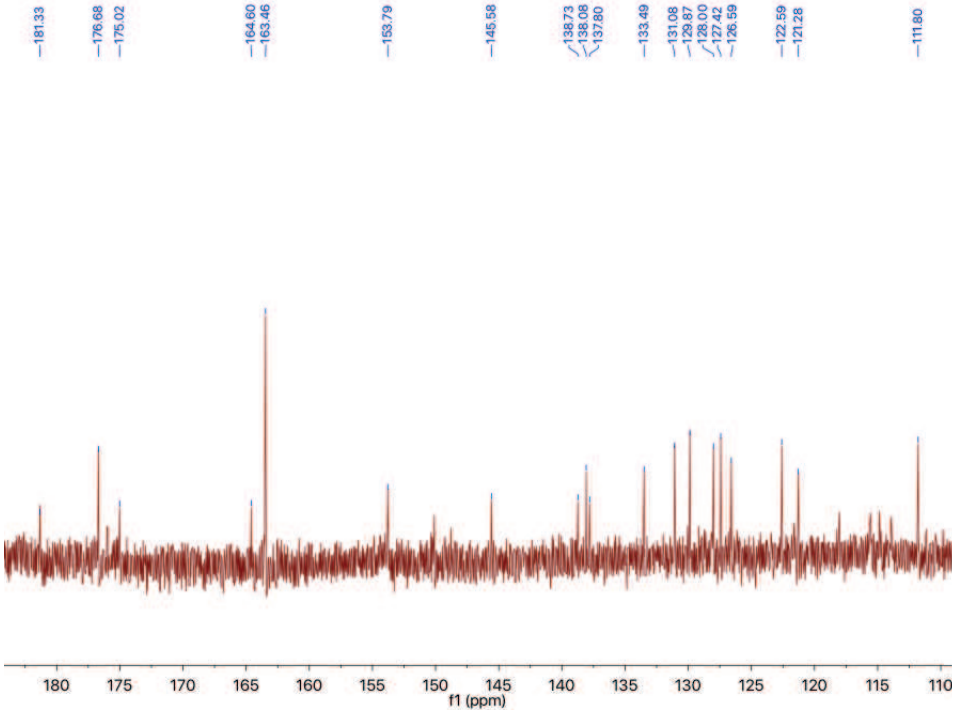

Figure C.27: ^{13}C NMR of CaSPA-550 carboxylic acid **118** from 180-110 ppm range.

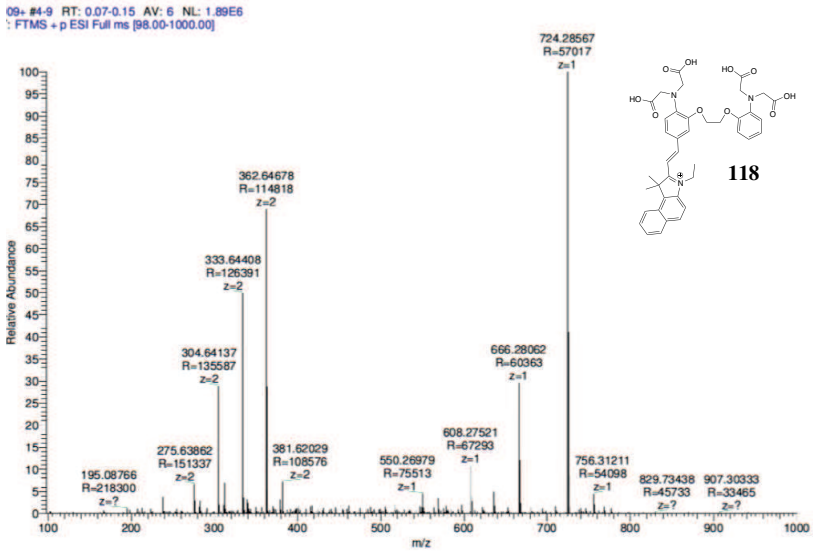

Figure C.28: High-resolution mass spectrometry (HRMS) of CaSPA-550 carboxylic acid **118**.

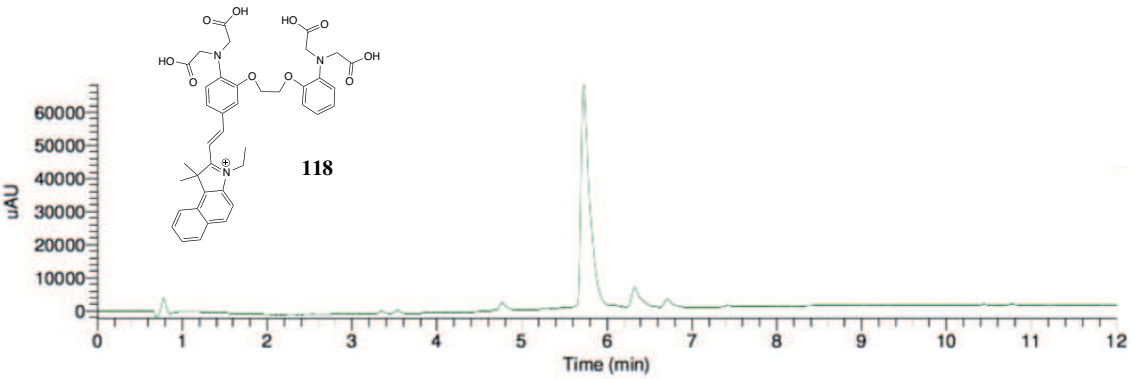

Figure C.29: ^{1}H NMR of CaSPA-550 AM **118**.

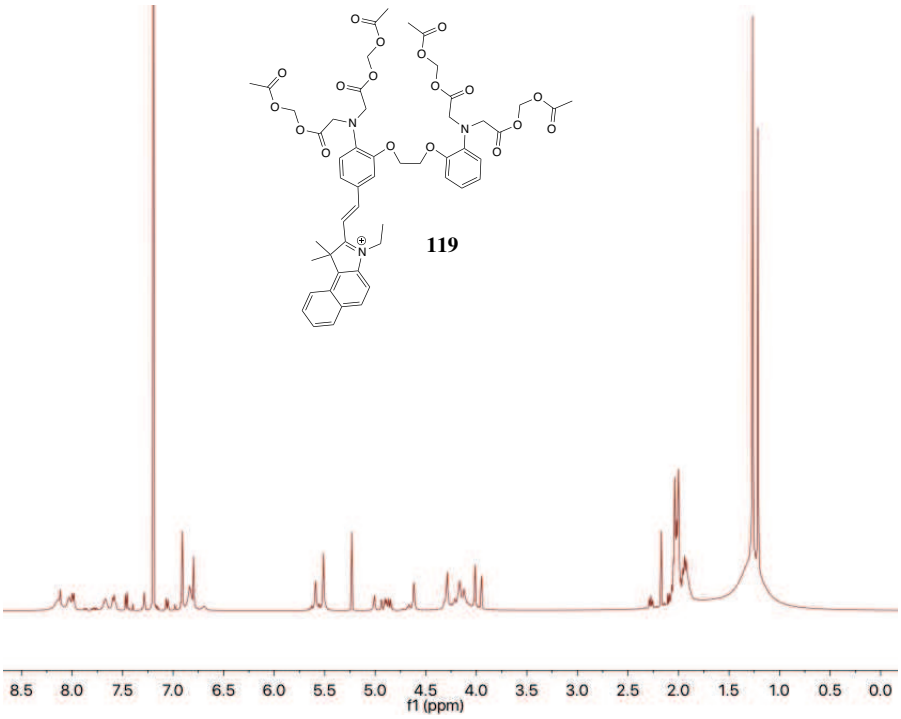

Figure C.30: ^{1}H NMR of CaSPA-550 AM **119**.

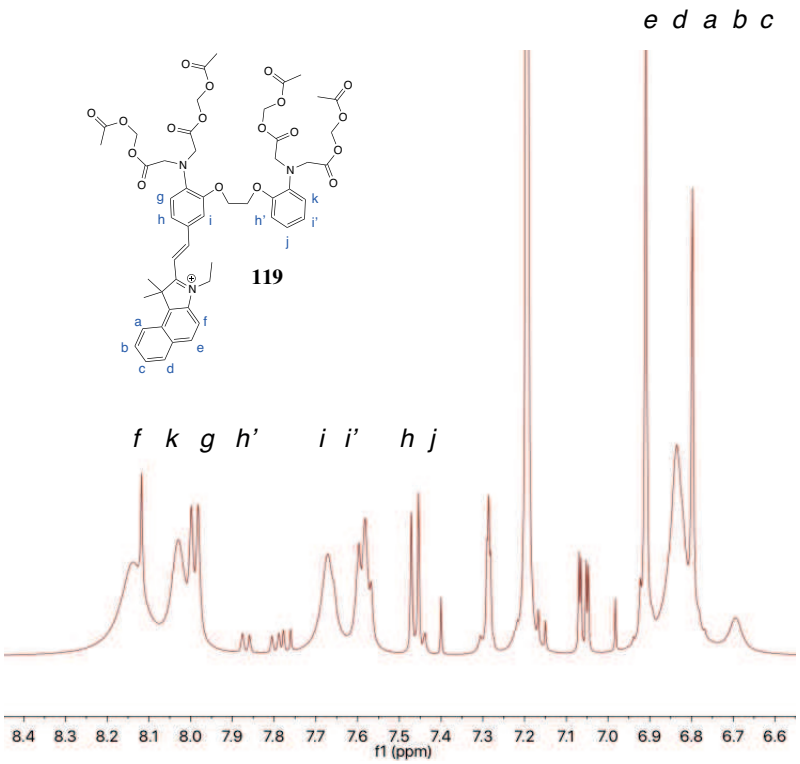

Figure C.31: ^{1}H NMR of CaSPA-550 AM **119** in the aromatic region.

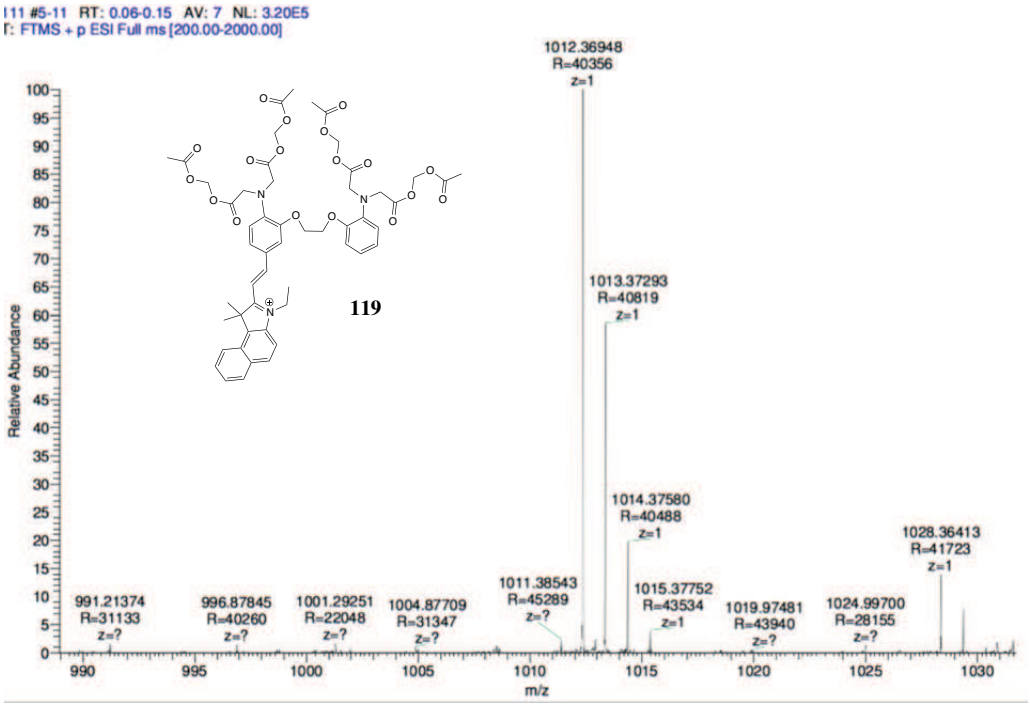

Figure C.32: High-resolution mass spectrometry (HRMS) of CaSPA-550 AM **119**.

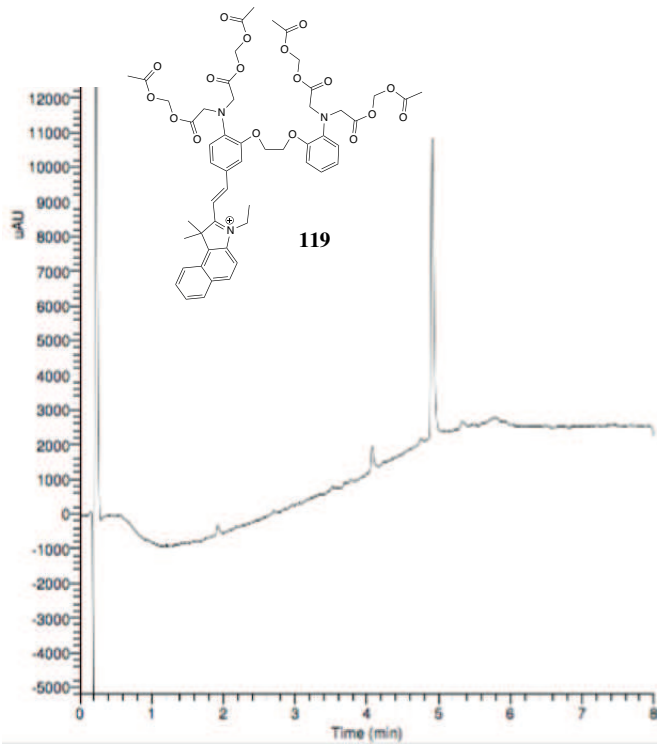

Figure C.33: High-resolution mass spectrometry (HRMS) of CaSPA-550 AM **119**.

Abbreviations

ε extinction coefficient. 20, 22, 38, 76

ϕ quantum yield. 20, 22, 38, 100

ACG asante calcium green. 30

ACR asante calcium red. 30

AM acetoxymethoxy. 79

Arsenazo-III 2,2'-(1,8-dihydroxy-3,6- disulfonaphthylene-2,7-bisazo)bisbenzenearsonic acid. 22, 73, 74, 149

BAPTA 1,2-bis(o)-aminophenoxy)ethane-N,N,N',N'-tetraacetic acid. 37

BBB blood brain barrier. 22, 38

BODIPY 4,4-difluoro-4-bora-3a,4a-diaza-s-indacene. 22

CAs contrast agents. 10, 16, 19, 20, 22, 32, 33, 41, 73

CaSPA Ca^{2+}-Selective Photoacoustic Agent. 11, 78, 79, 87, 100

CHO Chinese Hamster Ovary. 79, 100

CPZ-III cholorophosphonazo-III. 73, 74, 149

DCM dichloromethane. 58

DIPEA N,N-Diisopropylethylamine. 54, 107

EGTA ethylene glycol-bis(β-aminoethyl ether)-N,N,N',N'-tetraacetic acid. 46

EPR enhanced permeability and retention. 41

FC flash chromatography. 96

FMT fluorescence molecular tomography. 22

FMT-XCT Fluorescence molecular tomography–X-ray computed tomography. 14

FONT Functional optoacoustic neuro-tomography. 33

fPAI functional photoacoustic imaging. 16

fPAM functional photoacoustic microscopy. 32

FPs fluorescent proteins. 19

GECI genetically encoded calcium indicator. 33

GFP green fluorescent protein. 19

HCl hydrochloric acid. 54, 55

HEK293 Human Embryonic Kidney Cells. 79, 100

HOMO highest occupied molecular orbital. 21, 100

HPLC High performance liquid chromatography. 96

HSA human serum albumin. 41

ICG Indocyanine green. 22, 37, 41

LUMO lowest unoccupied molecular orbital. 21, 100

MB methylene blue. 22

MOPS 3-(N-morpholino)propanesulfonic acid. 99

MSOT Multi-spectral optoacoustic tomography. 14, 22

MTT 3-(4,5-dimethylthiazol-2-yl)-2,5-diphenyltetrazolium bromide. 73

NIR near-infrared. 15, 19, 20, 21, 22, 34, 37, 38, 39, 40, 41, 42, 43, 45, 49, 51, 58, 60, 65, 68, 73

NP Nanoparticle. 27

OGB1 oregon green BAPTA-1. 30, 32

PA photoacoustic. 7, 14, 16, 19, 20, 21, 22, 33, 45, 49, 68, 73

PAI Photoacoustic imaging. 11, 14, 15, 16, 17, 20, 21, 22, 27, 33, 34, 37, 41, 45, 60, 68, 73, 88

PAT photoacoustic tomography. 22, 32

PBS phosphate-bufferred saline. 99

PCT photoinduced charge transfer. 88

Pd-cat. palladium catalyst. 67

Pd-cat. palladium catalyzed. 49, 63, 67

PEG polyethylene glycol. 22, 41

PET Positron emmission tomography. 14

PLE porcine liver esterase. 99

PPCy pyrrolopyrrole cyanine. 22

RM reaction mixture. 110, 113, 171, 173

RT room temperature. 96, 171, 173

SLN sentinel lymph node. 41

SN nucleophilic substitution. 40

SPECT Single-photon emission computed tomography. 14

SR101 sulforhodamine 101. 32

SS stock solution. 99

SWNT single-walled nanotube. 22

TLC thin layer chromatography. 96, 115, 116

UV ultraviolet. 30

Bibliography

[1] J. Weber, P. C. Beard and S. E. Bohndiek, *Nat Meth*, 2016, **13**, 639–650.

[2] V. Ntziachristos and D. Razansky, *Chemical Reviews*, 2010, **110**, 2783–2794.

[3] S. Gottschalk, T. F. Fehm, X. L. Dean-Ben and D. Razansky, *Journal of Cerebral Blood Flow & Metabolism*, 2015, **35**, 531–535.

[4] H. Li, P. Zhang, L. P. Smaga, R. A. Hoffman and J. Chan, *Journal of the American Chemical Society*, 2015, **137**, 15628–15631.

[5] J. A. Cotruvo, Jr., A. T. Aron, K. M. Ramos-Torres and C. J. Chang, *Chem. Soc. Rev.*, 2015, **44**, 4400–4414.

[6] L.-D. Liao, M.-L. Li, H.-Y. Lai, Y.-Y. I. Shih, Y.-C. Lo, S. Tsang, P. C.-P. Chao, C.-T. Lin, F.-S. Jaw and Y.-Y. Chen, *NeuroImage*, 2010, **52**, 562 – 570.

[7] L. V. Wang and J. Yao, *Nat Meth*, 2016, **13**, 627–638.

[8] A. Taruttis, G. M. van Dam and V. Ntziachristos, *Cancer Research*, 2015, **75**, 1548–1559.

[9] V. Ntziachristos, *Nat Meth*, 2010, **7**, 603–614.

[10] P. Beard, *Interface Focus*, 2011, **1**, 602–631.

[11] J. Levi, S.-R. Kothapalli, S. Bohndiek, J.-K. Yoon, A. Dragulescu-Andrasi, C. Nielsen, A. Tisma, S. Bodapati, G. Gowrishankar, X. Yan, C. Chan, D. Starcevic and S. S. Gambhir, *American Association for Cancer Research*, 2013, **19**, 1494–1502.

[12] P.-C. Li, C.-R. C. Wang, D.-B. Shieh, C.-W. Wei, C.-K. Liao, C. Poe, S. Jhan, A.-A. Ding and Y.-N. Wu, *Opt. Express*, 2008, **16**, 18605–18615.

[13] J. Laufer, P. Johnson, E. Zhang, B. Treeby, B. Cox, B. Pedley and P. Beard, *Journal of Biomedical Optics*, 2012, **17**, 056016–1–056016–8.

[14] G. P. Luke, J. N. Myers, S. Y. Emelianov and K. V. Sokolov, *Cancer Research*, 2014, **74**, 5397–5408.

[15] J. A. Guggenheim, T. J. Allen, A. Plumb, E. Z. Zhang, M. Rodriguez-Justo, S. Punwani and P. C. Beard, *Journal of Biomedical Optics*, 2015, **20**, 050504.

[16] S. E. Bohndiek, L. S. Sasportas, S. Machtaler, J. V. Jokerst, S. Hori and S. S. Gambhir, *Journal of Nuclear Medicine*, 2015, **56**, 1942–1947.

[17] H. F. Zhang, K. Maslov, G. Stoica and L. V. Wang, *Nat Biotech*, 2006, **24**, 848–851.

[18] J.-T. Oh, M.-L. Li, H. F. Zhang, K. Maslov, G. Stoica and L. V. Wang, *Journal of Biomedical Optics*, 2006, **11**, 034032–034032–4.

[19] I. Stoffels, S. Morscher, I. Helfrich, U. Hillen, J. Leyh, N. C. Burton, T. C. P. Sardella, J. Claussen, T. D. Poeppel, H. S. Bachmann, A. Roesch, K. Griewank, D. Schadendorf, M. Gunzer and J. Klode, *Science Translational Medicine*, 2015, **7**, 317ra199–317ra199.

[20] Z. Xu, C. Li and L. V. Wang, *Journal of Biomedical Optics*, 2010, **15**, 36019.

[21] X. Luis and D. Razansky, *Light Sci Appl*, 2014, **3**, e137.

[22] A. Krumholz, G. S. Filonov, J. Xia, J. Yao, V. V. Verkhusha and L. V. Wang, *Photoacoustic imaging of the near-infrared fluorescent protein iRFP in vivo*, 2012, `http://dx.doi.org/10.1117/12.908927`.

[23] G. S. Filonov, A. Krumholz, J. Xia, J. Yao, L. V. Wang and V. V. Verkhusha, *Angewandte Chemie International Edition*, 2012, **51**, 1448–1451.

[24] A. Krumholz, D. M. Shcherbakova, J. Xia, L. V. Wang and V. V. Verkhusha, *Scientific Reports*, 2014, **4**, 3939.

[25] D. Razansky, M. Distel, C. Vinegoni, R. Ma, N. Perrimon, R. W. Koster and V. Ntziachristos, *Nat Photon*, 2009, **3**, 412–417.

[26] Y. Li, A. Forbrich, J. Wu, P. Shao, R. E. Campbell and R. Zemp, *Scientific Reports*, 2016, **6**, 22129.

[27] A. Miyawaki, J. Llopis, R. Heim, J. M. McCaffery, J. A. Adams, M. Ikura and R. Y. Tsien, *Nature*, 1997, **388**, 882–887.

[28] A. Miyawaki, O. Griesbeck, R. Heim and R. Y. Tsien, *Proceedings of the National Academy of Sciences*, 1999, **96**, 2135–2140.

[29] G. Sela, A. Lauri, X. L. Dean-Ben, M. Kneipp, V. Ntziachristos, S. Shoham, G. G. Westmeyer and D. Razansky, *arXiv preprint arXiv*, 2015, **1501**, 1–4.

[30] M. Frenette, M. Hatamimoslehabadi, S. Bellinger-Buckley, S. Laoui, J. La, S. Bag, S. Mallidi, T. Hasan, B. Bouma, C. Yelleswarapu and J. Rochford, *Journal of the American Chemical Society*, 2014, **136**, 15853–15856.

[31] L. Xiang, B. Wang, L. Ji and H. Jiang, *Scientific Reports*, 2013, **3**, 1113.

[32] S. Bhattacharyya, S. Wang, D. Reinecke, J. William Kiser, R. A. Kruger and T. R. DeGrado, *Bioconjugate Chemistry*, 2008, **19**, 1186–1193.

[33] K. Kanazaki, K. Sano, A. Makino, A. Takahashi, J. Deguchi, M. Ohashi, T. Temma, M. Ono and H. Saji, *J. Biomed. Opt.*, 2014, **19(9)**, 096002.

[34] C. Li, A. Aguirre, J. Gamelin, A. Maurudis, Q. Zhu and L. V. Wang, *Journal of Biomedical Optics*, 2010, **15**, 010509.

[35] C. Grienberger and A. Konnerth, *Neuron*, 2016, **73**, 862–885.

[36] V. Barone, A. Baiardi, M. Biczysko, J. Bloino, C. Cappelli and F. Lipparini, *Phys. Chem. Chem. Phys.*, 2012, **14**, 12404–12422.

[37] X. Wang, G. Ku, M. A. Wegiel, D. J. Bornhop, G. Stoica and L. V. Wang, *Opt. Lett.*, 2004, **29**, 730–732.

[38] B. Wang, Q. Zhao, N. M. Barkey, D. L. Morse and H. Jiang, *Medical Physics*, 2012, **39**, 2512–2517.

[39] D. Razansky, C. Vinegoni and V. Ntziachristos, *Opt. Lett.*, 2007, **32**, 2891–2893.

[40] M. Bai and S. Achilefu, *Heterocycl. Commun.*, 2010, **16(4-6)**, 213–216.

[41] E. J. Cooley, P. Kruizinga, D. W. Branch and S. Emelianov, *Proc. SPIE*, 2010, **7576**, 75761J–75761J–8.

[42] N. Dana, R. A. Fowler, A. Allen, J. Zoldan, L. Suggs and S. Emelianov, *Laser Physics Letters*, 2016, **13**, 075603.

[43] S. M. Baylor and S. Hollingworth, *The Journal of Physiology*, 1988, **403**, 151–192.

[44] A. Abuteen, S. Zanganeh, J. Akhigbe, L. P. Samankumara, A. Aguirre, N. Biswal, M. Braune, A. Vollertsen, B. Roder, C. Bruckner and Q. Zhu, *Phys. Chem. Chem. Phys.*, 2013, **15**, 18502–18509.

[45] E. Morgounova, Q. Shao, B. J. Hackel, D. D. Thomas and S. Ashkenazi, *Journal of Biomedical Optics*, 2013, **18**, 056004.

[46] T. Temma, S. Onoe, K. Kanazaki, M. Ono and H. Saji, *Journal of Biomedical Optics*, 2014, **19**, 090501.

[47] S. Onoe, T. Temma, K. Kanazaki, M. Ono and H. Saji, *Journal of Biomedical Optics*, 2015, **20**, 096006.

[48] A. Bag and P. K. Ghorai, *RSC Adv.*, 2015, **5**, 31575–31583.

[49] A.-P. Xu, H.-H. Han, J. Lu, P.-P. Yang, Y.-J. Gao, H.-W. An, D. Zhanng, L.-Z. Li, J.-P. Zhang, D. Wang, L. Wang and H. Wang, *Dyes and Pigments*, 2016, **125**, 392 – 398.

[50] T. Repenko, S. Fokong, L. De Laporte, D. Go, F. Kiessling, T. Lammers and A. J. C. Kuehne, *Chem. Commun.*, 2015, **51**, 6084–6087.

[51] C. Kim, K. H. Song, F. Gao and L. V. Wang, *Radiology*, 2010, **255**, 442–450.

[52] K. Kanazaki, K. Sano, A. Makino, A. Takahashi, J. Deguchi, M. Ohashi, T. Temma, M. Ono and H. Saji, *Journal of Biomedical Optics*, 2014, **19**, 096002.

[53] N.-Y. Kang, S.-J. Park, X. W. E. Ang, A. Samanta, W. H. P. Driessen, V. Ntziachristos, K. O. Vasquez, J. D. Peterson, S.-W. Yun and Y.-T. Chang, *Chem. Commun.*, 2014, **50**, 6589–6591.

[54] M. R. Chatni, J. Xia, R. Sohn, K. Maslov, Z. Guo, Y. Zhang, K. Wang, Y. Xia, M. Anastasio, J. Arbeit and L. V. Wang, *Journal of Biomedical Optics*, 2012, **17**, 76012.

[55] J. L. Kovar, W. Volcheck, E. Sevick-Muraca, M. A. Simpson and D. M. Olive, *Analytical biochemistry*, 2009, **384**, 254–262.

[56] K. M. Stantz, M. Cao, B. Liu, K. D. Miller and L. Guo, *Molecular imaging of neutropilin-1 receptor using photoacoustic spectroscopy in breast tumors*, 2010, `http://dx.doi.org/10.1117/12.842271`.

[57] M. L. Li, J. T. Oh, X. Xie, G. Ku, W. Wang, C. Li, G. Lungu, G. Stoica and L. V. Wang, *Proceedings of the IEEE*, 2008, **96**, 481–489.

[58] Q. Yang, H. Cui, S. Cai, X. Yang and M. L. Forrest, *J. Biomed. Opt.*, 2011, **16(11)**, 116026.

[59] N. Sim, S. Gottschalk, R. Pal, M. Delbianco, O. Degtyaruk, D. Razansky, G. G. Westmeyer, V. Ntziachristos, D. Parker and A. Mishra, *Chem. Commun.*, 2015, **51**, 15149–15152.

[60] L. Song, C. Kim, K. Maslov, K. K. Shung and L. V. Wang, *Medical Physics*.

[61] K. H. Song, E. W. Stein, J. A. Margenthaler and L. V. Wang, *Journal of Biomedical Optics*, 2008, **13**, 054033–054033–6.

[62] C. Kim, T. N. Erpelding, L. Jankovic and L. V. Wang, *Philosophical Transactions of the Royal Society of London A: Mathematical, Physical and Engineering Sciences*, 2011, **369**, 4644–4650.

[63] Q. Shao, E. Morgounova, C. Jiang, J. Choi, J. Bischof and S. Ashkenazi, *Journal of Biomedical Optics*, 2013, **18**, 076019–076019.

[64] S. Ashkenazi, *Journal of Biomedical Optics*, 2010, **15**, 040501–040501–3.

[65] N. Bèzière and V. Ntziachristos, *Journal of Nuclear Medicine*, 2015, **56**, 323–328.

[66] H. Huang, D. Wang, Y. Zhang, Y. Zhou, J. Geng, U. Chitgupi, T. R. Cook, J. Xia and J. F. Lovell.

[67] K. V. Kong, L.-D. Liao, Z. Lam, N. V. Thakor, W. K. Leong and M. Olivo, *Chem. Commun.*, 2014, **50**, 2601–2603.

[68] Y. Zhang, X. Cai, Y. Wang, C. Zhang, L. Li, S.-W. Choi, L. V. Wang and Y. Xia, *Angewandte Chemie International Edition*, 2011, **50**, 7359–7363.

[69] Y. Jiang, F. Sigmund, J. Reber, X. Luís Deán-Ben, S. Glasl, M. Kneipp, H. Estrada, D. Razansky, V. Ntziachristos and G. G. Westmeyer, *Scientific Reports*, 2015, **5**, 11048 EP –.

[70] S. Laoui, S. Bag, O. Dantiste, M. Frenette, M. Hatamimoslehabadi, S. Bellinger-Buckley, J.-C. Tseng, J. Rochford and C. Yelleswarapu, *Proc. SPIE*, 2014, **8956**, 895609–895609–9.

[71] C. W. Kimbrough, A. Khanal, M. Zeiderman, B. R. Khanal, N. C. Burton, K. M. McMasters, S. M. Vickers, W. E. Grizzle and L. R. McNally, *Clinical Cancer Research*, 2015, **21**, 4576–4585.

[72] M. R. Chatni, J. Yao, A. Danielli, C. P. Favazza, K. I. Maslov and L. V. Wang, *Journal of Biomedical Optics*, 2011, **16**, 100503–100503–3.

[73] T. D. Horvath, G. Kim, R. Kopelman and S. Ashkenazi, *Analyst*, 2008, **133**, 747–749.

[74] S. V. Hudson, J. S. Huang, W. Yin, S. Albeituni, J. Rush, A. Khanal, J. Yan, B. P. Ceresa, H. B. Frieboes and L. R. McNally, *Cancer Research*, 2014, **74**, 6271–6279.

[75] J. Levi, A. Sathirachinda and S. S. Gambhir, *Clinical Cancer Research*, 2014, **20**, 3721–3729.

[76] A. Dragulescu-Andrasi, S.-R. Kothapalli, G. A. Tikhomirov, J. Rao and S. S. Gambhir, *Journal of the fAmerican Chemical Society*, 2013, **135**, 11015–11022.

[77] C. Zhang, R. Kimura, L. Abou-Elkacem, J. Levi, L. Xu and S. S. Gambhir, *Journal of Nuclear Medicine*, 2016.

[78] J. Hu, X. Zhu, H. Li, Z. Zhao, X. Chi, G. Huang, D. Huang, G. Liu, X. Wang and J. Gao, *Theranostics*, 2014, **4**, 534–545.

[79] L. Wu, X. Cai, K. Nelson, W. Xing, J. Xia, R. Zhang, A. J. Stacy, M. Luderer, G. M. Lanza, L. V. Wang, B. Shen and D. Pan, *Nano research*, 2013, **6**, 312–325.

[80] H. Qin, T. Zhou, S. Yang and D. Xing, *Small*, 2015, **11**, 2675–2686.

[81] Y.-W. Wang, Y.-Y. Fu, Q. Peng, S.-S. Guo, G. Liu, J. Li, H.-H. Yang and G.-N. Chen, *J. Mater. Chem. B*, 2013, **1**, 5762–5767.

[82] R. Romero-Aburto, T. N. Narayanan, Y. Nagaoka, T. Hasumura, T. M. Mitcham, T. Fukuda, P. J. Cox, R. R. Bouchard, T. Maekawa, D. S. Kumar, S. V. Torti, S. A. Mani and P. M. Ajayan, *Advanced Materials*, 2013, **25**, 5632–5637.

[83] D. Hu, J. Zhang, G. Gao, Z. Sheng, H. Cui and L. Cai, *Theranostics*, 2016, **6**, 1043–1052.

[84] A. de la Zerda, S. Bodapati, R. Teed, S. Y. May, S. M. Tabakman, Z. Liu, B. T. Khuri-Yakub, X. Chen, H. Dai and S. S. Gambhir.

[85] J. Jian, C. Liu, Y. Gong, L. Su, B. Zhang, Z. Wang, D. Wang, Y. Zhou, F. Xu, P. Li, Y. Zheng, L. Song and X. Zhou, *Theranostics*, 2014, **4**, 1026–1038.

[86] A. d. l. Zerda, Z. Liu, S. Bodapati, R. Teed, S. Vaithilingam, B. T. Khuri-Yakub, X. Chen, H. Dai and S. S. Gambhir.

[87] A. De La Zerda, C. Zavaleta, S. Keren, S. Vaithilingam, S. Bodapati, Z. Liu, J. Levi, B. R. Smith, T.-J. Ma, O. Oralkan, Z. Cheng, X. Chen, H. Dai, B. T. Khuri-Yakub and S. S. Gambhir, *Nat Nano*, 2008, **3**, 557–562.

[88] T. Zhang, H. Cui, C.-Y. Fang, L.-J. Su, S. Ren, H.-C. Chang, X. Yang and M. L. Forrest, *Journal of Biomedical Optics*, 2013, **18**, 026018–026018.

[89] T. Zhang, H. Cui, C.-Y. Fang, K. Cheng, X. Yang, H.-C. Chang and M. L. Forrest, *Nanomedicine (London, England)*, 2015, **10**, 573–587.

[90] T. Zhang, H. Cui, C.-Y. Fang, J. Jo, X. Yang, H.-C. Chang and M. L. Forrest, *Proceedings of SPIE–the International Society for Optical Engineering*, 2013, **8815**, 881504.

[91] Z.-H. Miao, H. Wang, H. Yang, Z. Li, L. Zhen and C.-Y. Xu.

[92] Y. Li, H. He, X. Jia, W.-L. Lu, J. Lou and Y. Wei, *Biomaterials*, 2012, **33**, 3899 – 3908.

[93] G. Balasundaram, C. J. H. Ho, K. Li, W. Driessen, U. S. Dinish, C. L. Wong, V. Ntziachristos, B. Liu and M. Olivo, *International Journal of Nanomedicine*, 2015, **10**, 387–397.

[94] Q. Fan, K. Cheng, X. Hu, X. Ma, R. Zhang, M. Yang, X. Lu, L. Xing, W. Huang, S. S. Gambhir and Z. Cheng.

[95] J. Liu, J. Geng, L.-D. Liao, N. Thakor, X. Gao and B. Liu, *Polym. Chem.*, 2014, **5**, 2854–2862.

[96] K. Pu, A. J. Shuhendler, J. V. Jokerst, J. Mei, S. S. Gambhir, Z. Bao and J. Rao, *Nat Nano*, 2014, **9**, 233–239.

[97] K. Pu, J. Mei, J. V. Jokerst, G. Hong, A. L. Antaris, N. Chattopadhyay, A. J. Shuhendler, T. Kurosawa, Y. Zhou, S. S. Gambhir, Z. Bao and J. Rao, *Advanced Materials*, 2015, **27**, 5184–5190.

[98] J. Wang, R. Yan, F. Guo, M. Yu, F. Tan and N. Li, *Nanotechnology*, 2016, **27**, 285102.

[99] J. Rieffel, F. Chen, J. Kim, G. Chen, W. Shao, S. Shao, U. Chitgupi, R. Hernandez, S. A. Graves, R. J. Nickles, P. N. Prasad, C. Kim, W. Cai and J. F. Lovell, *Advanced materials (Deerfield Beach, Fla.)*, 2015, **27**, 1785–1790.

[100] E. Huynh, L. Y. C., B. L. Helfield, M. Shakiba, J.-A. Gandier, C. S. Jin, E. R. Master, B. C. Wilson, D. E. Goertz and G. Zheng, *Nat Nano*, 2015, **10**, 325–332.

[101] E. Huynh, C. S. Jin, B. C. Wilson and G. Zheng.

[102] K. K. Ng, M. Shakiba, E. Huynh, R. A. Weersink, A. Roxin, B. C. Wilson and G. Zheng.

[103] M. Shakiba, K. K. Ng, E. Huynh, H. Chan, D. M. Charron, J. Chen, N. Muhanna, F. S. Foster, B. C. Wilson and G. Zheng, *Nanoscale*, 2016, –.

[104] *Biomaterials ", volume* =.

[105] R. J. Paproski, A. Forbrich, E. Huynh, J. Chen, J. D. Lewis, G. Zheng and R. J. Zemp, *Small*, 2016, **12**, 371–380.

[106] H. Aoki, M. Nojiri, R. Mukai and S. Ito, *Nanoscale*, 2015, **7**, 337–343.

[107] S. P. Egusquiaguirre, N. Beziere, J. L. Pedraz, R. M. Hernandez, V. Ntziachristos and M. Igartua, *Contrast Media & Molecular Imaging*, 2015, **10**, 421–427.

[108] K. Miki, T. Inoue, Y. Kobayashi, K. Nakano, H. Matsuoka, F. Yamauchi, T. Yano and K. Ohe, *Biomacromolecules*, 2015, **16**, 219–227.

[109] *Biomaterials ", volume* =.

[110] *International Journal of Pharmaceutics", volume* =.

[111] J. V. Jokerst, D. V. de Sompel, S. E. Bohndiek and S. S. Gambhir, *Photoacoustics*, 2014, **2**, 119 – 127.

[112] F.-F. An, Z.-J. Deng, J. Ye, J.-F. Zhang, Y.-L. Yang, C.-H. Li, C.-J. Zheng and X.-H. Zhang.

[113] A. Taruttis, M. Wildgruber, K. Kosanke, N. Beziere, K. Licha, R. Haag, M. Aichler, A. Walch, E. Rummeny and V. Ntziachristos, *Photoacoustics*, 2013, **1**, 3 – 8.

[114] Q. Chen, X. Liu, J. Chen, J. Zeng, Z. Cheng and Z. Liu, *Advanced Materials*, 2015, **27**, 6820–6827.

[115] J. F. Lovell, C. S. Jin, E. Huynh, H. Jin, C. Kim, J. L. Rubinstein, W. C. W. Chan, W. Cao, L. V. Wang and G. Zheng, *Nat Mater*, 2011, **10**, 324–332.

[116] A. Hannah, G. Luke, K. Wilson, K. Homan and S. Emelianov.

[117] W. J. Akers, C. Kim, M. Berezin, K. Guo, R. Fuhrhop, G. M. Lanza, G. M. Fischer, E. Daltrozzo, A. Zumbusch, X. Cai, L. V. Wang and S. Achilefu, *ACS Nano*, 2011, **5**, 173–182.

[118] Q. Fan, K. Cheng, Z. Yang, R. Zhang, M. Yang, X. Hu, X. Ma, L. Bu, X. Lu, X. Xiong, W. Huang, H. Zhao and Z. Cheng, *Advanced Materials*, 2015, **27**, 843–847.

[119] S. Mallidi, T. Larson, J. Aaron, K. Sokolov and S. Emelianov, *Opt. Express*, 2007, **15**, 6583–6588.

[120] S. Mallidi, P. P. Joshi, K. Sokolov and S. Emelianov, 2009 Annual International Conference of the IEEE Engineering in Medicine and Biology Society, 2009, pp. 6338–6340.

[121] S. Mallidi, T. Larson, J. Tam, P. P. Joshi, A. Karpiouk, K. Sokolov and S. Emelianov.

[122] Z. Yasmin, E. Khachatryan, Y.-H. Lee, S. Maswadi, R. Glickman and K. L. Nash, *Biosensors and Bioelectronics*, 2015, **64**, 676 – 682.

[123] L. Jing, X. Liang, Z. Deng, S. Feng, X. Li, M. Huang, C. Li and Z. Dai, *Biomaterials*, 2014, **35**, 5814 – 5821.

[124] Q. Zhang, N. Iwakuma, P. Sharma, B. M. Moudgil, C. Wu, J. McNeill, H. Jiang and S. R. Grobmyer, *Nanotechnology*, 2009, **20**, 395102.

[125] R. Cheheltani, R. M. Ezzibdeh, P. Chhour, K. Pulaparthi, J. Kim, M. Jurcova, J. C. Hsu, C. Blundell, H. I. Litt, V. A. Ferrari, H. R. Allcock, C. M. Sehgal and D. P. Cormode, *Biomaterials*, 2016, **102**, 87 – 97.

[126] J. Song, J. Kim, S. Hwang, M. Jeon, S. Jeong, C. Kim and S. Kim, *Chem. Commun.*, 2016, **52**, 8287–8290.

[127] J. Vonnemann, N. Beziere, C. Böttcher, S. B. Riese, C. Kuehne, J. Dernedde, K. Licha, C. von Schacky, Y. Kosanke, M. Kimm, R. Meier, V. Ntziachristos and R. Haag, *Theranostics*, 2014, **4**, 629–641.

[128] E. Locatelli, W. Bost, M. Fournelle, J. Llop, L. Gil, F. Arena, V. Lorusso and M. Comes Franchini, *Journal of Nanoparticle Research", year=*.

[129] N. O. Mahmoodi, A. Ghavidast and N. Amirmahani, *Journal of Photochemistry and Photobiology B: Biology*, 2016, **162**, 681 – 693.

[130] S. Kim, Y. s. Chen, G. P. Luke and S. Y. Emelianov, *IEEE Transactions on Ultrasonics, Ferroelectrics, and Frequency Control*, 2014, **61**, 891–897.

[131] H. Yang, H. Liu, M. Li, I. Hsi, C. Fan, C. Huang, Y. Lu, M. Hua, H. Chou, J. Liaw, C. Ma and K. Wei, *Biomaterials*, 2013, **34(22)**, 5651–60.

[132] P. P. Joshi, S. J. Yoon, W. G. Hardin, S. Emelianov and K. V. Sokolov.

[133] J. V. Jokerst, M. Thangaraj, P. J. Kempen, R. Sinclair and S. S. Gambhir.

[134] J. V. Jokerst, A. J. Cole, D. Van de Sompel and S. S. Gambhir.

[135] S. Ha, A. Carson, A. Agarwal, N. A. Kotov and K. Kim, *Biomedical Optics Express*, 2011, **2**, 645–657.

[136] C. L. Bayer, Y.-S. Chen, S. Kim, S. Mallidi, K. Sokolov and S. Emelianov, *Biomedical Optics Express*, 2011, **2**, 1828–1835.

[137] A. Agarwal, X. Shao, J. R. Rajian, H. Zhang, D. L. Chamberland, N. A. Kotov and X. Wang, *Journal of Biomedical Optics*, 2011, **16**, 051307–051307–7.

[138] H. Moon, D. Kumar, H. Kim, C. Sim, J.-H. Chang, J.-M. Kim, H. Kim and D.-K. Lim.

[139] M. Zhang, H. S. Kim, T. Jin, A. Yi and W. K. Moon, *Biomedical Optics Express*, 2016, **7**, 1920–1931.

[140] H. Qin, Y. Zhao, J. Zhang, X. Pan, S. Yang and D. Xing, *Nanomedicine: Nanotechnology, Biology and Medicine*, 2016, **12**, 1765–1774.

[141] H. Chen, S. Yang, T. Zhou, J. Xu, J. Hu and D. Xing, *Nanomedicine: Nanotechnology, Biology and Medicine*, 2016, **12**, 1453–1462.

[142] W. Lu, M. P. Melancon, C. Xiong, Q. Huang, A. Elliott, S. Song, R. Zhang, L. G. Flores, J. G. Gelovani, L. V. Wang, G. Ku, R. J. Stafford and C. Li, *Cancer Research*, 2011, **71**, 6116–6121.

[143] L. Nie, S. Wang, X. Wang, P. Rong, Y. Ma, G. Liu, P. Huang, G. Lu and X. Chen, *Small*, 2014, **10**, 1585–1593.

[144] C. Kim, H.-M. Song, X. Cai, J. Yao, A. Wei and L. V. Wang, *J. Mater. Chem.*, 2011, **21**, 2841–2844.

[145] S. Liang, C. Li, C. Zhang, Y. Chen, L. Xu, C. Bao, X. Wang, G. Liu, F. Zhang and D. Cui, *Theranostics*, 2015, **5**, 970–984.

[146] K. Cheng, S.-R. Kothapalli, H. Liu, A. L. Koh, J. V. Jokerst, H. Jiang, M. Yang, J. Li, J. Levi, J. C. Wu, S. S. Gambhir and Z. Cheng.

[147] C. Bao, N. Beziere, P. del Pino, B. Pelaz, G. Estrada, F. Tian, V. Ntziachristos, J. M. de la Fuente and D. Cui, *Small*, 2013, **9**, 68–74.

[148] G. P. Luke, A. Bashyam, K. A. Homan, S. Makhija, Y.-S. Chen and S. Y. Emelianov, *Nanotechnology*, 2013, **24**, 455101.

[149] X. Cai, W. Li, C.-H. Kim, Y. Yuan, L. V. Wang and Y. Xia.

[150] A. Srivatsan, S. V. Jenkins, M. Jeon, Z. Wu, C. Kim, J. Chen and R. K. Pandey, *Theranostics*, 2014, **4**, 163–174.

[151] E. C. Cho, Y. Zhang, X. Cai, C. M. Moran, L. V. Wang and Y. Xia, *Angewandte Chemie International Edition*, 2013, **52**, 1152–1155.

[152] X. Xia, M. Yang, L. K. Oetjen, Y. Zhang, Q. Li, J. Chen and Y. Xia, *Nanoscale*, 2011, **3**, 950–953.

[153] C. Kim, E. C. Cho, J. Chen, K. H. Song, L. Au, C. Favazza, Q. Zhang, C. M. Cobley, F. Gao, Y. Xia and L. V. Wang, *ACS Nano*, 2010, **4**, 4559–4564.

[154] K. H. Song, C. Kim, C. M. Cobley, Y. Xia and L. V. Wang.

[155] Y. Jin, C. Jia, S.-W. Huang, M. O'Donnell and X. Gao, *Nat Commun*, 2010, **1**, 41.

[156] J. Lin, S. Wang, P. Huang, Z. Wang, S. Chen, G. Niu, W. Li, J. He, D. Cui, G. Lu, X. Chen and Z. Nie.

[157] S. Ye, G. Marston, J. R. McLaughlan, D. O. Sigle, N. Ingram, S. Freear, J. J. Baumberg, R. J. Bushby, A. F. Markham, K. Critchley, P. L. Coletta and S. D. Evans, *Advanced Functional Materials*, 2015, **25**, 2117–2127.

[158] J.-W. Kim, E. I. Galanzha, E. V. Shashkov, H.-M. Moon and V. P. Zharov, *Nat Nano*, 2009, **4**, 688–694.

[159] E. I. Galanzha, E. V. Shashkov, T. Kelly, J.-W. Kim, L. Yang and V. P. Zharov, *Nat Nano*, 2009, **4**, 855–860.

[160] J. Song, F. Wang, X. Yang, B. Ning, M. G. Harp, S. H. Culp, S. Hu, P. Huang, L. Nie, J. Chen and X. Chen.

[161] C. Wang, C. Bao, S. Liang, H. Fu, K. Wang, M. Deng, Q. Liao and D. Cui, *Nanoscale Research Letters*, 2014, **9**, 264.

[162] B. Zhang, C.-Y. Fang, C.-C. Chang, R. Peterson, S. Maswadi, R. D. Glickman, H.-C. Chang and J. Y. Ye, *Biomedical Optics Express*, 2012, **3**, 1629–1662.

[163] Y. Jin, Y. Li, X. Ma, Z. Zha, L. Shi, J. Tian and Z. Dai, *Biomaterials* , 2014, **35**, 5795 – 5804.

[164] L. Zhang, S. Gao, F. Zhang, K. Yang, Q. Ma and L. Zhu, *ACS Nano*, 2014, **8(12)**, 12250–12258.

[165] M. J. Berridge, M. D. Bootman and P. Lipp, *Nature*, 1998, **395**, 645–648.

[166] M. J. Berridge, *Nature*, 1993, **361**, 315–325.

[167] R. Y. Tsien, *Biochemistry*, 1980, **19**, 2396–2404.

[168] R. Tsien and T. Pozzan, in *Biomembranes Part S*, Academic Press, 1989, vol. 172, pp. 230 – 262.

[169] *The Journal of Cell Biology*, 1982, **94**, 325–334.

[170] G. Grynkiewicz, M. Poenie and R. Y. Tsien, 1985, **260**, 3440–3450.

[171] R. M. Paredes, J. C. Etzler, L. T. Watts and J. D. Lechleiter, *Methods (San Diego, Calif.)*, 2008, **46**, 143–151.

[172] K. L. Hyrc, A. Minta, P. R. Escamilla, P. P. Chan, X. A. Meshik and M. P. Goldberg, *Cell Calcium*, 2013, **54**, 320 – 333.

[173] K. Jahn and C. Hille, *PLoS ONE*, 2014, **9**, 1–13.

[174] M. Nasiriavanaki, J. Xia, H. Wan, A. Q. Bauer, J. P. Culver and L. V. Wang, *Proceedings of the National Academy of Sciences of the United States of America*, 2014, **111**, 21–26.

[175] J. Yao, L. Wang, J.-M. Yang, K. I. Maslov, T. T. W. Wong, L. Li, C.-H. Huang, J. Zou and L. V. Wang, *Nat Meth*, 2015, **12**, 407–410.

[176] J. N. D. Kerr and W. Denk, *Nat Rev Neuroscience*, 2008, **9**, 195–205.

[177] J. Sawinski, D. J. Wallace, D. S. Greenberg, S. Grossmann, W. Denk and J. N. D. Kerr, *Proceedings of the National Academy of Sciences*, 2009, **106**, 19557–19562.

[178] J. Tang, L. Xi, J. Zhou, H. Huang, T. Zhang, P. R. Carney and H. Jiang, *Journal of Cerebral Blood Flow & Metabolism*, 2015, **35**, 1224–1232.

[179] G. W. Gribble, *J. Chem. Soc., Perkin Trans. 1*, 2000, 1045–1075.

[180] H.-S. Mun, W.-H. Ham and J.-H. Jeong, *Journal of Combinatorial Chemistry*, 2005, **7**, 130–135.

[181] C. Lindquist, O. Ersoy and P. Somfai, *Tetrahedron*, 2006, **62**, 3439 – 3445.

[182] R. Sundberg, in *Indoles*, ed. R. Sundberg, Academic Press, London, 1996, pp. 1 – 6.

[183] R. C. Larock, E. K. Yum and M. D. Refvik, *The Journal of Organic Chemistry*, 1998, **63**, 7652–7662.

[184] C.-y. Chen, D. R. Lieberman, R. D. Larsen, T. R. Verhoeven and P. J. Reider, *The Journal of Organic Chemistry*, 1997, **62**, 2676–2677.

[185] Y. Dong and C. A. Busacca, *The Journal of Organic Chemistry*, 1997, **62**, 6464–6465.

[186] L. S. Hegedus, *Angewandte Chemie International Edition in English*, 1988, **27**, 1113–1126.

[187] G. Mann, J. F. Hartwig, M. S. Driver and C. Fernández-Rivas, *Journal of the American Chemical Society*, 1998, **120**, 827–828.

[188] A. Vasilev, T. Deligeorgiev, N. Gadjev, S. Kaloyanova, J. J. Vaquero, J. Alvarez-Builla and A. G. Baeza, *Dyes and Pigments*, 2008, **77**, 550 – 555.

[189] S. Druding, *Dye History from 2600 BC to the 20th Century*, Susan C. Druding, 1982.

[190] D. Razansky, N. Harlaar, J. Hillebrands, A. Taruttis, E. Herzog, C. Zeebregts, G. van Dam and V. Ntziachristos, *Mol Imaging Biol.*, 2012, **14(3)**, 277–85.

[191] H. Wang, C. Liu, X. Gong, D. Hu, R. Lin, Z. Sheng, C. Zheng, M. Yan, J. Chen, L. Caib and L. Song, *Nanoscale*, 2014, **6**, 14270–14279.

[192] G. Kim, S. Huang, K. Day, M. O'Donnell, R. Agayan, M. Day, R. Kopelman and S. Ashkenazi, *J Biomed Opt.*, 2007, **12(4)**, 044020.

[193] R. Y. Tsien, *Nature*, 1981, **290**, 527–528.

[194] N. Narayanan and G. Patonay, *The Journal of Organic Chemistry*, 1995, **60**, 2391–2395.

[195] S. B. Herzon, and A. G. Myers*, *Journal of the American Chemical Society*, 2005, **127**, 5342–5344.

[196] S. Kuster and T. Geiger, *Dyes and Pigments*, 2012, **95**, 657 – 670.

[197] L. Nie and X. Chen, *Chem. Soc. Rev.*, 2014, **43**, 7132–7170.

[198] S. Blechert, *Nachrichten aus Chemie, Technik und Laboratorium*, 1984, **32**, 45–45.

[199] S. Wagaw, B. H. Yang and S. L. Buchwald, *Journal of the American Chemical Society*, 1999, **121**, 10251–10263.

[200] S. Wagaw, B. H. Yang, and S. L. Buchwald, *Journal of the American Chemical Society*, 1998, **120**, 6621–6622.

[201] J. F. Hartwig, *Angewandte Chemie International Edition*, 1998, **37**, 2046–2067.

[202] B. Valeur and I. Leray, *Coordination Chemistry Reviews*, 2000, **205**, 3 – 40.

[203] L. Tei, Z. Baranyai, M. Botta, L. Piscopo, S. Aime and G. B. Giovenzana, *Org. Biomol. Chem.*, 2008, **6**, 2361–2368.

[204] R. B. Bedford, C. S. Cazin and D. Holder, *Coordination Chemistry Reviews*, 2004, **248**, 2283 – 2321.

[205] Z. Novak, P. Nemes and A. Kotschy, *Organic Letters*, 2004, **6**, 4917–4920.

[206] J. Li and P. Huang, *Beilstein Journal of Organic Chemistry*, 2011, **7**, 426–431.

[207] A. Smeyanov and A. Schmidt, *Synthetic Communications*, 2013, **43**, 2809–2816.

[208] P. Piatek, J. Kalisiak and J. Jurczak, *Tetrahedron Letters*, 2004, **45**, 3309 – 3311.

[209] J. Yuan, Y.-Q. Xu, N.-N. Zhou, R. Wang, X.-H. Qian and Y.-F. Xu, *RSC Adv.*, 2014, **4**, 56207–56210.

[210] J. L. Gragg, *Chem. Theses*, 2010, **28**, .

[211] A. Mishra, R. K. Behera, P. K. Behera, B. K. Mishra, and G. B. Behera, *Chemical Reviews*, 2000, **100**, 1973–2012.

[212] I. Davydenko, S. Barlow, R. Sharma, S. Benis, J. Simon, T. G. Allen, M. W. Cooper, V. Khrustalev, E. V. Jucov, R. Castañeda, C. Ordonez, Z. Li, S.-H. Chi, S.-H. Jang, T. C. Parker, T. V. Timofeeva, J. W. Perry, A. K.-Y. Jen, D. J. Hagan, E. W. V. Stryland and S. R. Marder, *Journal of the American Chemical Society*, 2016, **138**, 10112–10115.

[213] L. G. S. Brooker, G. H. Keyes, R. H. Sprague, R. H. VanDyke, E. VanLare, G. VanZandt, F. L. White, H. W. J. Cressman and S. G. Dent.

[214] D. Dougherty, R. Grubbs and C. REGAN, *Photoacid compounds, and related compositions, methods and systems*, 2013, `https://www.google.com/patents/WO2013086460A1?cl=en`, WO Patent App. PCT/US2012/068,629.

[215] J. McOmie, M. Watts and D. West, *Tetrahedron*, 1968, **24**, 2289 – 2292.

[216] A. Mishra, Y. Jiang, S. Roberts, V. Ntziachristos and G. G. Westmeyer, *Analytical Chemistry*, 2016, **88**, 10785–10789.

[217] A. Smeyanov and A. Schmidt, *Synthetic Communications*, 2013, **43**, 2809–2816.

[218] M. Desroses, K. Wieckowski, M. Stevens and L. R. Odell, *Tetrahedron Letters*, 2011, **52**, 4417 – 4420.

[219] S. Miltsov, V. Karavan, M. Goikhman, I. Podeshvo, S. G. de Pedro, M. Puyol and J. Alonso-Chamarro, *Dyes and Pigments*, 2014, **109**, 34 – 41.

[220] M. Y. Goikhman, N. P. Yevlampieva, N. V. Kamanina, I. V. Podeshvo, I. V. Gofman, S. A. Mil'tsov, A. P. Khurchak and A. V. Yakimanskii, *Polymer Science Series A*, 2011, **53**, 457–468.

[221] M. A. Williams and H. Rapoport, *The Journal of Organic Chemistry*, 1993, **58**, 1151–1158.

[222] L. Zuo, S. Yao, W. Wang and W. Duan, *Tetrahedron Letters*, 2008, **49**, 4054 – 4056.

[223] H. Ishii, H. Takeda, T. Hagiwara, M. Sakamoto, K. Kogusuri and Y. Murakami, *J. Chem. Soc., Perkin Trans. 1*, 1989, 2407–2414.

[224] M. TANI, T. ARIYASU, M. OHTSUKA, T. KOGA, Y. OGAWA, Y. YOKOYAMA and Y. MURAKAMI, *CHEMICAL & PHARMACEUTICAL BULLETIN*, 1996, **44**, 55–61.

[225] Y. Li-Smerin, E. S. Levitan and J. W. Johnson, *The Journal of physiology*, 2001, **533**, 729–43.

[226] C. J. Frederickson, S. W. Suh, D. Silva, C. J. Frederickson and R. B. Thompson, *The Journal of Nutrition*, 2000, **130**, 1471S–1483S.

[227] Y. V. Li, *Endocrine*, 2014, **45**, 178–189.

[228] J. T. Alander, I. Kaartinen, A. Laakso, T. Pätilä, T. Spillmann, V. V. Tuchin, M. Venermo and P. Välisuo, *International Journal of Biomedical Imaging*, 2012, **2012**, year.

[229] S. Hu and L. Wang, *Frontiers in Neuroenergetics*, 2010, **2**, 10.

[230] C. D. WILMS and J. EILERS, *Journal of Microscopy*, 2007, **225**, 209–213.

[231] A. C. Durham and J. M. Walton, *Cell Calcium*, 1983, **4**, 47 – 55.

[232] E. J. Cooley, P. Kruizinga, D. W. Branch and S. Emelianov, *Proc. of SPIE*, 2010, **7576**, 75761J–75761J–8.

[233] M. Oheim, M. van 't Hoff, A. Feltz, A. Zamaleeva, J.-M. Mallet and M. Collot, *Biochimica et biophysica acta*, 2014, **1843**, 2284—2306.

[234] M. Seeger, A. Karlas, D. Soliman, J. Pelisek and V. Ntziachristos, *Photoacoustics*, 2016, –.

[235] P. Piatek, J. Kalisiak and J. Jurczak, *Tetrahedron Letters*, 2004, **45**, 3309–3311.

[236] J. Kalisiak, P. Skowronek, J. Gawroński and J. Jurczak, *Chemistry – A European Journal*, 2006, **12**, 4397–4406.

[237] J. Oriou, F. Ng, G. Hadziioannou, G. Garbay, M. Bousquet, L. Vignau, E. Cloutet and C. Brochon, *Polym. Chem.*, 2014, **5**, 7100–7108.

[238] M. Takase and M. Inouye, *Molecular Crystals and Liquid Crystals Science and Technology. Section A. Molecular Crystals and Liquid Crystals*, 2000, **344**, 313–318.

[239] H. Langhals, D. Zgela and R. Lueling.

[240] M. Best, I. Porth, S. Hauke, F. Braun, D.-P. Herten and R. Wombacher, *Org. Biomol. Chem.*, 2016, **14**, 5606–5611.

[241] G. Y. Mitronova, V. Belov, M. Bossi, C. Wurm, L. Meyer, R. Medda, G. Moneron, S. Bretschneider, C. Eggeling, S. Jakobs and S. Hell, *Chemistry – A European Journal*, 2010, **16**, 4477–4488.

[242] A. R. Ballestas-Barrientos, A. W. Woodward, W. V. Moreshead, M. V. Bondar and K. D. Belfield, *The Journal of Physical Chemistry C*, 2016, **120**, 7829–7838.

[243] S. Sreejith, J. Joseph, M. Lin, N. V. Menon, P. Borah, H. J. Ng, Y. X. Loong, Y. Kang, S. W.-K. Yu and Y. Zhao, *ACS Nano*, 2015, **9**, 5695–5704.

[244] I.-T. Ho, J. L. Sessler, S. S. Gambhir and J. V. Jokerst, *Analyst*, 2015, **140**, 3731–3737.

List of Figures

List of Tables

List of publications

First author publication

Sheryl Roberts, Markus Seeger, Yuanyuan Jiang, Anurag Mishra, Felix Sigmund, Anja Stelzl, Antonella Lauri, Panagiotis Symvoulidis, Matthias Preller, X. Luís Deán-Ben, Daniel Razansky, Tanja Orschmann, Sabrina Desbordes, Paul Vetschera, Thorsten Bach, Vasilis Ntziachristos and Gil G. Westmeyer*, "Calcium Sensor for Photoacoustic Imaging," *Journal of the American Chemical Society*, in revision, 2017.

Co-author publications

Anurag Mishra*, Yuanyuan Jiang, **Sheryl Roberts**, Vasilis Ntziachristos, Gil G. Westmeyer*, "Near-Infrared photoacoustic imaging probe responsive to calcium," *Analytical Chemistry*, 2016, 88, 10785–10789.

Workshops

"Two-photon functional imaging in the living brain: theory and practice," Sept. 07-14th, 2014, Chongqing, China.

"EXCITE Summer School on Biomedical Imaging," Sept. 05-16th, 2016, Zürich, Switzerland.

Acknowledgements

I thank everyone who has been part of this journey, directly and indirectly. You know who you all are.

Foremost, my deepest gratitude to my PhD mentor, Prof. Gil Gregor Westmeyer, Institute of Biological and Medical Imaging, Helmholtz Zentrum Muenchen, for his invaluable guidance, providing valuable insights into our projects and providing me the facilities during the course of the investigation. With that, I extend my gratitude to my closest colleagues, Yuanyuan, Anurag, Ahne, Antonella, Anja, Michele, Carlos, Felix, Chris and Hannes whom I shared the past four years with, always learning and growing together. I have learnt many valuable biological experimental methods within this laboratory, mainly from Antonella, Felix, Chris and Anja. To Yuanyuan for introducing and showing me how photoacoustic imaging equipment works. Many thanks to Michelle (and Ahne) for teaching me how to write in LaTeX. Thanks especially to Anurag Mishra for believing in me, you were my foundation to my day-to-day work. Ahne Myklatun and Antonella Lauri, two amazing women in Science who I have gotten to know and lucky to have as not only colleagues but also whom I consider as best of friends.

I express my sincere gratitude to Prof. Thorsten Bach, Chair for Organic Chemistry, Technical University of Munich, for his support, guidance and to all those monthly meetings, together with Dr. Tomas Kubelka, which gave me invaluable insights and help in performing and designing chemical synthesis. A sincere thanks to Prof. Vasilis Nziachristos, Chair for Biological Imaging, Technical University Munich for his guidance, co-operation and providing the facilities and scientific environment during my course of investigation.

I thank and acknowledge the Laura Bassi Award, Technical University Munich, for supporting me with my studies for one year. I thank the Life Science and Technology programme, specifically Dessi Zlatanova, for allowing me to be part of it and giving me the opportunity to enhance my work through multi-disciplinary training and courses.

Last Updated on 22nd July 2017

Sheryl Roberts

de.linkedin.com/in/sherylroberts
sheryl.roberts@tum.de | +1.646.886.1794

EDUCATION

TU MÜNCHEN
PHD IN MEDICAL LIFE SCIENCES & TECHNOLOGY
Expected Sept 2017 | Munich, Germany

UNIVERSITY OF ST. ANDREWS
MCHEM CHEMISTRY WITH MEDICINAL CHEMISTRY
Sept 2006- June 2011 | St. Andrews, Scotland
Organic chemistry
Industrial Placement
PUBLICATION: Heterocycles, 2014, 88, 1135-1147.

LINKS

LinkedIn:// sheryl.roberts
Twitter:// @ImagingT
TUM:// reseach
Helmholtz Zentrum:// research

TRAINING

GRADUATE
Preclinical Imaging
Basic Principles of Light Microscopy
Human in-vivo multimodal neuroimaging
Neuroscience
Principles of neurobiological imaging& engineering
Molecular Medicine
Basic Proteomics
Statistics

UNDERGRADUATE
Advanced Pharmaceutical
Synthetic Methodology
Molecular Recognition
Natural Products
Asymmetric Catalysis
Mini Chemistry Project (Research Asst.)
Chemical Biology

SKILLS

ChemBioDraw Ultra
ChemAxon • SciFinder •
ACD Labs 12.0 • Adobe Illustrator •
OriginPro 7.5 • AMIDE • Matlab •
LaTeX

EXPERIENCE

TU MÜNCHEN | PHD RESEARCHER
Expected Nov 2013 – Sep 2017 | Munich, Germany
- Ranked 1st PhD candidate, included a 1 year monetory award for research.
- PUBLICATIONS: Mishra et. al., Analytical chemistry, 2016; Roberts et. al., JACS, in revision, 2017

HELMHOLTZ ZENTRUM MÜNCHEN | GUEST CHEMICAL RESEARCHER
Nov 2012 – Sept 2016 | Munich, Germany
- Enhancing the use of OA technologies by developing novel and e ective CAs.
- Collaborative German research on the highest scientific level.

EUROPEAN PATENT OFFICE (EPO) | SCIENCE & ENGINEERING PROGRAMME
Oct 2011 – May 2012 | Munich, Germany
- Complex patent re-classifications in the field of homogeneous catalysis.
- Received patent related training & other areas of intellectual property (IP) law.

AGFA GEVAERT N.V | INDUSTRIAL PLACEMENT
Sept 2009 – Aug 2010 | Antwerpen, Belgium
- Identifed the key factors and processes in achieving max. sensitivity of chemical systems in printing plates using Hansen solubility parameters (HSP).

RESEARCH

INSTITUTE OF MEDICAL & BIOLOGICAL IMAGING | PHD TRAINING
Nov. 2012 – Present | Munich, Germany
- Developing and synthesising novel functional optoacoustic contrast agents.
- Key skill sets: Adept at synthetic design schemes, syntheses and optimization of key target functional small molecules.
- Extensive knowledge in heterocyclic NIR organometallic chemistry, air & light sensitive reactions, scale-up activities & project management
- Skilled at validation of novel small molecules (NMR, ESI-LCMS, pur cation, chromatographic & UV/Vis & fluorescent spectroscopic techniques.
- Experienced in in-vitro evaluation of probes on cell model studies.
- Experienced in in-vivo evaluation of CAs in relevant biological model.

AWARDS

2016	Laura Bassi Award
2016	EXCITE Summer School Biological Imaging
2015	European Molecular Imaging Conference
2014	Sino-German Summer Course
2013	Life Science and Technology Award
2013	Medical Life Science and Technology Programme
2009	Erasmus+ mobility award

SOCIETIES

2015- present	Assistant Teacher	HMGU Dancing Club
2007- present	MRSC	Royal Society of Chemistry
2014- present	Women Right's Campaign	Amnesty International